CHEMISTRY OF *PNP* BIS(PHOSPHIDE) PINCER LIGANDS

and

PALLADIUM(II) DIMERS AS ROBUST, VERSATILE PRECATALYSTS FOR OLEFIN ISOMERIZATION, OLIGOMERIZATION, AND OXIDATION

Thesis by

Matthew S. Winston

In Partial Fulfillment of the Requirements

For the Degree of

Doctor of Philosophy

California Institute of Technology

Pasadena, California

2013

(Defended October 1, 2012)

To Grandpa Stu

ACKNOWLEDGEMENTS

Now here is the part of my thesis that I have been thinking about since the first day I arrived at Caltech. Depending on your outlook, this section may be just as important as the rest of the thesis, as it is an excellent measure of my own personal growth in the last 5 years. Sure, the science beckons me to this place, but when the science does not work, it is the relationships I have made with others that convince me to stay.

John Bercaw's shining reputation in the scientific community is every bit earned. He is a mentor's mentor (literally… the Bercaw mafia is spread far and wide, from Canada to South America, and more than a few alum in Europe), a beacon of scientific integrity, and, without a doubt, one of the most creative and forward-thinking scientists I have ever known. Although I will never reach John's intellectual heights, he has taught me to think critically about chemistry. Even more importantly, he has taught me to think constructively. All this stems from his commitment to mentorship in and outside of the classroom. Perhaps this is why he allowed an organic chemist who wanted to learn a little bit more about organometallic mechanism into his group…. I cannot express enough gratitude to John for his guidance and support.

Where John is Captain Kirk, Jay Labinger is Mr. Spock. Scholarly and wise, Jay is an integral part of the lab who technically works in another building. His knowledge of the literature is astounding, even intimidating, but more importantly, he has uncanny scientific instincts. Like an oracle, Jay knows what will work and what will not. Chemistry has a long and storied history, but it is often overlooked by experimentalists

for more current pursuits. Jay is a historian, and his appreciation of the history of our science has inspired me to embrace it as well. Working closely with John and Jay, I truly feel that I am standing on the shoulders of giants.

Something must be said about Brian Stoltz, whose group I was a member of for a year and a half. It was from him that I learned proper organic technique and how to approach the synthesis of a complex molecule. Brian's door is never closed, and he is always eager to discuss science because he is constantly thinking about it. His lab was an ideal place for a first year, and it made an indelible impression upon me.

My committee has provided invaluable insight into my scientific proposals, which will ultimately be used when I apply for jobs. Thank you to Sarah Reisman, Jonas Peters, and Bob Grubbs for your time and consideration!

The Bercaw group is and always has been a colorful cast of characters. Do they intrinsically gravitate toward our group, or does the group change them? After all, where else will you find someone who recreationally drinks two liters of soda in an hour? Everyone is approachable, open, and willing to discuss chemistry, and, perhaps most importantly, supportive of one another. A great result is celebrated by all, a rejected paper mourned; for better or worse, everyone has a personal stake in each other's work.

Some words to those who sit in my sphere of influence: the Knitting Circle (the KC) has a collective, dynamic personality that changes when someone leaves and someone new arrives. The equilibrium is perturbed even when someone has woken up on the wrong side of the bed. This current KC incarnation — Rachel Klet, Taylor Lenton, Dave Leitch, and I — is unstoppable. We discuss our respective projects, scientific ideas,

life goals, and weekend plans with each other, and nothing is more amusing than seeing four people crowd around a computer to look at a single NMR spectrum. Amaruka Hazari was an integral member of our circle and a great friend. I still roll into work expecting to see her, and am legitimately disappointed every time I realize she won't be coming in. Finally, Suz Golisz made me feel welcome in my first days as an "organic transplant".[1]

Thanks to everyone else I overlapped with for your enthusiasm for chemistry and commitment to rigorous scientific thinking. I have learned something from each of you. A special thanks to Loi Do (who no doubt will trailblaze in his independent scientific career), Ted Weintrob (the most enthusiastic man I have ever met with a practical or chemical solution to every problem), Ian Tonks (the second most enthusiastic man I have ever met), Paul Oblad (who generously allowed me to jump on the hydroxy dimer bandwagon) and Carl "Let's-Go-to-the-Ath" Laskowsi; these friendships are important to me — you kept me grounded — and I hope you remember little old me when you all are off shaking the Earth. Everyone I overlapped with really ought to be thanked in their own special way, since they all had a positive effect on me. Suffice it to say, I am indebted to all of you.

Hosea Nelson, Gloria Sheng, Liz Santori, and Jevgenij Raskatov have accepted me at my lowest lows, and never turned a deaf ear when I was singin' them grad school blues. My first friend here, Allen Hong, is more of a brother to me. We have had similar graduate school experiences and share a love for Asian cuisine from questionably sanitary restaurants. He brings me out of the doldrums. Allen is an endless source of

[1] Dr. Ned West (March 2009).

ideas, and his creativity and synthetic abilities will take him far. Perhaps one day he will hire me. Kevin Allan… How does he make it look so simple? This guy synthesizes complex molecules like it is going out of style. Kevin has been a pillar of support and inspiration for me in and outside of the lab, and I only wish we could have overlapped at Caltech for more time.

Young In Oh, graduate school would have been miserable without your unwavering support. You helped me delineate my professional life from my personal life; each day, regardless of whether the science worked or failed, my personal life remained happy and healthy. You are a constant reminder that there are more important things than work.

Finally, my family must be thanked for their love and support.

ABSTRACT

The first half of this thesis details the synthesis and coordination chemistry of a very unusual pyridine-linked bis(secondary phosphine) pincer ligand system. Despite the highly nucleophilic phosphide donors, this dianionic system is an unexpectedly poor pincer ligand. Crystallographic and DFT studies reveal that both phosphide→metal σ- and π-bonding is compromised by long metal-phosphorus bonds, which result in significant distortions to the chelate ring. The neutral ligand coordinates readily κ^2 (via phosphines) to late metals, such as palladium(II), affording *P*-chirogenic diastereomers. Crystallographic and spectroscopic analysis of a series of palladium(II) dihalides stabilized by this bis(phosphine) indicate that one diastereomer is enthalpically favored, while the other more structurally versatile diastereomer is favored entropically. There is also evidence of an interesting phosphine epimerization pathway assisted by the non-coordinated pyridine ring.

Ethylene polymerization and ethylene/1-hexene copolymerization activities of several zirconium(IV) and vanadium(III) polymerization precatalysts supported by heterocycle-linked bis(phenolate) ligands are also discussed. Activities as high as 10^6 g PE/(mol•h) were observed, but only the vanadium catalyst incorporates comonomer, albeit with low efficiency (<1 mol%).

Finally, catalytic applications of air- and water-tolerant bis(μ-hydroxy) palladium(II) dimers have been investigated. Mechanistic studies show that this precatalyst can oxygenate olefins via a Wacker-type mechanism upon dimer dissociation. In the absence of stoichiometric oxidant, the resulting palladium(II) hydride intermediate

can then isomerize and oligomerize olefins with turnover numbers at room temperature as high as 2100/h and 600/h, respectively. We also show that the catalyst is insensitive to water and air, so that olefin isomerization and oligomerization can be carried out on the benchtop in the absence of activators. In the presence of excess *tert*-butylhydroperoxide, Wacker-type behavior is favored, and neither isomerization nor oligomerization is observed. These dimers can also catalyze the aerobic dehydrogenation of cyclohexene to benzene with relatively low turnover numbers (1/h). Nevertheless, mechanistic studies indicate a C-H activation/β-hydride elimination sequence that does not involve an allylic-activated species.

TABLE OF CONTENTS

LIST OF FIGURES

Chapter 1. Dianionic Bis(Phosphido) Pincer Ligands for High-Valent Early Transition Metals

Chapter 2. Synthesis, Solid-State, and Solution-State Behavior of a Palladium(II) Halide Series Supported by a Structurally Versatile Bidentate Bis(Secondary Phosphine) Ligand

LIST OF SCHEMES

LIST OF TABLES

GENERAL INTRODUCTION

The studies presented in this thesis appear to be tenuously connected, but were each initiated for the same fundamental reason: to develop and understand transition metal catalysts for the conversion of cheap, carbon feedstocks to value-added products. Polyethylene, polypropylene, and polystyrene are ubiquitous materials found in many households. Their rate of production exceeds 10^{11} pounds per year using traditional Ziegler-Natta catalysts.[1] Likewise, olefin oligomerization processes, such as the Shell higher olefin process, produces valuable products that may be taken on to fuel, plasticizers, detergents, and lubricants. The importance of new transition metal complexes to catalyze both polymerization and oligomerization cannot be overstated, given the growing catalyst "patent minefield"[2] and an increased need for material with new and interesting properties.

Chapters 1 and 2 detail the synthesis, properties, and coordination chemistry of a very unusual ligand that we had initially pursued to confer properties favorable to a class of non-metallocene early metal polymerization catalysts developed in our laboratory. Chapter 3 discusses the ethylene polymerization and ethylene/1-hexene copolymerization behavior of said class of catalysts. Finally, Chapter 4 presents investigations into the mechanism and reaction behavior of late transition metal oligomerization catalysts that do not require any activator to initiate.

REFERENCES

1. Golisz, S. R.; Bercaw, J. E. *Macromolecules* **2009**, *42*, 8751.
2. Gibson, V. C.; Spitzmesser, S. K. *Chem. Rev.* **2003**, *103*, 283.

CHAPTER 1

Dianionic Bis(Phosphido) Pincer Ligands for High-Valent Early Transition Metals

Parts of this work appear in:

Winston, M. S.; Bercaw, J. E. *Organometallics* **2010**, *29*, 6408.

ABSTRACT

A dianionic pyridine-linked bis(phosphido) pincer ligand (PNP^{2-}) has been synthesized. Unlike its bis(amine) congener, the donating atom of the neutral, non-coordinated bis(secondary phosphine) ligand is chirogenic. Characterization of the ligand by NMR spectroscopy reveals a 1:1 mixture of non-interconverting *rac* and *meso* bis(secondary phosphine) diastereomers, but coordination of the dianionic form to potassium and zirconium allows for isolation of a single diastereomer in nearly quantitative yield. The crystallographic structure of a PNP-supported bis(dimethylamido)zirconium(IV) complex, as well as DFT calculations, suggest that the phosphides do not π-bond to early transition metals, primarily due to long Zr-P bonds that result in geometric strain of the six-membered chelate. Furthermore, despite the increased nucleophilicity of phosphides, PNP σ-bonding to zirconium(IV) is also compromised by the distortions of the ligand to accommodate metal coordination. As a result, the phosphide donors are prone to bridging to other metal centers, forming oligomeric products. These investigations provide insight into the nature of rare bis(phosphide) pincer ligand bonding to early metals, and suggest that future studies and ligand development should focus on bis(phosphide) pincers capable of less strained five-membered chelates.

INTRODUCTION

The last half-century has seen impressive developments in olefin polymerization catalysis.[1] In particular, studies of well-behaved, single-site Group 4 metallocene catalysts have provided valuable insight into not only the nature of the catalytically active species, but the relationship between catalyst structure and resulting polymer architecture.[2] Indeed, metallocenes can adopt a wide variety of symmetries to allow strict stereotactic control of growing polypropylene chains. Because these systems are so well understood, the rational design of metallocene ligand frameworks to access unusual polymers has saturated the patent polymerization literature. To harness the potential of other metals to polymerize olefinic monomers, including late metals, there has been an increased interest in using well-defined polydentate *non-metallocene* ligand sets to support transition metal catalysts.[3]

Non-metallocenes pose several advantages over metallocene ligands. First, metallocenes are often synthetically cumbersome to access and modify.[3] Issues of regioselectivity often plague their synthesis, and planar chirality upon metalation can result in diastereomeric metal complexes. Alternatively, many non-metallocenes can be synthesized using sequences of well-behaved, high-yielding reactions — such as Pd-catalyzed cross-coupling — to install functional groups, allowing for fast modification to the ligand for catalyst screening studies. Both metallocenes and non-metallocenes offer a wide variety of symmetries, but non-metallocenes are not restricted to anionic carbon donors (such as cyclopentadienyl anion.) Ligand sets coordinating via combinations of anionic and neutral nitrogen and oxygen group members have thus been explored.[3] While these traits are particularly desirable for developing catalysts that affect new

stereocontrolled reactions, gross changes in ligand architecture necessitate new understanding of how the scaffold affects the physical properties of a polymer.

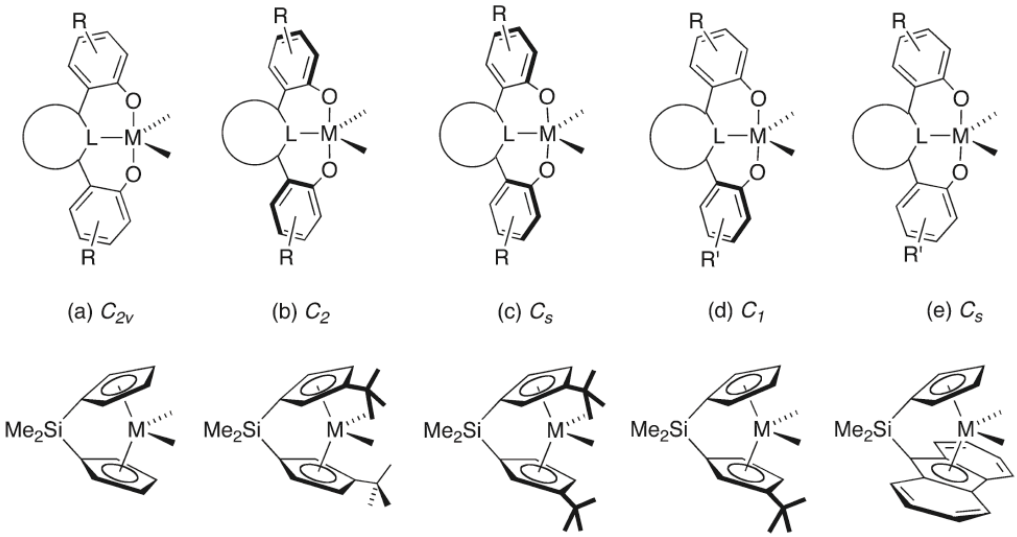

Figure 1.1. Like metallocenes, complexes supported by heterocycle-linked bis(phenolate) ligands can achieve a wide variety of geometries. Figure from reference 4a.

Some of the most successful non-metallocene polymerization catalysts are supported by polydentate anilide and phenolate ligands. In light of these findings, our group reported in 2008 that Group 4 and Group 5 metal complexes supported by tridentate heterocycle-linked bis(phenolate) ligands can polymerize propylene with good to excellent activity in the presence of methylaluminoxane (MAO).[4a-c] Importantly, these ligand sets are connected through sp^2-sp^2 aryl-heterocycle linkages instead of more flexible sp^3-sp^3 linkages, imparting ligand rigidity. Not only are the frontier molecule orbitals of complexes supported by these ligands similar to metallocenes, but they can

achieve a wider range of symmetries depending on the phenolate ligand twist angles (Figure 1.1).

A series of tantalum amine, amido, and imido complexes supported by pyridine-linked bis(phenolate) ligands were synthesized to study the relationship between phenolate-metal π-bonding and solid-state geometry of the metal complex.[5] X-ray crystallographic analysis, DFT calculations, and molecular orbital considerations reveal that the preference for C_s-symmetry results from strong phenolate-Ta π-bonding. On the other hand, C_2-symmetry is preferred in complexes in which phenolate-Ta π-bonding is overridden by stronger ancillary ligand N-Ta π-bonding (Table 1.1). Unlike metallocenes, pyridine-linked bis(phenolate) pincer ligands are not strong enough π-bonding to exert dominant control over the electronic and geometric properties of the complex.

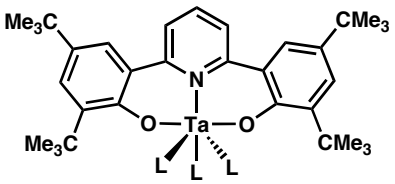

L_3 for (ONO)TaL_3	symmetry	# of Ta=L p-bonds	average TaO bond order	d(TaO)$_{ave}$ (Å)
(NPh)(NHPh)(NH_2Ph)	C_2	3	1	2.002(1)
(NMe_2)$_3$	C_2	3	1	1.985(2)
(NMe_2)$_2$Cl	C_s	2	1.5	1.924(3)
(NPh)($NHMe_2$)Cl	C_s	2	1.5	1.954(2)
(NPh)(NH_2Ph)Cl	C_s	2	1.5	1.948(3)
(NMe_2)(CH_3)Cl	C_s	1	2	1.887(2)
(=CHPh)(CH_2Ph)(PR_3)	C_s	1	2	1.922(1)
(CH_3)$_3$	C_s	0	2	1.906(1)

Table 1.1. Selected geometric parameters of pyridine-linked bis(phenolate)-supported tantalum(V) amine, amido, and imido complexes. Table adapted from reference 5.

The geometric dependence on ancillary ligand p-bonding can be rationalized using molecular orbital theory (Figure 1.2). C_s-symmetric bis(phenolate) ligands can π-bond through p_z and p_y atomic orbitals on oxygen to the d_{xz} and d_{xy} orbitals on tantalum, respectively. In the case of mono(amide) bis(phenolate)-stabilized tantalum complexes, the O-Ta π-bonding interactions are strong enough to force the amide to π-bond with d_{yz}, despite the steric interactions arising between the amide methyls and bulky phenolate *tert*-butyl groups. While two strong N-Ta π-bonds (as in the amide tantalums complex) sacrifice phenolate π-bonding into the tantalum d_{xy} orbital, it preserves the O-Ta π-bonding interaction involving the d_{xz} orbital of the metal. When there are three N-Ta π-bonds (as in the amide-imide tantalum complexes), the remaining O-Ta π-bonding interaction involving the tantalum d_{xz} orbital is sacrificed to allow π-bonding with the amide p_x orbital. As the phenolate-tantalum interaction becomes exclusively σ-bonding, the O-Ta bond length increases. A shift from C_s to C_2-symmetry accommodates the lengthened bonds between the phenolate ligands and the large tantalum atom. Furthermore, twisting to C_2-symmetry avoids electronically unfavorable filled-filled orbital repulsion between the full amide p_x-d_{xz} molecular orbital and the bonding orbital involving the phenolate p_z orbital.

While the symmetries of Group 4 and Group 5 bis(phenolate)-supported precatalysts are observed in the solid state, propylene polymerization using C_2-symmetric precatalysts yields stereoirregular, atactic polypropylene. The lack of stereocontrol exhibited by these bis(phenolate)-supported catalysts suggests the ligand scaffold may not be geometrically rigid enough to impart enantiomorphic site control. Despite the rigorous analysis of the solid-state geometries of hexacoordinate tantalum complexes

discussed above, the molecular orbital-based argument may not accurately describe the relationship between pincer ligand π-bonding to the metal and the overall geometry of the *cationic active catalyst* upon treatment with MAO. On the other hand, perhaps the argument holds for the active species, yet the effects of phenolate-metal π-bonding (favoring C_s-symmetry) and six-membered ring strain (favoring C_2-symmetry) are simply comparable.

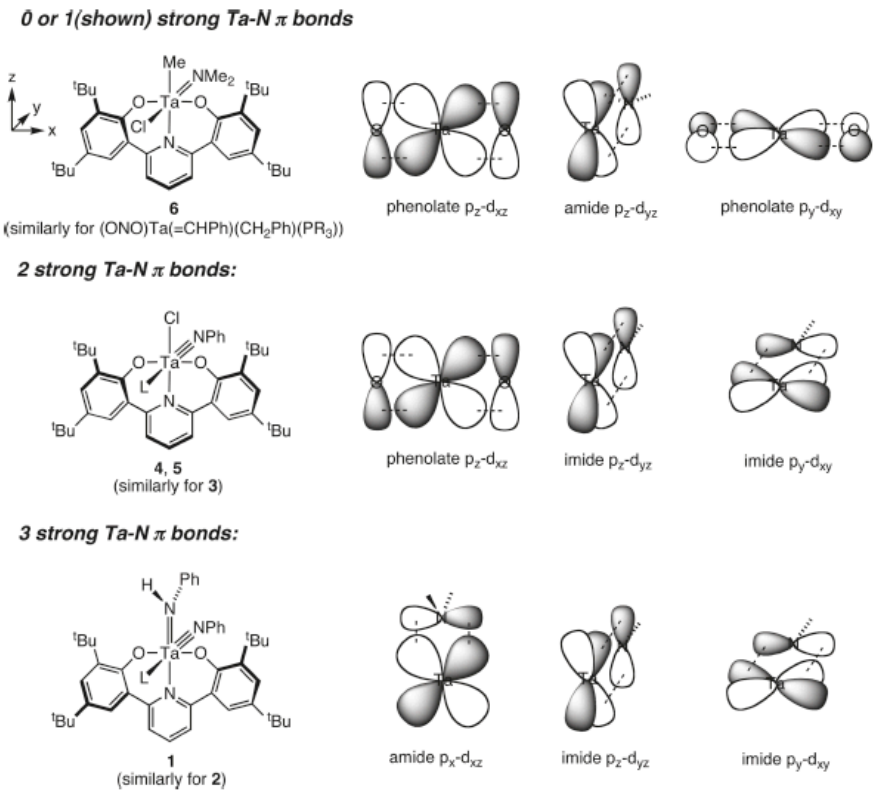

Figure 1.2. Bonding model describing the relationship between phenolate O-Ta π-bonding and overall geometry. Greater O-Ta π-bonding favors C_s symmetry, while C_2 symmetry is favored by complexes engaged in weaker O-Ta π-bonding (and stronger N-Ta π-bonding.) Figure from reference 5.

To investigate related frameworks where electronic factors may completely dominate the solution-state geometry of active catalysts, metal complexes stabilized by pincer ligands with more electron-donating pyridine-linked bis(anilides) (NNN) were synthesized and evaluated as propylene polymerization catalysts.[4c] However, x-ray crystallographic studies and DFT analysis reveal that, unlike related bis(phenolate) complexes, six-coordinate bis(anilide) metal complexes do not adopt C_s-symmetry. The bis(anilide) geometry in the solid state seems dictated entirely by chelate ring strain, not metal-ligand π-bonding, and as such, retains C_2-symmetry when complexed to Group 4 metals, regardless of ancillary ligand. In addition to longer anilide N-M bonds (relative to phenolate O-M bonds), it is also possible that anilide substitution encourages C_2-twisting to avoid the steric clash that would otherwise destabilize a C_s-symmetric complex. Unfortunately, Group 4 bis(anilide) complexes provide stereoirregular, atactic polypropylene in poor to moderate yield (10^2–10^4 g/mol•h) when activated by MAO — a consequence perhaps of fluxional geometry of the active catalyst in solution.

If the degree of π-donation from the pincer ligand to the metal indeed enforces overall symmetry of the complex, pincer ligands with anionic, highly nucleophilic third row donors could in fact provide more electronic bias than their second row congeners for one geometry over the other. Therefore, in hopes of developing a rigid, non-fluxional active catalyst, we turned our attention to a pyridine-linked bis(phosphide) (PNP) ligand analogous to the bis(anilide) (NNN) ligand discussed above. Due to the scarcity of reported bis(phosphides), we hoped to also gain insight into the solution-state behavior and diastereomerism of the non-coordinated ligand PNP-H_2. In addition, the coordination

chemistry of even rarer dianionic bis(phosphide) *pincer* ligands with early transition metals could be probed.

The chemistry of phosphines is largely centered on the ability of the nucleophilic *P*-centered lone pair to form new bonds to electrophilic centers.[6] In particular, tertiary phosphines are often used as ligands to stabilize transition metal complexes. Their relatively straightforward synthesis allows steric and electronic tuning, and access to optically active phosphines with chiral substituents.[7] Although both phosphines and their amine congeners have pyramidal geometries, inversion occurs rapidly at room temperature for amines. In contrast, phosphine inversion has an energy barrier of 30–35 kcal/mol, making it immeasurably slow at room temperature; even at 130 °C, the half-life of a simple tertiary phosphine is about 3.5 hours.[8] This unique property allows the synthesis and isolation of *P*-chiral phosphines, which are often used as ligands in metal-catalyzed asymmetric processes.

Secondary phosphines and their conjugate phosphides, on the other hand, are far less explored as ligands than tertiary phosphines or amine/amide congeners.[9] Their biological toxicity and sensitivity toward autoxidation requires rigorously air-free handling and storage, and their synthesis often involves sensitive, reactive intermediates and protecting groups for purification.[10] While some secondary phosphines may be accessed by reductive cleavage of either diphosphine P-P bonds or tertiary phosphine C-P bonds,[11] most are derived from the reduction of chlorophosphines.[12] These precursors are often synthesized by careful organomagnesium addition to PCl_3. While reductions of chlorophosphines to install P-H bonds are typically high yielding, the sensitive products are often purified by vacuum distillation or chromatography in degassed solvents under

inert gas. To ameliorate their reactivity and simplify their purification, secondary phosphines can be protected as phosphine-boranes, oxides, sulfides, or selenides (Scheme 1.1).[13]

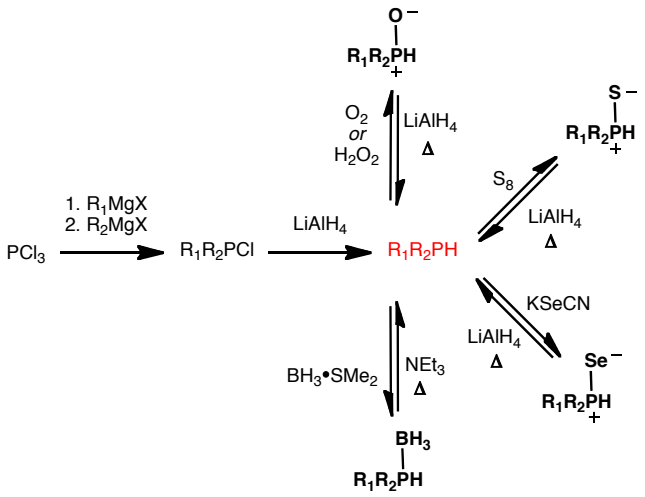

Scheme 1.1. General synthesis and protection/deprotection of asymmetrically substituted secondary phosphines (red)

Metal phosphidos are important intermediates in catalytic reactions that form P-C bonds, such as hydrophosphination of alkenes and phosphination of aryl and alkyl halides. As such, the structure, bonding, and reactivity of the M-PR_2 functional group are well understood. Whereas amidos are typically planar, phosphide ligands are often pyramidal.[14] Due to the higher quantum number of phosphorus, the lone pair resides in an extensive orbital that can also coordinate in L-type fashion to another metal in polynuclear complexes. As a result of longer M-P bonds (relative to M-N bonds) and reduced steric congestion, X-type phosphides tend to be stronger bridging ligands than amides. Phosphide planarity, on the other hand, occurs upon donation of the phosphorus

p-orbital into a vacant metal *d*-orbital. LX-type phosphides engaged in this M-P π-bonding are three-electron donors (Figure 1.3), and are observed most often when coordinated to high-valent early transition metals.

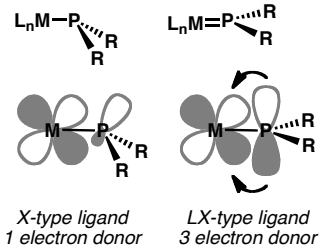

Figure 1.3. Relationship between phosphide ligand type and phosphorus geometry

Complexes with pyramidal X-type phosphides see longer, weaker M-P bonds and compressed M-P-R bond angles, while complexes with planar LX-type phosphides see shorter, stronger M-P bonds and large M-P-R bond angles.[14] Some of the first examples of well-defined early transition metal phosphides were reported by Baker in 1983.[15] These zirconocene and hafnocene bis(phosphides) ($(\eta^5\text{-}C_5H_5)_2M(PR_2)_2$ (M = Zr, Hf; R = Et, Cy, Ph)) contain both X-type and LX-type phosphides that interconvert in solution, but not in the solid state. Conveniently, their crystal structures provide a direct comparison of both phosphide ligand bonding types. For instance, in the solid-state structure of $Cp_2Hf(PEt_2)_2$, one pyramidal phosphide is engaged in a long, single bond to hafnium (2.682(1) Å), whereas a trigonal planar phosphide seeing lone pair donation to the metal is engaged in a shorter, double bond (2.488(1) Å) (Figure 1.4). Indeed, this π-donation is substantial, since the trigonal planar PEt_2 ligand is orthogonal to the P-Hf-P

plane, allowing maximum overlap between the phosphorus *p*-orbital and the empty hafnocene a_1 molecular orbital.

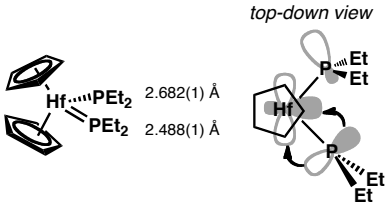

Figure 1.4. Hafnocene with inequivalent phosphide ligands in the solid state

Middle and late transition metal complexes with both phosphide and phosphine ligands have also been reported, and serve as convenient systems to compare metal bonds to neutral and anionic phosphorus donors. For instance, Schrock reported a PEt_3-stabilized tungsten(VI) phosphido complex $W(CCMe_3)(PHPh)(PEt_3)_2Cl_2$ (Figure 1.5).[16] The phosphide is trigonal planar, and the W-PHPh bond (2.291(1) Å) is substantially shorter than the W-PEt_3 bonds (2.553(1) Å), a difference that likely reflects π-bonding between the phosphido ligand and the d^0 tungsten center. The diagnostically large W-P-C angle (140°) is also characteristic of an LX-type bonding mode. Expectedly, the analogous amido complex $W(CCMe_3)(NHPh)(PEt_3)_2Cl_2$ sees a significantly shorter W-N bond (~2.0 Å). Conversely, the reported phosphine-coordinated osmium(II) phosphido complex $Os(PHPh)(PPh_3)_2(CO)_2Cl$ has a pyramidal phosphide, and a slightly longer Os-PHPh bond (2.523(7) Å) compared to the Os-PPh_3 distances (2.414(7) and 2.423(6) Å) (Figure 1.6).[17] Although not discussed by the authors, the Os-PHPh bond may be longer than the Os-PPh_3 bond due to both electron repulsion between the lone pair on phosphorus and a filled orbital on the d^6 metal, and the greater p-acidity of PPh_3 which

encourages Os→PPh_3 backbonding. The phosphide geometry, Os-PHPh distance and the compressed Os-P-C angle (113.0(1.1)°) indicate that the phosphide coordinates to the osmium(II) center in an X-type fashion.

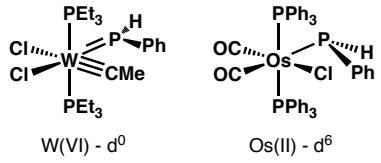

Figure 1.5. Transition metal phosphides with L-type tertiary phosphine ligands as benchmarks for comparison

Pincer bis(phosphides) are extremely rare, likely owing to challenges in controlling phosphorus reactivity in a many step synthesis and isolation. In fact, to our knowledge, only one pincer bis(phosphide), a xanthene-derived POP-type pincer ligand, had been reported prior to our investigations.[18] The ligand itself is synthesized in a three-step sequence involving double *ortho*-deprotonation of a xanthene, anion quenching with $^tBuPCl_2$, and P-Cl bond reduction (Scheme 1.2). The bis(phosphine) is obtained in 59% overall yield in a 2:3 *rac*:*meso* ratio. Deprotonation and salt metathesis with $Zr(NMe_2)_2Cl_2(DME)$ affords $(POP)Zr(NMe_2)_2$ in 53% yield as a single diastereomer. X-ray crystallographic studies reveal that the phosphorus atoms exhibit pyramidal geometry and relatively long Zr-P bonds (2.6305(5) and 2.6387(6) Å). Despite coordination to a d^0 metal center, these structural features are consistent with minimal P→Zr π-bonding, although no explanation is offered.

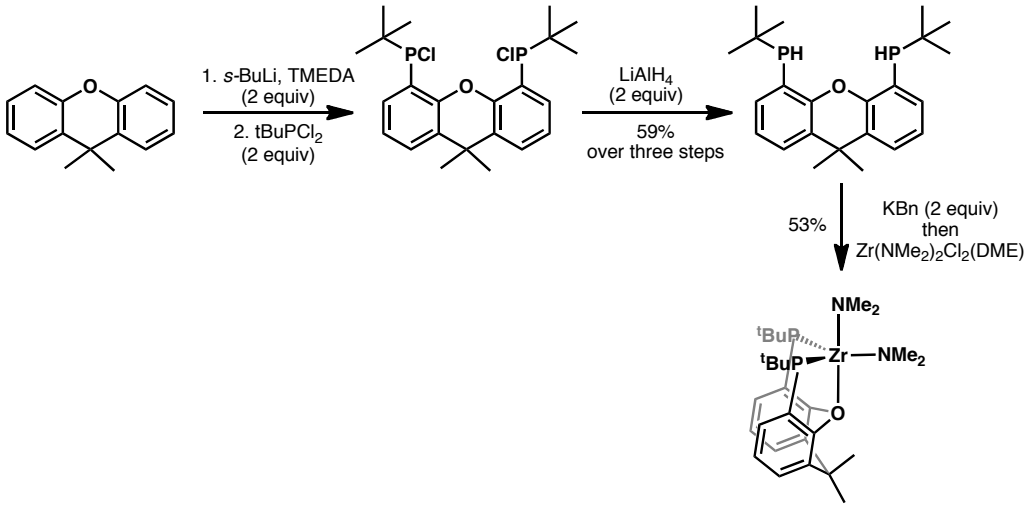

Scheme 1.2

The inversion barrier of phosphides in metal-phosphido complexes is generally lower (~2–20 kcal/mol) than that of phosphines (~30–35 kcal/mol).[14] The large range of values reflects a barrier dependent on metal, oxidation state, phosphide substitution, and non-phosphide ligands. Inversion has been suggested to proceed through one of two mechanisms. In each, inversion of a pyramidal phosphide involves a planar transition state. However, for early, high-valent transition metals, the phosphorus *p*-orbital in the transition state is stabilized by a vacant acceptor orbital on the metal; the transition state sees M-P π-bonding, but often at the expense of metal π-bonding to some other ligand. For middle and late metals that are often low-valent, electrons from the metal impart inductive effects on the phosphide lone pair, presumably increasing the energy of the ground state (more than the planar transition state) and decreasing the overall activation barrier. Consequently, some metal phosphides can invert at room temperature.

RESULTS AND DISCUSSION

C-P Cross-Coupling Approach

Semi-rigid pyridine-linked bis(phenolate) and bis(anilide) ligands **1** – **4** have been previously described by our group.[4] The triaryl frameworks are prepared conveniently by robust Pd-catalyzed carbon-carbon bond-forming reactions. We hoped to develop a versatile and modular synthesis of an analogous bis(secondary phosphine)pyridine ligand (**5**) using a sequence of similar cross-coupling reactions — one to establish the carbon skeleton of the ligand framework via arene-arene bond construction, and the other to effect a less conventional C-P coupling (Figure 1.6). Promisingly, there are several reports of Pd-catalyzed monoarylation of primary phosphines using iodo- and bromoarene coupling partners.[19] These transformations are moderate-to-high yielding, but suffer from narrow substrate scopes.

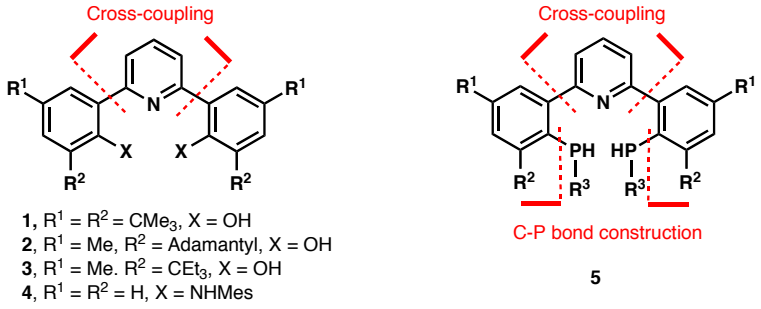

Figure 1.6. Modular, cross-coupling approach toward pyridine-linked bis(phenolates) and bis(anilides), and a plausible analogous strategy toward pyridine-linked bis(phosphides)

Readily available ONO-type ligand **1** was investigated as an intermediate in the potential synthesis of PNP-type ligand **5** (Scheme 1.3). Deprotonation of **1** with BuLi and *O*-triflation at room temperature affords bis(triflate) **6**. However, treatment of **6** with a variety of traditional nickel and palladium carbon-heteroatom bond-forming catalysts in the presence of phenylphosphine ($PhPH_2$) only results in the formation of a single, unidentified phenylphosphine-coordinated metal complex by ^{31}P NMR. These species are spectroscopically observed even in the absence of substrate **6.** Indeed, it may be that these complexes are productive and form *in situ* in reported C-P bond-forming reactions with aryl halide partners, but oxidative insertion into the C-OTf bonds of **6** may be too slow to compete with some phosphine dissociation pre-equilibrium, or may be reversible (although the product would be stabilized by chelation to the pyridine ring). Alternatively, the insertion step may simply be highly discouraged due to the bulky *ortho tert*-butyl group.

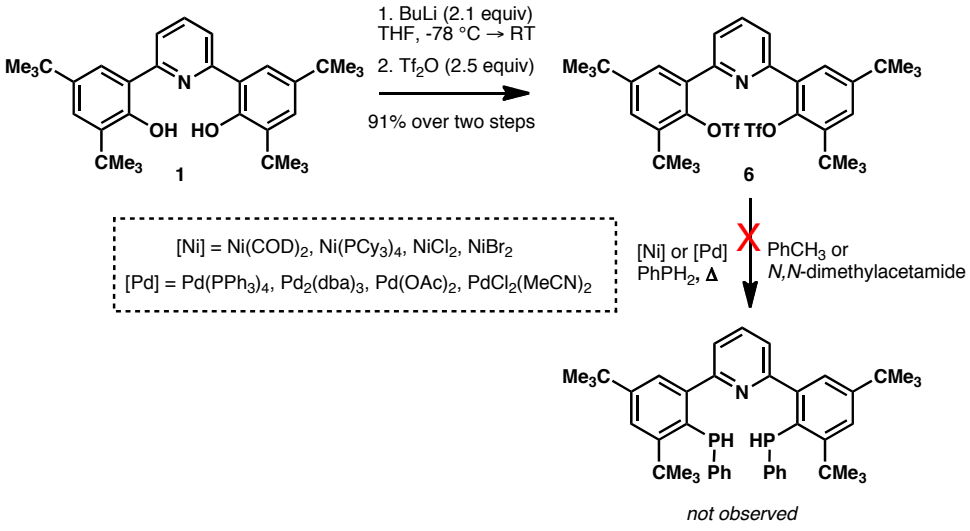

Scheme 1.3

To explore a C-P coupling approach involving aryl bromide coupling partners, sterically unencumbered dibromide **7** was synthesized via two high-yielding sequences of pyridine-directed mercuration/lithiation/bromination (Scheme 1.4).[20] We did not pursue a cross-coupling strategy toward **7** due to potential issues of chemoselectivity of the catalyst between the commercially available 2,6-dibromopyridine and an *ortho*-brominated coupling partner (2-bromophenylboronic acid, for instance.) Attempted C-P coupling reactions of **7** and $PhPH_2$ with traditional nickel and palladium catalysts afforded intractable mixtures with multiple ^{31}P NMR signals. Importantly, diagnostic doublets with typical $^{1}J_{P\text{-}H}$ values (indicative of a secondary phosphine) were not observed.

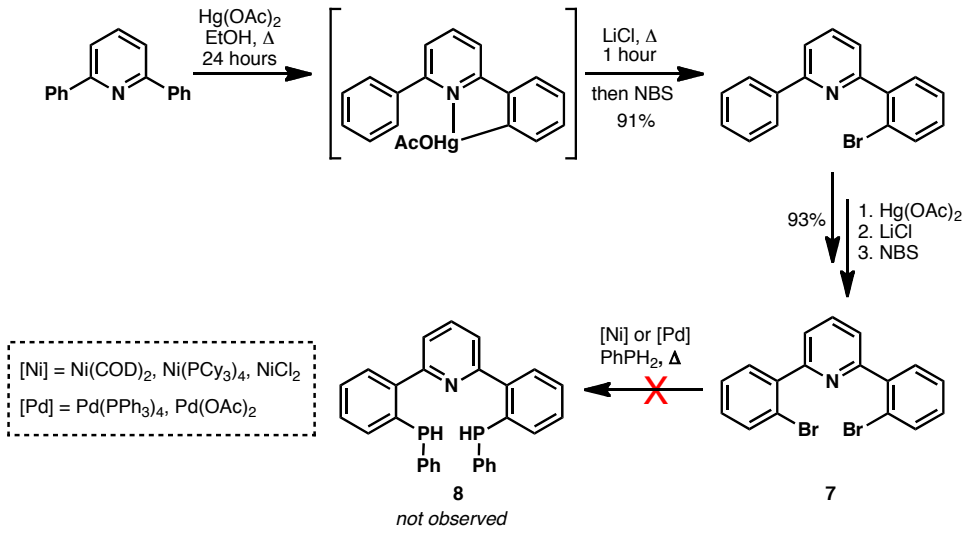

Scheme 1.4

Nucleophilic Aromatic Substitution Approach

Developing a late-metal-catalyzed C-P cross-coupling reaction with aryl triflates and bromides is beyond the scope of this project. Due to the undesired catalyst reactivity in the presence of $PhPH_2$, we were instead encouraged to pursue a transition metal-free route to PNP-type ligand **8**. The route could exploit the nucleophilicity of a primary phosphine in an S_NAr-type reaction with aryl halides (in particular chlorides and fluorides) that would install the problematic C-P bond.

Although aryl bromides are typically less reactive in S_NAr reactions than their chloride or fluoride analogs, we first investigated dibromide **7** as a substrate in the nucleophilic reaction with a phosphide. Phenylphosphine can be quantitatively deprotonated under superbasic conditions (KOH in DMSO, eq. 1), then treated with dibromide **7**. Perhaps due to deleterious radical formation, the aryl bromide does not react cleanly with PhPHK, affording intangible mixtures of multiply phosphinated products by ^{31}P NMR.[21]

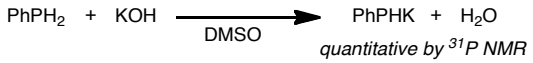

(1)

Surprisingly, there are no reported cross-coupling methods for the synthesis of 2,6-di(*ortho*-chloroaryl)pyridines. While transition metal-free approaches can access 2,4,6-polychloroaryl pyridines, issues of chemoselectivity would arise using these substrates with PhPHK under S_NAr conditions.[22] Nevertheless, we envisioned that dichloride **9** could arise from a Suzuki coupling of 2-chlorophenyl boronic acid and 2,6-dibromopyridine (Scheme 1.5, Table 1.2). The cross-reaction was complicated, however,

by pyridine-directed activation of the C-Cl bond of the monocoupled product to afford **10** and generally <5% of desired product **9** by GC-MS.

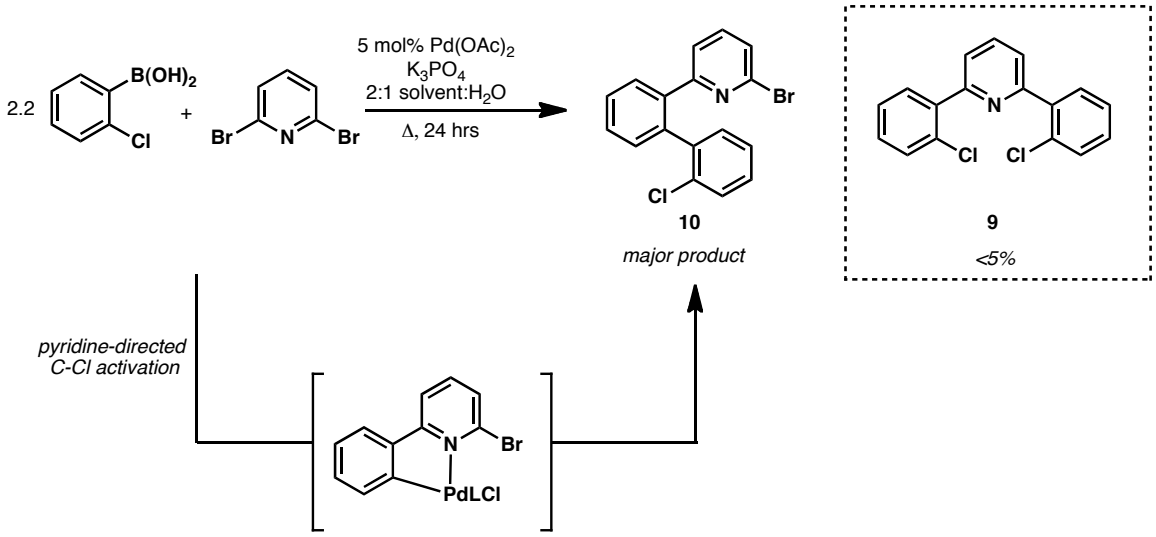

Scheme 1.5

Catalyst	Solvent	T (°C)	Yield (10)
Pd(OAc)2	DMF	100	76%
Pd(OAc)2	THF	60	60%
Pd(PPh3)4	THF	60	65%
Pd(PPh3)2Cl2	THF	60	67%
Pd(PPh3)2Cl2	dioxane	60	83%
Pd(PPh3)2Cl2	DME	60	81%
Pd(PPh3)2Cl2	DME	60	25%

Table 1.2. Effects of catalyst, solvent, and temperature on the synthesis of dichloride **9** and pyridine-directed C-Cl activated product **10**

Alternative, unexplored routes to dichloride **9**, such as a double mercuration/lithiation/chlorination sequence[20] or Pd-catalyzed oxidative chlorination, may be effective.[23] However, given the greater reactivity of aryl fluorides in S_NAr reactions and the reduced likelihood of pyridine-directed C-F bond activation in the cross-coupling of 2,6-dibromopyridine and 2-fluorophenylboronic acid, we synthesized difluoride **11** in excellent yield (eq. 2, Table 1.3).

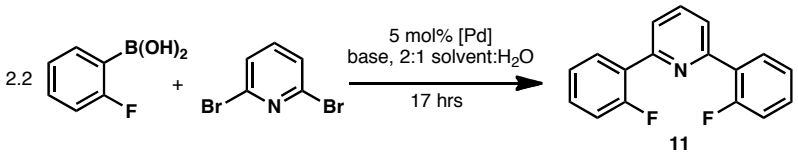

(2)

Catalyst	Base	Solvent	T (°C)	Yield (11)
$Pd(OAc)_2$	K_3PO_4	DMF	RT	16%
$Pd(OAc)_2$	K_3PO_4	DMF	100	48%
$Pd(PPh3)_4$	K_3PO_4	DMF	100	35%
$Pd(PPh_3)_2Cl_2$	K_3PO_4	DMF	100	66%
$Pd(PPh_3)_2Cl_2$	K_3PO_4	DME	100	87%
$Pd(PPh_3)_2Cl_2$	K_2CO_3	DME	100	92%

Table 1.3. Effects of catalyst, base, solvent, and temperature on the synthesis of **11**

Treating **11** with PhPHK affords bis(phosphine)pyridine **8** in 70% yield as a 1:1 *rac:meso* mixture of diastereomers (eq. 3). Conveniently, an air-free workup and aqueous wash of the reaction removes all products but the desired. Solvent effects typical of nucleophilic substitution reactions are observed: while the reaction occurs on the order of days in nonpolar solvents, gratifyingly full conversion occurs in 20 hours in DMF and 5 hours in DMSO. Interestingly, the S_NAr reaction is remarkably sensitive to the counterion stabilizing the phenylhydrophosphide nucleophile (Table 1.4). Lithium or sodium

phenylhydrophosphide reacts with **10** to afford the desired bis(phosphine) in only 15% or 36% yield. A near doubling of yield was observed for the potassium salt, likely a result of softer potassium phosphide and/or subsequent side reactions that occur more readily for the lithium and sodium salts.[24]

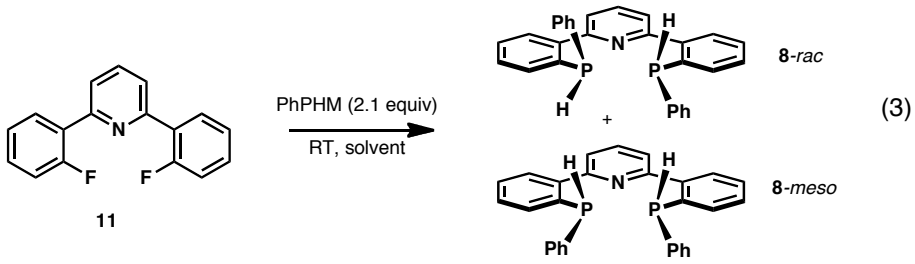

(3)

PhPH-M	Solvent	Time	Yield 8
PhPH-K	DMSO	5 hrs	70%
PhPH-K	DMF	20 hrs	66%
PhPH-K	THF	20 hrs	22%
PhPH-Na	DMSO	5 hrs	15%
PhPH-Li	DMSO	5 hrs	36%

Table 1.4. Effects of alkali earth metal counterions and solvent on the synthesis of bis(phosphine) **8**

In summary, PNP-type ligand **8** may be synthesized in two steps in 67% overall yield from commercially available starting material (Scheme 1.6). Analytically pure material can be accessed via a chromatography-free route, thus avoiding technical difficulties inherent to purifying air-sensitive secondary phosphines. The synthesis should be modular, with opportunities to create PNP-type pincer libraries from variously substituted fluorophenylboronic acids in combination with aryl and alkyl primary phosphines.

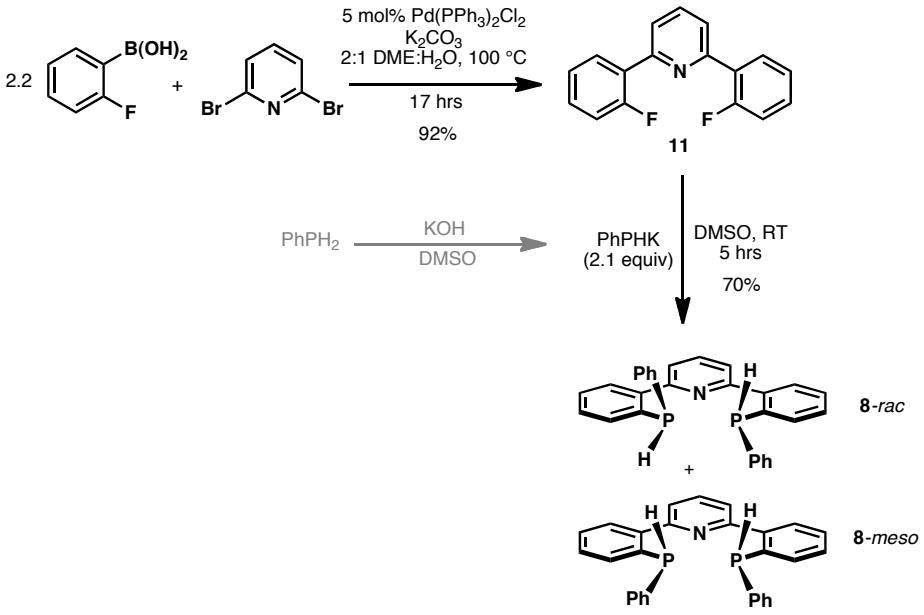

Scheme 1.6

*Spectroscopic Properties and Dynamic Processes of PNP Ligand **8***

The diagnostic ^{1}H NMR signals for P-H protons of **8-*rac*** and **8-*meso*** reveal typically large one-bond coupling to phosphorus ($^{1}J_{P\text{-}H}$ = 223 Hz, 224 Hz) (Figure 1.7). The ^{31}P NMR spectrum reveals two doublets, each corresponding to a pair of magnetically equivalent phosphorus atoms on either **8-*rac*** or **8-*meso***; as expected, the $^{1}J_{P\text{-}H}$ values agree with those in the ^{1}H spectrum. The equilibrium diastereomeric ratio has not been investigated in detail, but the ratio of diasteromers does not differ greatly from one in any solvent examined thus far (CH_2Cl_2, THF, MeCN, $PhCH_3$, tetrachloroethane). Variable-temperature NMR experiments (Figures 1.8 and 1.9) reveal diastereomeric interconversion of **8-*rac*** and **8-*meso*** at elevated temperatures: coalescence is achieved at roughly 380 K (110 °C, ^{1}H NMR, 500 MHz, tetrachloroethane-d_2), corresponding to a rate constant k_{380} = 254 s^{-1} and free energy of activation $\Delta G_{380}^{\ddagger}$ = 18.3 kcal/mol (eq. 4). However, attempts to resolve the diastereomers were unsuccessful, and crystals of either diastereomer or co-crystallized diastereomers sufficient for x-ray structure determination could not be obtained.

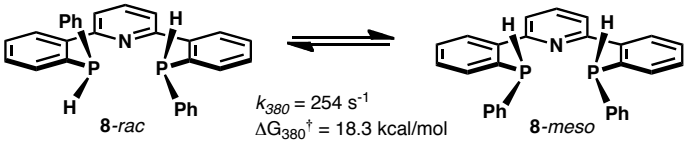

(4)

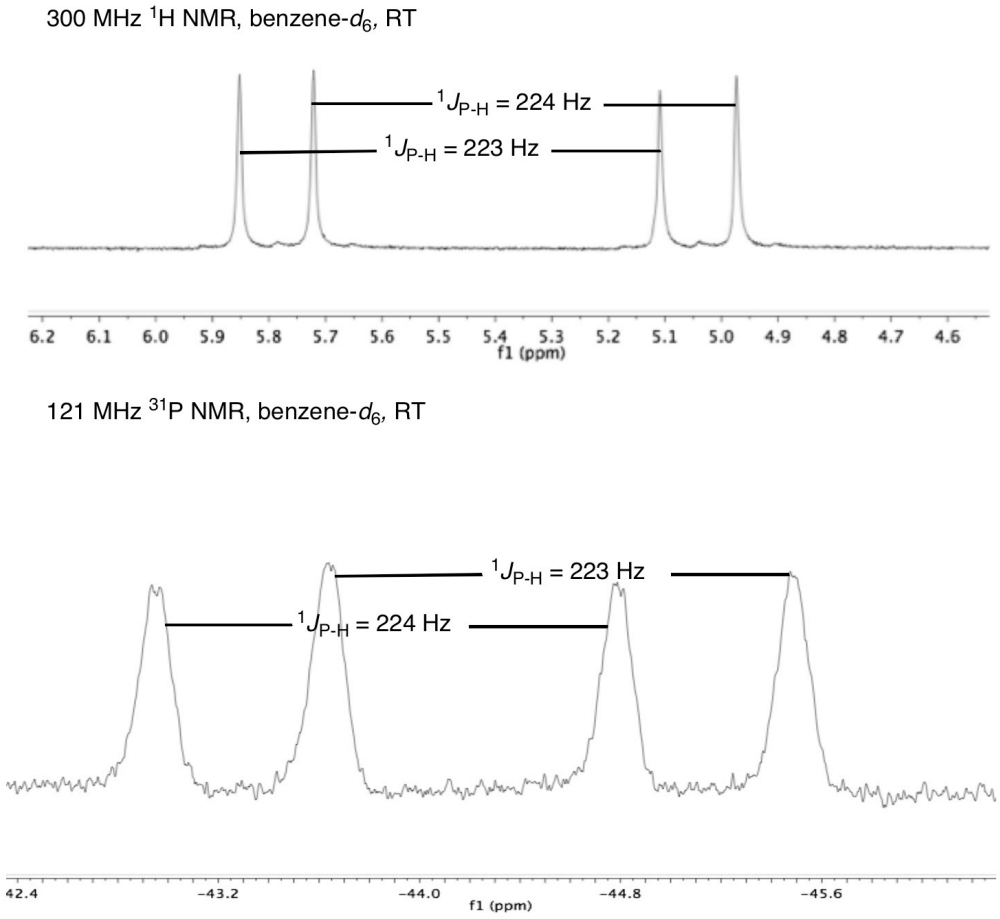

Figure 1.7. Selected regions of ^{1}H (top) and ^{31}P (bottom) NMR spectra in benzene-d_6 revealing P*H*(C_6H_6) and *P*H(C_6H_6) signals, respectively, for *rac* and *meso* diastereomers of **8**

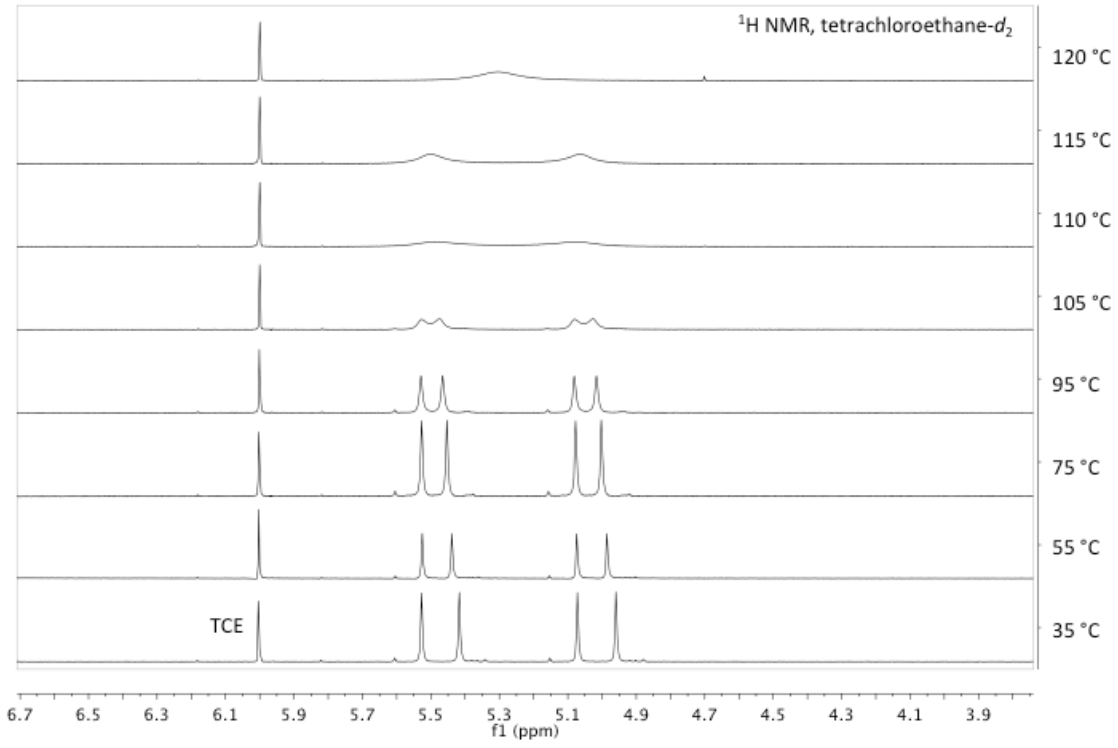

Figure 1.8. Variable-temperature ^{1}H NMR spectra in d_2-TCE revealing coalescence of P*H*(C_6H_6) signals of **8-***rac* and **8**-*meso* at 110 °C

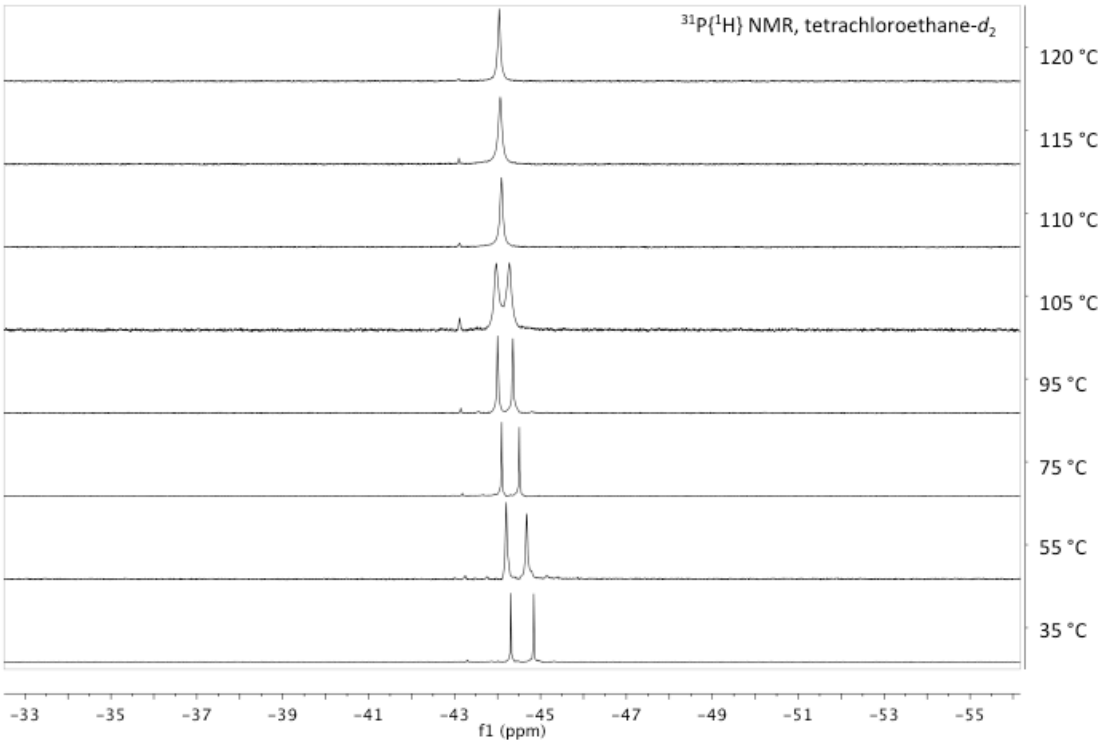

Figure 1.9. Variable-temperature $^{31}P\{^{1}H\}$ NMR spectra in d_2-TCE revealing coalescence of *P*H(C_6H_6) signals of **8-***rac* and **8**-*meso* at 110 °C

Synthesis and Characterization of (PNP)K_2

Fast double deprotonation of the bis(phosphine)pyridine can be achieved quantitatively with KHMDS or benzylpotassium in THF to afford dipotassium-bridged bis(phosphide) **12**. The presence of a single ^{31}P singlet in the NMR spectrum immediately following deprotonation indicates that both **8-*rac*** and **8-*meso*** share the same conjugate base in solution (Figure 1.10). Slow evaporation of a THF solution of **12** produces crystals that analyze as tetrapotassium bis(bis(phosphide)pyridine) complex **13**, a C_i-symmetric dimer with an octanuclear, ladder-like potassium-phosphorus core (Figure 1.11). The dimer does not persists in solution, since the ^{31}P NMR spectrum at -80 °C indicates equivalent phosphorus atoms. Therefore, **12** is regenerated upon dissolution of **13** (Scheme 1.7).

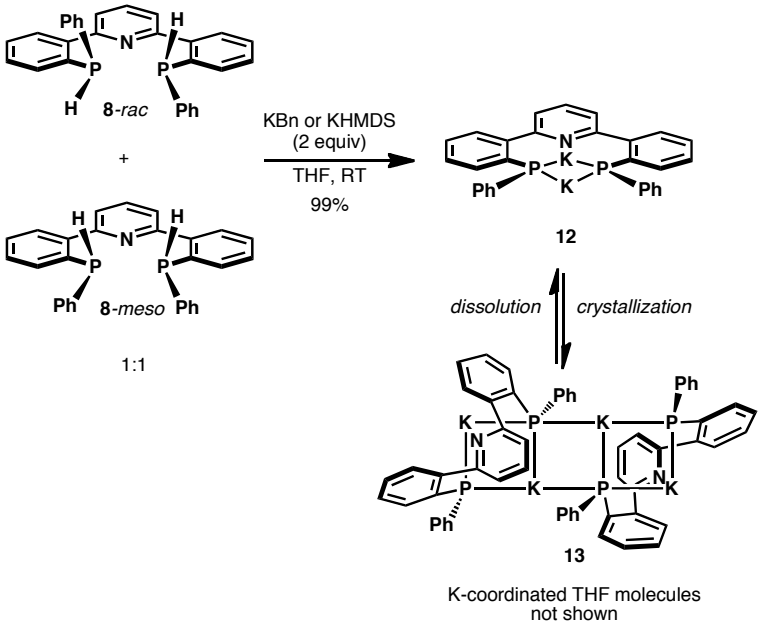

Scheme 1.7

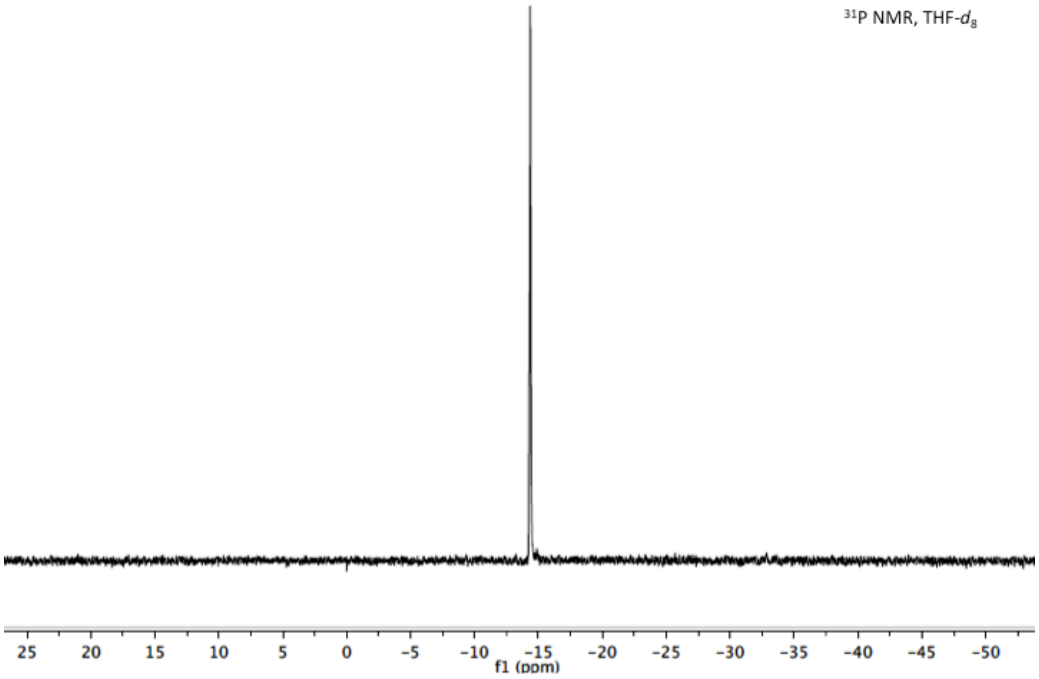

Figure 1.10. ^{31}P NMR spectrum of PNP-K_2 (**12**) in THF-d_8 at -80 °C

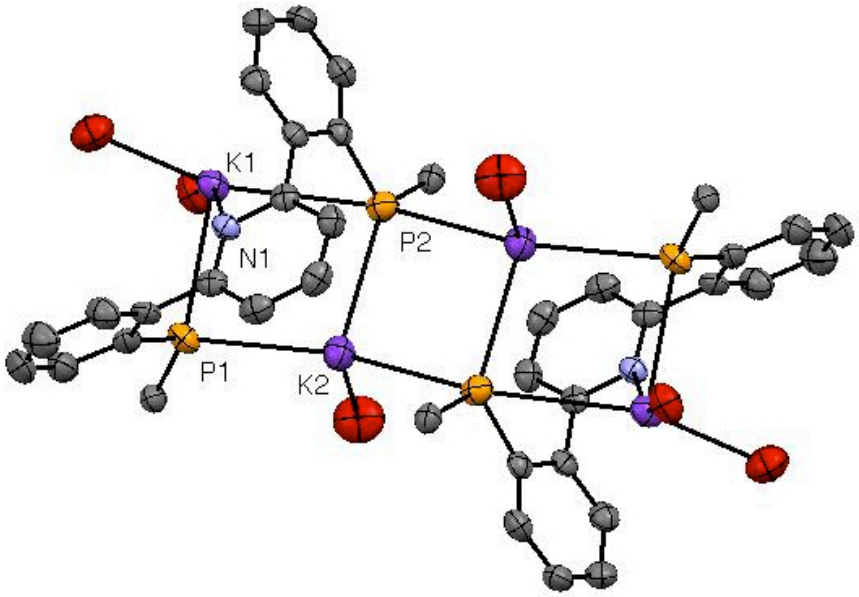

Figure 1.11. Thermal ellipsoid representation of dimeric **13** at the 50% probability level. All hydrogens, THF carbons and *P*-phenyl carbons omitted for clarity, and ellipsoids at the 50% probability level. Selected bond lengths (Å) and angles (deg): K(1)-P(2) 3.5380(10); K(1)-P(1) 3.2276(10); K(1)-N(1) 2.9943(19); K(2)-P(2) 3.2479(11); K(2)-P(1) 3.3030(10); P(2)-K(1)-P(1) 90.90(2); P(2)-K(2)-P(1) 94.91(2); K(1)-P(2)-K(2) 84.69(2); K(1)-P(1)-K(2) 88.96(2)

The potassium and phosphorus atoms in the K_4P_4 core are arranged as alternating vertices of three conjoined quadrilateral, nearly square arrays. The potassium atoms making up the corner vertices of the core are within bonding distance to only one P (K1-P1 = 3.2276(10) Å), but bridge weakly to the other P of the same molecule (K1-P2 = 3.5380(10) Å). Potassium atoms shared by both ligands in the center of the cluster engage in bonding to two phosphorus atoms of one ligand (K2-P2 = 3.2479(11), K2-P1 = 3.3030(10) Å), and less strongly interact with P2 of the other ligand across the inversion center (K2-P2a = 3.3943(10) Å). The ligand pyridine ring is canted about 66° from the

flanking phenyl rings to accommodate nitrogen-coordination to potassium(1). However, the large N1-K1 internuclear distance (2.9943(19) Å), and the vector's 31° dihedral angle from the pyridine plane suggests only a weak interaction.

To our knowledge, Turculet has synthesized and characterized the only other known alkali metal-stabilized bis(phosphide) pincer ligand **(14)**.[18] Crystallographic analysis of the dipotassium xanthene bis(phosphide) conjugate base of the POP-type ligand discussed previously has a quadrilateral K_2P_2 core in the solid state. Unlike **13,** this bis(phosphide) is monomeric in the unit cell, possibly due to the steric encumbrance of the *tert*-butyl substituents on the phosphorus atoms. K-P distances are unremarkable (K-P = 3.128(1) Å, 3.220(1) Å, 3.254(1) Å, 3.288(1) Å), yet on average slightly shorter than the K-P bond distances in **13**, although this may be a result of the different chelate sizes of both ligands, different phosphide substituents, and/or the crowded, dimeric structure of **13** relative to monomeric **14.**

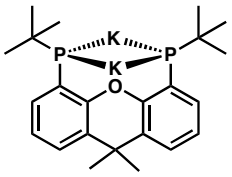

14

K-coordinated Et_2O molecules not shown

Synthesis and Characterization of (PNP)Zr(NMe$_2$)$_2$

We envisioned that metalation of PNP-type ligand **8** could be achieved by protonolysis of a metal complex, or salt metathesis from dipotassium bis(phosphide) **12**. Unfortunately, attempted preparations of well-defined Group 4 and Group 5 metal

complexes with two or three simple X-type (e.g., chloride or benzyl) ligands were unsuccessful, due to the propensity of phosphides to form extensive bridging networks with two or more metals.[14] Indeed, these reactions resulted in the immediate precipitation of insoluble and unreactive oligomeric products that analyzed as the desired stoichiometry, even under dilute conditions.

We therefore examined homoleptic metal complexes stabilized by strong π-donor ancillary ligands as precursors to reduce coordinative unsaturation of the products. Indeed, we were pleased to discover that the roughly C_2-symmetric zirconium bis(phosphide)pyridine-bis(dimethylamido) zirconium(IV) complex **15** can be synthesized racemically and quantitatively via treatment of $Zr(NMe_2)_4$ with a 1:1 mixture of **8**-*rac* and **8**-*meso* in benzene at room temperature, through a mechanism that likely involves protonolytic release of two equivalents of dimethylamine (eq. 5). Both enantiomers of **15** were co-crystallized for x-ray analysis from toluene. The structure reveals the desired tridentate, pincer-type interaction with the bis(phosphide)pyridine ligand (Figure 1.12).

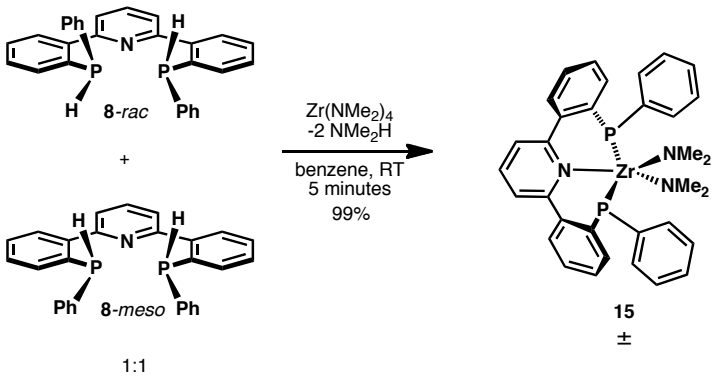

(5)

$(PNP)Zr(NMe_2)_2$ (**15**) exhibits one of the largest (C_2 twist) torsional angle (79.77°) between the aromatic pyridine substituents observed in any of our reported C_2-

symmetric pyridine-linked bis(phenolate) or bis(anilide) complexes prepared to date (Table 1.5). The long Zr-P bonds (2.6853(13) and 2.7002(12) Å) and the pyramidal geometry of phosphorus, reflected by the sum of the angles around each atom ($\Sigma\angle_P$ = 300.28(48)°, 292.6(8)°), strongly indicate that each phosphide donates only one electron in an X-type fashion through a single bond to the metal. Phosphide lone pair donation to Zr $d\pi$ would require planarization of the ligand skeleton to allow for phosphorus sp^2 hybridization. Considering the long Zr-P and P-C_{pincer} bonds (P1A-C1A = 1.839(5), P2A-C17A = 1.832(4) Å), models suggest that this rehybridization and planarization of phosphorus, in addition to shortening of the Zr-P bond, would involve severe distortions to the ligand framework. Correspondingly, significant ring strain from planarization of the 6-membered [-Zr-P-C-C-C-N-] rings (vide supra) is expected to make for a very high energy barrier for racemization through a C_{2v}-symmetric intermediate. The relatively short Zr-N_{amide} bond lengths (2.007(3) and 1.991(4) Å) and the planarity of each amide nitrogen ($\Sigma\angle_N \approx 360°$) are as expected for strong LX-type bonds.

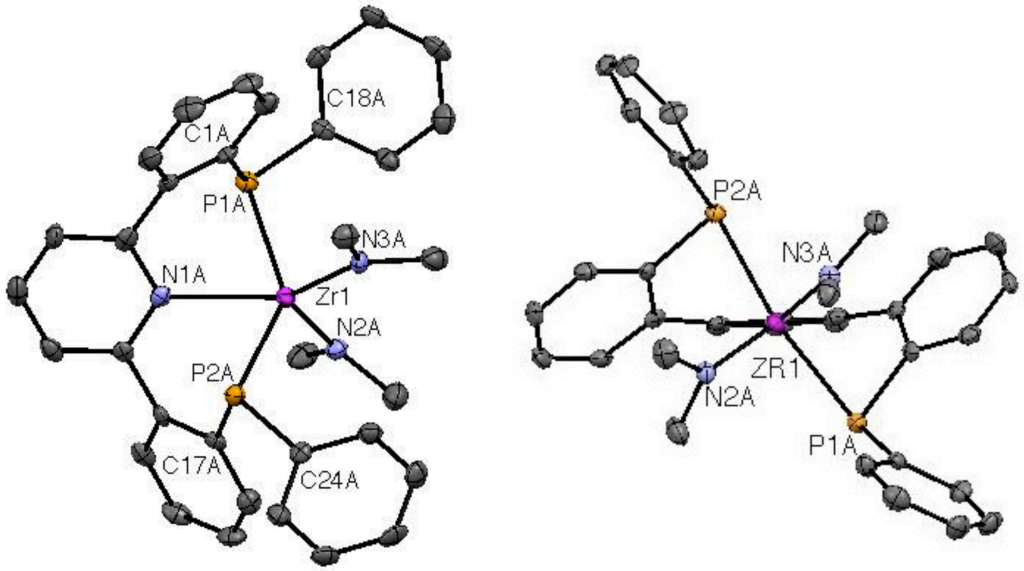

Figure 1.12. Thermal ellipsoid representation of one enantiomer of (PNP)Zr(NMe_2)$_2$ (**15**) at the 50% probability level. Hydrogens are omitted for clarity. The left perspective is a top-down view. The right perspective is viewing down the Zr-N1A bond. Selected bond lengths (Å) and angles (deg): Zr(1)-P(1A) 2.6853(13); Zr(1)-P(2A) 2.7002(12); Zr(1)-N(1A) 2.406(3); Zr(1)-N(2A) 2.007(3); Zr(1)-N(3A) 1.991(4); P(1A)-Zr(1)-P(2A) 141.26(4); Zr(1)-P(1A)-C(1A) 83.56(14); Zr(1)-P(1A)-C(18A) 115.08(15); C(18A)-P(1A)-C(1A) 102.18(19); Zr(1)-P(2A)-C(17A) 80.20(13); Zr(1)-P(2A)-C(24A) 109.76(14); C(17A)-P(2A)-C(24A) 102.7(2)

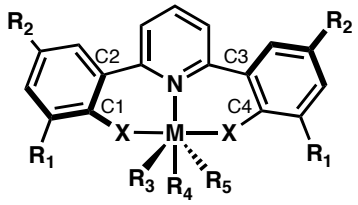

Complex	X	M	R_1, R_2	R_3, R_4, R_5	$\angle_{torsion}$(C1-C2-pyr)	$\angle_{torsion}$(C3-C4-pyr)	$\angle_{torsion}$(C1-C2-C3-C4)
16	O	Ta	CMe_3, CMe_3	NH_2Ph, NHPh, NPh	38.84°	27.25°	56.67°
17	O	Ta	CMe_3, CMe_3	$NNPh_2$, Cl pyridine	29.61°	35.29°	57.03°
18	O	Ta	CMe_3, CMe_3	NMe_2, NMe_2, NMe_2	36.03°	30.94°	59.12°
19	O	Ti	CEt_3, Me	CH_2Ph, -, CH_2Ph	30.69°	34.31°	58.11°
20	O	Ti	CMe_3, CMe_3	CH_2Ph, -, CH_2Ph	25.64°	27.06°	48.90°
21	O	Ti	Ad, Me	$OCH(CH_3)_2$, -, OiPr	36.31°	32.93°	63.01°
22	N(Mes)	Ti	H, H	NMe_2, -, NMe_2	41.50°	36.92°	81.15°
23	N(Mes)	Zr	H, H	NMe_2, -, NMe_2	41.13°	45.33°	80.29°
24	N(Mes)	Zr	H, H	Cl, THF, Cl	37.96°	35.09°	61.82°
15	P(Ph)	Zr	H, H	NMe_2, -, NMe_2	44.13°	50.75°	79.77°

Complexes 16-18: ref. 5
Complexes 19-21: ref. 4a
Complexes 22-24: ref. 4c

Table 1.5. Geometric parameters of pyridine-linked bis(phenolate), bis(anilide), and bis(phosphide)-supported early metal complexes

Frontier Molecular Orbitals as Predicted by Density Functional Theory

DFT calculations were performed on the frontier molecular orbitals of (PNP)Zr(NMe_2)$_2$ (**15**) using both 6-31G and LANL2DZ basis sets to gain further insight into electronic structure. The HOMO is non-bonding, residing primarily on each phosphorus atom of the ligand (Figure 1.13). That the HOMO is comprised of extensive, essentially pure 3*p* phosphorous orbitals compliments the experimentally observed tendency of electron-deficient PNP-ligated metal complexes to form phosphide-bridging oligomers.

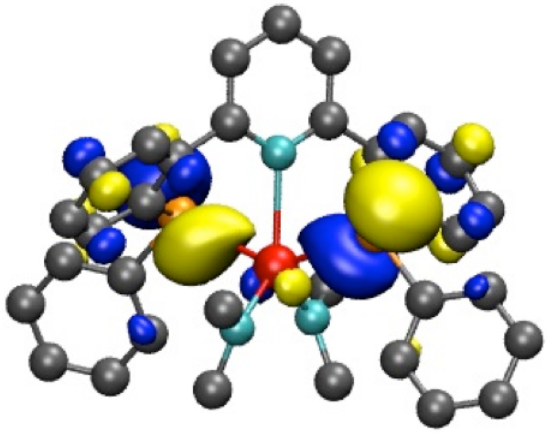

Figure 1.13. DFT-predicted HOMO of (PNP)Zr(NMe_2)$_2$ (**15**). Atoms are color coded: nitrogen (turquoise), carbon (gray), phosphorus (orange), zirconium (red)

In contrast, the HOMO-1 is mostly comprised of the Zr-P σ-bonding interactions between a primarily phosphorus 3*p* and a well-defined Zr d_{Z^2} orbital (Figure 1.14). Because of the geometric strain of the ligand's six-membered chelate, the individual phosphorus and zirconium atomic orbitals do not achieve an ideal 180° overlap. This has

important, perhaps general, implications on the bonding strength of PNP-type ligands to early metals. For one, despite the highly nucleophilic phosphide donors, geometric strain not only discourages Zr-P π-bonding, but sacrifices some degree of Zr-P σ-bonding as well. Thus, the PNP-type ligand is not as electron-donating as monodentate phosphides or less constrained bis(phosphides). The reduced donation to the metal likely increases the overall nucleophilicity of the non-bonding *3p* phosphorus orbital, so that in complexes with non-p-bonding ancillary ligands unable to stabilize electron-deficient metal centers, the phosphide lone pairs are even more prone to bridge to other metals and form oligomeric products.

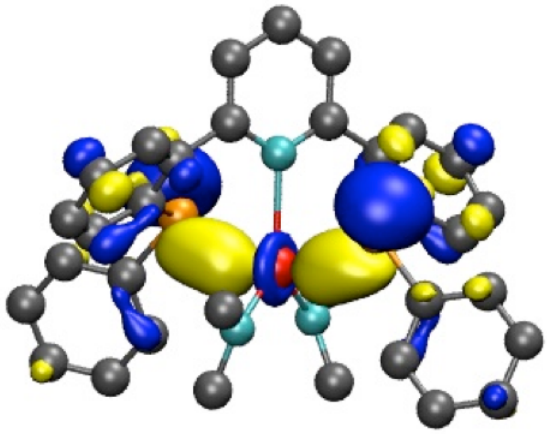

Figure 1.14. DFT-predicted HOMO-1 of (PNP)Zr(NMe_2)$_2$ (**15**). Atoms are color coded: nitrogen (turquoise), carbon (gray), phosphorus (orange), zirconium (red)

Interestingly, calculations of the LUMO reveal substantial density at the pyridine ring, suggesting that this is where reaction with a nucleophile is likely to occur (Figure 1.15). While reaction with strong nucleophiles such as MeLi, NaOMe, and NaSMe may

in fact occur at the pyridine ring, we obtained intractable mixtures in each case, unsurprising if irreversible addition of these nucleophiles eliminates aromaticity and kinks the heterocycle to weaken the chelate to the metal.

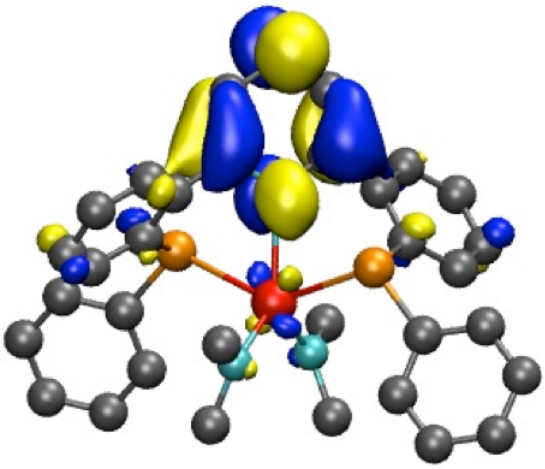

Figure 1.15. DFT-predicted LUMO of (PNP)Zr(NMe_2)$_2$ (**15**). Atoms are color coded: nitrogen (turquoise), carbon (gray), phosphorus (orange), zirconium (red)

Reactivity of (PNP)Zr(NMe_2)$_2$ (**15**)

We further explored the reactivity of (PNP)Zr(NMe_2)$_2$ (**15**), but were surprised to find that it remains stable in solution at 90°C for 3 days, after which products of decomposition could be detected by NMR. Similarly, we observed neither phosphidation with diphenylphosphine or dicyclohexylphosphine, nor transamidation with diethylamine, diphenylamine, or di(*p*-tolyl)amine, even after heating at similarly elevated temperatures for 2 days. Attempts to generate an imido complex by treatment with aniline, *p*-fluoroaniline, and toluidine failed as well. Perhaps most surprisingly, complex **13** does not react with 2 equivalents of TMSCl at room temperature, but instead reacts at 50

degrees after 3 hours to form a red precipitate with concomitant release of $TMS(NMe_2)$. That this precipitate is insoluble in a variety of solvents suggests that the dichloride may be generated, but quickly oligomerizes even under dilute conditions (Scheme 1.8). These findings reveal the stability conferred upon **15** by the π-donating dimethylamido ligands. Disappointingly, **15** exhibited no activity as a propylene polymerization catalyst, likely due to an excess (200–500 equivalents) of the Lewis acidic cocatalyst MAO, which can coordinate to either phosphide or amide ligands.

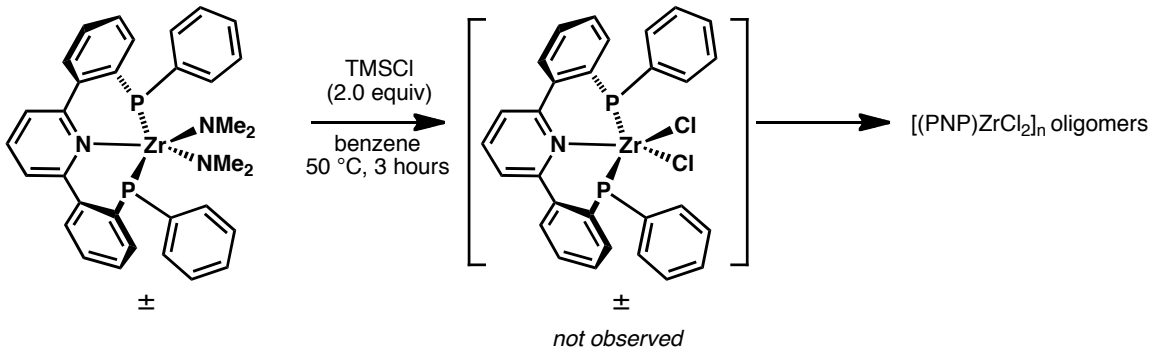

Scheme 1.8

CONCLUSIONS

We have developed a short, modular, and efficient synthesis of a novel pyridine-linked bis(phosphide) pincer ligand as a 1:1 mixture of non-interconverting *rac* and *meso* diastereomers. Metalation with potassium or zirconium generates extremely rare bis(phosphide) pincer-supported complexes. The solid-state structures reveal significant ring strain within the six-membered chelates as a result of long bonds to phosphorus. This ring strain prevents P→Zr π-donation by discouraging planarization of the phosphide donor. As a result, the pincer ligand phosphides are highly pyramidalized X-type donors.

Despite phosphide nucleophilicity, early transition metal complexes coordinated to the PNP pincer ligand require π-bonding ancillary ligands to stabilize the electron-deficient metal center. While the PNP ligand coordinates to metals with non-π-donating ligands, monomeric complexes are highly unstable and ultimately engage in phosphide bridging interactions with other metal complexes to afford oligomeric products. This observation agrees with DFT modeling of the HOMO and HOMO-1 molecular orbitals of (PNP)Zr(NMe_2)$_2$. The HOMO, which resides on phosphorus and is comprised of a large, non-bonding *3p* orbital, is likely responsible for the tendency of the phosphide ligand to bridge to other metals, while the HOMO-1 suggests weak Zr-P σ-bonding. These features may be general of all bis(phosphide) pincer ligands engaged in six-membered chelates, since M-P bond lengths are not expected to change significantly from one phosphide to the next. Therefore, it stands to reason that similar bis(phosphide) pincers are not effective ligands for early metals. To encourage phosphide π-donation by the PNP ligand to a transition metal center, further investigations into its coordination chemistry and that of its analogs are underway. Bis(phosphide) pincers that can engage in five-membered chelates will also be explored as stronger donors.

EXPERIMENTALS

General Considerations and Instrumentation. All air- and moisture-sensitive compounds were manipulated using standard high vacuum and Schlenk techniques or manipulated in a glovebox under a nitrogen atmosphere using degassed solvents. n-Butyllithium solution was titrated with salicylaldehyde phenylhydrazone.[25] KBn was prepared according to literature methods.[26] Zr(NMe_2)$_4$ was prepared according to

literature precedent.[27] Phenylphosphine was purchased from Strem. Triflic anhydride was distilled over P_2O_5 prior to use. KOH was crushed into a fine powder using a mortar and pestle, and dried overnight at 100 °C under vacuum. DMSO and DME were distilled over CaH_2. All other solvents were dried over sodium benzophenone ketyl and stored over titanocene dihydride where compatible or dried by the method of Grubbs.[28] All NMR solvents were purchased from Cambridge Isotopes. Benzene-d_6 and THF-d_8 were dried over sodium benzophenone ketyl, while acetonitrile-d_3, methylene chloride-d_2, and tetrachloroethane-d_2 were dried over CaH_2 and stored over molecular sieves. Chloroform-*d* was used as is. All other chemicals were used as received. ^{1}H, ^{13}C, ^{31}P, and ^{19}F NMR spectra were recorded on Varian Mercury 300 or Varian INOVA-500 spectrometers and unless otherwise indicated at room temperature. Chemical shifts are reported with respect to internal solvent: 7.16 and 128.38 (t) ppm (C_6D_6); 7.27 and 77.23 (t) ppm ($CDCl_3$); 1.72 and 3.58, and 67.21 (p) and 25.37 (p) ppm (THF-d_8); 6.0 and 73.78 (t) ppm (TCE-d_2); for ^{1}H and ^{13}C data. ^{31}P chemical shifts are reported with respect to an external H_3PO_4 85% reference (0 ppm).

Pyridine-linked bis(triflate) 6. To an oven-dried 100 mL round-bottom flask equipped with a stirbar and charged with bis(phenol) **1** (2.0 g, 4.1 mmol, 1.0 equiv) was added 50 mL Et_2O. After cooling the flask to -78 °C, n-butyllithium (3.6 mL, 9.0 mmol, 2.2 equiv, 2.6 M in hexane) was added dropwise. The dark red solution was warmed to room temperature and stirred for 2 h. Triflic anhydride (2.5 g, 9.0 mmol, 2.2 equiv) was added dropwise and the reaction was stirred for 16 h at room temperature. The reaction was poured into ice-cold water (50 mL) and extracted 3 times with Et_2O (50 mL). The organic extracts were washed with brine (50 mL), and dried over Na_2SO_4. Filtration and

concentration *in vacuo* afforded an off-white solid. The solid was washed with petroleum ether to afford 2.8 g of analytically pure **6** (91% yield). ^{1}H NMR (300 MHz, $CDCl_3$) δ: 1.34 (s, 18H, C(C*H*$_3$)$_3$), 1.52 (s, 18H, C(C*H*$_3$)$_3$), 7.47 (d, 2H, J = 6 Hz, 3,5-NC_5H-*H*$_2$), 7.54 (d, 2H, J = 3 Hz, aryl-*H*), 7.61 (d, 2H, J = 3 Hz, aryl-*H*), 7.78 (t, 1H, J = 8 Hz, 4-NC_5H_2-*H*). ^{13}C NMR (75 MHz $CDCl_3$) δ: 31.4 (C(*C*H$_3$)$_3$), 32.0 (C(*C*H$_3$)$_3$), 35.1 (*C*(CH$_3$)$_3$), 36.4 (*C*(CH$_3$)$_3$), 118.3 (q, J = 319 Hz, $ArOSO_2CF_3$), 124.0, 127.8, 128.1, 136.1, 136.7, 141.3, 143.6, 150.9, 156.4 (aryl). ^{19}F (282 MHz, $CDCl_3$) δ: 73.8 ($ArOSO_2CF_3$). HRMS (ESI): calcd mass 752.2509; exact mass 752.2526.

2,6-bis(2'-fluorophenyl)pyridine (10). A 500 mL bomb equipped with a stirbar was charged with 2,6-dibromopyridine (6.2 g, 26 mmol, 1.0 equiv), 2-fluorophenylboronic acid (9.6 g, 69 m mol, 2.6 equiv), $Pd(PhCN)_2Cl_2$ (0.50 g, 1.3 mmol, 0.050 equiv) and triphenylphosphine (0.68 g, 2.6 mmol, 0.10 equiv). 1,2-dimethoxyethane was added (66 mL) to afford a canary yellow suspension, after which an aqueous solution of 4M K_2CO_3 (33 mL) was added. The flask was sealed and heated to 100°C. After 16 h stirring, the brown solution was cooled to room temperature and filtered through Celite. The brown filtrate was partitioned with EtOAc (200 mL), and the organic layer extracted from the aqueous layer with EtOAc (100 mL) four times. The combined organic fractions were washed with brine (100 mL), and dried over $MgSO_4$. The reaction was filtered and concentrated in vacuo to afford a dark brown solid, which was redissolved in Et_2O and filtered through a silica plug. The filtrate was concentrated to afford an off-white solid, which was washed with petroleum ether to afford 6.7 g of **10** in 95% yield as a white solid. ^{1}H NMR (300 MHz, $CDCl_3$) δ: 7.18 (ddd, 2H, J = 8 Hz, J = 5 Hz, J = 1 Hz), 7.26-7.32 (m, 2H), 7.35-7.44 (m, 2H), 7.77-7.87 (m, 2H), 7.79-7.81 (m, 1H), 8.15 (td, 2H, J_1 =

8 Hz, J_2 = 2 Hz). ^{13}C NMR (125 MHz, $CDCl_3$) 116.18 (d, J = 23 Hz), 123.12 (d, J = 10 Hz), 124.47 (d, J = 4 Hz), 127.44 (d, J = 12 Hz), 130.39 (d, J = 9 Hz), 131.19 (d, J = 3 Hz), 136.787 (s), 153.05 (d, J = 2 Hz), 160.70 (d, J = 249 Hz). ^{19}F (282 MHz, $CDCl_3$) δ: 117.02 (m). HRMS (FAB+) $C_{17}H_{12}F_2N$: calcd mass 268.0938, measured mass 268.0942.

(PNP)H$_2$ 11 (*rac* and *meso*). To an oven-dried 250 mL round-bottom flask equipped with a stirbar and charged with powdered KOH (2.6 g, 47 mmol, 2.1 equiv) was added degassed DMSO (10 mL) and $PhPH_2$ (5.2 g, 47 mmol, 5.2 mL, 2.1 equiv). The canary yellow solution was stirred for 2 h at room temperature, followed by dropwise addition of **10** (6.0 g, 22 mmol, 1.0 equiv) as a DMSO solution (10 mL), taking care to avoid an exotherm. After 5 h stirring, the dark red solution was quenched and diluted with an excess of degassed water (100 mL). The addition of benzene (50 mL) then afforded a slightly yellow biphasic mixture. The benzene layer was extracted into a 500 mL bomb with a cannula, and the aqueous/DMSO layer was extracted with benzene (50 mL) two more times. The combined organic extracts were washed with degassed water (200 mL) four times, filtered through a pad of alumina, and concentrated *in vacuo* to afford a viscous oil, that when taken up in Et_2O and concentrated again, afforded 7.0 g of **11** as a white powder in 70% yield. NMR analysis reveals a 1:1 mixture of diastereomers. ^{1}H NMR (300 MHz, C_6D_6)[41] δ: 5.31 (d, J = 224 Hz, 2H, ArP*H*(C_6H_5)), 5.44 (d, J = 223 Hz, 6H, ArP*H*(C_6H_5)), 6.85-7.00 (m, 14H, aryl-*H*, *rac*/*meso*), 7.04-7.18 (m, 14H, aryl-*H*, *rac/meso*), 7.24-7.34 (m, 6H, aryl-*H*, *rac*/*meso*), 7.34-7.42 (m, 4H, aryl-*H*, *rac*/*meso*), 7.48-7.59 (m, 4H, aryl-*H*, *rac*/*meso*). ^{31}P{^{1}H} NMR (121 MHz, C_6D_6) δ: -44.54 (d, J = 227 Hz), -43.85 (d, J = 224 Hz). HRMS (FAB+) $C_{29}H_{24}NP_2$: calcd mass 448.1384, measured mass 448.1371.

(PNP)K_2 12a. To an oven-dried 50 mL round-bottom flask equipped with a stirbar and charged with **11** (500 mg, 1.1 mmol, 1.0 equiv) was added THF (5 mL). The clear solution was cooled to -40 °C, after which KBn (290 mg, 2.2 mmol, 2.0 equiv) dissolved in cold THF (2 mL) was added dropwise. The dark red solution was warmed to ambient temperature and concentrated *in vacuo* to approximately 1 mL for growth of red crystals of **12b** by slow evaporation of THF into toluene. For quantitative isolation, the THF solution is completely evaporated, washed with pentane, and dried *in vacuo* to afford 0.58 g of the dipotassium salt as a red powder, which was stored at -15 °C. ^{1}H NMR (300 MHz, d^8-THF) δ: 6.44 (td, J = 7.2, 1.2 Hz, 2H), 6.57-6.73 (m, 6H), 6.85 (t, J = 15.1 Hz, 4H), 7.35 (d, J = 7.6 Hz, 2H), 7.42-7.53 (m, 4H), 7.69 (t, J = 7.6 Hz, 1H), 7.72 (d, J = 7.9 Hz, 2H). ^{31}P{^{1}H} NMR (121 MHz, d^8-THF) δ: -14.35 (s).

(PNP)Zr(NMe_2)$_2$ 13. An oven-dried 50 mL round-bottom flask equipped with a stirbar is charged with bis(phosphine) **11** (57 mg, 130 μmol, 1.0 equiv) and Zr(NMe_2)$_4$ (34 mg, 130 μmol, 1.0 equiv). Benzene (5 mL) is vacuum transferred at 0°C, and the solution stirred rapidly while warming to ambient temperature. After 5 min stirring at room temperature, the dark red solution is concentrated *in vacuo* to afford a red oil. Pentane is then vacuum transferred onto the oil, and the pink suspension is concentrated *in vacuo* to afford 80 mg of a pink solid in 99% yield. Crystals suitable for x-ray analysis were obtained in toluene at -35 °C. ^{1}H NMR (300 MHz, C_6D_6) δ: 2.64 (s, Zr(N(CH_3)$_2$)$_2$, 12H), 6.66 (d, J = 7.9 Hz, 2H), 6.70 (td, J = 7.5, 1.2 Hz, 2H), 6.88 (td, J = 7.7, 1.4 Hz, 2H), 6.95 (ddd, J = 7.5, 2.8, 1.3 Hz, 2H), 7.09-7.01 (m, 3H), 7.18 (t, J = 7.9 Hz, 4H), 7.47 (dd, J = 7.5, 2.8 Hz, 2H), 7.70 (t, J = 6.6 Hz, 4H). ^{31}P{^{1}H} NMR (121 MHz, C_6D_6) δ: 0.00 (br s).

Anal. Calcd. for $C_{33}H_{33}N_3P_2Zr$: C, 63.44; H, 5.32; N, 6.73. Found: C, 63.66; H, 5.24; N, 6.60.

Variable-Temperature NMR Procedure. All variable-temperature NMR experiments were performed on a Varian INOVA-500 spectrometer. An oven-dried J. Young NMR tube was charged with 7 mg of **8**. On a high-vacuum-line setup, the tube was evacuated and 1.2 mL of tetrachloroethane-d_2 was vacuum transferred onto the solid. The solution was then blanketed in argon and sealed. The desired temperature of the NMR probe was set, and after reaching said temperature, the temperature of the tube was allowed to stabilize for 15 minutes before acquiring a spectrum.

X-Ray Crystal Data: General Procedure. Crystals grown from THF (**13**) and toluene (**15**) were removed quickly from a scintillation vial to a microscope slide coated with Paratone N oil. Samples were selected and mounted on a glass fiber with Paratone N oil. Data collection was carried out on a Bruker KAPPA APEX II diffractometer with a 0.71073 Å MoKα source. The structures were solved by direct methods. All non-hydrogen atoms were refined anisotropically. Some details regarding refined data and cell parameters are available in Crystallographic Information. Selected bond distances and angles are supplied as well.

Computational Details. Density functional calculations were carried out using Gaussian 03 Revision D.01.[29] Calculations were performed using the nonlocal exchange correction by Becke[30] and nonlocal correlation corrections by Perdew,[31] as implemented using the b3lyp[32,33] keyword in Gaussian. The following basis sets were used: LANL2DZ[34-36] for Zr atoms and 6-31G** basis set for all other atoms. Pseudopotentials were utilized for Zr

atoms using the LANL2DZ ECP. All optimized structures were verified using frequency calculations and did not contain any imaginary frequencies. Isosurface plots were made using the Visual Molecular Dynamics program.[37]

REFERENCES

1. McKnight, A. L.; Waymouth, R. M. *Chem. Rev.* **1998**, *98*, 2587.
2. Brintzinger, H. H.; Fischer, D.; Mulhaupt, R.; Rieger, B.; Waymouth, R. M. *Angew. Chem., Int. Ed.* **1995**, *34*, 1143.
3. Gibson, V. C.; Spitzmesser, S. K. *Chem. Rev.* **2003**, *103*, 283.
4. (a) Agapie, T.; Henling, L. M.; DiPasquale, A. G.; Rheingold, A. L.; Bercaw, J. E. *Organometallics* **2008**, *27*, 6245. (b) Golisz, S. R.; Bercaw, J. E. *Macromolecules* **2009**, *42*, 8751. (c) Tonks, I. A.; Tofan, D.; Weintrob, E. C.; Agapie, T.; Bercaw, J. E. *Organometallics* **2012**, *31*, 1965.
5. Tonks, I. A.; Henling, L. M.; Day, M. W.; Bercaw, J. E. *Inorg. Chem.* **2009**, *48*, 5096.
6. Tolman, C. A. *Chem. Rev.* **1977,** *77*, 313.
7. Richards, C. J.; Locke, A. J. *Tetrahedron: Asymmetry* **1998**, *9*, 2377.
8. Horner, L.; Winkler, H.; Rapp, A.; Mentrup, A.; Hoffmann, H.; Beck, P. *Tetrahedron Lett.* **1961**, *161*, 161.
9. Jiang, X.; Minnaard, A. J.; Hessen, B.; Feringa, B. L.; Duchateau, A. L. L.; Andrein, J. G. O.; Boogers, J. A. F.; de Vries, J. G. *Org. Lett*. **2003**, *5*, 1503.
10. Quin, L. D. *A Guide to Organophosphorus Chemistry*, 1st ed.; John Wiley & Sons: New York, 2000.
11. For examples, see: (a) Chou, T.; Tsao, C.; Hung, S. C. *J. Org. Chem.* **1985**, *50*, 4329. (b) Dickson, R. S.; Elmes, P. S.; Jackson, W. R. *Organometallics* **1999**, *18*, 2912.
12. Honaker, M. T.; Hovland, J. M.; Salvatore, R. N. *Curr. Org. Synth.* **2007**, *4*, 31.
13. For examples, see: (a) Petit, C.; Favre-Réguillon, A.; Mignani, G.; Lemaire, M. *Green Chem.*, **2010**, *12*, 326. (b) Berthod, M.; Favre-Réguillon, A; Mohamad, J.; Mignani, G.; Docherty, G.; Lemaire, M. *Synlett*, **2007**, *10*, 1545. (c) Wolfe, B.; Livinghouse, T. *J. Am. Chem. Soc.* **1998**, *120*, 5116. (d) Imamoto, T.; Oshiki, T.; Onozawa, T.; Kusumoto, T.; Sato, K. *J. Am. Chem. Soc.* **1990**, *112*, 5244. (e) Imamoto, T.; Kusumoto, T.; Suzuki, N.; Sato, K. *J. Am. Chem. Soc*. **1985**, *107*, 5301. (f) Gusarova, N. K.; Malysheva, S. F.; Belogorlova, N. A.; Sukhov, B. G.;

Trofimov, B. A. *Synthesis* **2007**, *18*, 2849. (g) Peters, G. *J. Am. Chem. Soc.* **1960**, *82*, 4752.

14. Rogers, J. R.; Wagner, T. P. S.; Marynick, D. S. *Inorg. Chem.* **1994**, *33*, 3104.
15. Baker, R. T.; Whitney, J. F.; Wreford, S. S. *Organometallics* **1983**, *2*, 1049.
16. Rocklage, S. M.; Schrock, R. R.; Churchill, M. R.; Wasserman, H. J. *Organometallics* **1982**, *1*, 1332.
17. Bohle, D. S.; Jones, T. C.; Rickard, C. E. F.; Roper, W. R. *Organometallics* **1986**, *5*, 1612.
18. Turculet, L.; McDonald, R. *Organometallics* **2007**, *26*, 6821.
19. Herd, O.; Heβler, A.; Hingst, M.; Tepper, M.; Stelzer, O. *J. Organomet. Chem.* **1996**, *522*, 69.
20. Kui, S. C. F.; Huang, J.-S.; Sun, R. W.-Y.; Zhu, N.; Che, C.-M. *Angew. Chem., Int. Ed.* **2006**, *45*, 4663.
21. Kim, J. K.; Bunnett, J. F. *J. Am. Chem. Soc.* **1970**, *92*, 7463.
22. Tu, S.; Jia, R.; Jiant, B.; Zhang, J.; Zhang, Y.; Yao, C.; Ji, S. *Tetrahedron* **2007**, *63*, 381.
23. Whitfield, S. R.; Sanford, M. S. *J. Am. Chem. Soc.* **2007**, *129*, 15142.
24. Pearson, R. G. *J. Am. Chem. Soc.* **1963**, *85*, 3533.
25. Love, B. E.; Jones, E. G. *J. Org. Chem.* **1999**, *64*, 3755.
26. Bailey, P. J.; Coxall, R. A.; Dick, C. M.; Fabre, S.; Henderson, L. C.; Herber, C.; Liddle, S. T.; Lorono-Gonzales, D.; Parkin, A.; Parsons, S. *Chem. Eur. J.* **2003**, *9*, 4820.
27. Bradley, D. C.; Thomas, I. M. *J. Chem. Soc.* **1960**, 3857.
28. Pangborn, A. B.; Giardello, M. A.; Grubbs, R. H.; Rosen, R. K.; Timmers, F. J. *Organometallics* **1996**, *15*, 1518.
29. Frisch, M. J.; Trucks, G. W.; Schlegel, H. B.; Scuseria, G. E.; Robb, M. A.; Cheeseman, J. R.; Montgomery, Jr., J. A.; Vreven, T.; Kudin, K. N.; Burant, J. C.; Millam, J. M.; Iyengar, S. S.; Tomasi, J.; Barone, V.; Mennucci, B.; Cossi, M.; Scalmani, G.; Rega, N.; Petersson, G. A.; Nakatsuji, H.; Hada, M.; Ehara, M.; Toyota, K.; Fukuda, R.; Hasegawa, J.; Ishida, M.; Nakajima, T.; Honda, Y.; Kitao, O.; Nakai, H.; Klene, M.; Li, X.; Knox, J. E.; Hratchian, H. P.; Cross, J. B.; Bakken, V.; Adamo, C.; Jaramillo, J.; Gomperts, R.; Stratmann, R. E.; Yazyev,

O.; Austin, A. J.; Cammi, R.; Pomelli, C.; Ochterski, J. W.; Ayala, P. Y.; Morokuma, K.; Voth, G. A.; Salvador, P.; Dannenberg, J. J.; Zakrzewski, V. G.; Dapprich, S.; Daniels, A. D.; Strain, M. C.; Farkas, O.; Malick, D. K.; Rabuck, A. D.; Raghavachari, K.; Foresman, J. B.; Ortiz, J. V.; Cui, Q.; Baboul, A. G.; Clifford, S.; Cioslowski, J.; Stefanov, B. B.; Liu, G.; Liashenko, A.; Piskorz, P.; Komaromi, I.; Martin, R. L.; Fox, D. J.; Keith, T.; Al-Laham, M. A.; Peng, C. Y.; Nanayakkara, A.; Challacombe, M.; Gill, P. M. W.; Johnson, B.; Chen, W.; Wong, M. W.; Gonzalez, C.; Pople, J. A. *Gaussian 03*, revision C.02; Gaussian, Inc.: Wallingford, CT, 2004.

30. (a) Becke, A. D. *Phys. Rev. A: At., Mol., Opt. Phys.* **1988**, *38*, 3098. (b) Becke, A. D. *J. Chem. Phys.* **1988**, *88*, 1053.
31. Perdew, J. P. *Phys. Rev. B* **1986**, *33*, 8800.
32. Lee, C.; Yang, W.; Parr, R. G. *Phys. Rev. B* **1988**, *37*, 785.
33. Miehlich, B.; Savin, A.; Stoll, H.; Preuss, H. *Chem. Phys. Lett.* **1989**, *157*, 200.
34. Hay, P. J.; Wadt, W. R. *J. Chem. Phys.* **1985**, *82*, 270.
35. Wadt, W. R.; Hay, P. J. *J. Chem. Phys.* **1985**, *82*, 284.
36. Hay, P. J.; Wadt, W. R. *J. Chem. Phys.* **1985**, *82*, 299.
37. Humphrey, W.; Dalke, A.; Schulten, K. *J. Mol. Graphics* **1996**, *14*, 33.

CHAPTER 2

Synthesis, Solid-State, and Solution-State Behavior of a Palladium(II) Halide Series Supported by a Structurally Versatile Bidentate Bis(Secondary Phosphine) Ligand

ABSTRACT

A neutral bis(secondary phosphine) ligand coordinates readily κ^2 to late metals, such as palladium(II), affording *P*-chirogenic diastereomers. Crystallographic and spectroscopic analysis of a series of palladium(II) dihalides stabilized by this bis(phosphine) indicate that one diastereomer is enthalpically favored, while the other more structurally versatile diastereomer is favored entropically. There is also evidence of an interesting phosphine epimerization pathway assisted by the non-coordinated pyridine ring.

INTRODUCTION

Tertiary phosphines are widely utilized ligands due to their strong σ-donating abilities and steric and electronic tunability.[1] Their relatively high inversion barrier (30–35 kcal/mol) allows the synthesis and isolation of asymmetrically substituted *P*-chiral phosphines.[2] In contrast, secondary phosphines are less bulky and prone to irreversible coordination to transition metals. Due to their reactivity and susceptibility to autoxidation, their synthesis and coordination chemistry are far less explored than that of their tertiary analogs.

General approaches to asymmetrically substituted secondary phosphines have been discussed in Chapter 1, as well as the solid-state structures of potassium and zirconium(IV) complexes supported by ligand **1**.

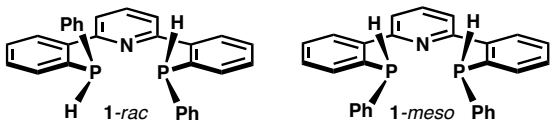

With an understanding of dianionic PNP^{2-} bonding to high-valent metals, we explored the coordination of neutral PNP-H_2 (**1**) to metals of lower valency. We envisioned that the potential redox non-innocence of PNP-H_2 could be exploited to access high-valent metal species generated by oxidation; in particular, the tridentate binding mode could conceivably stabilize octahedral d^6 palladium(IV) and platinum(IV) complexes (Scheme 2.1).

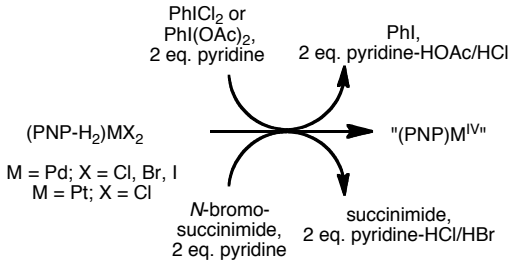

Scheme 2.1

Many late-metal complexes stabilized by relatively simple, symmetrically substituted monodentate secondary phosphines have been reported, but relatively few have actually been structurally characterized by x-ray crystallographic analysis. Of particular interest to the studies disclosed herein, Glueck[3] and Pasquali[4] have synthesized and structurally characterized numerous palladium(II) and platinum(II) complexes bound to secondary phosphines. However, all are stabilized by monodentate secondary phosphines with symmetrical diaryl substitution (Figure 2.1). The catalytic activity of these complexes, unfortunately, has not been probed.

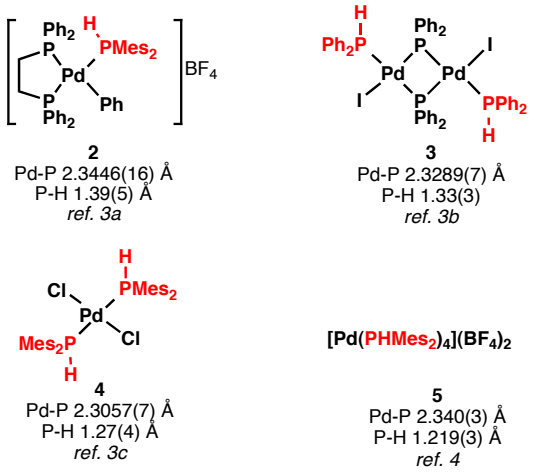

Figure 2.1. Structurally characterized palladium(II) complexes stabilized by secondary diarylphosphines (red) and selected bond lengths

The average Pd-P bond length in the solid-state structures of **2** – **5** is 2.330(3) Å. It seems that Pd→P backbonding to secondary phosphines significantly influences Pd-P bond lengths. As such, a direct comparison of the complexes above reveal that Ar_2HP-Pd bonds are longer in cationic complexes (**2** and **5**), and shorter in neutral complexes (**3** and **4**) whose metals are more prone to donate *d*-electrons into empty phosphine P-R σ^*-orbitals. Indeed, the crystal structure of reduced species $Pd(PHMes_2)_4$ indicates an average Pd-P bond length of 2.3213(6) Å,[4] slightly shorter than the average Pd-P bond length in cationic palladium(II) analog $[Pd(PHMes_2)_4]^{2+}$ (**5**). Structural comparison of *trans*-$(PHMes_2)_2PdCl_2$ (**4**) and triarylphosphine-stabilized *trans*-$(PPh_3)PdCl_2$ reveals an important difference between diaryl and triaryl phosphines:[5] the Pd-P bond in **4** is slightly shorter than in *trans*-$(PPh_3)PdCl_2$ (2.337(1) Å), a discrepancy that reflects greater σ-donation by $PHMes_2$ relative to PPh_3, and the reduced steric encumbrance of secondary phosphines compared to tertiary phosphines.[6]

The relationship between P-H bond length and the electronic environment of the metal is more nebulous. Clearly, there is significantly more error involved in determining the structural parameters of the P-H proton by x-ray diffraction, and it seems from the small set of complexes in Figure 2.1 that this parameter is neither predictable nor very useful in concluding much about phosphorus donation to palladium (gas-phase P-H bond length of $PHMes_2$ is 1.36(7) Å).[3c] The P-H bond, however, is spectroscopically distinct in palladium(II) complexes stabilized by secondary phosphines. The ^{1}H NMR signals of *P*-bound protons generally lies between 6 and 7 ppm and exhibits phosphorus coupling ($^1J_{P-H}$) between 350 and 400 Hz, while the ^{31}P signals are often found between 0 and 100 ppm.[3,4] Unsurprisingly, the location of both ^{1}H and ^{31}P NMR resonances are strongly dependent upon phosphine substitution. Infrared (IR) bands corresponding to P-H bond stretching typically appear in the range 2200–2400 cm^{-1}. The diagnostic ^{1}H NMR and IR signals of Pd-bound secondary phosphines do not differ significantly from unbound phosphines, but the ^{31}P NMR signal of uncoordinated phosphines generally appear upfield of 0 ppm. In summary, while these spectroscopic properties are useful diagnostic tools to verify the existence of secondary phosphine ligands, they are insufficient to determine the nature of the Pd-P bond.

RESULTS AND DISCUSSION

Due to the prevalence of Group 10 metal complexes supported by bi- and tridentate ligands with tertiary phosphines, we focused on the synthesis and structural analysis of late metals stabilized by much rarer neutral bis(secondary phosphine) pincer

ligands, such as **1**. In particular, we hoped to understand the electronic and steric effects of a P-H bond on coordination to a metal, and the consequences of using diastereomeric ligands with *P*-chirality. Indeed, reactions of a 1:1 mixture of **1**-*rac* and **1**-*meso* with palladium(II) dihalides cleanly produce low-valent coordination complexes that can be spectroscopically characterized and crystallized. In all cases, PNP-type ligand **1** coordinates in a *cis*-κ^2-fashion without participation of the pyridine nitrogen.

Synthesis, Characterization, and VT-NMR Analysis of meso-(PNP-H_2)$PdCl_2$ (**6-***meso*)

Treatment of (COD)$PdCl_2$ (COD = cyclooctadiene) with 1:1 **1**-*rac* and **1-** *meso* in benzene for 3 hours affords a single species by ^{1}H and ^{31}P NMR (eq. 1). Diagnostic one-bond coupling to the *P*-bound proton ($^1J_{P\text{-}H}$ = 378 Hz) splits the ^{31}P NMR signal at δ 12.0 ppm to a doublet. X-ray diffraction of crystals grown from a saturated CH_2Cl_2 solution analyze as the (*meso*-PNP-H_2)$PdCl_2$ diastereomer (Figure 2.2). As expected, the Pd is square planar ($\Sigma\angle_{Pd}$ = 360.028(24)°). The P-Pd bond lengths in **6-***meso* (Pd-P1 = 2.2319(3), Pd-P2 = 2.2211(3) Å) are reasonably shorter than in monodentate secondary phosphine-stabilized complexes **2** – **5**, but comparable to P-Pd bond lengths in palladium(II) dichlorides stabilized by traditional bidentate bis(tertiary phosphines), such as diphenylphosphinomethane (dppm, P-Pd = 2.234(1) and 2.250(1) Å), diphenylphosphinoethane (dppe, 2.233(2) and 2.226(2) Å), and diphenylphosphinopropane (dppp, 2.244(1) and 2.249(1) Å).[7] The ligand bite angle is typical (P1-Pd-P2 = 91.342(13)°), and the P-Pd-Cl angles are slightly decreased (P1-Pd-Cl2 = 86.874(12), P2-Pd-Cl1 = 87.887(12)°) and the Cl1-Pd-Cl2 angle slightly increased

from an ideal square planar arrangement (93.925(11)°). Furthermore, P1-H (1.297(15) Å) and P2-H (1.309(14) Å) are within error of one another (the *P*-bound hydrogen atoms have been located).

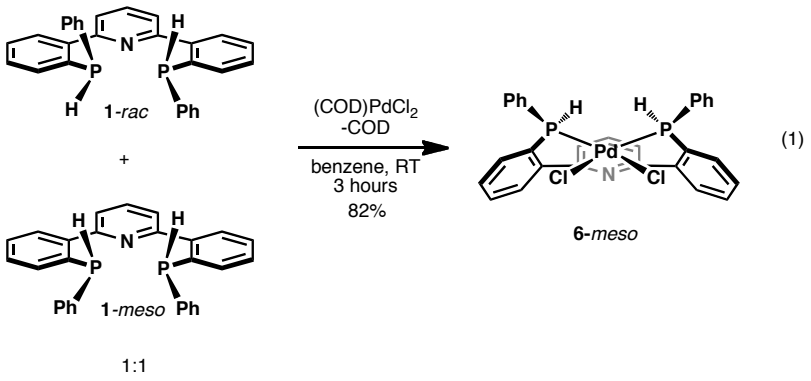

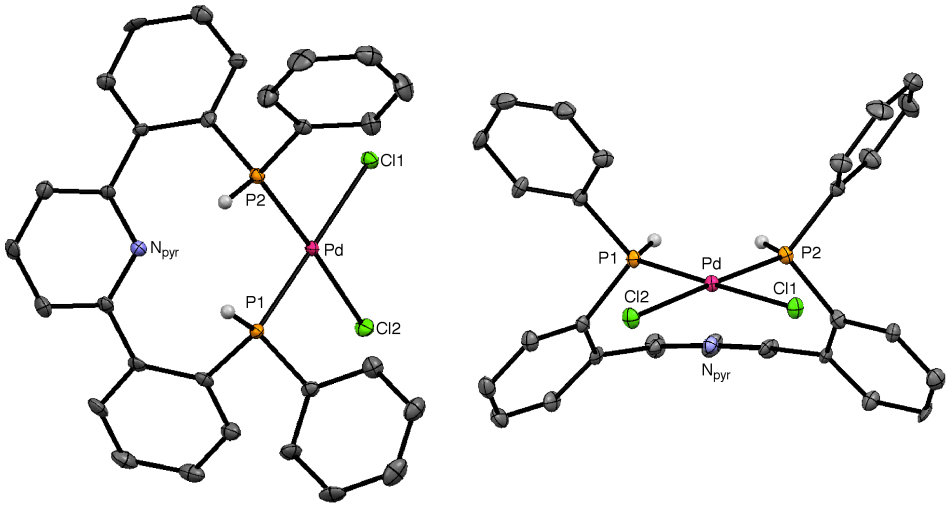

Figure 2.2. Thermal ellipsoid representation of (*meso*-PNP-H_2)$PdCl_2$ (**6**-*meso*) at the 50% probability level. All C-bound hydrogens have been omitted. Atoms are color coded: carbon (gray), hydrogen (light gray), chlorine (green), nitrogen (blue), palladium (pink), phosphorus (orange). Selected bond lengths (Å) and angles (°): P1-H 1.297(15); P2-H 1.309(14); Pd-P1 2.2319(3); Pd-P2 2.2211(3); Pd-Cl1 2.3443(3); Pd-Cl2 2.3614(3); P1-Pd-P2 91.342(13); P1-Pd-Cl2 86.874(12); P2-Pd-Cl1 87.887(12); Cl1-Pd-Cl2 93.925(11)

Selected $^{31}P\{^{1}H\}$ VT-NMR spectra of **6**-*meso* in CD_2Cl_2 are shown in Figure 2.3. A scenario can be envisioned in which **6**-*meso* and the *rac*-PNP-H_2-supported complex (**6**-*rac*) interconvert rapidly in solution at room temperature, yet **6**-*meso* preferably crystallizes. However, the possibility that the singlet at δ 12.0 ppm is simply an average of two interconverting species is discounted since the signal remains unchanged at -80 °C. Even at 60 °C, **6**-*meso* remains the only species in solution, although the signal broadens somewhat, possibly due to ligand fluxionality.

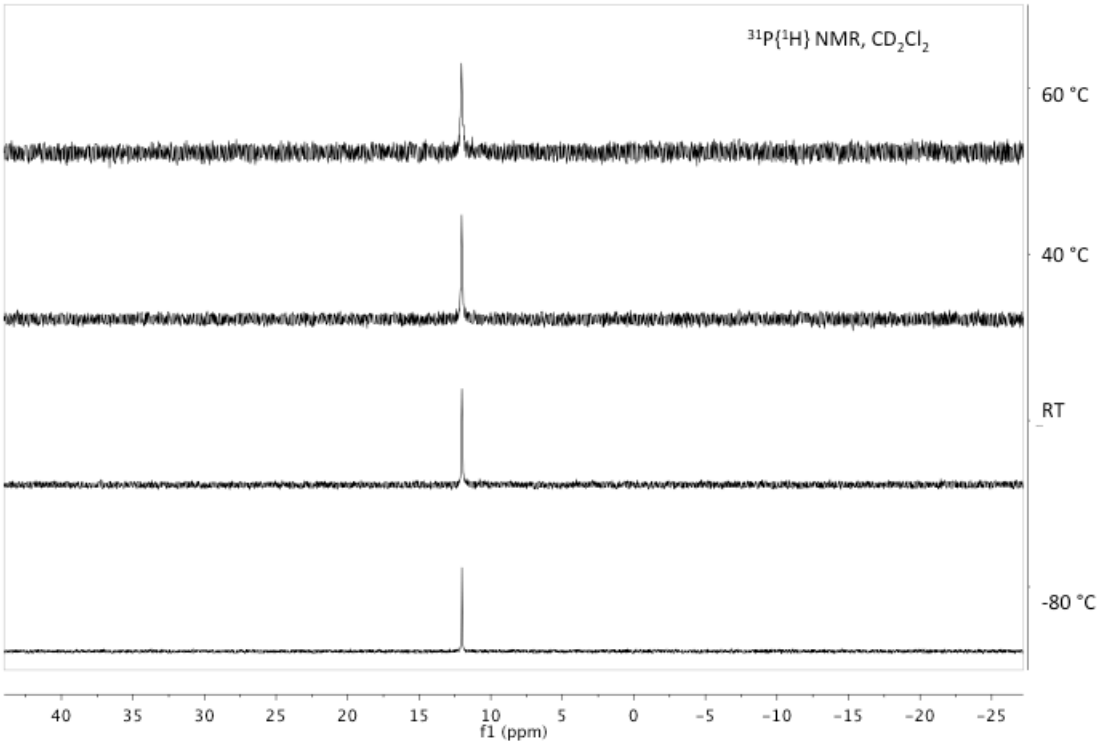

Figure 2.3. Selected region of variable-temperature $^{31}P\{^{1}H\}$ NMR spectra in CD_2Cl_2 of **6**-*meso*

Synthesis, Characterization, and VT-NMR Analysis of rac- and meso-(PNP-H$_2$)PdBr$_2$ (**7**)

The reaction of *trans*-(MeCN)$_2$PdBr$_2$ with PNP-H$_2$ (**1**) in benzene for 3 hours at room temperature generates two species by ^{1}H and ^{31}P NMR in a roughly 5:1 (*meso:rac*) ratio (eq. 2). Slow evaporation of a saturated CH_2Cl_2 solution affords two physically different monoclinic crystals that have each been analyzed by x-ray diffraction. The large, block-shaped yellow crystals correspond to (*meso*-PNP-H$_2$)PdBr$_2$ (**7**-*meso*), which is isostructural to the dichloride **6**-*meso*. Smaller, blade-like yellow crystals analyze as (*rac*-PNP-H$_2$)PdBr$_2$ (**7**-*rac*), the solid-state structure of which is unexpected.

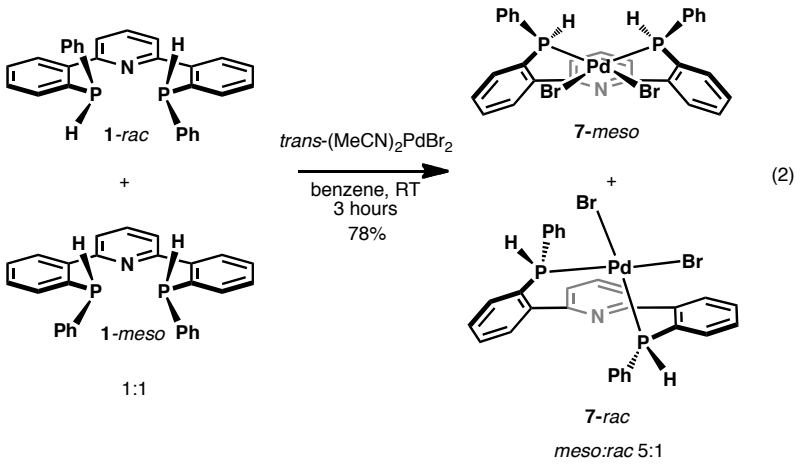

Like **6**-*meso*, the solid-state structure of **7**-*meso* is roughly C_s-symmetric (Figure 2.4). Pd-P bond lengths (Pd-P1 = 2.2328(3), Pd-P2 = 2.2452(3) Å) vary only slightly from those in the dichloride. The complex is also square planar at the Pd center ($\Sigma\angle_{Pd}$ = 360.047(20)°), with P-H bonds (P1-H = 1.259(17), P2-H = 1.276(19) Å) within error of one another, and very nearly within error of those in the dichloride analog.

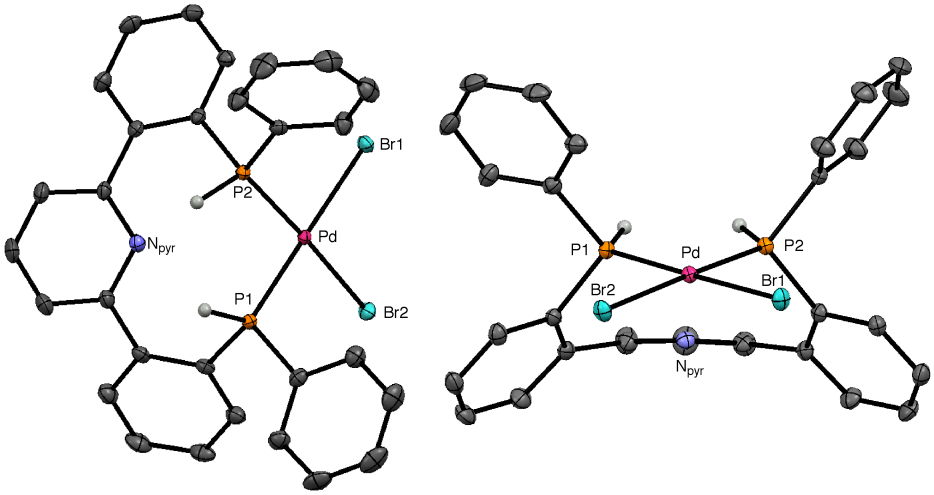

Figure 2.4. Thermal ellipsoid representation of (*meso*-PNP-H_2)$PdBr_2$ (**7**-*meso*) at the 50% probability level. All C-bound hydrogens have been omitted. Atoms are color coded: carbon (gray), hydrogen (light gray), bromine (turquoise), nitrogen (blue), palladium (pink), phosphorus (orange). Selected bond lengths (Å) and angles (°): P1-H 1.259(17); P2-H 1.276(19); Pd-P1 2.2328(3); Pd-P2 2.2452(3); Pd-Br1 2.48284(16); Pd-Br2 2.46995(17); P1-Pd-P2 91.289(13); P1-Pd-Br2 88.422(10); P2-Pd-Br1 87.000(10); Br1-Pd-Br2 93.336(6)

The alternate diastereomer **7**-*rac* exhibits a remarkably different, C_1-symmetric geometry in the solid state (Figure 2.5). The palladium center is planar ($\Sigma\angle_{Pd}$ = 360.126(25)°), but the ligand itself coordinates with an enlarged bite angle (P1-Pd-P2 = 99.031(17)°) roughly the same as (diphenylphosphinoferrocene)$PdCl_2$ (P-Pd-P = 99.07(5)°).[8] The bite angle is approximately 8° greater than that of **7**-*meso*, likely due to canting of just one ligand aryl ring that results in a longer linear distance between the phosphine donors (versus canting of both aryl rings in the C_s-symmetric **7**-*rac*.) The Br1-Pd-Br2 angle (91.414(7)°) is typical, but to accommodate the larger bite angle, P1-Pd-

Br2 (83.031(13) °) and P2-Pd-Br1 (86.650(12)°) are relatively distorted. Pd-P bonds (2.2407(4) and 2.2761 Å) are slightly longer than in **7**-*meso,* while P-H bonds (1.259(18) and 1.26(2) Å) bond lengths are comparable. The centroid-centroid distance between the *P*-phenyl substituent and ligand framework aryl ring is 3.466(3) Å, suggestive of a π-stacking interaction in the solid state.[9]

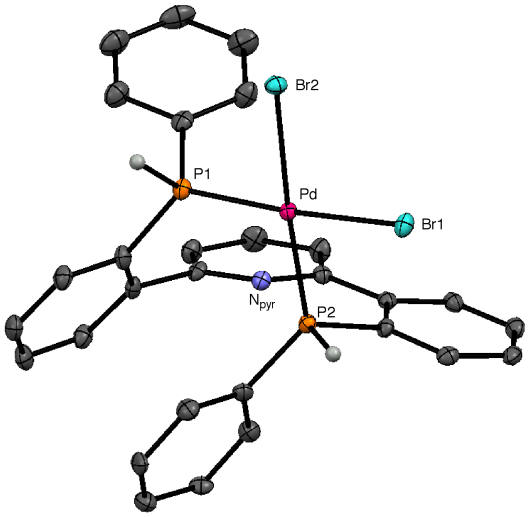

Figure 2.5. Thermal ellipsoid representation of (*rac*-PNP-H_2)$PdBr_2$ (**7**-*rac*) at the 50% probability level. All C-bound hydrogens have been omitted. Atoms are color coded: carbon (gray), hydrogen (light gray), bromine (turquoise), nitrogen (blue), palladium (pink), phosphorus (orange). Selected bond lengths (Å) and angles (°): P1-H 1.259(18); P2-H 1.26(2); Pd-P1 2.2407(4); Pd-P2 2.2761(5); Pd-Br1 2.5020(2); Pd-Br2 2.4894(2); P1-Pd-P2 99.031(17); P1-Pd-Br2 83.031(13); P2-Pd-Br1 86.650(12); Br1-Pd-Br2 91.414(7)

The ^{31}P NMR spectrum of the products shows two doublets. The signal at δ 11.5 ppm ($^{1}J_{P-H}$ = 378 Hz) likely corresponds to **7**-*meso* given the similar chemical shift and ^{1}H coupling values of structurally analogous **6**-*meso*. The signal at δ 5.0 ppm ($^{1}J_{P-H}$ = 411

Hz) is presumably **7**-*rac*. Due to the unreliability of ^{31}P signal integration (particularly when one-bond ^{1}H coupling is involved), the diagnostic triplet corresponding to the 4-hydrogen on the ligand pyridine ring in the ^{1}H NMR spectrum has been used to quantify the ratio of **7**-*meso*:**7**-*rac* (Figure 2.6). The ^{31}P NMR spectrum over a temperature range is shown in Figure 2.7. While the ratio of **7**-*meso* and **7**-*rac* at room temperature is 5.0:1, the ratio is 4.0:1 at 40 °C, and 2.7:1 at 60 °C. A van't Hoff analysis (Figure 2.8) of the equilibrium constants (K_{eq}) for isomerization indicates that **7**-*meso* is enthalpically favored by 3.5 kcal/mol but entropically disfavored by 8.3 cal/mol•K (eq. 3).

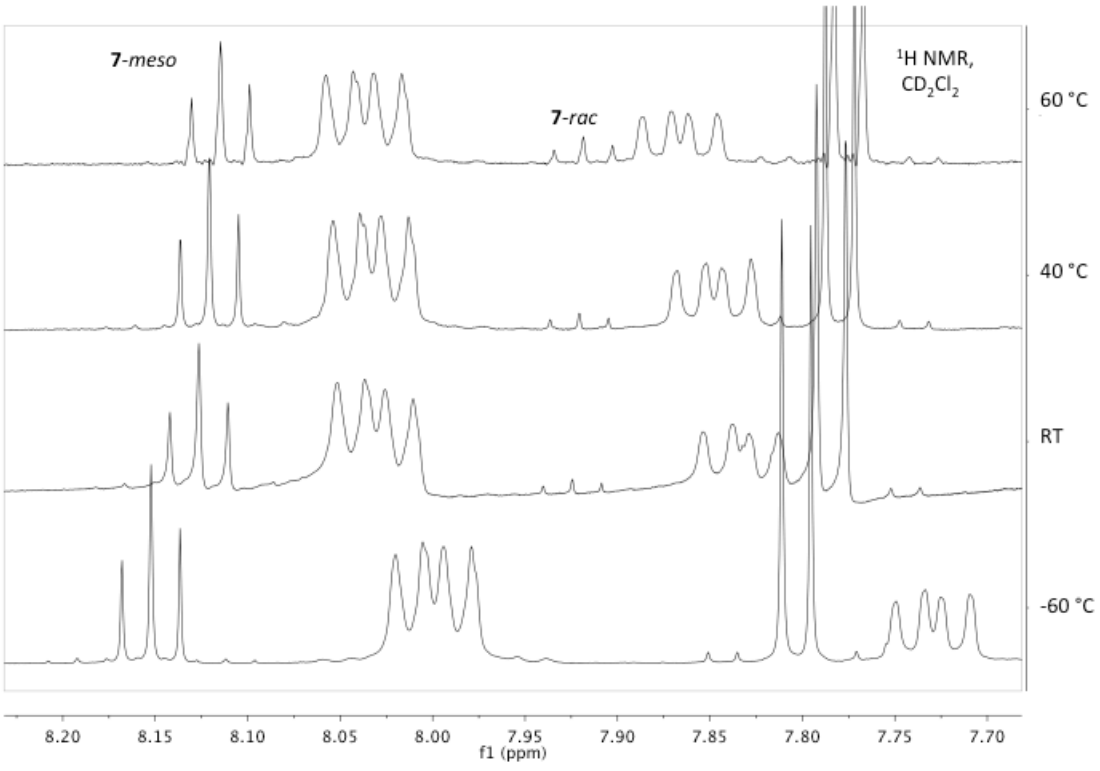

Figure 2.6. Selected region of variable-temperature ^{1}H NMR spectra in CD_2Cl_2 of **7**-*meso* and **7**-*rac.* Labeled triplets correspond to the 4-^{1}H on the pyridine ring of PNP-H_2

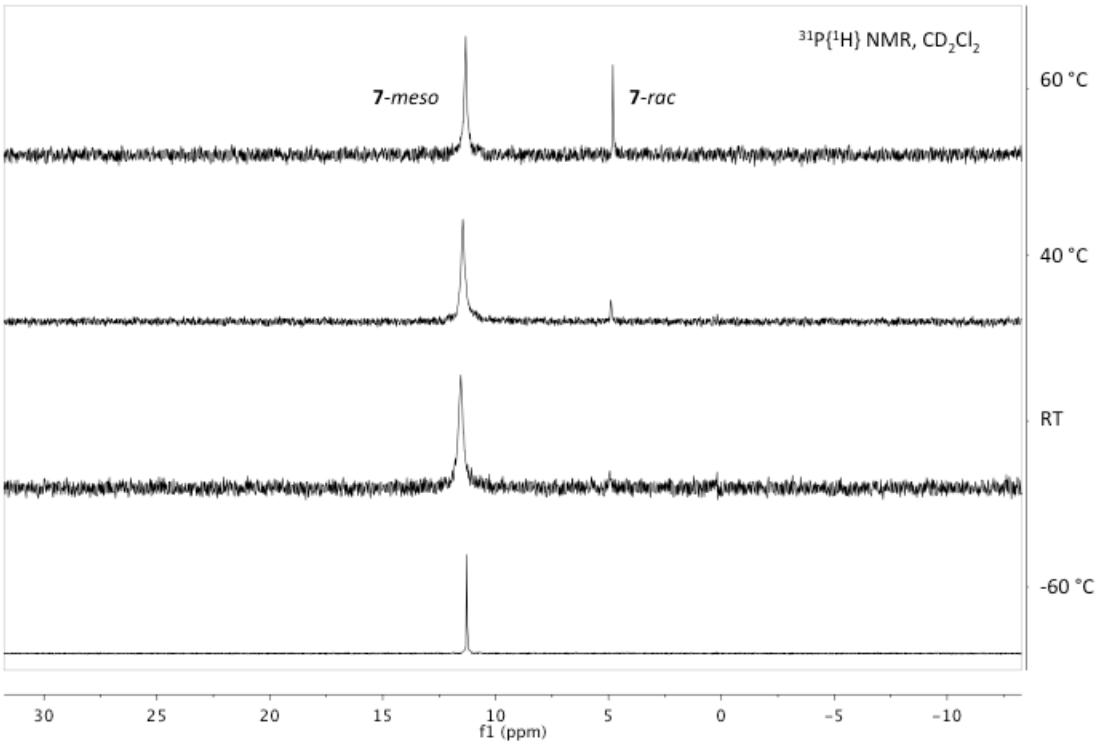

Figure 2.7. Selected region of variable-temperature $^{31}P\{^{1}H\}$ NMR spectra in CD_2Cl_2 of **7**-*meso* and **7**-*rac*

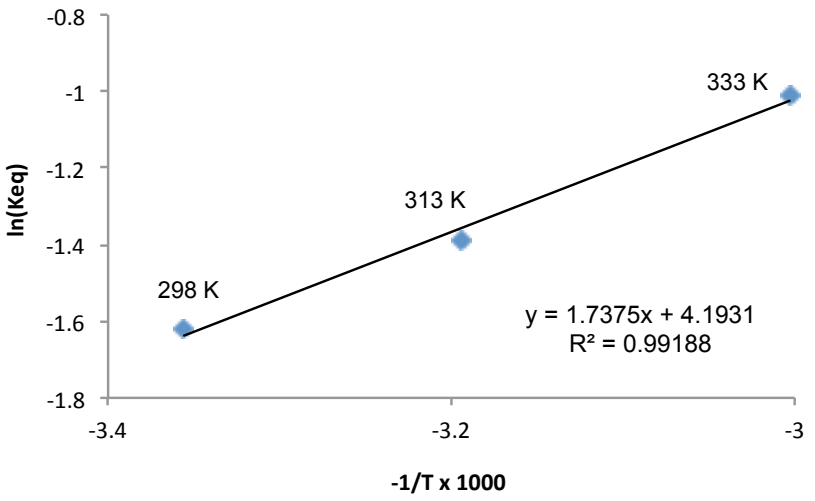

Figure 2.8. van't Hoff plot of **7**-*rac* and **7**-*meso* isomerization. Black line (linear regression). X-axis in units of K^{-1}

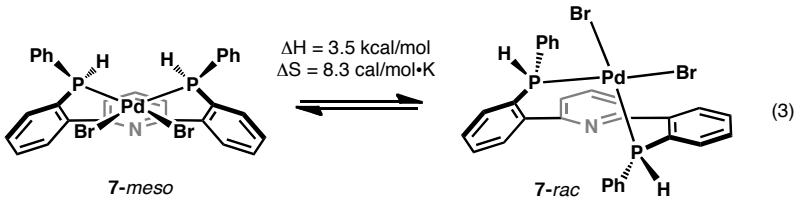

Synthesis, Characterization, and VT-NMR Analysis of rac- and meso-(PNP-H$_2$)PdI$_2$ (**8**)

The reaction of *trans*-$(PPh_3)_2PdI_2$ with PNP-H_2 (**1**) in benzene for 12 hours affords two species in a roughly 1:1.5 (*meso:rac*) ratio by ^1H and ^{31}P NMR (eq. 4). Crystallization by slow evaporation of a saturated solution of THF gives two types of crystal that analyze as (*meso*-PNP-H_2)PdI_2 (**8**-*meso*) and (*rac*-PNP-H_2)PdI_2 (**8**-*rac*).

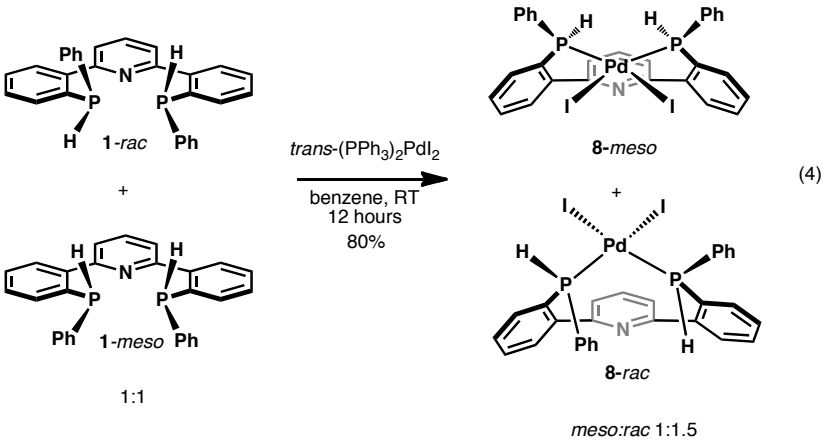

(4)

The solid-state structure of **8**-*meso* is roughly C_s-symmetric, like its dichloride and dibromide analogs (Figure 2.9). Pd-P bond lengths are slightly larger than in **6**-*meso* or **7**-*meso* (Pd-P1 = 2.2515(15), Pd-P2 = 2.2546(14) Å), and the complex is square planar at the Pd center ($\Sigma\angle_{Pd}$ = 361.09(8)°), with unremarkable P-H bonds (P1-H = 1.30(3), P2-H = 1.30(3) Å).

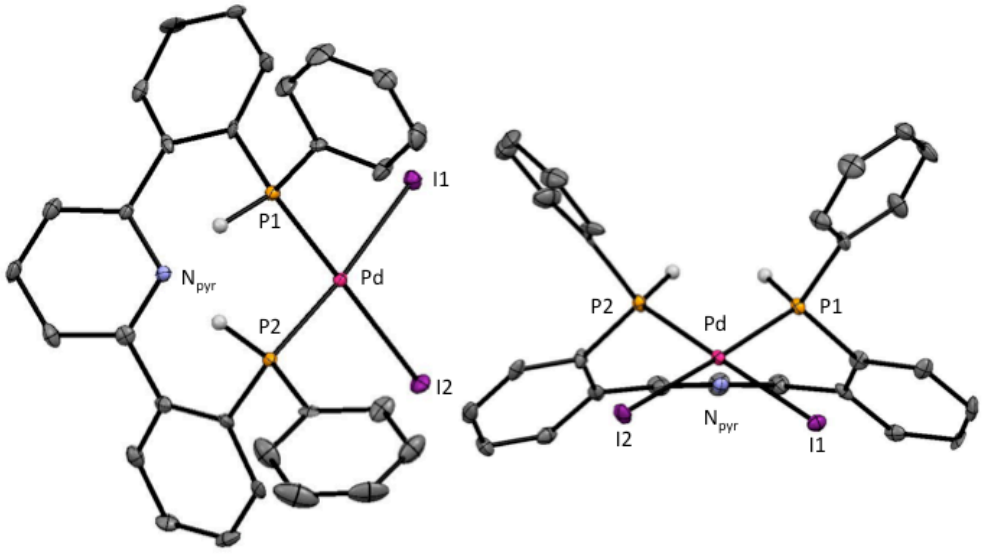

Figure 2.9. Thermal ellipsoid representation of (*meso*-PNP-H_2)PdI_2 (**8**-*meso*) at the 50% probability level. All C-bound hydrogens have been omitted. Atoms are color coded: carbon (gray), hydrogen (light gray), iodine (purple), nitrogen (blue), palladium (pink), phosphorus (orange). Selected bond lengths (Å) and angles (°): P1-H 1.30(3); P2-H 1.30(3); Pd-P1 2.2515(15); Pd-P2 2.2546(14); Pd-I1 2.6387(6); Pd-I2 2.6546(6); P1-Pd-P2 87.53(5); P1-Pd-I1 88.76(4); P2-Pd-I2 91.22(4); I1-Pd-I2 93.58(2)

The solid-state structure of **8**-*rac* is C_1-symmetric and substantially different from dibromide **7**-*rac* (Figure 2.10). Unlike in **7**-*rac*, the metal coordination plane pivots over the pyridine ring. The palladium center is planar ($\Sigma\angle_{Pd}$ = 360.18(4)°), with slight distortions in P2-Pd-I1 (85.013(19) °), P1-Pd-I2 (91.65(2) °), and I1-Pd-I2 (93.510(8)°) bond angles. Unlike **7**-*rac*, whose distortions result in a relatively large bite angle to the metal, the bite angle of **8**-*rac* (90.01(3)°) is more similar to the *meso*-PNP-H_2-supported complexes due to canting of both ligand aryl rings. Pd-P bond lengths (2.2568(8) and 2.2628(7) Å) are typical.

For a comparison of selected bond lengths and angles of complexes reported in this work, previously reported palladium complexes stabilized by secondary diarylphosphines, and palladium dichlorides supported by traditional bis(phosphine) ligands, see Tables 2.1 and 2.2.

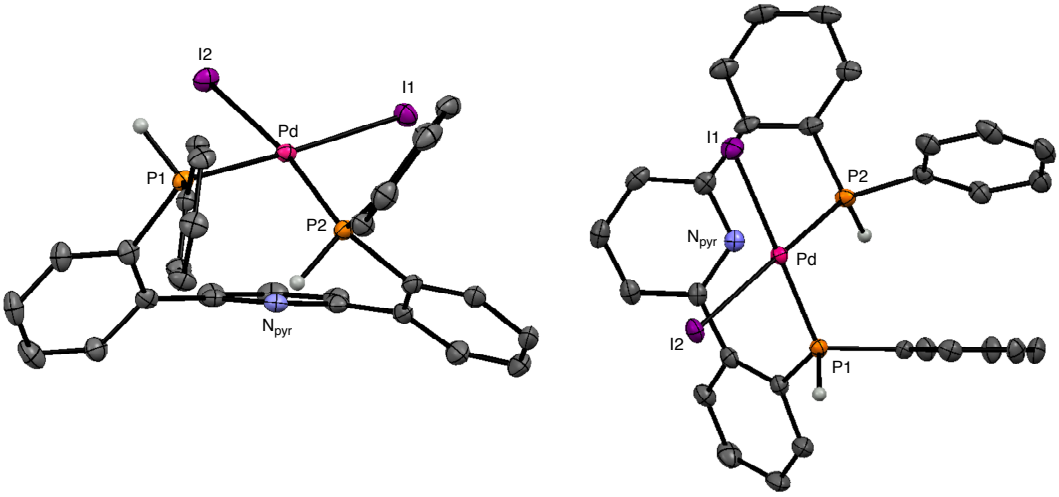

Figure 2.10. Thermal ellipsoid representation of (*rac*-PNP-H_2)PdI_2 (**8**-*rac*) at the 50% probability level. All C-bound hydrogens have been omitted. Atoms are color coded: carbon (gray), hydrogen (light gray), iodine (purple), nitrogen (blue), palladium (pink), phosphorus (orange). Selected bond lengths (Å) and angles (°): P1-H 1.34(3); P2-H 1.34(3); Pd-P1 2.2568(8); Pd-P2 2.2628(7); Pd-I1 2.6608(3); Pd-I2 2.6405(3); P1-Pd-P2 90.01(3); P1-Pd-I2 85.013(19); P2-Pd-I1 91.65(2); I1-Pd-I2 93.510(8)

The minor product by ^{1}H and ^{31}P NMR spectroscopy, **8**-*meso*, exhibits similar chemical shifts and coupling values to analogous **6**-*meso* and **7**-*meso*. This species appears as a doublet at δ 7.6 ppm ($^{1}J_{P\text{-}H}$ = 373.2 Hz) in the ^{31}P NMR spectrum. Like **7**-*rac*, the major diastereomer **8**-*rac* appears upfield as a doublet at δ -2.0 ppm ($^{1}J_{P\text{-}H}$ = 415.5 Hz). At room temperature in CD_2Cl_2, both isomers are in equilibrium with one another in

a 1:1.67 (**8**-*meso*:**8**-*rac*) ratio (Figures 2.11 and 2.12). At lower temperatures, the proportion changes to as low as 1:1.25 (**8**-*meso*:**8**-*rac*). A van't Hoff analysis (Figure 2.13) over -60 °C to 40 °C reveals that the **8**-*meso* is enthalpically favored by 0.40 kcal/mol, but entropically disfavored by 2.3 cal/mol•K (eq. 5). Unfortunately, due to signal overlapping in the ^{1}H NMR at temperatures greater than 0 °C, diastereomer ratio could not be quantified accurately. However, extrapolation using the regression in Figure 2.13 suggests that at room temperature (298 K, 25 °C), the ratio of **8**-*meso* to **8**-*rac* is 1:1.6.

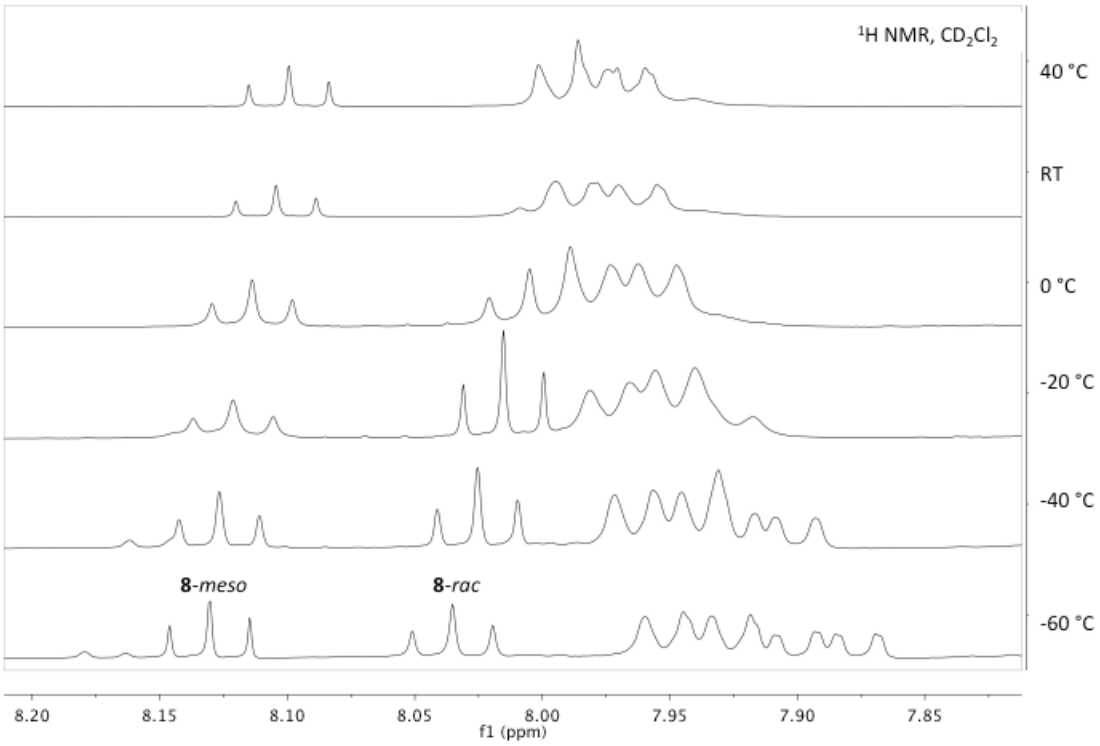

Figure 2.11. Selected region of variable-temperature ^{1}H NMR spectra in CD_2Cl_2 of **8**-*meso* and **8**-*rac.* Labeled triplets correspond to the 4-^{1}H on the pyridine ring of PNP-H_2

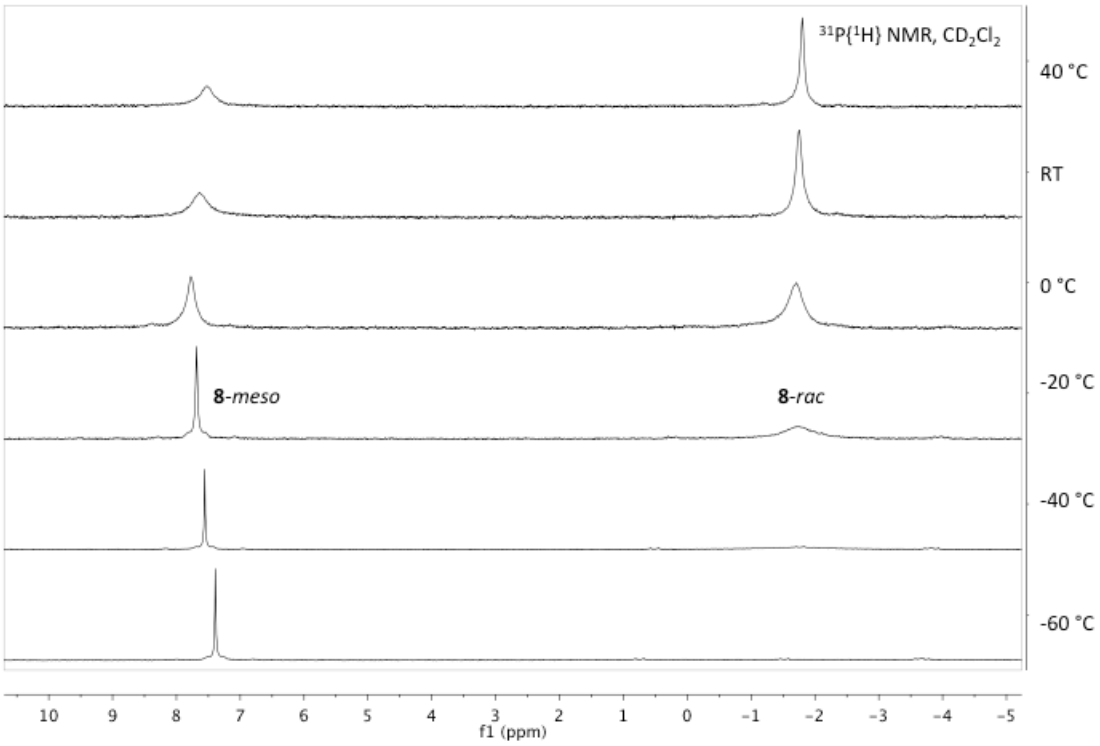

Figure 2.12. Selected region of variable-temperature $^{31}P\{^{1}H\}$ NMR spectra in CD_2Cl_2 of **8**-*meso* and **8**-*rac.* Note substantial broadening of the signal corresponding to **8**-*rac*

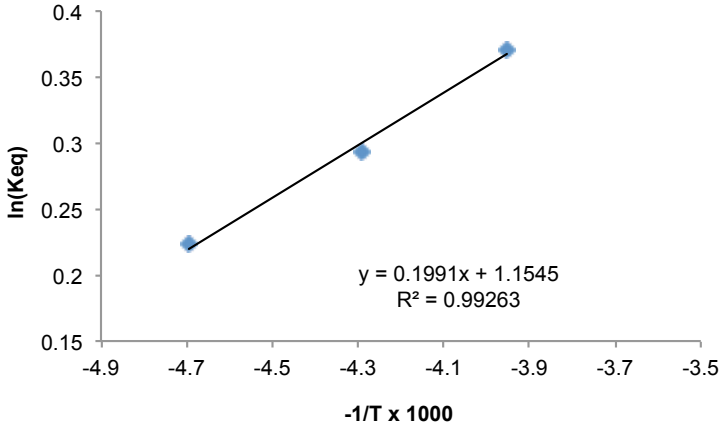

Figure 2.13. van't Hoff plot of **8**-*rac* and **8**-*meso* isomerization. Black line (linear regression). X-axis in units of K^{-1}

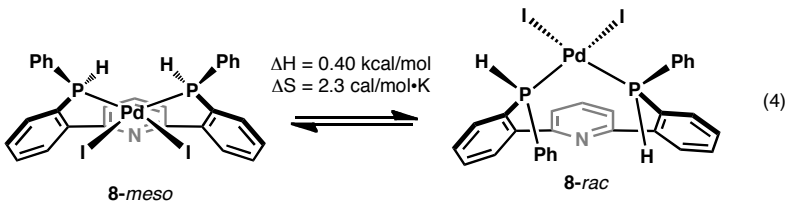

(4)

Table 2.1. Structural comparison of a series of palladium dihalide complexes supported by ligand **1.**

	Complex	P-Pd (Å)	X-Pd (Å)	P-H (Å)	P1-Pd-P2 (°)	reference
this work	(*meso*-PNP-H_2)$PdCl_2$ (**6**-*meso*)	2.2211(3); 2.2319(3)	2.3443(3); 2.3614(3)	1.297(15); 1.309(14)	91.342(13)	-
	(*meso*-PNP-H_2)$PdBr_2$ (**7**-*meso*)	2.2328(3); 2.2453(3)	2.46995(17); 2.48284(16)	1.259(17); 1.276(19)	91.289(13)	-
	(*rac*-PNP-H_2)$PdBr_2$ (**7**-*rac*)	2.2407(4); 2.2761(5)	2.4894(2); 2.5020(2)	1.259(18); 1.26(2)	99.031(17)	-
	(*meso*-PNP-H_2)PdI_2 (**8**-*meso*)	2.2515(15); 2.2546(14)	2.6387(6); 2.6546(6)	1.30(3); 1.30(3)	87.53(5)	-
	(*rac*-PNP-H_2)PdI_2 (**8**-*rac*)	2.2568(8); 2.2628(7)	2.6405(3); 2.6608(3)	1.34(3); 1.34(3)	90.01(3)	-

Table 2.2. Structural comparison between reported Pd complexes supported by relevant secondary and tertiary phosphines.

	Complex	P-Pd (Å)	X-Pd (Å)	P-H (Å)	P1-Pd-P2 (°)	reference
secondary phosphines	[Pd(dppe)(**Mes_2PH**)(Ph)]BF_4	2.3446(16)	-	1.39(5)	-	3a
	[Pd(**PPh_2H**)(I)(μ-PPh_2)]$_2$	2.2901(7); 3.6400(7)	2.6630(3)	1.33(3)	72.08(3)	3b
	trans-(Mes_2PH)$_2$$PdCl_2$	2.3057(7); 2.3057(7)	2.3028(7); 2.3028(7)	1.27(4)	180	3c
	Pd(Mes_2PH)$_4$	2.3213(6)	-	1.33(2)	-	4
	[Pd(Mes_2PH)$_4$](BF_4)$_2$	2.340(3)	-	1.219(3)	-	4
	Mes_2PH	-	-	1.36(7)[a]	-	3c
	Mes_2PH•BH_3	-	-	1.35(3)	-	3c
tertiary phosphines	(dppm)$PdCl_2$	2.234(1); 2.250(1)	2.362(1); 2.352(1)	-	72.68(3)	7
	(dppe)$PdCl_2$	2.233(2); 2.226(2)	2.361(2); 2.357(2)	-	85.82(7)	7
	(dppp)$PdCl_2$	2.244(1); 2.249(1)	2.351(1); 2.358(2)	-	90.58(5)	8
	(dppf)$PdCl_2$	2.283(1); 2.301(1)	2.348(1); 2.347(1)	-	99.07(5)	8

[a]Gas-phase measurement

Thermodynamic Trends of the (PNP-H_2)PdX_2 (X = halogen) Series

VT-NMR analysis of (PNP-H_2)PdI_2 diastereomers shows broadening at low temperature of the $^{31}P\{^1H\}$ signal presumably corresponding to **8**-*rac* (Figure 2.12). In fact, at -60 °C, the signal is so broad it disappears completely into the baseline, while the ^1H NMR spectrum clearly reveals two species still in solution in a 1:1.25 ratio (Figure 2.11). We suspect that at temperatures above -60 °C, phosphine interconversion in **8**-*rac* is rapid, giving rise to the singlet at δ -2.0 ppm in the $^{31}P\{^1H\}$ spectrum. Therefore, at very low temperatures, we expect **8**-*rac* to give rise to two singlets corresponding to each phosphorus atom. This suggests that the complex is not only unsymmetrical in the solid state, but interconverting between unsymmetrical antipodes in solution as well.

A similar dynamic process may be occurring with dibromide **7**-*rac* at higher temperatures. However, we cannot determine whether disappearance of the $^{31}P\{^1H\}$ NMR signal at room temperature is due to signal broadening or the equilibrium which favors **7**-*meso* (or both). It should be noted that signals corresponding to the minor diastereomer can be observed in the ^1H NMR spectrum (Figure 2.6), which suggest that broadening does occur in the room temperature $^{31}P\{^1H\}$ NMR spectrum of **7**-*rac*. Furthermore, **7**-*rac* and **8**-*rac* appear more fluxional than their *meso*-supported analogs, which presumably can retain the higher order of symmetry (C_s) exhibited in the solid state that results in equivalent phosphorus signals. Indeed, the entropic favorability of **7**-*rac* and **8**-*rac* over **7**-*meso* and **8**-*meso* agree with their increased fluxionality and lower symmetry (in the solid state, both *rac*-supported complexes exhibit C_1-symmetry). Furthermore, the *rac*-PNP-H_2 framework itself is versatile and flexible enough to adopt the two different geometries exhibited in the solid-state structures of **7**-*rac* and **8**-*rac.* The

meso-PNP-H_2 framework may not be as versatile as the *rac* framework, as evidenced by the similar C_s-symmetric conformation it adopts in **6**-*meso,* **7**-*meso,* and **8**-*meso.*

Unfortunately, dichloride **6**-*rac* has not been observed spectroscopically or by crystallographic analysis. Isomerization of **6**-*rac* to **6**-*meso* is likely occurring, however, given that an equivalent mixture of both PNP-H_2 ligand diastereomers is resolved completely to **6**-*meso* upon complexation to palladium. Furthermore, it is not obvious why formation of **6**-*meso* would be irreversible while *rac*-to-*meso* isomerization is reversible for the dibromide or diiodide species. Therefore, ΔG_{298K} in the equilibrium below (eq. 6) decreases (i.e., *rac* preference increases) in the order Cl > Br > I.

$$(\textit{meso}\text{-PNP-H}_2)\text{PdX}_2 \underset{}{\overset{K_{eq}}{\rightleftharpoons}} (\textit{rac}\text{-PNP-H}_2)\text{PdX}_2 \qquad (6)$$

X = Cl, Br, I

$$K_{eq} = e^{-\Delta G/RT}$$

$$\Delta G = \Delta H - T\Delta S$$

$$T = 298\ \text{K}\textbf{:}\ K_{eq}(X = Cl) < K_{eq}(X = Br) < K_{eq}(X = I)$$

When X = Br, I, the *rac* diastereomer is entropically favored. By this precedent, it stands to reason that dichloride **6**-*rac* may be entropically favored over **6**-*meso* as well. If **6**-*rac* is entropically favored, but only **6**-*meso* is observed spectroscopically at 60 °C, then $\Delta H > T\Delta S$ in the expression for ΔG_{333K}, and **6**-*meso* is favored enthalpically. Therefore, for each dihalide in the series, the *meso* isomer is enthalpically preferred. Perhaps the *rac*-PNP-H_2 ligand distorts unfavorably to accommodate coordination to a metal, or as demonstrated in the solid-state structures of **7**-*rac* and **8**-*rac*, the metal square plane is brought closer to the bulky ligand framework. However, it is not completely

understood why the *rac* diastereomer is favored (or *meso* disfavored) for larger halide ligands.

Epimerization of Phosphorus Stereocenters in rac- and meso-(PNP-H_2)PdX_2 (X = halide) Complexes

The phosphorus stereocenters of a 1:1 *rac*:*meso* mixture of ligand PNP-H_2 (**1**) epimerize rapidly upon complexation to palladium. This must necessarily be the case if a rapid equilibrium between metal complexes supported by **1**-*rac* and **1**-*meso* is achieved. Unfortunately, data on the acidity of P-H bonds of secondary phosphines coordinated to palladium has not been reported, but we envision that coordination to the metal center sufficiently decreases the pK_a of the secondary phosphine proton and facilitates intramolecular pyridine-assisted phosphine epimerization through a phosphine-phosphide palladium dihalide intermediate (Scheme 2.2).

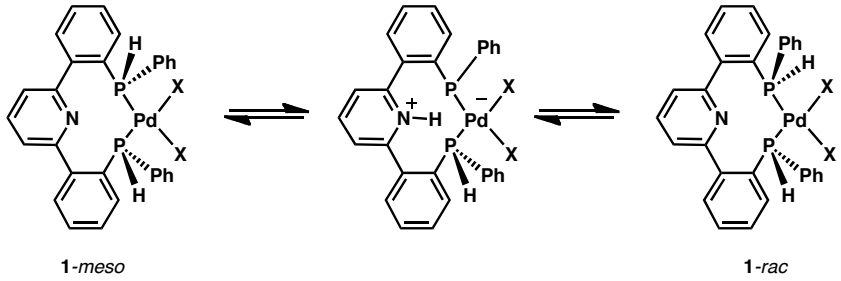

Scheme 2.2

To test this hypothesis, we treated PNP-H_2 ligand **1** with $HBAr_4$•Et_2O (Ar = 3,5-$(CF_3)_2C_6H_3$) to generate pyridinium bis(phosphine) (**1**-H)$^+BAr_4^-$ *in situ,* then (COD)$PdCl_2$. We hoped that protonation of the pyridine nitrogen would deactivate its role in phosphine epimerization by discouraging proton transfer. Indeed, metalation of (**1**-H)$^+BAr_4^-$

generates a mixture of what is presumably [(*rac*-**1**-H)$PdCl_2$]$^+BAr_4^-$ and [(*meso*-**1**-H)$PdCl_2$]$^+BAr_4^-$ (Figure 2.14). Unfortunately, the ratio of these products cannot be determined by ^{1}H NMR due to overlap of diagnostic signals. However, it is clear from the $^{31}P\{^1H\}$ NMR spectrum that the proportion of *rac*:*meso*-supported products is greater than in the reaction of neutral PNP-H_2 ligand **1** with (COD)PdCl$_2$ in which only (*meso*-PNP-H_2)$PdCl_2$ (**6**-*meso*) is generated.

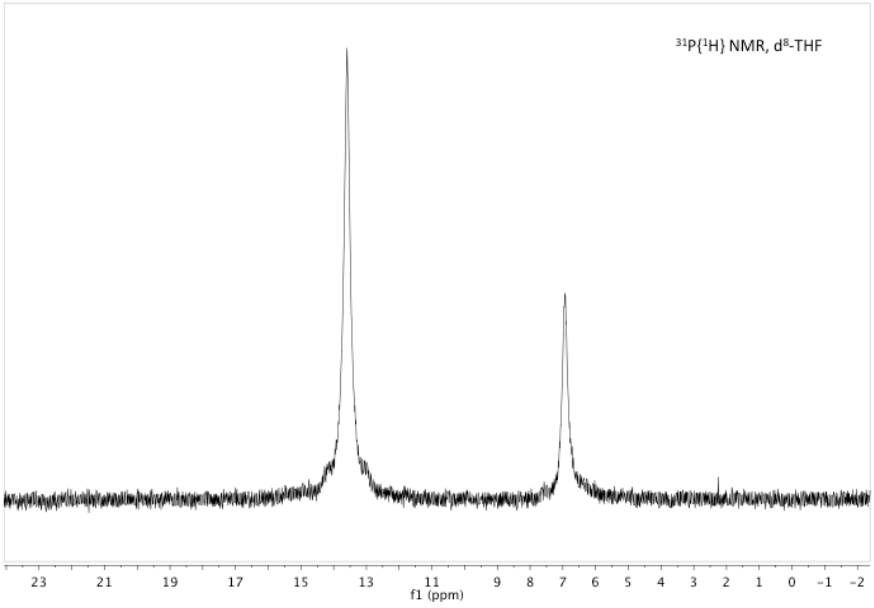

Figure 2.14. $^{31}P\{^1H\}$ NMR spectrum of [(**1**-H)]$PdCl_2^+BAr_4^-$ (Ar = 3,5-$(CF_3)_2C_6H_3$)

To ensure that the observed ratio in Figure 2.14 is not a result of some alternative epimerization pathway, a solution of **6**-*meso* was treated with $HBAr_4$•Et_2O (Figure 2.15). A single species was generated by $^{31}P\{^1H\}$ NMR with the same chemical shift as the most upfield signal in Figure 2.14, presumably [(*meso*-**1**-H)$PdCl_2$]$^+BAr_4^-$. Therefore, it appears that the pyridine ring plays an important role in secondary phosphine epimerization.

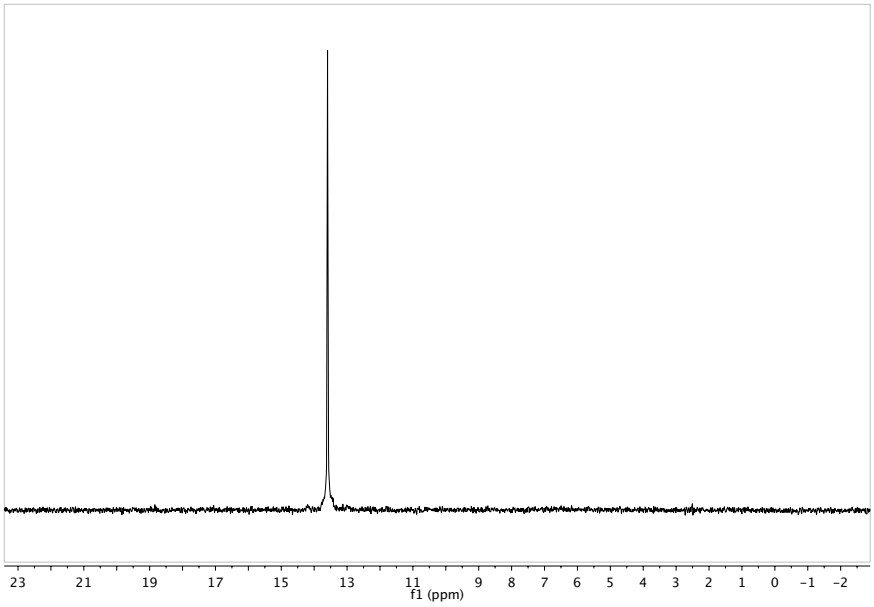

Figure 2.15. $^{31}P\{^{1}H\}$ NMR spectrum of [*meso*-(**1**-H)]$PdCl_2^+BAr_4^-$ (Ar = 3,5-$(CF_3)_2C_6H_3$)

Oxidation of Palladium(II) Dihalides

Diastereomeric mixtures of **6, 7,** and **8** were treated with a variety of oxidants at low temperature. Concentrations were kept dilute to discourage the formation of palladium-phosphide networks upon oxidation (as observed for high-valent early metals, discussed in Chapter 1.) Unfortunately, insoluble products that are likely metal-ligand oligomers are still formed. When oxidants such as $PhICl_2$, $PhI(OAc)_2$, or *N*-bromosuccinimide (NBS) are used in the presence of pyridine, reduced iodobenzene and succinimide can be detected quantitatively by GC, indicating that oxidation at either the ligand's phosphorus donors or the metal are indeed taking place. However, we suspect that the antibond resulting from mixing between the phosphide lone pair and the filled metal d_{xy}, d_{xz}, or d_{yz} orbitals of π-symmetry likely has substantial density on phosphorus.

This destabilizing filled-filled orbital interaction therefore encourages phosphide bridging to the relatively electron poor metal center, which due to initial coordinative saturation, must undergo ligand exchange to accommodate an L-type phosphide bridge.

CONCLUSIONS

A 1:1 non-interconverting mixture of *rac* and *meso* diastereomers of a neutral, bidentate bis(secondary phosphine) ligand has been synthesized. A series of palladium dihalides stabilized by this ligand has been spectroscopically and crystallographically characterized. These studies suggest that one diastereomer of the bis(phosphine) ligand is quite structurally versatile, capable of coordinating metals with a number of geometries. This may be due to the reduced sterics of a P-H bond in a secondary phosphine relative to a tertiary phosphine. The pyridine-linker between both phosphine donors appears to assist epimerization of the chirogenic phosphines to equilibrium diastereomeric ratios. Similar analysis with a benzene-linked bis(phosphine) analog of **1** would be informative, since the diastereomeric mixture would presumably no longer be able to attain equilibrium ratios without the pendant pyridine ring.

EXPERIMENTALS

General Considerations and Instrumentation. All air- and moisture-sensitive compounds were manipulated using standard high vacuum and Schlenk techniques or manipulated in a glovebox under a nitrogen atmosphere using degassed solvents. All

solvents were dried over sodium benzophenone ketyl and stored over titanocene dihydride where compatible or dried by the method of Grubbs.[10] All NMR solvents were purchased from Cambridge Isotopes. Benzene-d_6 was dried over sodium benzophenone ketyl, while CD_2Cl_2 was dried over CaH_2 and stored over molecular sieves. All other chemicals were used as received. $(COD)PdCl_2$ was purchased from Strem Chemical. $(MeCN)_2PdBr_2$[11] and $(PPh_3)_2PdI_2$[12] were prepared according to literature procedure. Ligand **1** was prepared as described in Chapter 1. ^1H, ^{13}C, ^{31}P, and ^{19}F NMR spectra were recorded on Varian Mercury 300 or Varian INOVA-500 spectrometers and unless otherwise indicated at room temperature. Chemical shifts are reported with respect to internal solvent: 7.16 and 128.38 ppm (C_6D_6); 5.32 and 53.84 ppm (CD_2Cl_2) for ^1H and ^{13}C data. ^{31}P chemical shifts are reported with respect to an external 85% H_3PO_4 reference (0 ppm).

(PNP-H$_2$)PdCl$_2$ (6). To a vial equipped with a stirbar and charged with $(COD)PdCl_2$ (32.5 mg, 0.114 mmol, 1.00 equiv) was added benzene (4.0 mL). A benzene solution (1 mL) of **1** (51.5 mg, 0.115 mmol, 1.01 equiv) was added dropwise. A pink suspension formed immediately, which was stirred for 3 hours. After filtering the suspension, the solid was washed with benzene (2 mL), Et_2O (2 mL), then pentane (2 mL), then dried *in vacuo* to afford 71.2 mg of **6** as an off-white solid in 82% yield. **6** is slightly soluble in chlorinated solvents, THF, and MeCN. Crystals suitable for x-ray diffraction analysis were grown by slow evaporation of CH_2Cl_2 at room temperature. ^1H NMR (500 MHz, CD_2Cl_2) δ: 5.89 (dd, J_1 = 392.4 Hz, J_2 = 31.3 Hz, 2H, ArP*H*(C_6H_5)-Pd), 7.47 (m, 6H), 7.54 (dd, J_1 = 8.2 Hz, J_2 = 6.3 Hz, 2H), 7.62 (m, 4H), 7.73 (dd, J_1 = 13.1 Hz, J_2 = 7.8 Hz, 2H), 7.80 (d, J = 7.8 Hz, 2H), 8.06 (dd, J_1 = 12.7 Hz, J_2 = 7.7 Hz, 4H), 8.14 (t, J = 7.9 Hz, 1H). ^{13}C NMR (126 MHz, CD_2Cl_2) δ: 123.8 (s), 125.3 (s), 125.8 (s), 126.4 (s), 126.8 (s),

129.1 (at, $J_1 = J_2 = 11.0$ Hz), 130.9 (d, J = 8.2 Hz), 131.9 (s), 132.4 (s), 136.6 (dd, $J_1 = 20.8$ Hz, $J_2 = 10.0$ Hz), 139.8 (s), 143.0 (s), 158.4 (s). $^{31}P\{^1H\}$ NMR (202 MHz, CD_2Cl_2) δ: 12.0 (s). Anal. Calcd. for $C_{29}H_{23}Cl_2NP_2Pd$: C, 55.75; H, 3.71; N, 2.24. Found: C, 55.31; H, 3.55; N, 2.20.

(PNP-H$_2$)PdBr$_2$ (7). To a vial equipped with a stirbar and charged with $(MeCN)_2PdBr_2$ (38.6 mg, 0.111 mmol, 1.00 equiv) was added benzene (4 mL). A benzene solution (1 mL) of **1** (50.0 mg, 0.112 mmol, 1.01 mmol) was added dropwise. After 30 minutes, a light yellow suspension persisted. The reaction was stirred for 3 hours. After filtering the suspension, the solid was washed with benzene (2 mL), Et_2O (2 mL), and pentane (2 mL), then dried *in vacuo* to afford 60.0 mg of **7** as a yellow solid in 78% yield. Crystals suitable for x-ray diffraction analysis were grown by slow evaporation of CH_2Cl_2 at room temperature. ^1H NMR (500 MHz, CD_2Cl_2) δ: 5.96 (dd, $J_1 = 397.4$ Hz, $J_2 = 34.6$ Hz, 2H, ArP*H*(C_6H_5)-Pd), 7.45 (m, 6H), 7.54 (t, J = 7.5 Hz, 2H), 7.58 (dd, $J_1 = 7.2$ Hz, $J_2 = 4.0$ Hz, 2H), 7.63 (t, J = 7.5 Hz, 2H), 7.73 (dd, $J_1 = 12.0$ Hz, $J_2 = 7.9$ Hz, 2H), 7.80 (d, J = 7.9 Hz, 2H), 8.00 (dd, $J_1 = 13.1$ Hz, $J_2 = 7.5$ Hz, 4H), 8.15 (t, J = 7.9 Hz, 1H). ^{13}C NMR (126 MHz, CD_2Cl_2) δ: 124.2 (s), 125.8 (s), 126.3 (s), 127.3 (s), 127.7 (s), 129.2 (m), 131.2 (at, $J_1 = J_2 = 4.0$ Hz), 132.2 (s), 132.5 (s), 136.9 (m), 139.9 (s), 143.3 (s), 158.6 (s). $^{31}P\{^1H\}$ NMR (202 MHz, CD_2Cl_2) δ: 11.1 (s). Anal. Calcd. for $C_{29}H_{23}Br_2NP_2Pd$: C, 48.81; H, 3.25; N, 1.96. Found: C, 49.07; H, 3.33; N, 2.11.

(PNP-H$_2$)PdI$_2$ (8). To a vial equipped with a stirbar and charged with $(PPh_3)_2PdI_2$ (70.6 mmol, 0.080 mmol, 1.00 equiv) was added benzene (3 mL). A benzene solution (1 mL) of **1** (36.1 mg, 0.081 mmol, 1.01 equiv) was added dropwise. A clear dark orange

solution formed, which became an orange suspension after 1 hour. After 12 hours stirring at room temperature, the suspension was filtered. The orange solid was washed with benzene (3 mL), Et_2O (5 mL), and pentane (5 mL), then dried *in vacuo* to afford 51.2 mg of **8** as a powder in 80% yield. NMR analysis reveals two isomers in about 1:1.5 ratio. Compound **8** is slightly soluble in benzene, but dissolves readily in chlorinated solvents and THF. Crystals were grown from a saturated solution in CH_2Cl_2. ^{1}H NMR (500 MHz, CD_2Cl_2) δ: 6.11 (dd, J_1 = 381.2 Hz, J_2 = 30.7 Hz, ArP*H*(C_6H_5)-Pd *minor isomer*), 6.99 (dd, J_1 = 416.2 Hz, J_2 = 10.8 Hz, ArP*H*(C_6H_5)-Pd *major isomer*)[8], 7.21 (t, J = 7.5 Hz), 7.30 (dd, J_1 = 11.6 Hz, J_2 = 7.9 Hz), 7.41 (m), 7.52 (m), 7.58 (m), 7.62 (d, J = 7.9 Hz), 7.66 (m), 7.76 (d, J = 7.9 Hz), 7.97 (m), 8.00 (t, J = 8.0 Hz), 8.11 (t, J = 7.8 Hz). ^{13}C NMR (126 MHz, CD_2Cl_2) δ: 124.5 (s), 124.9 (s), 125.6 (s), 126.0 (s), 126.8 (s), 127.2 (s), 129.0 (m), 131.3 (m), 131.7 (s), 132.1 (d, J = 8.5 Hz), 132.4 (s), 132.5 (s), 134.7 (d, J = 10.0 Hz), 135.5 (s), 136.9 (m), 139.1 (s), 139.7 (s), 145.3 (d, J = 10.23 Hz), 157.6 (s). ^{31}P{^{1}H} NMR (202 MHz, CD_2Cl_2) δ: -2.0 (s), 7.6 (s). ^{31}P NMR (202 MHz, CD_2Cl_2) δ: -2.0 (d, J = 415.5 Hz), 7.6 (d, J = 373.2 Hz). Anal. Calcd. for $C_{29}H_{23}I_2NP_2Pd$: C, 43.12; H, 2.87; N, 1.73. Found: C, 43.09; H, 2.84; N, 1.55.

Variable-Temperature NMR Procedure. All variable-temperature NMR experiments were performed on a Varian INOVA-500 spectrometer. In a glovebox, an oven-dried J. Young NMR tube was charged with 5-10 mg of analyte and 1.2 mL of CD_2Cl_2 was added. The desired temperature of the NMR probe was set, and after reaching said temperature, the temperature of the tube was allowed to stabilize for 15 minutes before acquiring a spectrum.

X-Ray Crystal Data: General Procedure. Crystals grown from CH_2Cl_2 (**6**-*meso*, **7**-*meso*, **7**-*rac,* **8**-*meso*, **8**-*rac*) were removed quickly from a scintillation vial to a microscope slide coated with Paratone N oil. Samples were selected and mounted on a glass fiber with Paratone N oil. Data collection was carried out on a Bruker KAPPA APEX II diffractometer with a 0.71073 Å MoKα source. The structures were solved by direct methods. All non-hydrogen atoms were refined anisotropically. Some details regarding refined data and cell parameters are available in Crystallographic Information. Selected bond distances and angles are supplied as well.

REFERENCES

1. Tolman, C. A. *Chem. Rev.* **1977,** *77*, 313.
2. Horner, L.; Winkler, H.; Rapp, A.; Mentrup, A.; Hoffmann, H.; Beck, P. *Tetrahedron Lett.* **1961**, *161*, 161.
3. Among others: a) Zhuravel, M. A.; Grewal, N. S.; Glueck, D. S. *Organometallics* **2000**, *19*, 2882. b) Zhuravel, M. A.; Moncarz, J. R.; Glueck, D. S. *Organometallics* **2000**, *19*, 3447. c) Pelczar, E. M.; Nytko, E. A.; Zhuravel, M. A.; Smith, J. R.; Glueck, D. S.; Sommer, R.; Incarvito, C. D.; Rheingold, A. L. *Polyhedron* **2002**, *21*, 2409.
4. Leoni, P.; Marchetti, F.; Papucci, S.; Pasquali, M. *J. Organomet. Chem.* **2000**, *593-594*, 12.
5. Ferguson, G.; McCrindle, R.; McAlees, A. J.; Parvez, M. *Acta. Cryst.* **1982**, *B38*, 2679.
6. Quin, L. D. *A Guide to Organophosphorus Chemistry*; **2000**, John Wiley and Sons, New York, Chapter 3.
7. Steffen, W. L.; Palenik, G. J. *Inorg. Chem.* **1976**, *15*, 2432.
8. Hayashi, T.; Konishi, M.; Kobori, Y.; Kumada, M.; Higuchi, T.; Hirotsu, K. *J. Am. Chem. Soc.* **1984**, *106*, 158.
9. Roesky, H. W.; Andruh, M. *Coord. Chem. Rev.* **2003**, *236*, 91.
10. Pangborn, A. B.; Giardello, M. A.; Grubbs, R. H.; Rosen, R. K.; Timmers, F. J. *Organometallics* **1996**, *15*, 1518.
11. Tan, E. H. P.; Lloyd-Jones, G. C.; Harvey, J. N.; Lennox, A. J. J.; Mills, B. M. *Angew. Chem., Int. Ed.* **2011**, *50,* 9602.
12. Hahn, F. E.; Luegger, T.; Beinhoff, M. *Z. Naturforsch. B.* **2004**, *59*, 196.

CHAPTER 3

Ethylene Polymerization and Ethylene/1-Hexene Copolymerization Reactions Catalyzed by Early Metal Non-Metallocene Complexes

All polymerization reactions and polymer analysis were performed at King Fahd University of Petroleum and Minerals in Dhahran, Saudi Arabia, with the aid of Dr. Muhammad Atiqullah, Dr. Mamdouh Al-Harthi, and Anwar Hossaen.

ABSTRACT

Ethylene polymerization and ethylene/1-hexene copolymerization activities of several zirconium(IV) and vanadium(III) polymerization precatalysts supported by heterocycle-linked bis(phenolate) ligands are discussed. Under 2 bar ethylene at 30 °C, all catalysts produce linear polyethylene (T_m ~ 136) with activities as high as 10^6 g PE/(mol•h). In the presence of 1-hexene as a comonomer, comparable activities are also observed, but only the vanadium catalyst incorporates comonomer, albeit with low efficiency (<1 mol%).

INTRODUCTION

The last half-century has seen significant advances in metallocene-catalyzed olefin polymerization.[1] Metallocenes can adopt a variety of symmetries to allow strict stereotactic control of growing polypropylene chains. Because these systems are relatively well-behaved and understood,[2] metallocene catalysts are widely used in industrial processes, and therefore present a "patent minefield" to future investigators.[3] To access new polymers in a controlled manner with interesting structural properties, such as branched polymers or material derived from polar monomers, there has been an increased interest in using well-defined polydentate *non-metallocene* ligand sets to support transition metal catalysts.

Non-metallocenes pose several advantages over metallocenes. For one, they are synthetically more accessible; in some cases, ligand syntheses are modular to allow rapid catalyst screening. While both types of catalysts can adopt a variety of symmetries, non-metallocenes are not restricted to anionic carbon donors (such as the L_2X-type cyclopentadienyl anion), and systems supported by combinations of anionic and neutral members of the nitrogen and oxygen families have been reported.[3] Indeed, this ligand versatility has led to the development of not just new early transition metal catalysts, but lower-valent late-metal catalysts as well.

η^5:η^1-cyclopentadienyl-amides are just one of a few examples of industrially exploited non-metallocene ligands for early metal catalysts. First introduced by our group in 1990 as scaffolds for scandium(III) catalysts,[4] they have since been explored as ligands for Group 4 metals (Figure 3.1a).[5] The absence of a second cyclopentadienyl ring, as well

as the short silane bridge, presumably results in a more unencumbered active site at the metal. Furthermore, the amido group renders the metal center more Lewis acidic, encouraging olefin coordination and insertion relative to β–hydride elimination and chain transfer. The kinetic and steric properties of these catalysts allow the production of linear low-density polyethylene (LLPDE) with small amounts of long chain branching, and high activities exhibited for ethylene copolymerizations with long α-olefins, such as 1-hexene and 1-octene.[1]

Pyridine diimine-supported iron(II) and cobalt(II) precatalysts (Figure 3.1b) have also been demonstrated as outstanding non-metallocene catalysts for the production of highly linear polyethylene.[6,7] The ligands themselves are readily synthesized in one step, allowing for facile screening of electronically and sterically modified catalysts. Indeed, it was found that catalysts supported by ligands with bulky aryl substitution on the diimine donors generate higher molecular weight polymer. With iron, incredibly high ethylene polymerization activities (10^8 g mmol^{-1} h^{-1}) can be realized.

Group 10 complexes stabilized by neutral α-diimine ligands (Figure 3.1c) have been exploited for their high activities, air-stability and functional group tolerance that permits polymerization of polar monomers.[8] Perhaps most unique, however, is their ability to traverse a growing polymer chain; this chain-walking behavior allows for the production of highly branched linear, low-density ethylene homopolymers with desirable properties, such as elastomers.

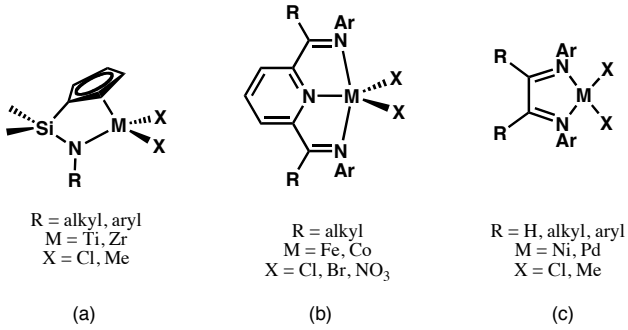

Figure 3.1. Representative non-metallocene transition metal polymerization precatalysts

Given the promising ability of non-metallocene catalysts to generate interesting polymers in a controlled manner, we investigated the ability of new heterocycle-linked bis(phenolate) ligands (Figure 3.2) on early metals to control polymer tacticity in propylene polymerization.[9] In this framework, the phenols are connected to the central pyridine, furan or thiophene donor via robust sp^2-sp^2 aryl-aryl linkages, lending not only stability, but rigidity to the triaryl pincer system. Furthermore, these ligands can be constructed sequentially using well-developed aryl-aryl cross-coupling chemistry. We envisioned that a host of symmetries could be adopted by simple twisting of the aryl-aryl bonds to cant the rings relative to one another (Figure 1.1), and in 2009, in attempts to predict and control catalyst geometry, we reported a model describing the relationship between overall precatalyst symmetry and pincer ligand π-donation.[10]

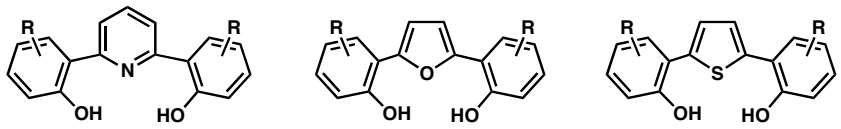

Figure 3.2. Heterocycle-linked bis(phenol) ligands for early metal polymerization catalysts developed in our laboratory

Upon activation with methylaluminoxane (MAO), Group 4 and 5 complexes supported by these triaryl pincer ligands are active for propylene oligomerization or polymerization. Zirconium(IV) complexes show excellent activity (10^5–10^6 g mmol^{-1} h^{-1}) regardless of ligand, while titanium(IV) precatalysts supported by pyridine-linked bis(phenolates) generate higher molecular weight polymer while significantly less active (10^2–10^3 g mmol^{-1} h^{-1}). When coordinated to the furan- or thiophene-linked ligands, titanium(IV) complexes oligomerize propylene with high activity (10^5 g mmol^{-1} h^{-1}). Hafnium(IV) complexes, on the other hand, are essentially unreactive. The group 4 catalysts generate essentially stereoirregular polypropylene with with PDIs as low as 1.62 and as high as 31.8; in addition, depending on the ligand, high molecular weight isotactic polypropylene (PDI = 3.22–7.08) is also generated. That these catalysts exhibit relatively broad PDIs and in some cases generate two polymer types suggest the presence of at least two catalytically active species in the reaction. A vanadium(III) precatalyst supported by the pyridine-linked ligand is highly active (10^5 g mol^{-1} h^{-1}), but little is known about the active species generated upon MAO activation. The polymer is essentially stereoirregular with slight syndiotactic enrichment and narrow PDI (2.03). Unlike the Group 4 catalysts, the vanadium(III) precatalyst discussed above generates polymer with a large amount of regioerror.

In ethylene/1-octene copolymerization studies of Group 4 and Group 5 metals supported by pyridine-linked bis(phenolate) ligands, it was found that titanium(IV) and hafnium(IV) complexes are essentially inactive. While the zirconium(IV) precatalyst presents an activity of 1.6 x 10^5 g $mmol^{-1}$ h^{-1}, it displays a strong preference for ethylene incorporation over 1-octene (0.5 mol% 1-octene incorporation). The vanadium(III) precatalyst, however, sees a reduction in activity (5.0 x 10^4 g $mmol^{-1}$ h^{-1}), but is slightly more efficient at incorporating 1-octene into a growing polyethylene chain (6.6 mol% 1-octene incorporation.)

RESULTS AND DISCUSSION

Synthesis of Pincer Ligands and Polymerization Precatalysts

In the ethylene and ethylene/1-hexene polymerization trials discussed below, we focused on three of our previously reported early metal precatalysts (**1-ZrBn$_2$, 2-ZrBn$_2$, 3-VCl(THF)$_2$**), synthesized according to literature procedure.[9a,9b,11]

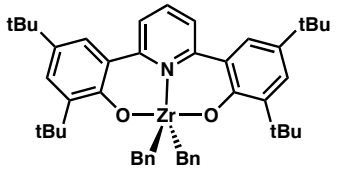

1-ZrBn$_2$

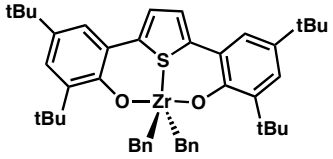

2-ZrBn$_2$

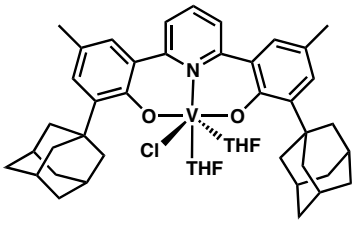

3-VCl(THF)$_2$

Ethylene Homopolymerization Trials

Precatalysts **1-ZrBn$_2$, 2-ZrBn$_2$,** and **3-VCl(THF)$_2$** are activated with 300 equivalents MAO under 2 bar ethylene to generate linear, high-density polyethylene with activities comparable to or greater than Cp_2ZrCl_2 (Table 3.1).

Precatalyst	M_w (x 10^{-3})	M_n (x 10^{-3})	M_w/M_n	T_m (°C)	Polymization Time (min)	Polymer Yield (g)	Activity (g mol^{-1} h^{-1})
1-ZrBn$_2$	220.7	10.3	21.4	136	20	20.8	3.9 x 10^6
2-ZrBn$_2$	335.4	19.0	17.7	138	20	24.4	4.6 x 10^6
3-VCl(THF)$_2$	223.8	34.7	6.5	140	20	15.0	2.8 x 10^6
Cp_2ZrCl_2	717.4	187.2	3.8	134	15	11.0	2.8 x 10^6

*500 mL *n*-hexane, 30 °C, 2 bar C_2H_4, 16 μmol catalyst, MAO co-catalyst with [Al]/[cat] = 300

Table 3.1. Catalyst activities and polymer properties

The melting temperatures (T_m) of the polymers is as expected for crystalline polyethylene (~137 °C). Furthermore, the ^{13}C NMR spectra reveal only a singlet at δ 29.8 ppm corresponding to the methylene backbone of linear polyethylene (see Figure 3.3 for an example). No signals corresponding to branched carbons or side-chains could be detected. This suggests that the active catalysts cannot insert growing polymer chains into chain-terminated polymers.

Catalysts **1-ZrBn$_2$** and **2-ZrBn$_2$** exhibit larger activities than metallocene catalyst Cp_2ZrCl_2, while **3-VCl(THF)$_2$** has a comparable activity. Nevertheless, the zirconocene precatalyst has a substantially narrower polydispersion index (PDI) than **1-ZrBn$_2$** and **2-ZrBn$_2$.** The PDI of **3-VCl(THF)$_2$**, on the other hand, is the smallest of the non-metallocene catalysts, but still slightly larger than Cp_2ZrCl_2. Clearly, in each non-metallocene-catalyzed polymerization reaction, more than one species is catalytically

active. That weight-averaged molecular weight (M_w) and number-averaged molecular weight (M_n) differ by an order of magnitude in each case suggest that one or more catalytically active species generates higher molecular weight polymer, while one or more generates significantly lower molecular weight polymer.

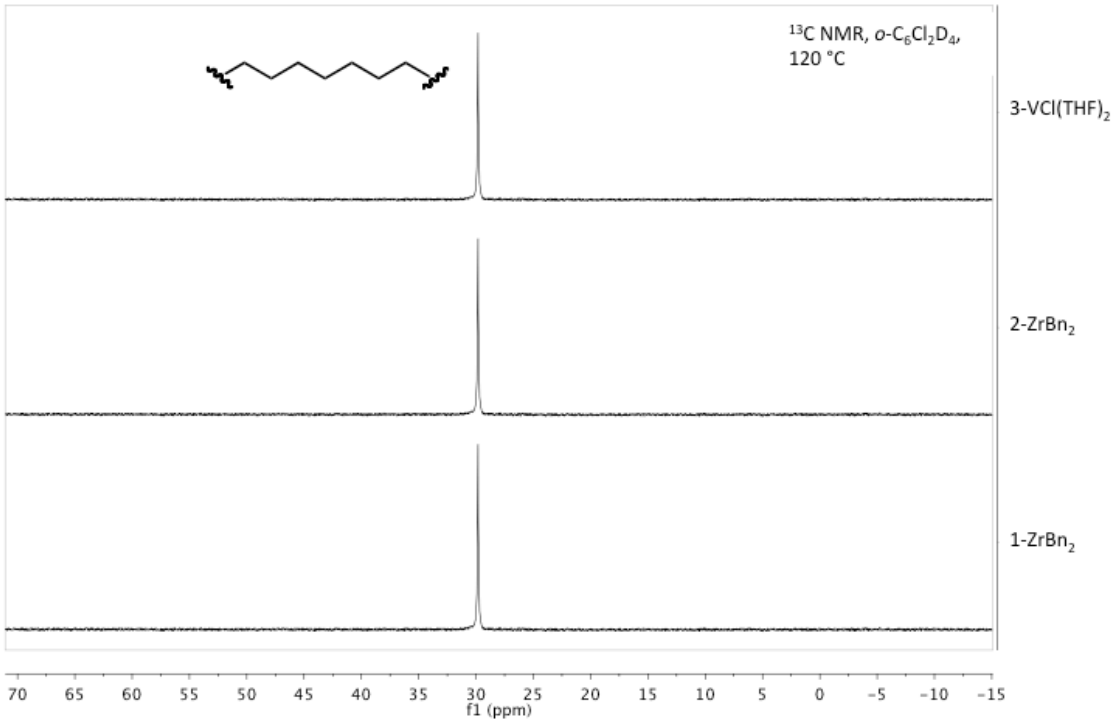

Figure 3.3. ^{13}C NMR spectra of linear polyethylene generated by precatalysts **1-ZrBn$_2$,** **2-ZrBn$_2$,** and **3-VCl(THF)$_2$.** All spectra were recorded in *ortho*-dichlorobenzene-d_4 at 120 °C

Ethylene/1-Hexene Copolymerization Trials

In the presence of varying amounts of comonomer (1-hexene), precatalysts **1-ZrBn$_2$, 2-ZrBn$_2$,** and **3-VCl(THF)$_2$** can be activated by MAO under ethylene (Table 3.2).

Precatalyst	1-hexene (mM)	M_w (x 10^{-3})	M_n (x 10^{-3})	M_w/M_n	T_m (°C)	Polymization Time (min)	Polymer Yield (g)	Activity (g mol^{-1} h^{-1})
1-ZrBn$_2$	80 (1 v%)	331.3	17.1	19.4	136	30	15.3	1.4 x 10^6
1-ZrBn$_2$	160 (2 v%)	385.2	11.1	34.7	134	40	22.3	2.1 x 10^6
1-ZrBn$_2$	320 (4 v%)	238.2	10.6	22.4	131	30	19.3	2.4 x 10^6
1-ZrBn$_2$	480 (6v%)	210.7	10.1	20.9	131	30	21.6	2.7 x 10^6
2-ZrBn$_2$	80	354.1	13.8	25.7	135	15	20.6	5.2 x 10^6
2-ZrBn$_2$	160	569.7	18.4	31.0	136	15	23.6	5.9 x 10^6
2-ZrBn$_2$	320	537.0	17.1	31.5	134	15	19.3	5.4 x 10^6
2-ZrBn$_2$	480	568.0	18.5	30.7	134	15	18.5	4.6 x 10^6
3-VCl(THF)$_2$	80	293.6	22.6	13.0	126	10	15.6	6.5 x 10^6
3-VCl(THF)$_2$	160	184.6	27.7	6.7	119	11	14.4	4.5 x 10^6
3-VCl(THF)$_2$	320	134.2	31.6	4.3	113	15	8.5	2.1 x 10^6
3-VCl(THF)$_2$	480	112.2	30.3	3.7	108	15	14.2	3.6 x 10^6

*Total volume = 500 mL. Conditions = *n*-hexane (solvent), 30 °C, 2 bar C_2H_4, 16 μmol catalyst, MAO co-catalyst with [Al]/[cat] = 300

Table 3.2 Catalyst activities and copolymer properties

The activity of pyridine-bis(phenolate)-supported precatalyst **1-ZrBn$_2$** displays an interesting dependence on comonomer concentration. Compared to the activity in the absence of comonomer, activity decreases more than two-fold with 80 mM (1 v%) 1-hexene. With higher concentrations of 1-hexene (up to 480 mM), activity increases, yet still remains lower than the original catalytic activity without comonomer. The melting temperatures (T_m) and polymer crystallinity decrease with increasing comonomer concentrations, but the ^{13}C NMR spectra of the polymers do not suggest any 1-hexene incorporation or branching. It may be that the observed T_m decrease may be a result of very small amounts of comonomer incorporation whose ^{13}C NMR resonances are too

weak to detect relative to the methylene backbone signal. The broad PDIs (19–35) suggest that more than one species is catalytically active and producing polymer in solution.

The activities of thiophene bis(phenolate)-supported precatalyst **2-ZrBn$_2$** see a small increase upon addition of comonomer. Nevertheless, T_m values remain roughly unchanged, and the ^{13}C NMR spectra reveal no 1-hexene incorporation or branching. Compared to no comonomer or 40 mM comonomer, the PDIs are substantially broader at higher concentrations of 1-hexene, due primarily to an increase in weight-averaged molecular weight M_w. Number-averaged molecular weight M_n, on the other hand, does not vary significantly, which may suggest that the active species responsible for low molecular-weight polymers is minimally affected by 1-hexene concentration. Perhaps 1-hexene coordinates to the active sites that produce higher molecular weight polymer and discourages chain transfer relative to coordination/insertion of ethylene, resulting in higher molecular weight polymer than observed in the absence of comonomer. The gel permeation chromatography (GPC) profiles for each polymer, which we unfortunately do not have on hand, would be quite informative. More investigation is surely needed.

Precatalyst **3-VCl(THF)$_2$** sees a significant increase in activity from no comonomer to 80 mM comonomer. Despite the T_m decrease, no ^{13}C NMMR resonances corresponding to 1-hexene incorporation or branching could be detected in this polymer. The broader PDI results from larger M_w or smaller M_n values, suggesting that one or more active sites are affected by the presence of 1-hexene, even if they do not incorporate it. Again, GPC would be informative. Unlike the other non-metallocene precatalysts, **3-VCl(THF)$_2$** incorporates a detectable amount of 1-hexene when present in concentrations

of 80 mM, 160 mM, and likely 240 mM. Not only is this apparent in the decreasing crystallinity of the polymer itself — suggested by the substantial reduction in T_m — but also in the ^{13}C NMR spectra (Figures 3.4 and 3.5); we unfortunately do not have the polymer sample generated at highest comonomer concentration for spectroscopic analysis, but it does follow the decreasing T_m/crystallinity trend established by differential scanning calorimetry. Furthermore, these polymers display substantially narrower PDIs. Indeed, the physical properties of the copolymers generated by **3-VCl(THF)$_2$** would be expected of linear low-density polyethylene (LLDPE).

The ^{13}C NMR spectrum of the copolymer generated by **3-VCl(THF)$_2$** under 2 bar ethylene and 160 mM 1-hexene indicates incorporation of a molecule of comonomer only after growth of a polyethylene chain, due to absence of signals corresponding to hexene-hexene-hexene (HHH) and hexene-hexene-ethylene (HHE) triads (Figure 3.4). Using the method of Randall,[12] comonomer incorporation was calculated to be <0.1 mol%. On the other hand, the polymer generated by **3-VCl(THF)$_2$** with twice the amount of 1-hexene (320 mM) sees 0.8 mol% comonomer incorporation (Figure 3.5). This is substantially less commoner incorporation than observed for the only reported example of homogeneous vanadium-catalyzed ethylene/1-hexene copolymerization (between 3–13%).[13] These results indicate the preference exhibited by the catalyst for ethylene over 1-hexene insertion, and that none of the catalysts incorporate a sufficient amount of comonomer to produce elastomeric polymers.

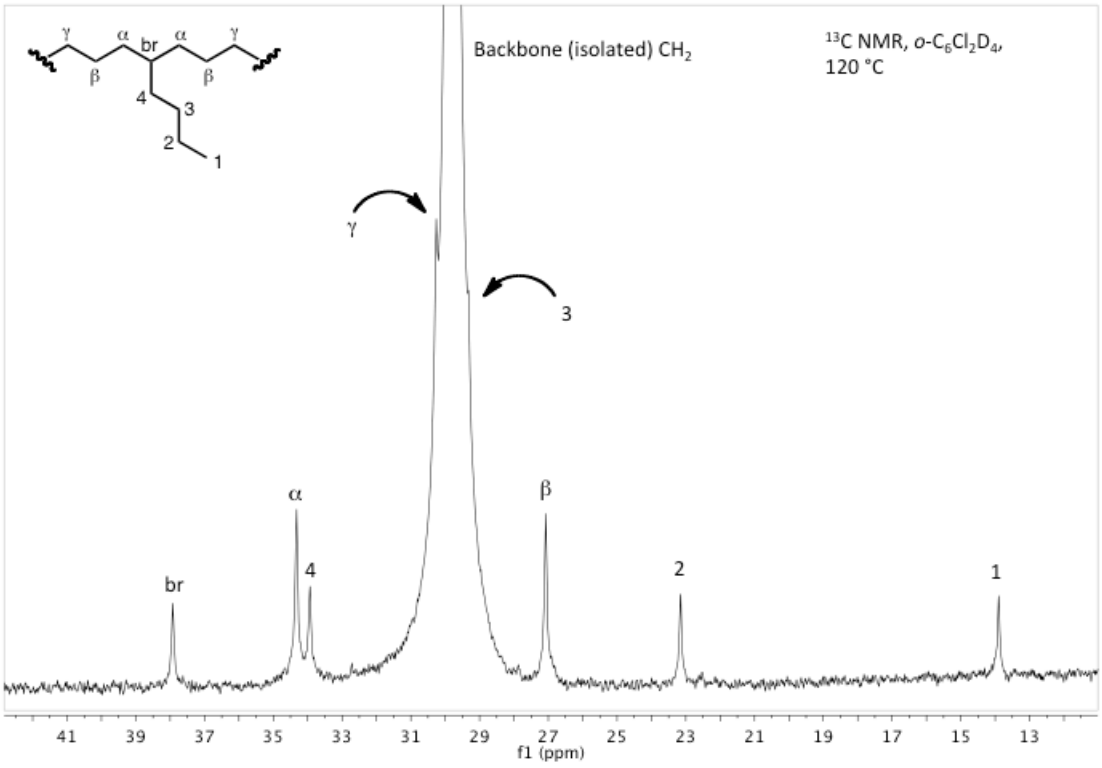

Figure 3.4. ^{13}C NMR spectrum of ethylene/1-hexene copolymer generated by precatalyst **3-VCl(THF)$_2$** in the presence of 160 mM 1-hexene**.** Spectrum was recorded in *ortho*-dichlorobenzene-d_4 at 120 °C

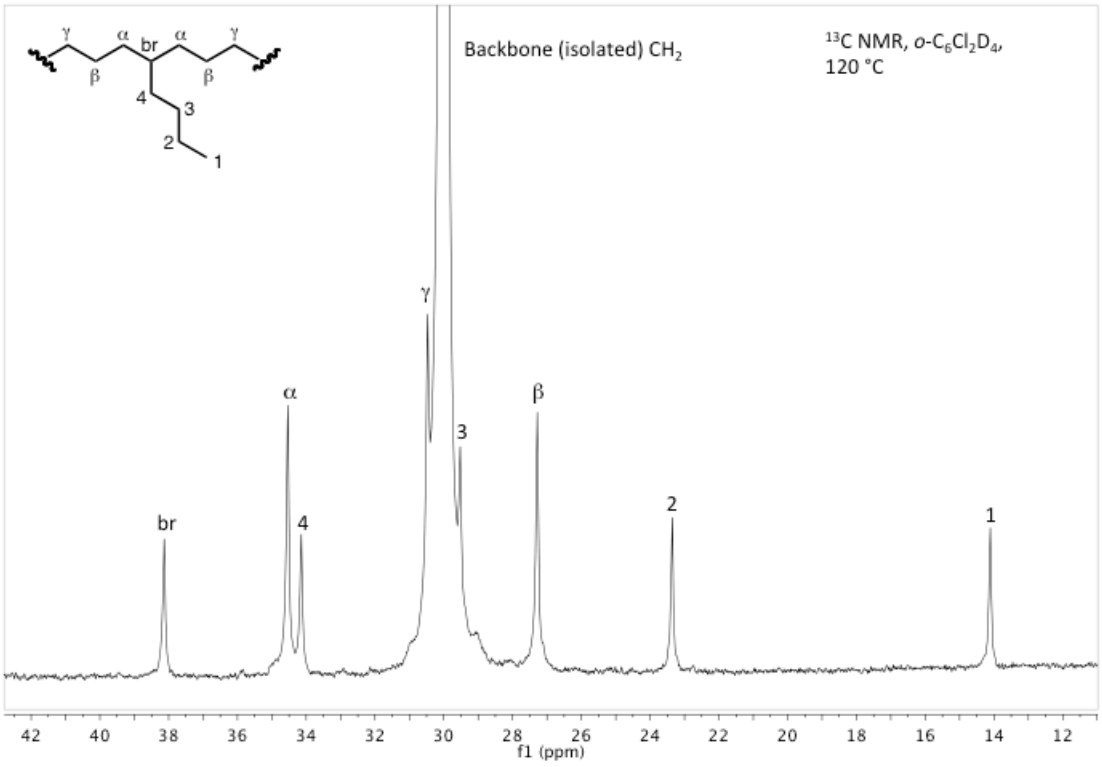

Figure 3.5. ^{13}C NMR spectrum of ethylene/1-hexene copolymer generated by precatalyst **3-VCl(THF)$_2$** in the presence of 320 mM 1-hexene**.** Spectrum was recorded in *ortho*-dichlorobenzene-d_4 at 120 °C

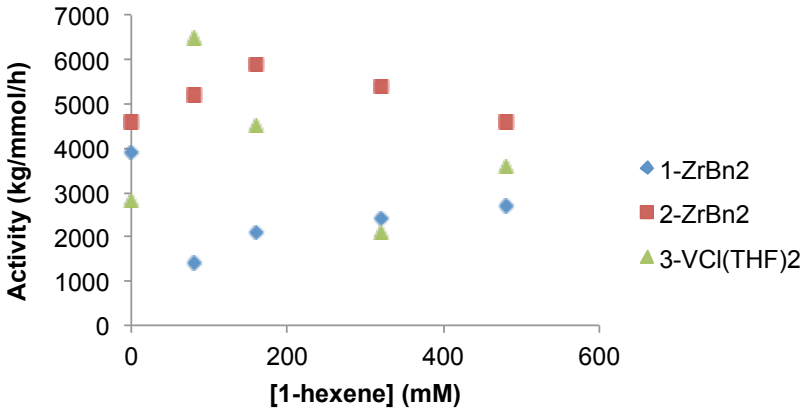

Figure 3.6. Dependence of catalyst activity on comonomer concentration

In 2009, we reported several ethylene/1-octene copolymerization trials with **3-VCl(THF)$_2$** and a precatalyst **6-ZrBn$_2$.**[9b] While experimental conditions are reasonably different (1 bar ethylene, 3.2 M 1-octene, MAO with [Al]/[cat] = 1000) from those described in the experiments above, the results agree somewhat with what we observe at higher pressures of ethylene and lower concentrations of comonomer. Precatalyst **6-ZrBn$_2$,** which is similar to **1-ZrBn$_2$,** shows a significantly larger preference for ethylene over 1-octene (0.5 mol% comonomer incorporation) than **3-VCl(THF)$_2$** (6.6 mol% comonomer incorporation.) It must be noted that comonomer insertion values may be substantially larger due to the greater concentration of comonomer and lower pressure of ethylene. The rate of insertion of 1-hexene and 1-octene are not expected to vary much.

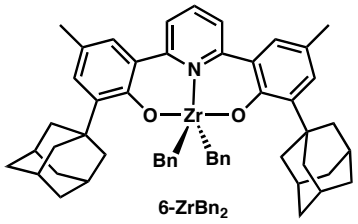

6-ZrBn$_2$

CONCLUSIONS

Previously reported early metal propylene polymerization catalysts supported by pincer non-metallocene ligands have been shown to be highly active at polymerizing ethylene. Activities higher than that of Cp_2ZrCl_2 can be achieved, but the polyethylenes exhibit broad PDIs, indicating that more than one catalyst is present upon activation with MAO. In the presence of 1-hexene, only vanadium(III) precatalyst **3-VCl(THF)$_2$**

incorporates comonomer in a detectable amount, yet the activities of each catalyst appear to be dependent on comonomer concentration (Figure 3.6). Investigations into stoichiometric, perhaps cleaner activations of precatalysts are underway. Future directions involve developing more rigid pincer ligands to reduce fluxionality in a catalytically active species that could contribute to PDI broadening.

EXPERIMENTALS

General Considerations and Instrumentation. All air- and moisture-sensitive compounds were manipulated using standard high vacuum and Schlenk techniques or manipulated in a glovebox under a nitrogen atmosphere using degassed solvents. All solvents for the synthesis of precatalysts were dried over sodium benzophenone ketyl and stored over titanocene dihydride where compatible or dried by the method of Grubbs.[14] All solvents and liquid monomers for polymerization trials were stored over 3Å molecular sieves. All NMR solvents were purchased from Cambridge Isotopes. Benzene-d_6 was dried over sodium benzophenone ketyl, while CD_2Cl_2 was dried over CaH_2 and stored over molecular sieves. Ethylene was dried through a Ridox column. All other chemicals were used as received. Precatalysts **1-ZrBn$_4$, 2-ZrBn$_4$,** and **3-VCl(THF)$_2$** were prepared according to literature procedure.[9a,9b] ^{1}H and ^{13}C spectra were recorded on Varian Mercury 300 or Varian INOVA-500 spectrometers and unless otherwise indicated at room temperature.

Ethylene Polymerization and Ethylene/1-Hexene Copolymerization Trials. All trials were carried out in the laboratory of Dr. Muhammad Atiqullah with the assistance of

technician Mr. Anwar Hossain at King Fahd University of Petroleum and Minerals in Dhahran, Saudi Arabia. A thick-walled, jacketed glass Büchi reactor was oven-dried and fastened to the installation shown in Figure 3.7. The air-tight reactor was evacuated for several hours and back-filled with ethylene. Under a positive pressure of ethylene, dry *n*-hexane (~500 mL for homopolymerizations, 500-x mL for copolymerizations with x mL 1-hexene) was cannulated into the reactor, followed by tri-isobutylaluminum (500 μL, 393 mg, 2.00 mmol) to scrub water. After 5 minutes, 10 wt% MAO in toluene (3.58 mL, 4.8 mmol) is added via syringe to afford a clear solution, which is stirred at 500 rpm under ethylene. For copolymerizations, comonomer 1-hexene (5 mL, 10 mL, 20 mL, or 30 mL) is added via syringe to the stirring solution. The solution is then stirred for 10 minutes and cooled to 10 °C using an ethylene glycol cooling bath connected to the outer jacket of the reactor. A solution of precatalyst (16 μmol) in 4 mL dry toluene is added quickly via syringe to the cooled, stirring suspension against a positive pressure of ethylene. The solution is warmed to 30 °C over 1–2 minutes and ethylene pressure increased to 2 bar. During the reaction, exotherms under kept under control and the temperature is maintained at or around 30 °C by periodically cycling coolant through the internal coils of the reactor. At the end of the reaction, the reactor is cooled to 0 °C and methanol is added slowly to quench MAO. The reactor is detached from the support and the polymer suspension is filtered through a sintered glass funnel, washed with methanol and hexanes and dried in air for 2 hours. The polymer is then weighed for calculation of catalyst activity.

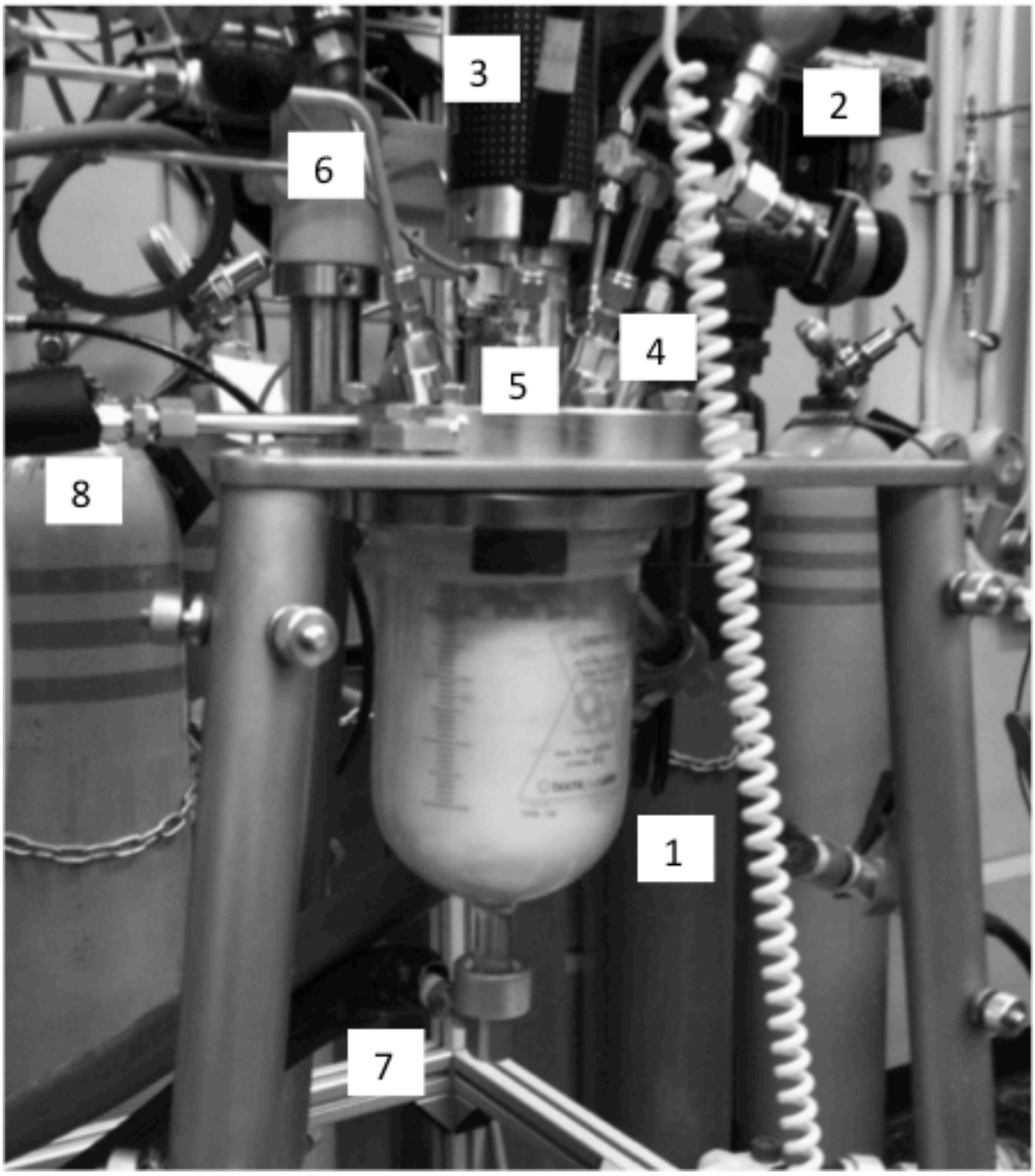

Figure 3.7. Glass Büchi reactor employed for all polymerization experiments described herein. (1) Thick-walled, jacketed glass reactor; (2) ethylene feed; (3) mechanical stirrer; (4) syringe port equipped with Swagelok; (5) electronic thermocoupler; (6) vacuum; (7) coolant feed to reactor jacket; (8) coolant outlet from reactor jacket

^{13}C NMR Analysis of Polymers. To an NMR tube, polymer (200 mg) was added followed by *o*-dichlorobenzene-d_4 (1.5 mL). The suspension is heated at 160 °C for 4–15 hours until the polymer is completely dissolved to afford a highly viscous solution. All spectra were taken on a Varian Inove 500 MHz spectrometer. The following acquisition parameters were used: 2.1 s relaxation delay, 2.3 s acquisition time, full NOE with Waltz decoupling, 2000–5000 scans. All measurements were taken without sample spinning at 120 °C, calibrated by ethylene glycol. The ^{13}C NMR spectra were referenced at 132.6 ppm for the apparent singlet of *o*-dichlorobenzene-d_4.

REFERENCES

1. McKnight, A. L.; Waymouth, R. M. *Chem. Rev.* **1998**, *98*, 2587.
2. Brintzinger, H. H.; Fischer, D.; Mulhaupt, R.; Rieger, B.; Waymouth, R. M. *Angew. Chem., Int. Ed.* **1995**, *34*, 1143.
3. Gibson, V. C.; Spitzmesser, S. K. *Chem. Rev.* **2003**, *103*, 283.
4. Shapiro, P. J.; Bunel, E.; Schaefer, W. P.; Bercaw, J. E. *Organometallics* **1990**, *9,* 867.
5. Okuda, J. *Chem. Ber.* **1990**, *123*, 1649.
6. Small, B. L.; Brookhart, M.; Bennett, A. M. A. *J. Am. Chem. Soc.* **1998**, *120*, 4049.
7. Britovsek, G. J. P.; Gibson, V. C.; Kimberley, B. S.; Maddox, P. J.; McTavish, S. J.; Solan, G. A.; White, A. J. P.; Williams, D. J. *Chem. Comm.* **1998**, 849.
8. (a) Johnson, L. K.; Killian, C. M.; Brookhart, M. B. *J. Am. Chem. Soc.* **1995**, *117*, 6414. *(*b) Svejda, S.; Brookhart, M. B. *Organometallics* **1999**, *18*, 65. (c) Ittel, S. D.; Johnson, L. K.; Brookhart, M. *Chem. Rev.*, **2000**, *100*, 1169. (d) Gates, D. P.; Svejda, S. A.; Oñate, E.; Killian, C. M.; Johnson, L. K.; White, P. S.; Brookhart, M. *Macromolecules* **2000**, *33*, 2320.
9. (a) Agapie, T.; Henling, L. M.; DiPasquale, A. G.; Rheingold, A. L.; Bercaw, J. E. *Organometallics* **2008**, *27*, 6245. (b) Golisz, S. R.; Bercaw, J. E. *Macromolecules* **2009**, *42*, 8751.
10. Tonks, I. A.; Henling, L. M.; Day, M. W.; Bercaw, J. E. *Inorg. Chem.* **2009**, *48*, 5096.
11. Agapie, T.; Bercaw, J. E. *Organometallics* **2007**, *26*, 2957.
12. Hsieh, E. T.; Randall, J. C. *Macromolecules* **1982**, *15*, 1402.
13. Wu, J.-Q.; Pan, L.; Liu, S.-R.; He, L.-P.; Li, Y.-S. *J. Polym. Sci. A Polym. Chem.* **2009**, *47*, 3573.
14. Pangborn, A. B.; Giardello, M. A.; Grubbs, R. H.; Rosen, R. K.; Timmers, F. J. *Organometallics* **1996**, *15*, 1518.

CHAPTER 4

Activator-Free Olefin Oligomerization and Isomerization Reactions Catalyzed by Palladium(II) Dimers

Parts of this work appear in:

Winston, M. S.; Oblad, P. F.; Labinger, J. A.; Bercaw, J. E.

Angew. Chem., Int. Ed. **2012**, *51*, 9822.

ABSTRACT

Industrial processes such as olefin oligomerization and polymerization require the use of catalyst activators, such as methylaluminoxane. Herein we report an air and water-tolerant bis(μ-hydroxy)palladium dimer supported by an α-diimine ligand that can self-activate to an olefin oligomerization and isomerization catalyst. Mechanistic studies indicate that the active catalyst is a palladium(II) hydride, formed by either a Wacker-type oxidation or C-H activation/dehydrogenation of olefin by the precatalyst dimer. The reactive palladium(II) hydride can isomerize and oligomerize olefins with turnover numbers at room temperature as high as 2100/h and 600/h, respectively. Catalytic activity is remarkably insensitive to water or air, so that catalytic isomerization/oligomerization reactions can be carried out on the benchtop. Dimer activation has also been shown to be highly sensitive to steric effects imparted by the α-diimine ligand.

INTRODUCTION

Olefin oligomerization is an important process that converts basic feedstocks, such as ethylene and propylene, into value-added olefins used in the production of ubiquitous products including linear low-density polyethylene, plasticizers, detergents, fuels, and lubricants.[1] α-Olefins are produced at a rate of $>10^9$ lb/year, primarily via ethylene oligomerization.[2] In contrast to polymerization catalysts that undergo fast chain propagation relative to chain termination,[3] homogeneous late-transition-metal complexes that exhibit fast rates of β-hydride elimination relative to propagation often exhibit oligomerization behavior.[4]

The nickel-based oligomerization step of the Shell higher olefin process (SHOP) represents one of the largest applications of homogeneous transition metal catalysis in industry.[1b] Pioneered by Keim, it is highly selective for producing linear α-olefins in the C_4-C_{30} range. The active catalyst — a nickel(II) hydride — is generated by β-hydride elimination from a nickel(II) alkyl precatalyst (eq. 1), and oligomerizes ethylene through a traditional step-growth process (discussed ahead) involving a sequence of insertion/coordination steps at elevated temperatures (~100 °C) and pressures (5–10 atm).

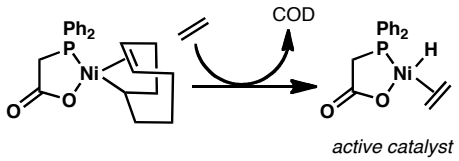

(1)

Many nickel-based ethylene oligomerization catalysts supported by various bidentate monoanionic ligands have since been reported upon Keim's initial disclosure.[4] Almost all involve an active nickel hydride species. Oligomerization catalysts that exploit

other metals, such as iron[2] and titanium,[5] have also been disclosed, but the nature of the active species is ambiguous.

Nickel(II) and Palladium(II) Polymerization and Oligomerization Catalysts Supported by α-Diimine Ligands

In 1995, Brookhart and coworkers reported a series of nickel(II) and palladium(II) complexes that convert ethylene and α-olefins to high molar mass polymers with highly branched microstructures.[6] Group 10 dimethyl precatalysts (**1**) stabilized by α-diimine ligands can be activated by acid to release methane, generating a reactive metal cation stabilized by a labile diethyl ether ligand (**2**) (Scheme 4.1). Alternatively, α-diimine-supported nickel(II) dibromide complexes may be activated *in situ* by methylaluminoxane (MAO, 1000 equiv Al/Ni). In the presence of ethylene or α-olefins, ligand exchange with **2** presumably generates an olefin-bound organometallic species that can initiate polymerization via an insertion reaction (not shown in Scheme 4.1). A sequence of monomer insertions and β-hydride elimination, followed by release of polymer and coordination of monomer, affords the active metal hydride catalyst (**3**).

Rigorous mechanistic studies by Brookhart and coworkers reveal a catalytic cycle from **3** that begins with hydride insertion into coordinated monomer to afford a metal alkyl complex with a vacant site.[6b,6c] Coordination of monomer, followed by a series of insertion/coordination reactions allows chain growth. A metal polymeryl complex with a vacant site can undergo β-hydride elimination/chain transfer with monomer to afford polymer with terminal unsaturation and regenerate catalyst **3,** or β-hydride

elimination/re-insertion to afford a secondary alkyl metal intermediate. This intermediate can either insert monomer or continue "chain-running" via a sequence of β-hydride elimination/re-insertion reactions to further internalize the olefin.[6c] This unique behavior allows the production of significantly branched polymers. For example, at the time of this report, these catalysts produced previously unobserved amorphous polyethylene that was far more highly branched than any reported low-density polyethylene in the literature.[1a] Turnover frequencies (TOF) as high as 3.9 x 10^5/h can be achieved under 1 atmosphere ethylene at room temperature.

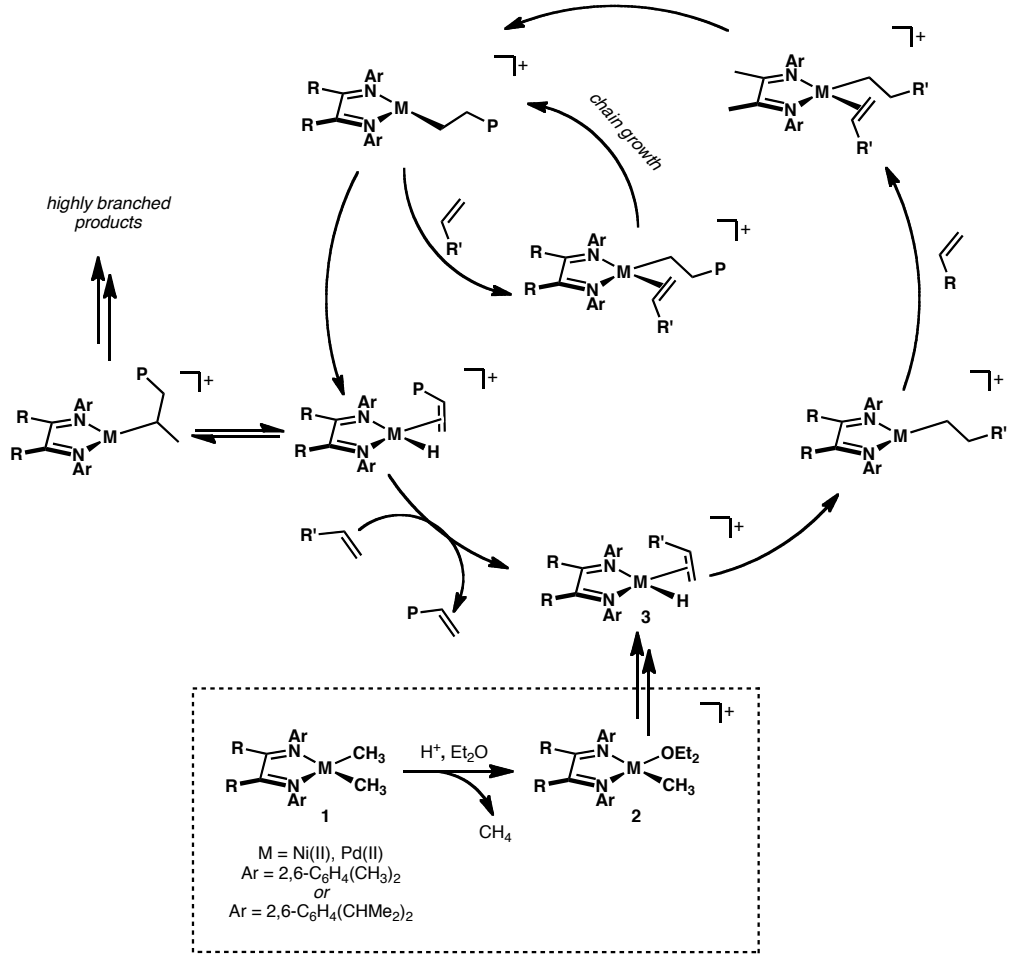

Scheme 4.1

Kinetic studies indicate that chain transfer is an associative process that requires initial coordination of monomer to the axial face of the tetracoordinate metal complex.[6a,6b] This has important consequences in determining the overall behavior of the catalyst. It is thought that *ortho* aryl substituents on α-diimine ligands can block axial approach of monomer to the metal, inhibiting chain transfer relative to monomer insertion, which requires olefin approach to the vacant site *in the plane*. Indeed, complexes supported by α-diimine ligands with *ortho iso*-propyl substituents (Ar = 2,6-$C_6H_4(CHMe_2)_2$) afford higher molecular weight polyethylene than those supported by ligands with less bulky *ortho* methyl groups (Ar = 2,6-$C_6H_4(CH_3)_2$). Furthermore, nickel(II) complexes supported by ligands with only *para* substitution exhibit ethylene oligomerization and propylene dimerization activity with a TON ~ 10^5 (Figure 4.1).[7]

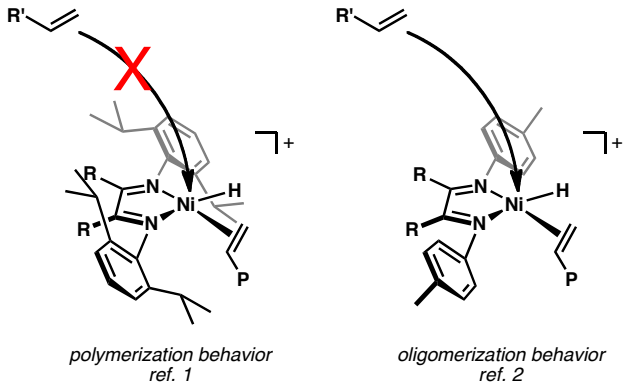

Figure 4.1. Two nickel(II) hydride cations that exhibit olefin polymerization (left) and oligomerization (right) behavior. Aryl substitution on the α-diimine appears to dictate behavior by inhibiting chain transfer relative to monomer insertion in polymerization catalysts.

Initial Synthesis and Isolation of Bis(μ–Hydroxy)palladium(II) Dimers

The versatility of α-diimine Group 10 complexes were brought to our attention in our forays into selective hydrocarbon functionalization.[8] Roughly forty years ago, Shilov and coworkers reported a platinum(II)-catalyzed oxidation of alkanes to alcohols or alkyl chlorides at high temperatures in the presence of stoichiometric platinum(IV) oxidant (eq. 2).[9]

$$RCH_3 + [PtCl_6]^{2-} + H_2O \xrightarrow[H_2O,\ 120\ °C]{\text{cat. } [PtCl_4]^{2-}} RCH_2OH + [PtCl_4]^{2-} + 2HCl \quad (RCH_2Cl) \qquad (2)$$

In our efforts to avoid stoichiometric platinum(IV) oxidant, we investigated the possibility of using significantly cheaper and more abundant O_2 as a terminal oxidant. Given recent reports of palladium(II)-catalyzed arene[10] and alcohol[11] oxidation using O_2 as a stoichiometric oxidant, we envisioned that O_2 could facilitate a Pd(0)/Pd(II) redox couple to achieve the desired alkane functionalization chemistry (eq. 3 and 4).

$$RCH_3 + O_2 + H_2O \xrightarrow{[Pd^{II}]} RCH_2OH + H_2O_2 \qquad (3)$$

$$RCH_3 + H_2O_2 \xrightarrow{[Pd^{II}]} RCH_2OH + H_2O \qquad (4)$$

Benzene C-H activation by palladium(II) methyl cations was first investigated as the microscopic reverse of methane C-H activation.[8h] Under O_2, benzene is activated and methane is released (Scheme 4.2). The product of benzene C-H activation — [(α-diimine)Pd(Ph)$(H_2O)]^{2+}$ — disproportionates to bis(aquo) dication [(α-diimine)Pd$(OH_2)_2]^{2+}$ (**5**) and (α-diimine)Pd$(Ph)_2$, which reductively eliminates biphenyl.

Oxidation of the reduced species by O_2 or H_2O_2 presumably generates **5**, bis(μ-hydroxy) dimer **4**.

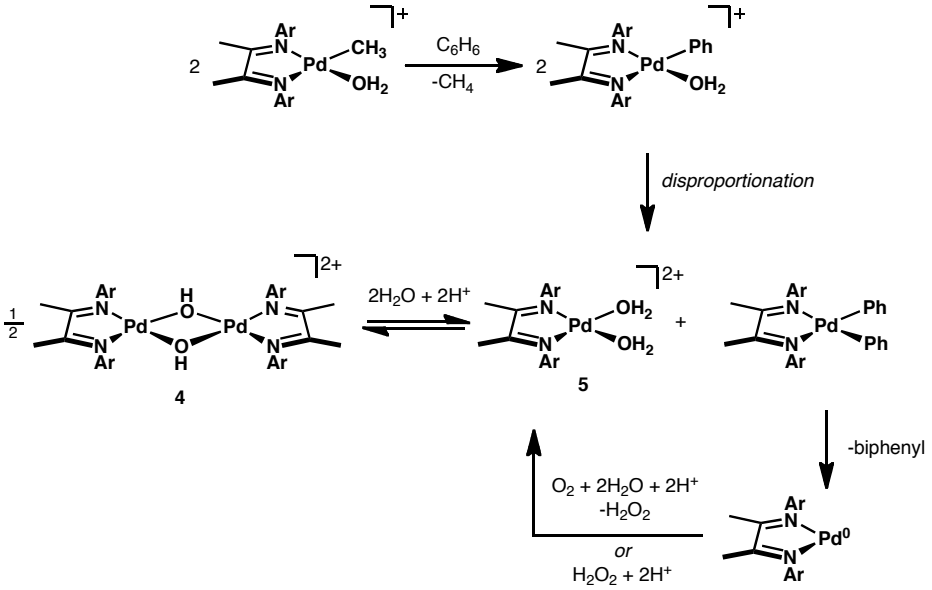

Scheme 4.2

That some Group 10 hydroxy-bridged dimers may be thermodynamic "dead states" under oxidative conditions is not unprecedented. For example, Vedernikov and coworkers[12] reported that the reaction of **6** with O_2 affords bis(μ-hydroxy) dimer **7** via pendant sulfonate-assisted oxidation to platinum(IV) and C-O bond coupling (Scheme 4.3). It should be noted that the dissociation of **7** was not observed even under ethylene at elevated temperatures to regenerate **6.**

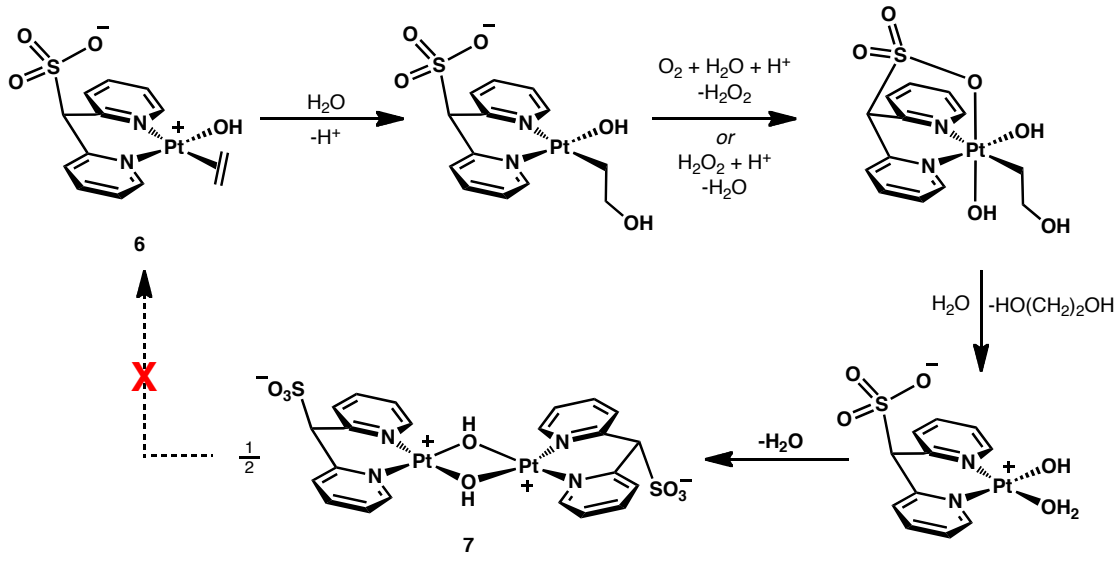

Scheme 4.3

On the other hand, Sodeoka and coworkers[13] reported that dimer [(*R*-BINAP)Pd(OH)]$_2^{2+}$ (**8**) is not chemically inert, but rather reacts with silyl enol ethers to dissociate to **9**, which catalyzes asymmetric Mannich reactions with imine substrates (Scheme 4.4).

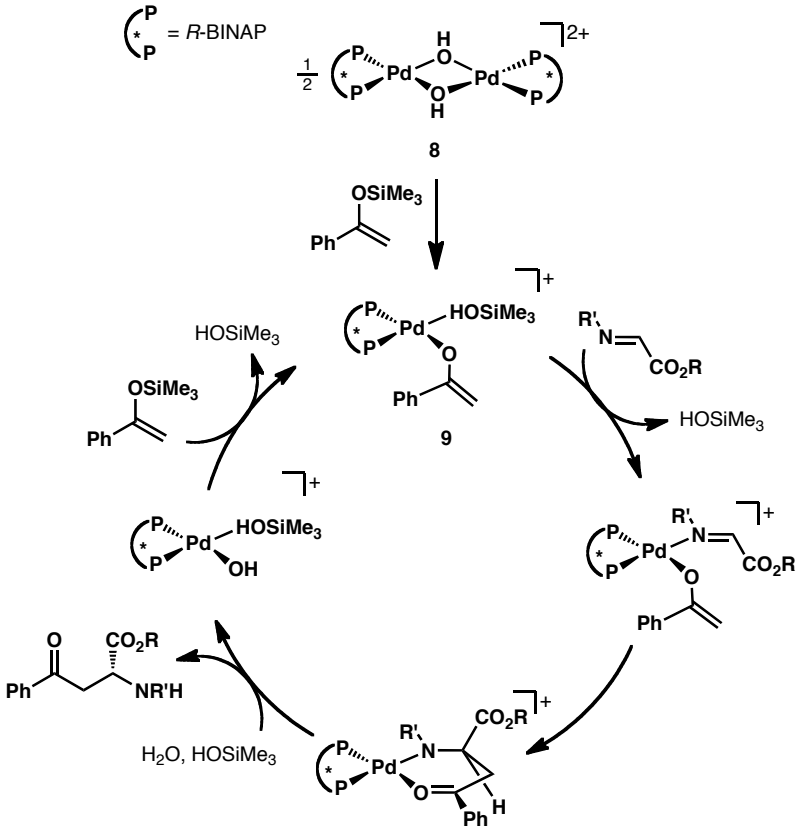

Scheme 4.4

Likewise, [(bathophenanthroline)Pd(OH)]$_2^{2+}$ (**10**) catalyzes the aerobic oxidation of secondary alcohols to ketones through the proposed catalytic cycle in Scheme 4.5.[14] The authors suggest that dimer dissociation and release of water affords a palladium(II)

alkoxide species from which substrate oxidation and deprotonation may take place. The resulting palladium(0) species is presumably re-oxidized by O_2 or H_2O_2 before dimerizing back to **10**, although this final step seems unlikely.

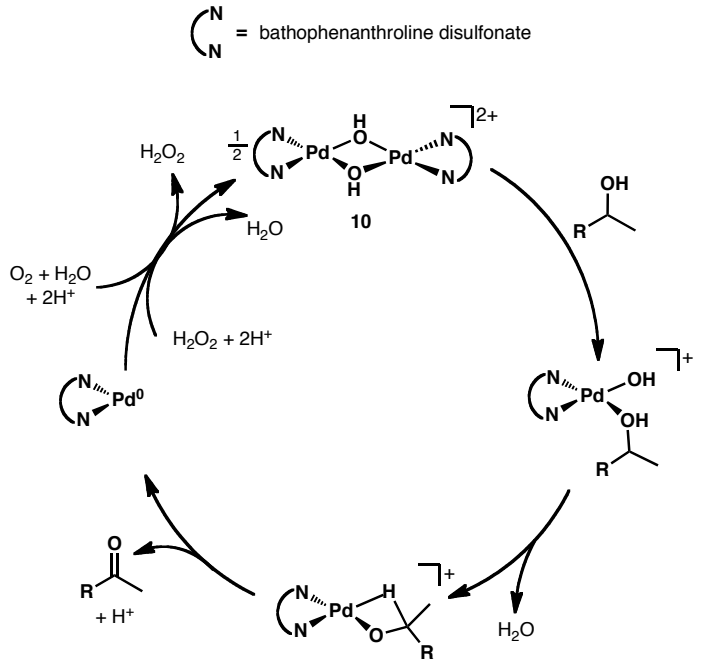

Scheme 4.5

Stoichiometric C-H Activation by α-Diimine-Supported Bis(μ–Hydroxy)palladium(II) Dimers

In 2008, our group reported[15] the isolation and spectroscopic characterization of a number of bis(μ–hydroxy) dimers of the type $[(\alpha\text{-diimine})M(OH)]_2^{2+}$ and bis(aquo) monomers $(\alpha\text{-diimine})M(H_2O)_2^{2+}$ (M = Pd(II), Pt(II)) (Figure 4.2). These complexes are not necessarily resting states, and can in fact activate a variety of C-H bonds in air and wet solvent under mild conditions (Scheme 4.6). A mixture of platinum(II) dimer **11a** and monomer **12a**, for instance, can activate indene, as well as the benzylic C-H bonds of 1,4-

diethyl-benzene. Aryl C-H bonds can also be activated, provided the metal is directed to the reacting C-H bond and a multidentate ligand is ultimately produced. With allyl benzene, the pendant olefin coordinates to the metal in the C-H activated product, while nitrogen coordinates to generate a cyclometalate in the reaction with aryl oximes.

In all cases, C-H activation with **11a/12a** can be carried out in benchtop solvent under air. In most cases, transformations are quantitative by NMR. This suggests that the reaction is not adversely affected by the water released upon coordination and activation of organic substrate.

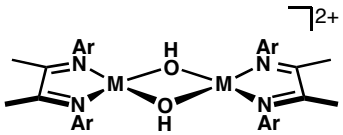

4: M = Pd, *characterized and isolated*

11: M = Pt, *characterized and isolated*

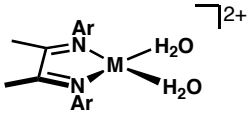

5: M = Pd, *characterized and isolated*

12: M = Pt, *characterized but not isolable*

Figure 4.2. Isolable and/or characterizable Group 10 bis((μ–hydroxy) dimers and bis(aquo) monomers

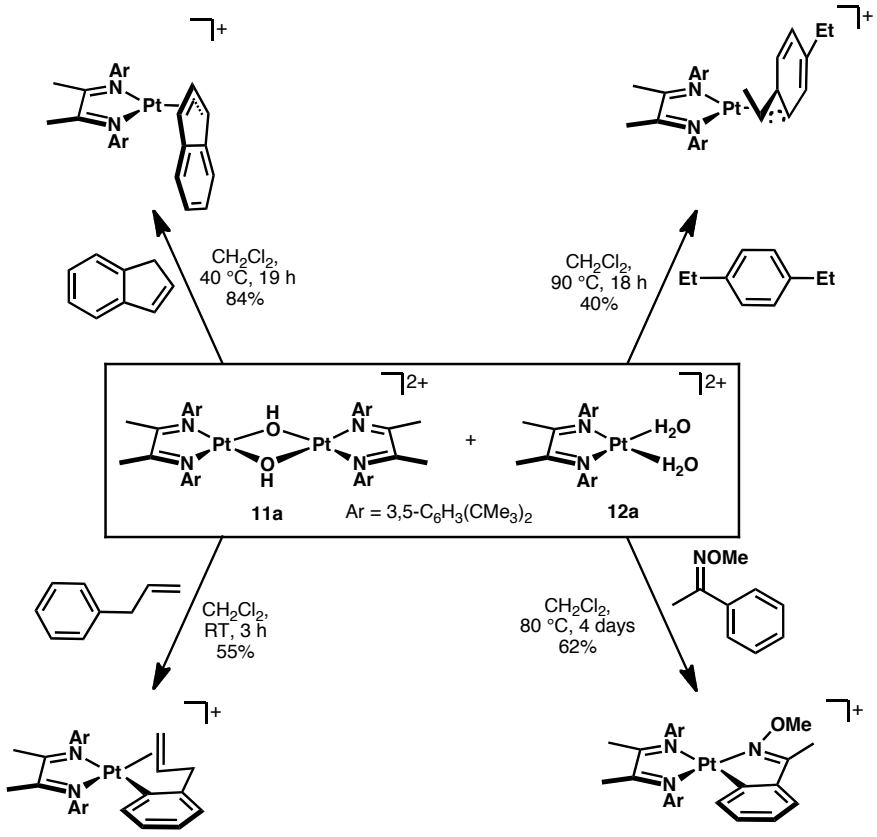

Scheme 4.6

While dimer **11a** and monomer **12a** are in equilibrium with one another, **12a** is the reactive species. Furthermore, acid not only drives the **11a**/**12a** equilibrium toward monomer, but accelerates the C-H activation step. Kinetic experiments of cyclohexene C-H activation (Scheme 4.7) have established that η^3-cyclohexenyl complex **13** forms slowly in the absence of acid. The first step – presumably dimer dissociation to **12a** – and the second C-H activation step exhibit a first-order dependence on acid (the first step obviously has a two-term rate law). The acid dependence of the second step suggests that general-acid catalysis may be needed to weaken the Pt-OH_2 bond. The second step is also first order in cyclohexene.

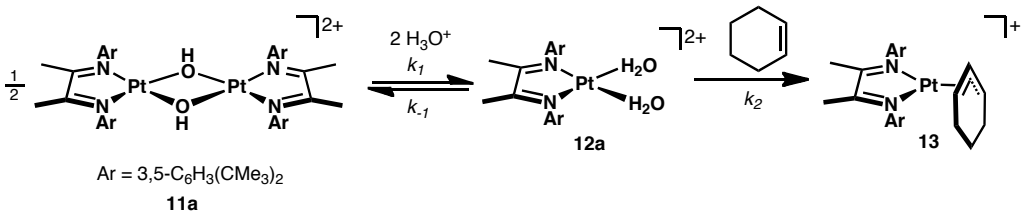

Scheme 4.7

Analogous bis(μ–hydroxy) palladium(II) dimer **4a** can also stoichiometrically activate C-H bonds under relatively mild conditions (Scheme 4.8). In benchtop solvent under air, **4a** has been shown to activate indene and aryl C-H bonds of oximes**.** Like the platinum(II) system, the palladium(II) dimers can only activate substrates that can coordinate in a bidentate or η^3 fashion once activated.

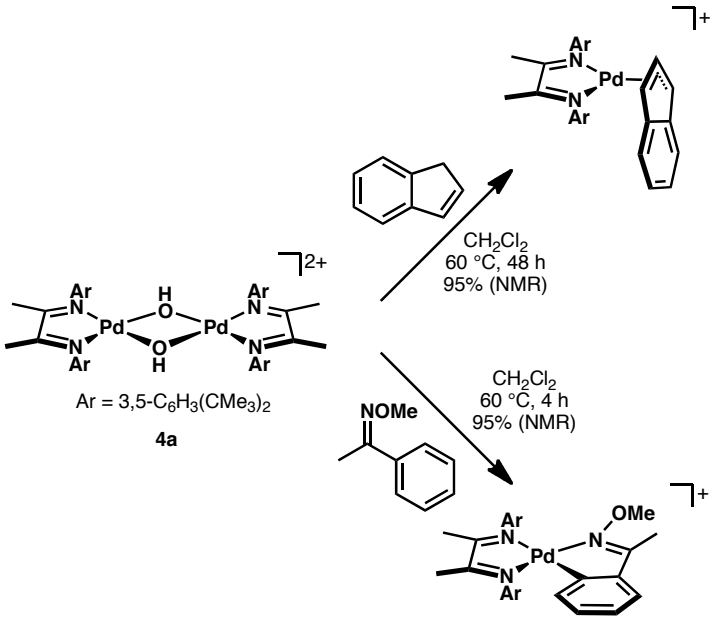

Scheme 4.8

Unlike platinum(II) dimer **11a**, however, palladium(II) dimer **4a** need not dissociate to the corresponding bis(aquo) monomer **5a.**[16] In fact, spectroscopic studies

with indene reveal that **4a** reacts faster than **5a** to generate a C-H activated η^3-indenyl complex (Scheme 4.9). Furthermore, the reaction of **4a** ($t_{1/2}$ ~ 2 days) is substantially accelerated in the presence of a small amount of nucleophilic co-solvent ($t_{1/2}$ ~ 5 minutes), such as trifluoroethanol (TFE) or MeOH. A half-order dependence on **4a** and first-order dependence on indene and co-solvent concentrations suggest a mechanism involving solvent-assisted dissociation of the dimer to monomeric solvent adduct **14**, followed by rate-limiting displacement of solvent by indene to generate substrate-bound intermediate **15**, which then undergoes C-H activation. Expectedly, the palladium(II) and platinum(II) monomers react with indene via the same mechanism.

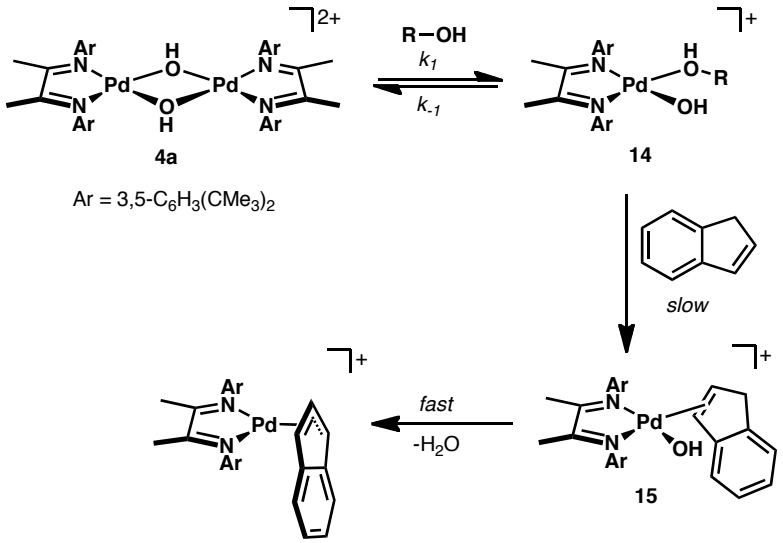

Scheme 4.9

To develop a practical method for C-H bond functionalization, we investigated oxidative strategies to achieve catalytic turnover in the C-H activation reactions by palladium(II) and platinum(II) bis(μ–hydroxy) dimers discussed above.[17] However, treating C-H activated palladium(II) and platinum(II) complexes with oxidants such as

$PtCl_6^{2-}$ and Br_2 only resulted in the release of halogenated (oxidized) organics and unreactive bis(μ–halo) metal dimers.

The reasons for the different activation mechanisms of palladium(II) and platinum(II) dimers are unclear. However, that generation of an active species from palladium(II) dimer **4a** is accelerated simply in the presence of nucleophilic co-solvent encouraged us to explore further dimer reactivity, namely the stoichiometric C-H bond activation of linear olefins and unactivated alkanes under mild conditions.

RESULTS AND DISCUSSION

Synthesis and Characterization of Bis(μ-Hydroxy) Palladium(II) Dimers

The original, reported synthesis[16] of palladium(II) dimer **1a** from bis(aquo) monomer **2a** is problematic and unreliable. A new, three-step route to **4a** was therefore developed from readily available starting material. *N*-Aryl α-diimine ligands may be synthesized in one step via aniline condensation with 2,3-butanedione[8h] in high yields (eq. 6).

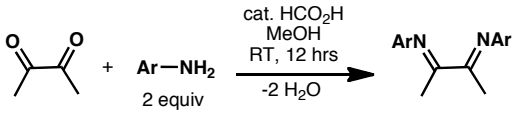

(6)

16a ($^{tBu}DAB_{Me}$)**:** Ar = 3,5-$C_6H_3(CMe_3)_2$
16b ($^{iPr}DAB_{Me}$): Ar = 2,6-$C_6H_4(CHMe_2)_2$
16c ($^{Me}DAB_{Me}$): Ar = 2,6-$C_6H_4(CH_3)_2$

The improved synthesis of bis(μ-hydroxy) palladium(II) dimers is outlined in Scheme 4.10. Reaction of $(PhCN)_2PdCl_2$ with α-diimine ligand **16a** affords dichloride

complex **17a** in quantitative yield. Silver-assisted halide abstraction in THF affords bis(solvento) complex **18a,** which on treatment with water in the presence of a polymer-supported base ("polymer-bound diethylamine") gives dimer **4a** in 70% overall yield from **17a**, which exhibits a diagnostic, upfield singlet in the ^{1}H NMR spectrum corresponding to the hydroxy bridge protons (Figure 4.3). In the presence of deuterated alcohol, these signals disappear over several hours due to H/D exchange.

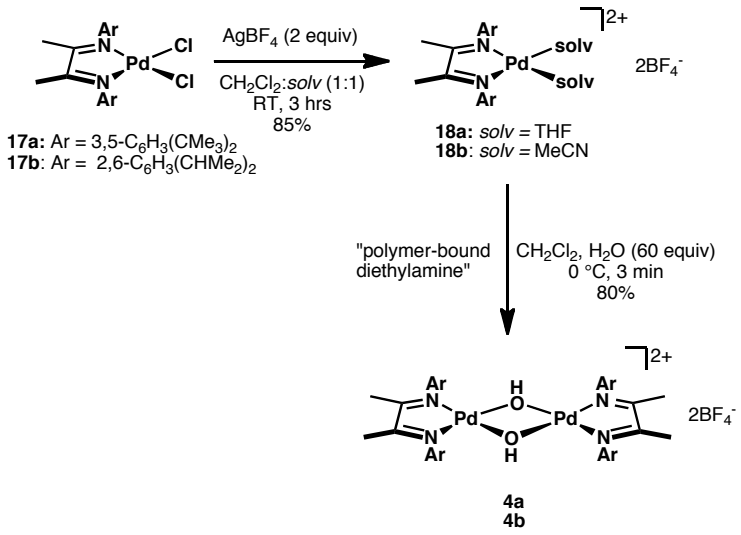

Scheme 4.10

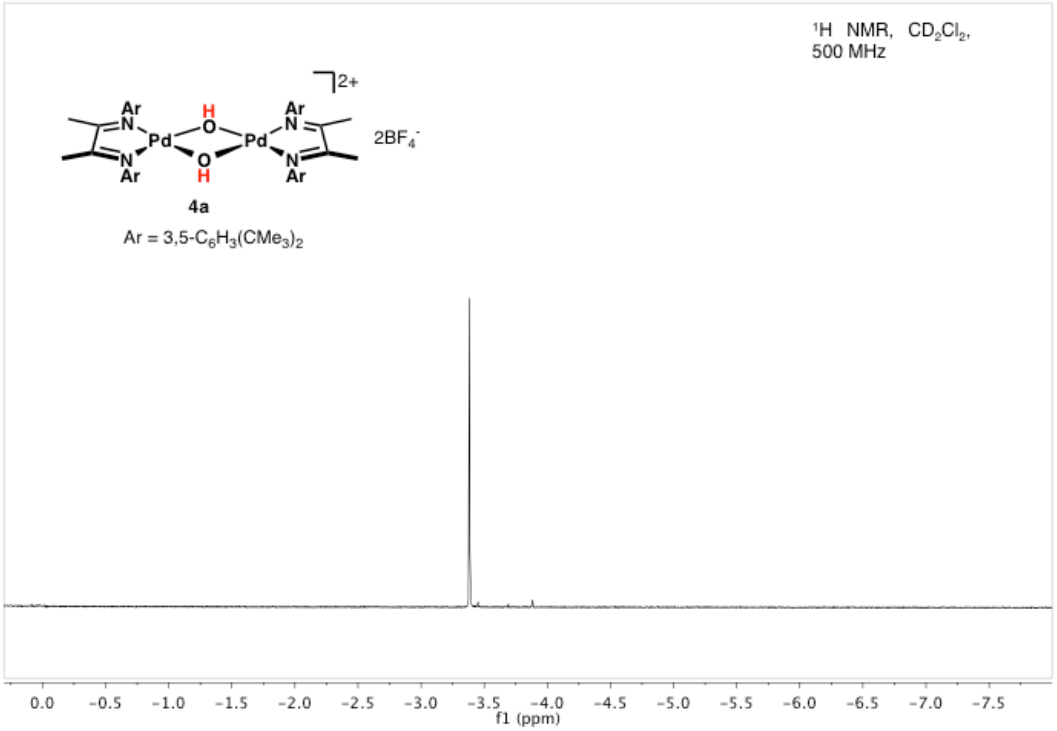

Figure 4.3. Selected region of ^{1}H NMR spectrum of bis(μ-hydroxy) dimer **4a** in CD_2Cl_2 indicating upfield resonance of OH protons

*1-Hexene Oligomerization and Isomerization Catalyzed by Dimer **4a***

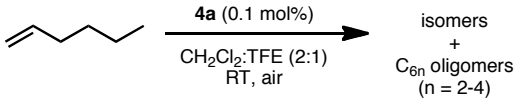

(7)

Treating 1-hexene with bis(μ-hydroxy) dimer **4a** under stoichiometric C-H activation conditions did not result in the formation of any (α-diimine)Pd(η^3-allyl) complexes. Instead, in the presence of 0.1 mol% **4a,** 1-hexene is almost entirely consumed within 40 minutes at room temperature by a combination of double-bond positional isomerization and oligomerization to yield a thermodynamic distribution of

linear hexenes (1% 1-hexene, 64% *cis*-2-hexene, 15% *trans*-2-hexene, 20% 3-hexenes), as well as dimers, trimers, and tetramers (eq. 7, Figures 4.4–4.6). As expected, the reaction of any other linear isomer of hexene with precatalyst **4a** affords an equivalent mixture of hexene isomers. Unfortunately, a rigorous kinetic analysis of the formation and consumption of each isomer is complicated by the isomerization behavior of the active catalyst.

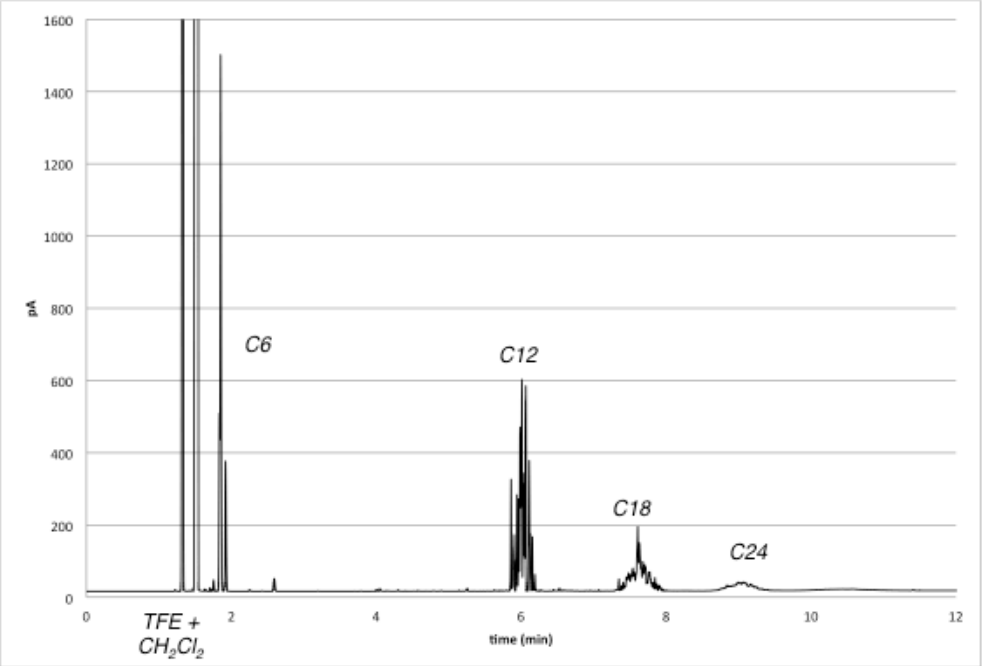

Figure 4.4. GC-MS trace of 1-hexene isomerization and oligomerization at 20 hours

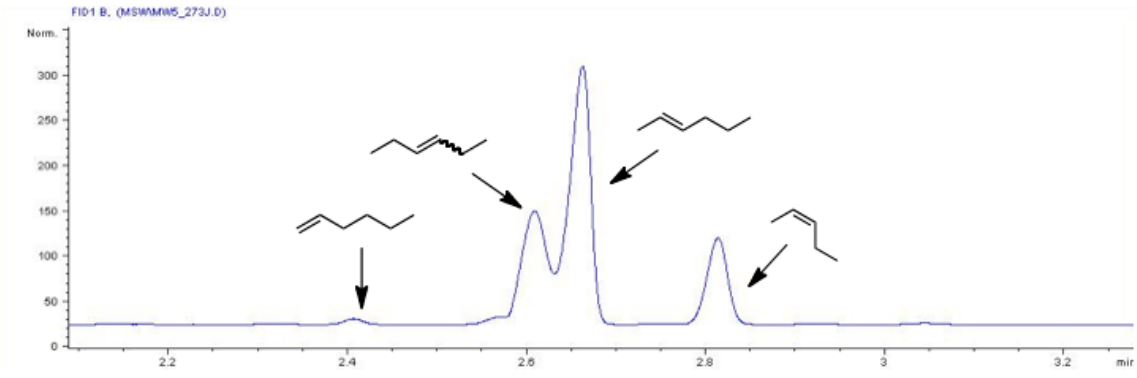

Figure 4.5. Selected region of GC trace of 1-hexene isomers at 20 hours

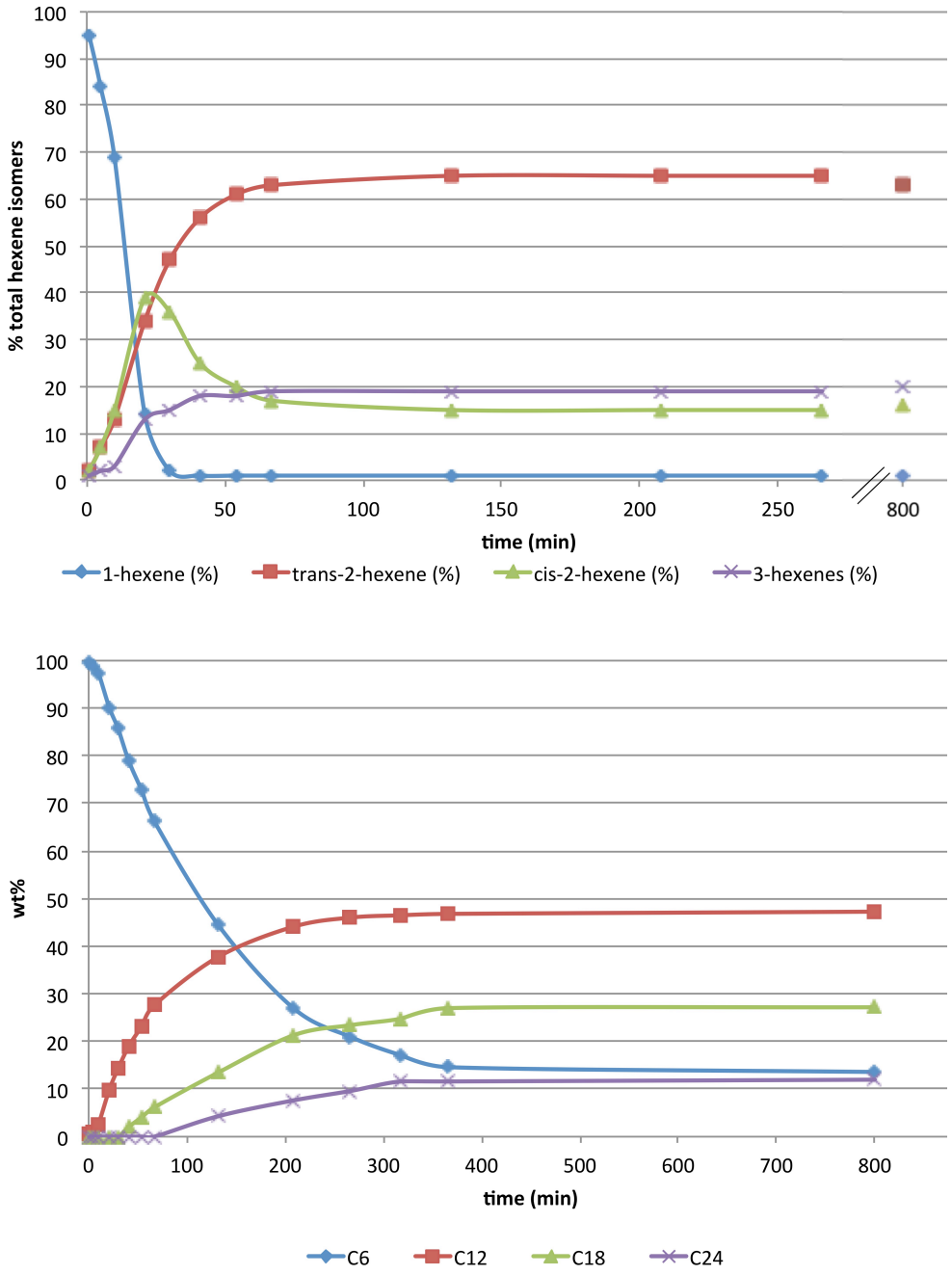

Figure 4.6. Isomerization (top) and oligomerization (bottom) of 1-hexene. Reaction conditions: 1-hexene (6.40 mmol), **4a** (0.1 mol%), CH_2Cl_2 (8 mL), TFE (4 mL), adamantane (internal gc standard), air, 25 °C

Isomerization of 1-hexene proceeds about an order of magnitude faster than oligomerization, with turnover frequencies (TOF) of about 2100/h and 200/h respectively. The concentrations of *cis* and *trans*-2-hexene increase at roughly the same rate until 1-hexene is mostly consumed (t ~ 30 minutes), at which point *cis*-2-hexene is preferably consumed over *trans*-2-hexene. After about 6 hours, the catalyst is no longer active. After this time, 1-hexene can be added but is not consumed. At the end of the reaction, the C_6 dimers, trimers and tetramers fit a Schulz-Flory distribution (determined by GC and fractional distillation) and consist primarily of branched isomers (Figure 4.7).

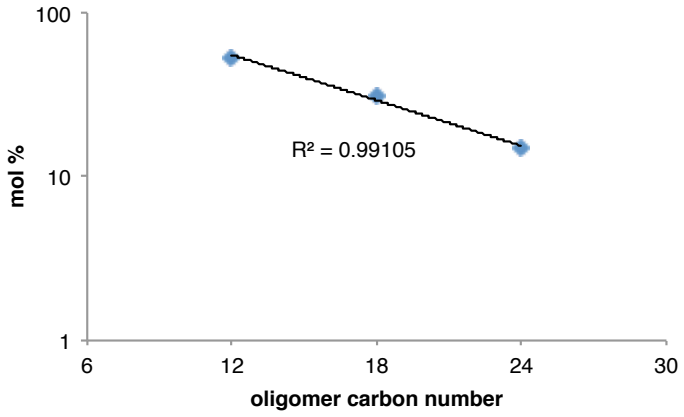

Figure 4.7. Schulz-Flory plot for hexene oligomer distribution (log(C_{6n} mol%) vs carbon number C_{6n}

Due to the dynamic isomerization behavior of the catalyst, the oligomerization feed is rapidly changing, as well as the ratio of terminal:internal olefins (which no doubt exhibit different rates of oligomerization). Nevertheless, the oligomers still fit a Schulz-Flory distribution, suggesting that oligomerization of α-olefins, even at very low concentrations, out-competes oligomerization of internal olefin isomers.

The isomerization/oligomerization catalyst obtained from **4a** appears to be quite insensitive to the presence of water or air, since the reaction rate and isomer/oligomer distributions remain essentially unchanged by addition of 2000 equivalents H_2O/Pd (Figure 4.8), or by running under 1 atm pure O_2 (Figure 4.9). To ensure that water simply is not saturating the system at very low concentrations and therefore exhibiting pseudo zero-order kinetics, reactivity was examined under dry conditions. Indeed, the rigorous exclusion of water by using dried, distilled solvents and molecular sieves seems not to affect reaction rate or isomer/oligomer distribution (Figure 4.10).

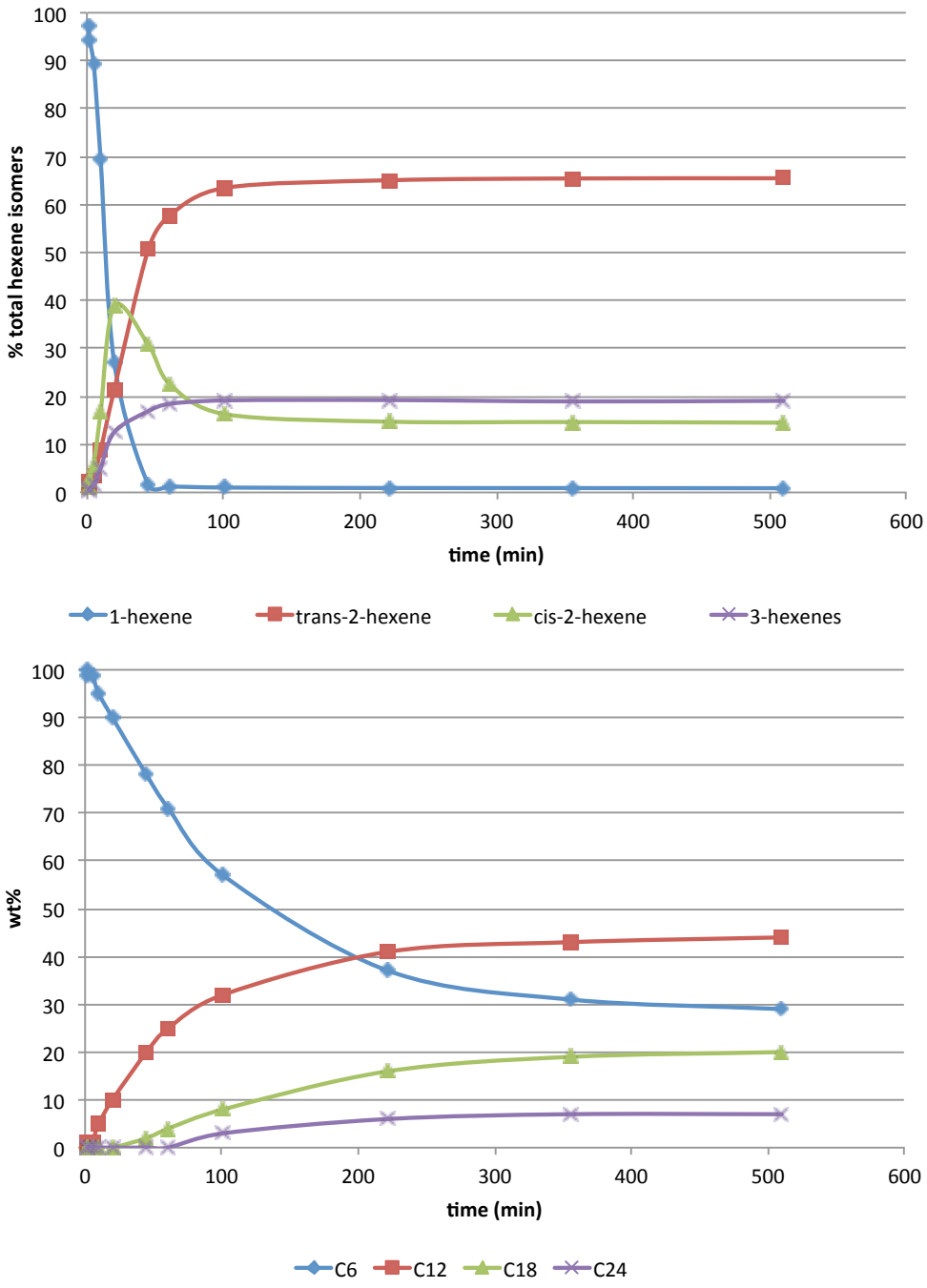

Figure 4.8. Isomerization (top) and oligomerization (bottom) of 1-hexene with 2000 equiv H_2O/Pd. Reaction conditions: 1-hexene (6.40 mmol), **4a** (0.1 mol%), CH_2Cl_2 (8 mL), TFE (4 mL), adamantane (internal standard), air, rt, H_2O (2000 equiv/Pd)

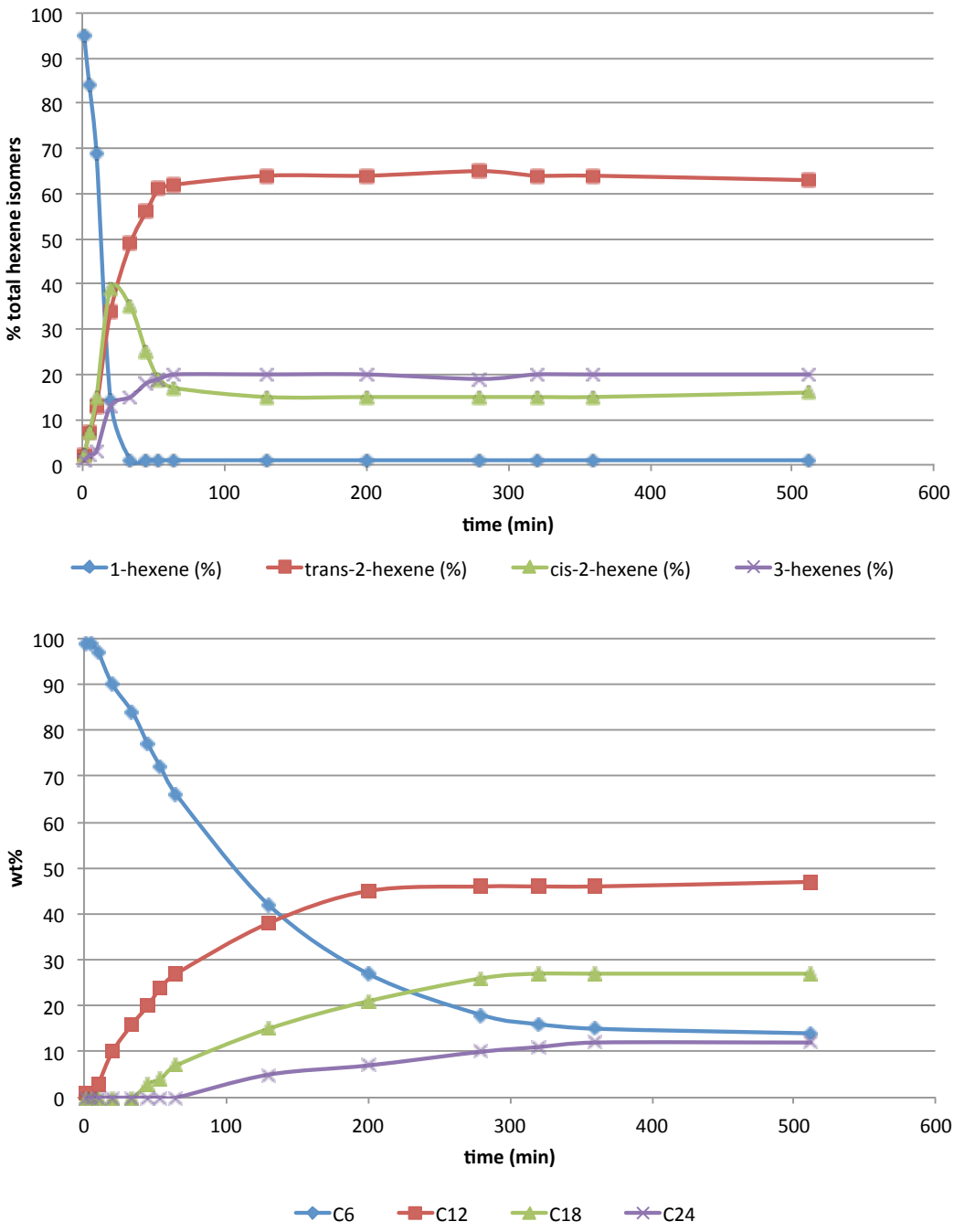

Figure 4.9. Isomerization (top) and oligomerization (bottom) of 1-hexene under 1 atm pure O_2. Reaction conditions: 1-hexene (6.40 mmol), **4a** (0.1 mol%), CH_2Cl_2 (8 mL, degassed), TFE (4 mL, degassed), adamantane (internal standard), O_2, rt

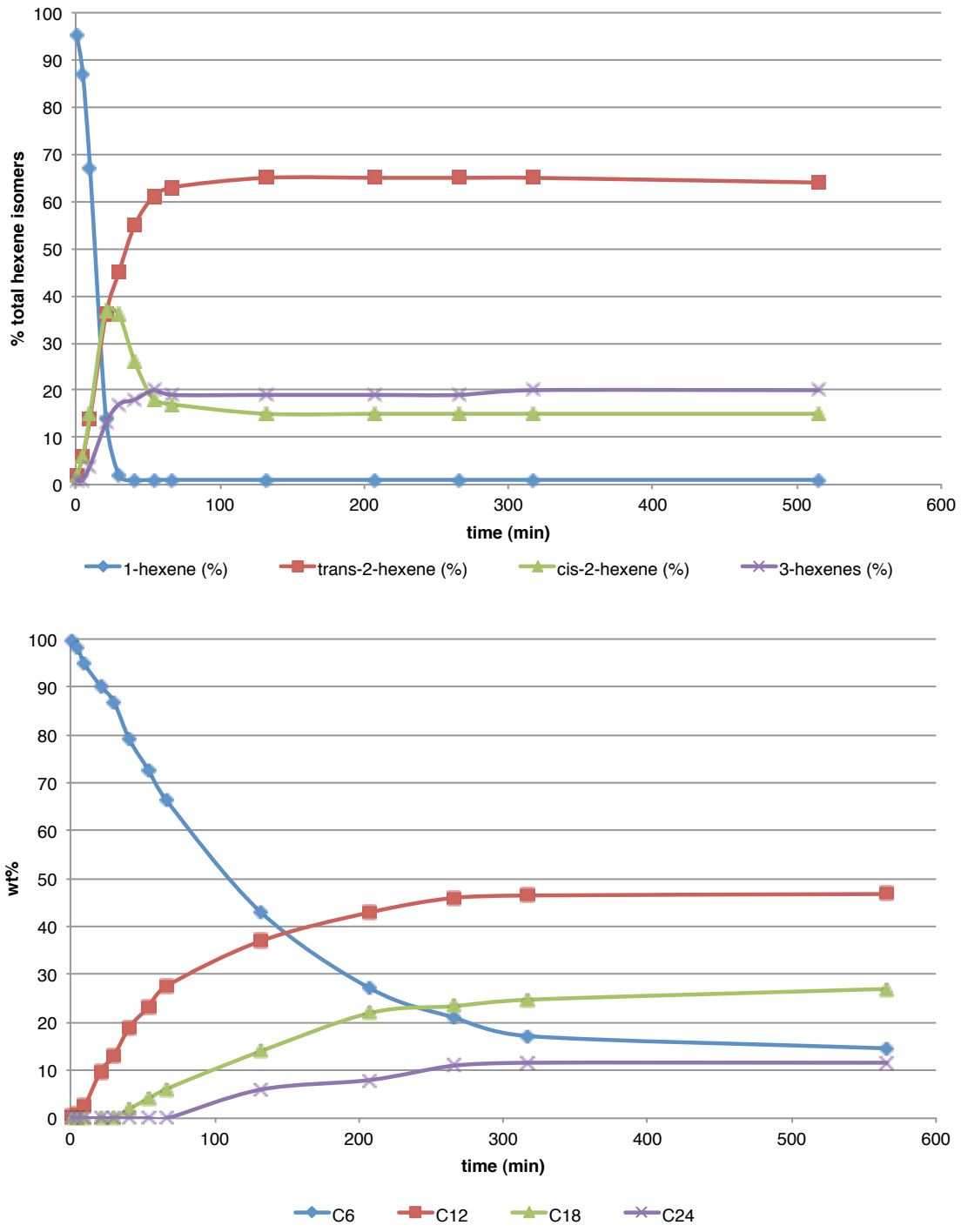

Figure 4.10. Isomerization (top) and oligomerization (bottom) of 1-hexene under 1 atm pure O_2 in dried solvent. Reaction conditions: 1-hexene (6.40 mmol), **4a** (0.1 mol%), CH_2Cl_2 (8 mL, degassed), TFE (4 mL, degassed), 4Å molecular sieves, adamantane (internal standard), O_2, rt

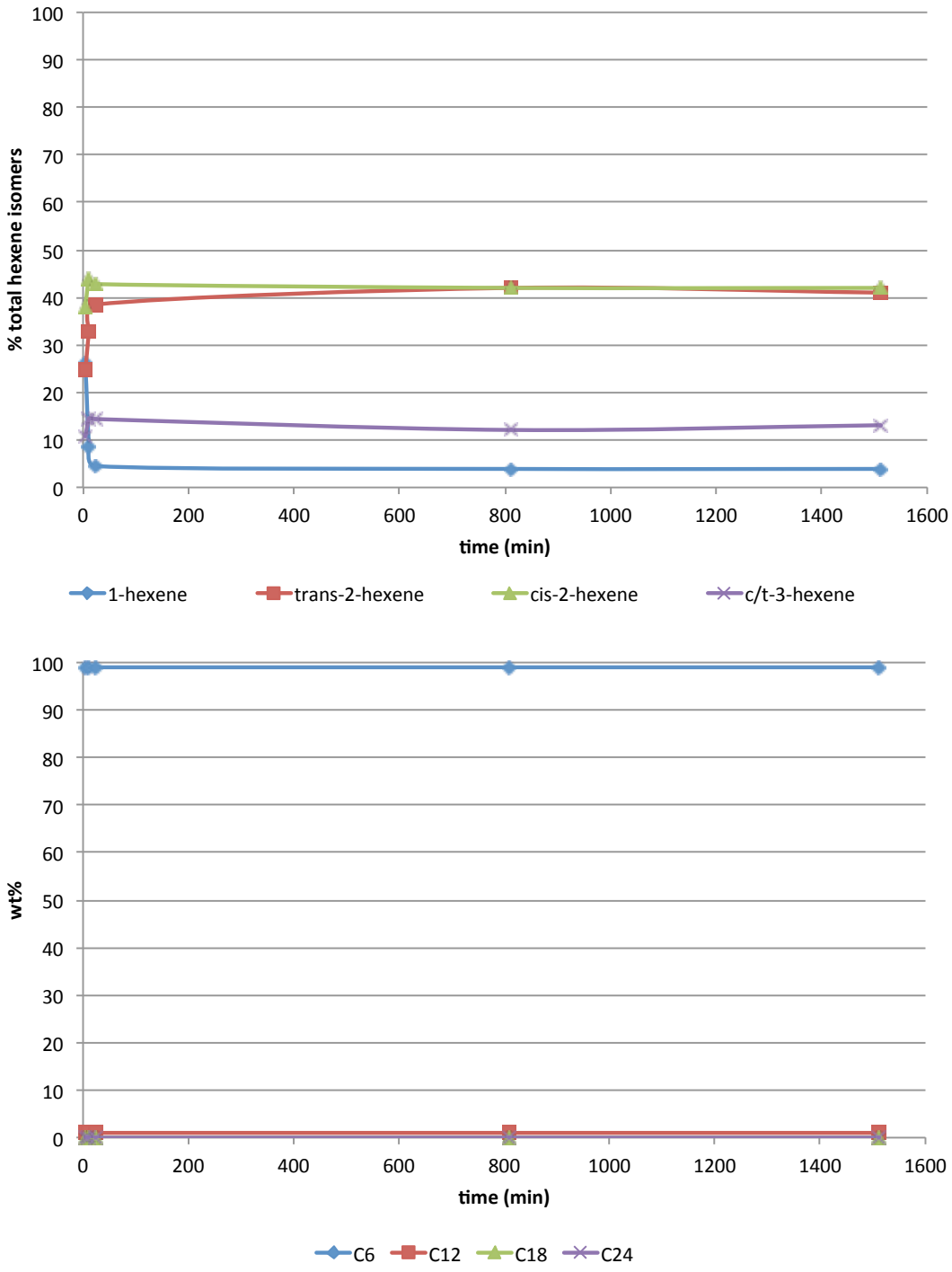

Figure 4.11. Isomerization (top) and oligomerization (bottom) of 1-hexene at 40 °C. Reaction conditions: 1-hexene (6.40 mmol), **4a** (0.1 mol%), CH_2Cl_2 (8 mL, degassed), TFE (4 mL, degassed), adamantane (internal standard), air, 40 °C

Precatalyst **4a** is stable in solution up to 100 °C. However, addition of olefin substrate at 40 °C results in significant precipitation to Pd black, suggesting that one or more post-activation species is temperature sensitive (Figure 4.11). It should be noted that almost all 1-hexene is consumed within 15 minutes, roughly representing more than a doubling in rate of hexene consumption. Oligomerized products are essentially undetectable, which suggests that the rate of isomerization is significantly increased relative to oligomerization rate. Thermodynamic ratios of hexene isomers are never achieved.

Due to discrepancies in the literature, a discussion of the thermodynamic ratio of linear hexene isomers is warranted. Previous reports have noted experimental distributions that differed substantially from thermochemically predicted values.[19-24] A variety of explanations have been offered to come to terms with this inconsistency, some more plausible than others. However, none consider the simplest explanation – the published thermodynamic data, based on theoretical values derived using group additivity methods, or experimental ΔH_f values (from measured heats of hydrogenation or hydration) combined with theoretical entropies, may be imprecise and unreliable. Our experimental results and those from several published papers are shown in Table 4.1 and compared to predicted values. That the experimental data agree amongst themselves, yet have been obtained using a range of catalysts and solvents, strongly suggests that the experimental values, not the predicted ones, correctly reflect the thermodynamic equilibrium ratios, and that the error involved in calculating distributions based on theoretical thermochemical values is simply too large to predict this particular system's thermodynamic isomer distribution with any accuracy.

Table 4.1. Predicted and observed thermodynamic distributions of linear hexene isomers.

1-hexene	*trans*-2-hexene	*cis*-2-hexene	3-hexenes	reference[a]
	---------- *predicted* ----------			
0.4%	35.8%	39.0%	24.8%	[18]
0.3%	36.5%	38.9%	24.3%	[19]
1%	47%	20%	32%	[20]
1.0%	51.2%	15.2%	32.5%	[21]
	---------- *observed* ----------			
1%	64%	15%	20%	this work
1.2%	61.4%	16.6%	20.8%	[22]
1-3%	60-67%	14-19%	16-20%	[23]
1.6%	57.6%	16.2%	25%	[24]

[a] **Reference (catalyst, solvent, temperature).** This work (**4a**, CH_2Cl_2:TFE, 25 °C); ref 23 (Pd/Cu, MeOH, 25 °C); ref 24 (Ni/Al, $PhCH_3$, 25 °C); ref 25 ($Fe_3(CO)_{12}$, neat 1-hexene, 63 °C reflux).

*1-Pentene Oligomerization and Isomerization Catalyzed by Dimer **4a***

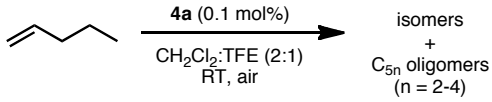

(8)

Treating 1-pentene with 0.1 mol% precatalyst **4a** under reaction conditions affords a thermodynamic mixture of linear pentene isomers (1% 1-pentene, 78% *trans*-2-pentene, 21% *cis*-2-pentene) and C_{5n} dimers, trimers and tetramers (eq. 8, Figure 4.12).

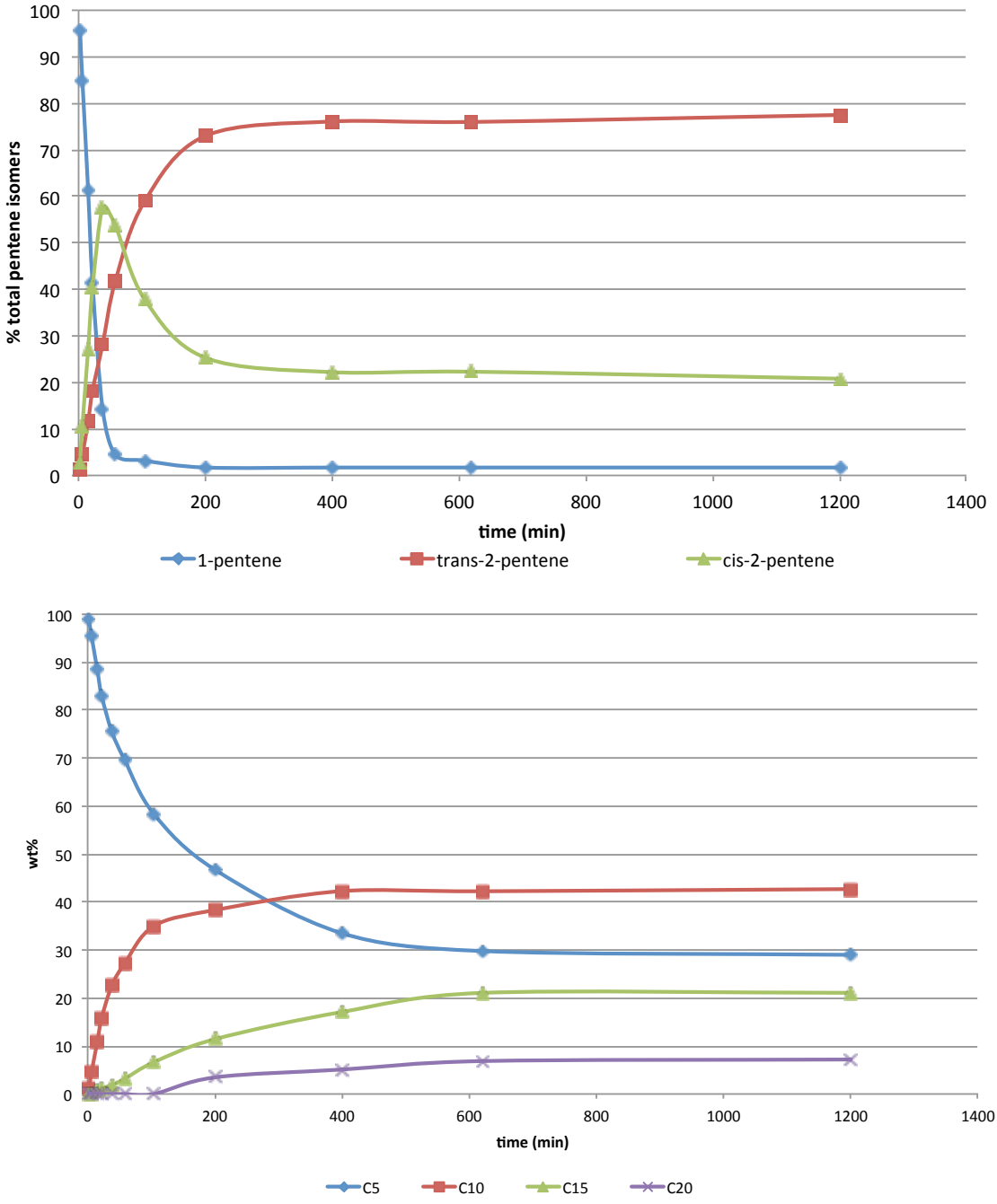

Figure 4.12. Isomerization/oligomerization profile for reaction of **4a** and 1-pentene. Reaction conditions: 1-pentene (6.40 mmol), 3a (0.1 mol%), 1,2-dichloroethane (8 mL), TFE (4 mL), adamantane (internal standard), air, rt

As with 1-hexene, the rates of consumption of 1-pentene and production of internal isomers appear constant in the first 20 minutes. The 1-pentene isomerization TOF (1100/h), which is only half that for 1-hexene, is likely only apparent and does not accurately reflect the actual TOF. On the other hand, the oligomerization TOF (500/h) is roughly 2.5 times larger than 1-hexene. This discrepancy between the pentene and hexene systems could presumably arise from a relatively faster rate of 1-pentene formation from 2- or 3-pentene (likely due to reduced sterics), compared to formation of 1-hexene from its isomers. Therefore, the (1-pentene):(total C_5) ratio will be higher than (1-hexene):(total C_6), However, if 1-pentene undergoes faster oligomerization than 1-hexene, then the total amount of pentene in solution may be less than that for 1-hexene. As with 1-hexene, the pentene oligomers fit a Schulz-Flory distribution (Figure 4.13).

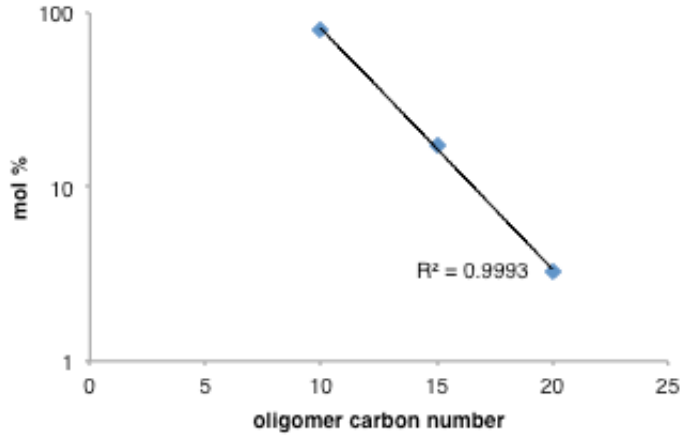

Figure 4.13. Schulz-Flory plot for pentene oligomer distribution (log(C_{5n} mol%) vs carbon number C_{5n})

Our observed thermodynamic distribution of linear pentene isomers agrees closely with the reported calculated values (1.6% 1-pentene, 72.1% *trans*-2-pentene,

26.2% *cis*-2-pentene).[25] Given the discrepancies of the experimental and predicted thermodynamic ratios of linear hexene isomers discussed above, this agreement must be viewed as simply a coincidence.

*Propylene Oligomerization and Isomerization Catalyzed by Dimer **4a***

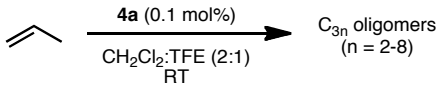

(9)

The reaction of propylene (1 atmosphere) with 0.1 mol% precatalyst **4a** under reaction conditions affords a mixture of branched C_6-C_{24} oligomers (eq. 9). Precatalyst **4a** oligomerizes propylene with a TOF of 600/h to afford a Schulz-Flory distribution that can be quantified by GC and fractional distillation (Figure 4.14).

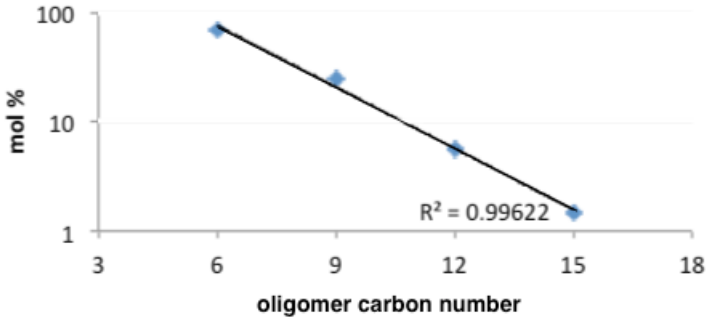

Figure 4.14. Schulz-Flory plot for propylene oligomer distribution (log(C_{3n} mol%) vs carbon number C_{3n}). Concentrations of oligomers larger than C_{18} could not be quantified due to poor signal-to-noise ratio in the GC trace.

*Ethylene Oligomerization and Isomerization Catalyzed by Dimer **4a***

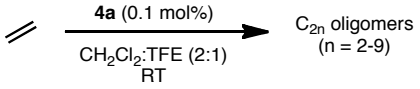

(10)

The reaction of ethylene (1 atmosphere) with 0.1 mol% dimer **4a** under reaction conditions affords a mixture of branched C_4-C_{18} oligomers (eq. 10). Precatalyst **4a** oligomerizes ethylene with a TOF of 600/h to afford a Schulz-Flory oligomer distribution that can be quantified by GC and fractional distillation (Figure 4.15).

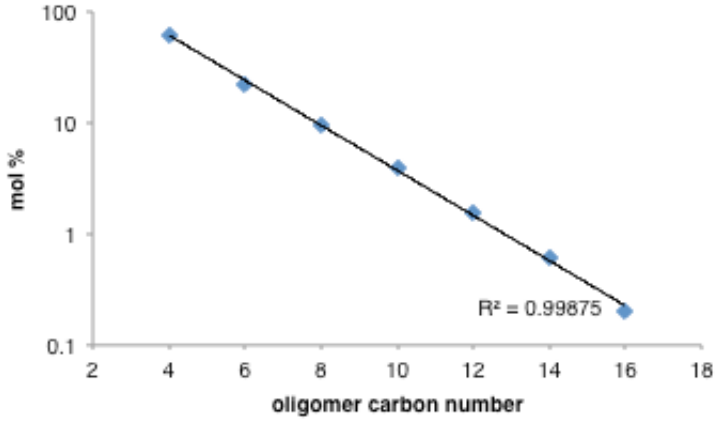

Figure 4.15. Schulz-Flory plot for ethylene oligomer distribution (log(C_{2n} mol%) vs carbon number C_{2n}). Concentrations of C_{20} oligomers could not be quantified due to poor signal-to-noise ratio.

*Mechanism of Isomerization and Oligomerization by Dimer **4a***

At the outset of these investigations, we envisioned two mechanisms by which precatalyst dimer **4a** could catalyze olefin isomerization and oligomerization. In light of the observed C-H activation behavior, we noted that allylic C-H activation of an olefin with loss of water could conceivably initiate oligomerization (Scheme 4.11). Dimer dissociation could presumably generate an olefin adduct (**19,** similar to indene-adduct **15**), which after C-H activation forms an η^3-allyl intermediate (**20**) and enters the catalytic cycle. **20** could coordinate monomer by alternating to the η^1-allyl coordination mode. After a sequence of monomer insertion/coordination events to grow the chain, chain transfer by C-H activation of monomer by a palladium(II) alkyl complex could regenerate **20.** If C-H activation to release water is reversible, the palladium(II) catalyst could potentially afford isomerized products from an η^1-allyl intermediate**.** Clearly, this mechanism is only operative for substrates with allylic C-H bonds. Alternatively, if **4a** could access a palladium(II) hydride (**3**), a catalytic cycle similar to that proposed by Brookhart could be in play (Figure 4.1). However, the route by which **4a** may activate to a hydride is not immediately obvious.

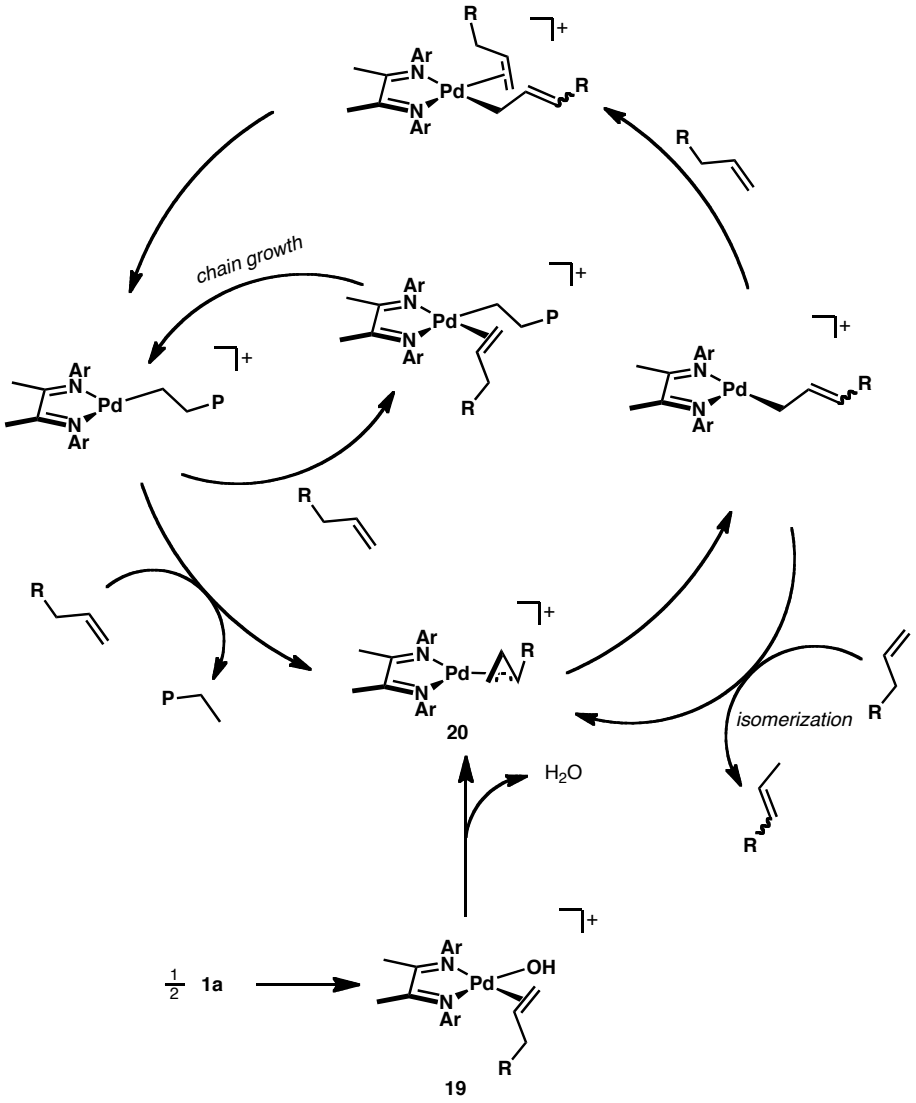

Scheme 4.11

Two observations seem to conclusively rule out the first mechanism. Ethylene, which does not have any allylic C-H bonds, obviously cannot undergo allylic activation, yet is readily oligomerized by precatalyst **4a** (eq. 10). To ensure that both mechanisms are not operative, the intermediate that would result from C-H activation of propylene was independently synthesized and subjected to reaction conditions (Scheme 4.12). Halide abstraction of **17a** generates bis(μ–chloro) dimer **21** in good yield, which can be taken to **22** upon treatment with allyltributylstannane. A non-refined solid-state structure of **22,** illustrated in Figure 4.16, is sufficient to establish connectivity.

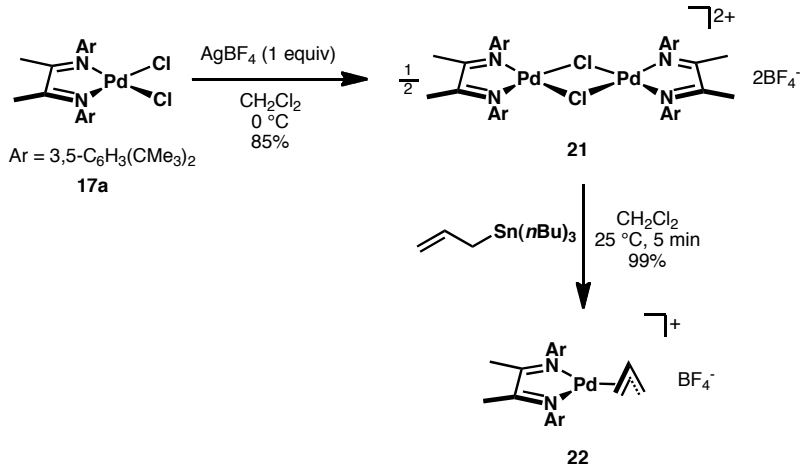

Scheme 4.12

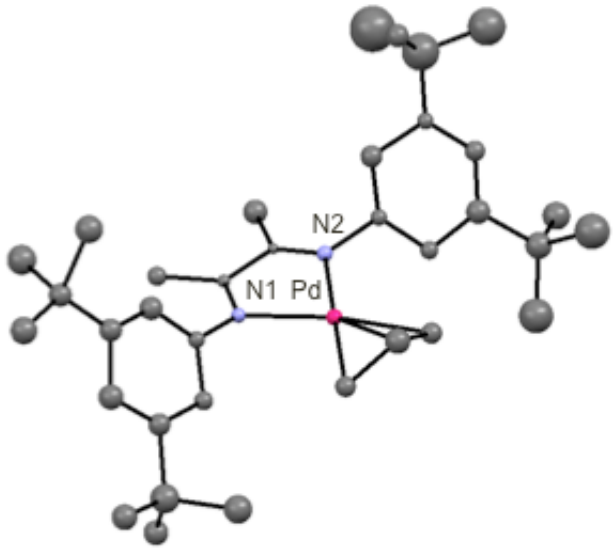

Figure 4.16. Isotropic, non-refined ball-and-stick depiction of [(^{t}BuDAB$_{Me}$)Pd(η^3-C_3H_5)](BF_4) (**22**). BF_4^- and all protons are omitted for clarity. Atoms are color coded: carbon (gray), nitrogen (blue), palladium (pink)

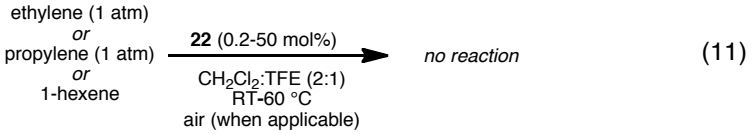

(11)

When ethylene, propylene, or 1-hexene are exposed to catalytic amounts of **22** under reaction conditions, neither isomerization nor oligomerization are observed by NMR or GC (eq. 11). In fact, there is no reaction with 50 mol% **22** at 60 °C**.** After three days heating, **22** can be quantitatively re-isolated. These results indicate that an oligomerization and isomerization mechanism involving monomer insertion into an allylic C-H activated product is not occurring, and that the reactions likely proceed through a palladium(II) hydride as illustrated in Figure 4.1, regardless of monomer.

*Activation Mechanisms of Dimer **4a***

For C_{4+} olefins, allylic C-H activation could presumably generate hydride **3** through β–hydride elimination and release of dehydrogenated product. Indeed, a small amount of linear hexadiene isomers can be detected by GC when 1-hexene is treated with precatalyst **4a**. Unexpectedly, though, about five times as much 2-hexanone is also formed (Figures 4.17 and 4.18). Under an ethylene atmosphere, acetaldehyde can be detected and quantified by VT-NMR against an internal standard (Figure 4.19). The presence of C-O bond containing products indicates a background palladium(II)-mediated Wacker oxidation. Palladium(II) hydrides have long been proposed as intermediates in these reactions,[26] but no reports to our knowledge have focused on exploiting the Wacer mechanism to access these potentially reactive hydrides. With either 1-hexene or ethylene, when 0.1 mol% dimer **4a** is used, roughly 0.2 mol% of oxidized product is detected; using 1 mol% **4a** results in 2 mol% oxidized product. That the total amount of oxidized products approximately equals the original amount of palladium(II) implies that activation of **4a** by reaction with olefin involves two distinct pathways: a C-H bond activation/dehydrogenation sequence, and a Wacker-like palladium(II)-mediated oxidation (Scheme 4.13).

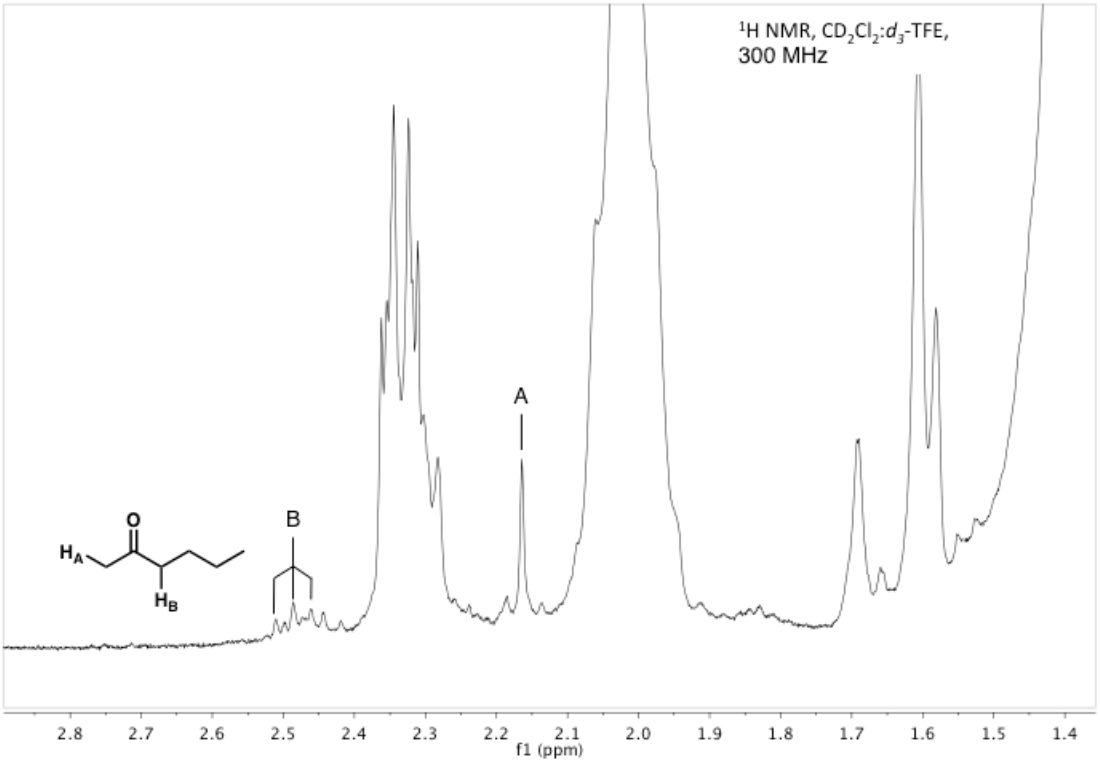

Figure 4.17. Selected region of ^{1}H NMR spectrum indicating presence of catalytic amounts of 2-hexanone after exposing 1-hexene to 0.1 mol% **4a** under reaction conditions for 1 hour. Total amount of 2-hexanone vs. 1-hexene (by GC) = 0.16 mol%.

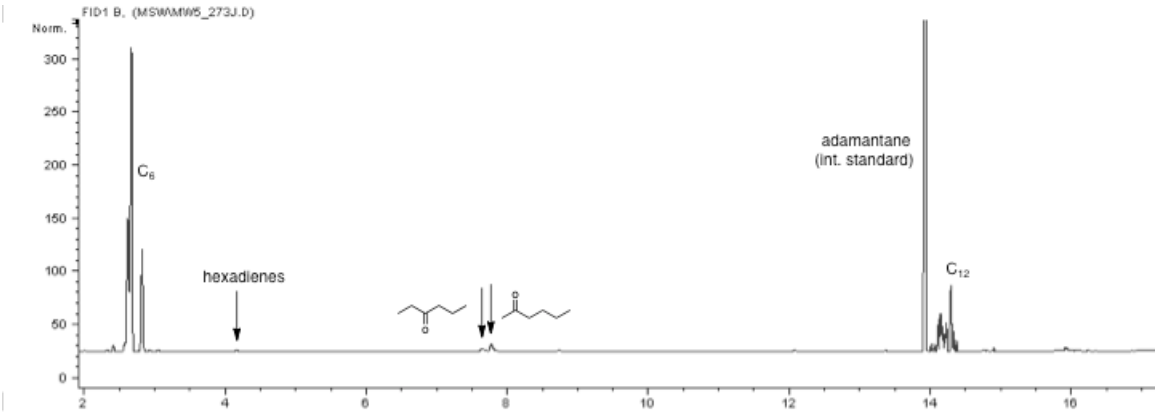

Figure 4.18. Selected region of GC trace indicating presence of oxidized C_6 products

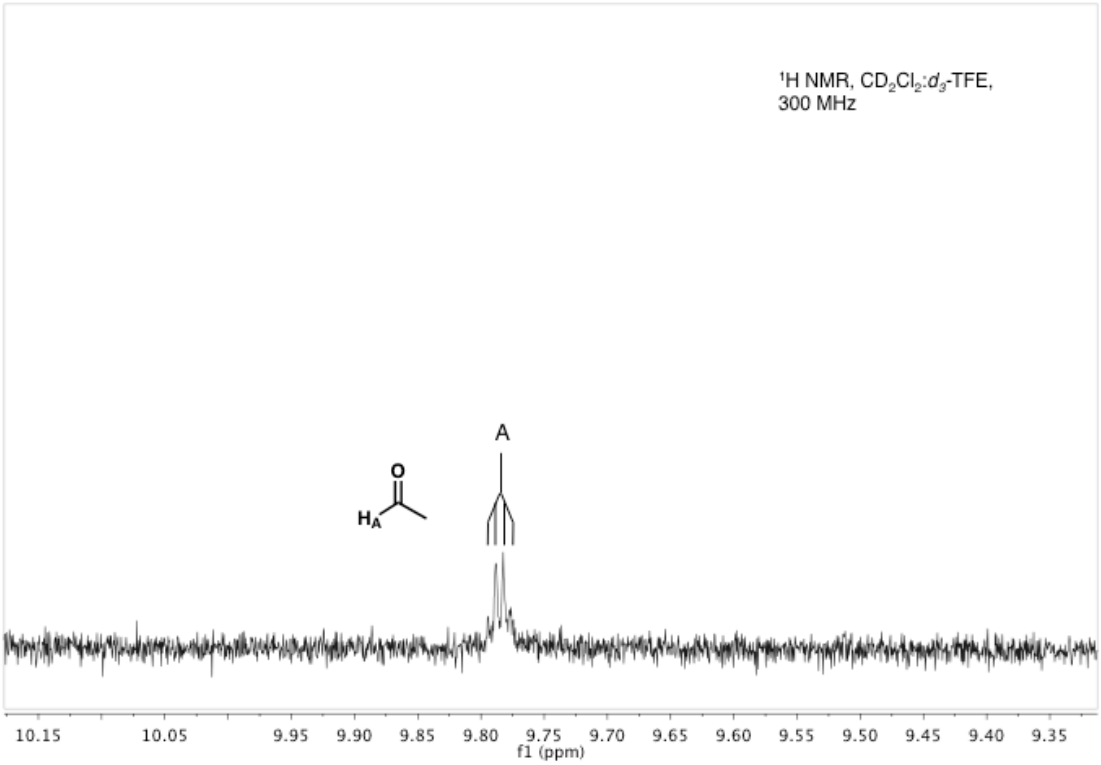

Figure 4.19. Selected region of ^{1}H NMR spectrum indicating presence of catalytic amounts of acetaldehyde after exposing ethylene (1 atm) to 0.1 mol% **4a** under reaction conditions for 1 hour. Total amount of acetaldehyde vs. ethylene (biphenyl NMR internal standard) = 0.23 mol%.

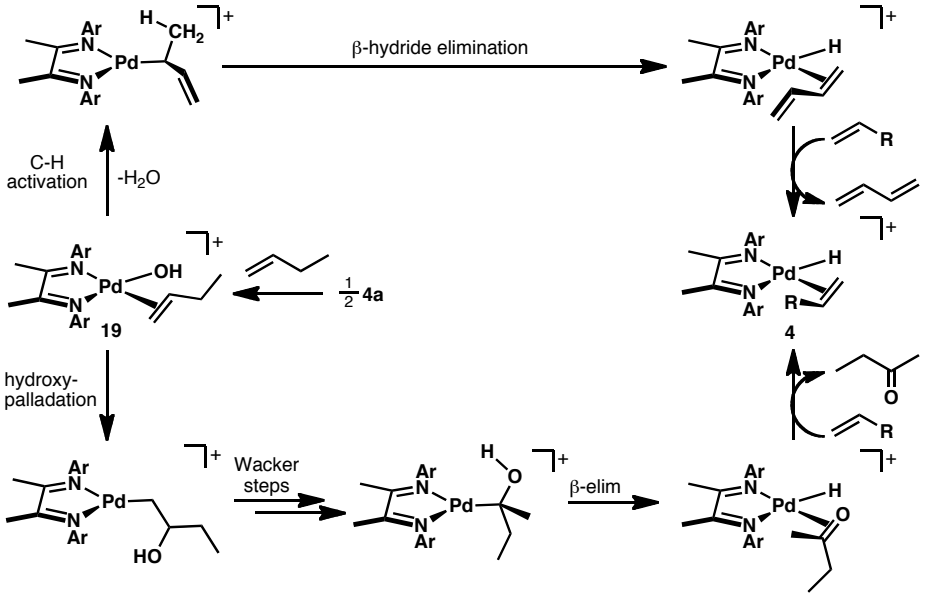

Scheme 4.13

The mechanism of olefin dehydrogenation is not entirely clear. β-Hydride elimination from an allylic C-H activated intermediate seems to be the most straightforward route, but two findings support some other, as yet undetermined, route. First, η^3-allyl complex **22** is completely unreactive at elevated temperatures; it obviously cannot undergo β-hydride elimination, but even small amounts of rearrangement to η^1-allyl coordination or monomer insertion are not observed. Second, and perhaps more convincingly, η^3-cyclohexenyl complex **23** (synthesis and solid-state structure is detailed in Appendix 3)**,** which *does* have β-hydrides, is also stable at elevated temperatures in the presence of monomer (eq. 12). Neither cyclohexadiene nor benzene are observed. Therefore, a C-H activated η^3-allyl intermediate is likely not involved in the olefin dehydrogenation activation pathway. If C-H activation directly generates a η^1-allyl

complex, clearly β-hydride elimination must be faster than rearrangement to the η^3-allyl species, which we have shown is likely irreversible.

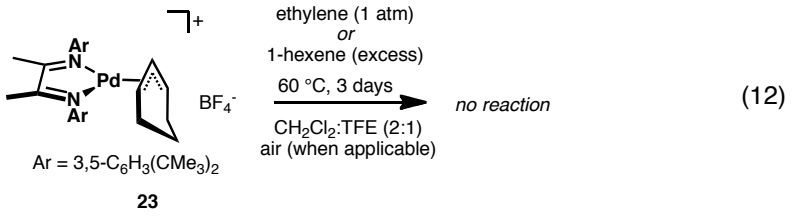

(12)

To support the feasibility of palladium(II)-mediated Wacker-type reactivity in these systems, metal-bound C-O bond containing products can be isolated and crystallographically and/or spectroscopically characterized. The reaction of **4a** with 1,3-butadiene in 2:1 CH_2Cl_2:TFE, for instance, results within minutes. Palladium(II) presumably coordinates and activates the diene toward attack by weakly nucleophilic TFE to generate 4-trifluoroethoxy-η^3-butenyl complex **24** (Scheme 4.14), the solid-state structure of which is shown in Figure 4.20.

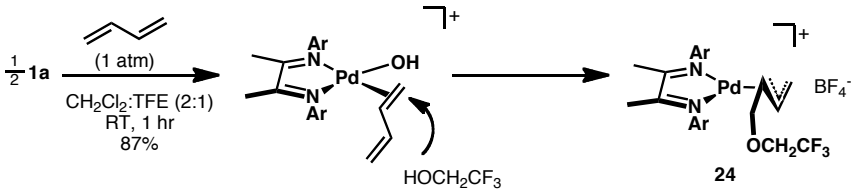

Scheme 4.14

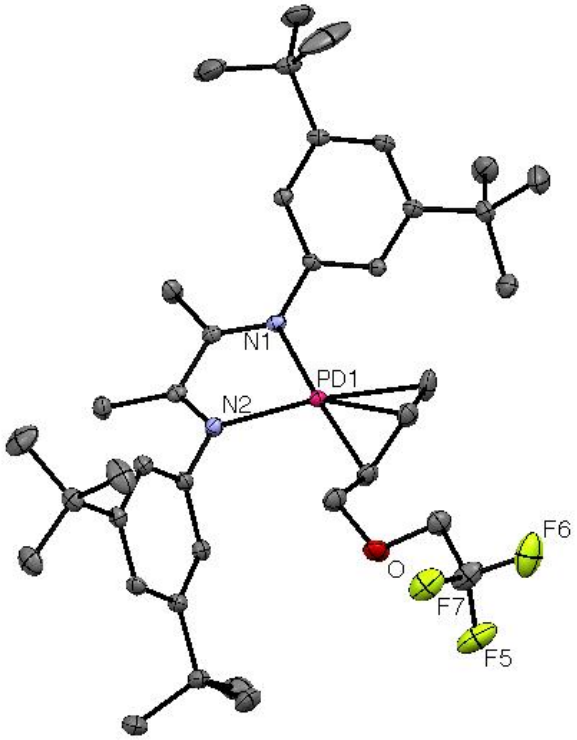

Figure 4.20. Thermal ellipsoid representation of [(^{tBu}DAB$_{Me}$)Pd(η^3-$C_4H_6OCH_2CF_3$)](BF$_4$) (**24**) at the 50% probability level. BF_4^- and all protons have been omitted for clarity. Atoms are color coded: carbon (gray), fluorine (yellow), nitrogen (blue), oxygen (red), palladium (pink)

The absence of trifluoroethyl enol ethers when monoolefin substrates are used (determined by ^{1}H and ^{19}F NMR and GC) suggests that catalyst initiation begins with intramolecular hydroxyl-palladation across the coordinated olefin, not nucleophilic attack by TFE. Even under dry conditions that preclude potential hydrolysis of a trifluoroethyl enol ether product, ketones are the only oxygenated products observed.

When **4a** is treated with excess ethylvinyl ether under reaction conditions, C_2-symmetric bis(μ-enolate) complex **25** is formed in moderate yield (Scheme 4.15). A

refined structure unfortunately cannot be obtained from crystals of the product, but a structure sufficient for establishing connectivity confirms that the dinuclear complex is bridged by two enolate fragments. We envision that hydroxyl-palladation across the ethylvinyl ether olefin may afford an unstable hemiacetal intermediate, which can eliminate EtOH and dimerize to **25**.

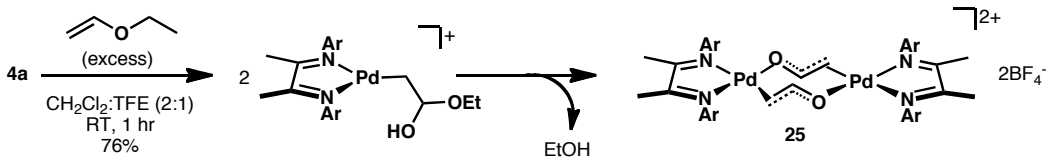

Scheme 4.15

Accessing a Catalytically Active Hydride from ($^{tBu}DAB_{Me}$)$PdMe_2$

In support of a mechanism involving a catalytically active palladium(II) hydride (**3**), we prepared the unreported $^{tBu}DAB_{Me}$-supported palladium(II) methyl cation (**2a**) via the method of Brookhart (Scheme 4.16).[6,7] (COD)$PdMe_2$ (COD = 1,5-cyclooctadiene) is treated with ligand $^{tBu}DAB_{Me}$ in Et_2O to provide dimethyl precursor **1a** in good yield. Protonolytic release of methane in the presence of 1 equivalent of acid generates methyl cation **2a.** This complex is generated in quantitative yield, with methane as the only other by-product; as such, the solution can be concentrated under vacuum and immediately dissolved in CH_2Cl_2 for oligomerization trials without further purification.

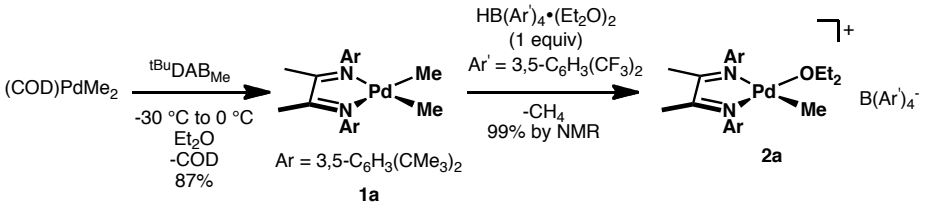

Scheme 4.16

Cation **2a** catalyzes the isomerization and oligomerization 1-hexene with a rate and product distribution almost identical to precatalyst **4a** (Figure 4.21). 1-Hexene is almost entirely consumed within the first half hour, while during this time, *cis*-2-hexene and *trans*-2-hexene concentrations increase at approximately equal rates. At about t = 30 minutes, when 1-hexene has reached its thermodynamic ratio relative to all other linear hexene isomers, *cis*-2-hexene is preferably consumed over *trans*-2-hexene. Thermodynamic ratios of all isomers are achieved by t = 80 minutes. As expected, the final thermodynamic ratio of linear hexenes is reached regardless of starting hexene isomer.

Since **4a** and **2a** likely access the same active palladium(II) hydride catalyst, and since there is no observable initiation period for **4a** upon comparing the isomer/oligomer traces between Figures 4.6 and 4.21, the rate of activation of dimer **4a** must be appreciably fast (comparable to the rate of displacement of Et_2O by 1-hexene in **2a.)** This is also suggested by the reaction of **2a** and 1,3-butadiene (Scheme 4.14), a reaction that requires dimer dissociation, but goes to completion within 5 minutes.

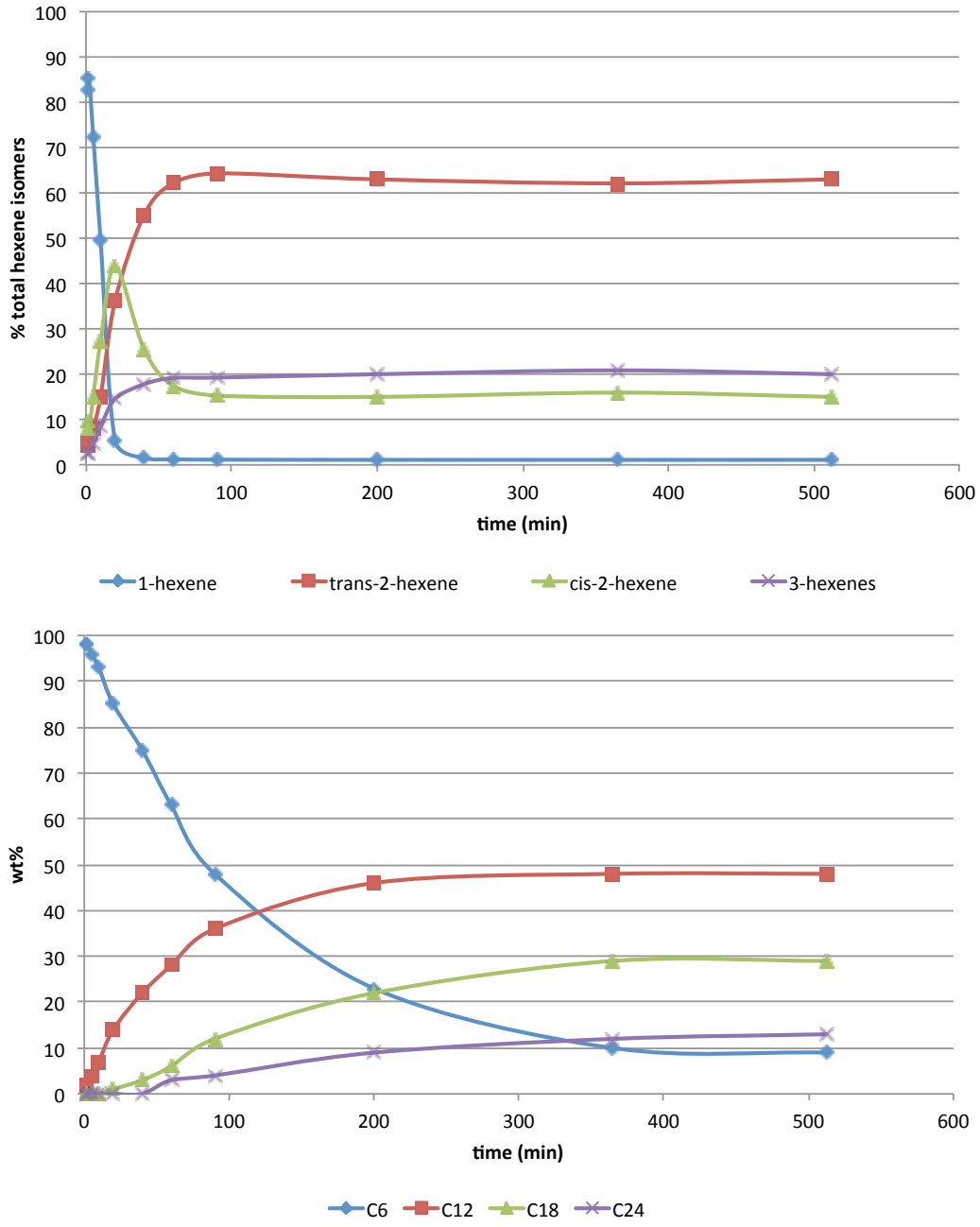

Figure 4.21. Isomerization (top) and oligomerization (bottom) of 1-hexene. Reaction conditions: 1-hexene (6.40 mmol), [(^{tBu}DAB$_{Me}$)Pd(Me)(OEt$_2$)][BAr'$_4$] (**2a,** Ar' = 3,5-$C_6H_3(CF_3)_2$) (0.2 mol%), CH_2Cl_2 (8 mL), TFE (4 mL), adamantane (internal gc standard), air, 25 °C

Role of TFE in Dimer Dissociation and Catalyst Longevity

The ^{1}H NMR spectrum of dimer **4a,** including the signal corresponding to the hydroxyl-bridge protons, is entirely unchanged in neat TFE in the absence of olefins, even at elevated temperatures (Figures 4.22).

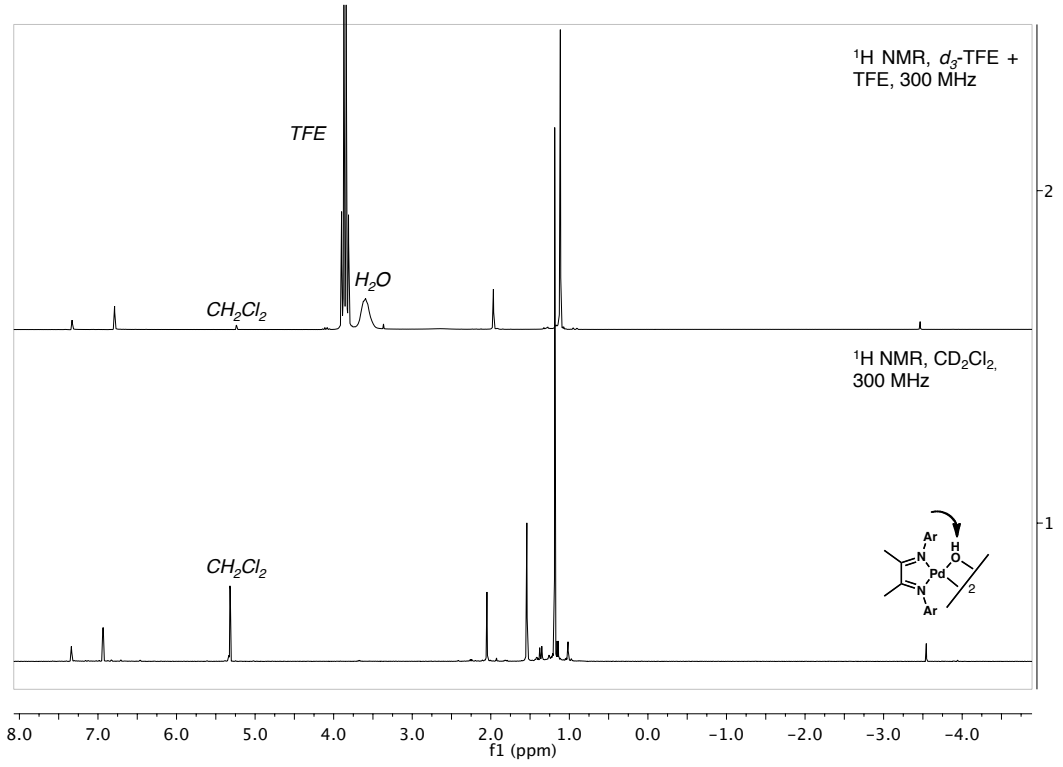

Figure 4.22. ^{1}H NMR of dimer **4a** dissolved in CD_2Cl_2 (bottom) and d_3-TFE/protio-TFE (top)

The reaction of **4a** with ethylene, propylene, or 1-hexene in the absence of TFE initiates on the order of days. This is perhaps unsurprising, given that C-H activation of indene with **4a,** a process that also requires dimer dissociation, takes 2 days in the absence of a nucleophilic co-solvent.[16] These observations suggest that the first steps of activation, including dimer dissociation, appear to require *both* TFE and olefin. Indeed, **4a** is stable at 40–60 °C in the presence of either TFE or olefin, but upon heating in the presence of both TFE *and* olefin, the dimer decomposes to palladium metal within 10 minutes.

One possible mechanism describing this dependence on TFE and monomer is illustrated in Scheme 4.17. Since ligand substitution in tetracoordinate (α-diimine)palladium(II) centers is an associative process,[6] we envision that axial coordination of olefin to one palladium(II) center in **4a** encourages cleavage of one μ-hydroxy bridge to afford an asymmetric mono-μ-hydroxy-bridged binuclear complex**.** Coordination of TFE can then induce cleavage of the second μ-hydroxy bridge, which generates solvento-adduct **2a** and olefin adduct **19.** As previously discussed, **19** can undergo hydroxy-palladation or C-H activation/β-hydride elimination to access a reactive palladium(II) hydride (**3**).

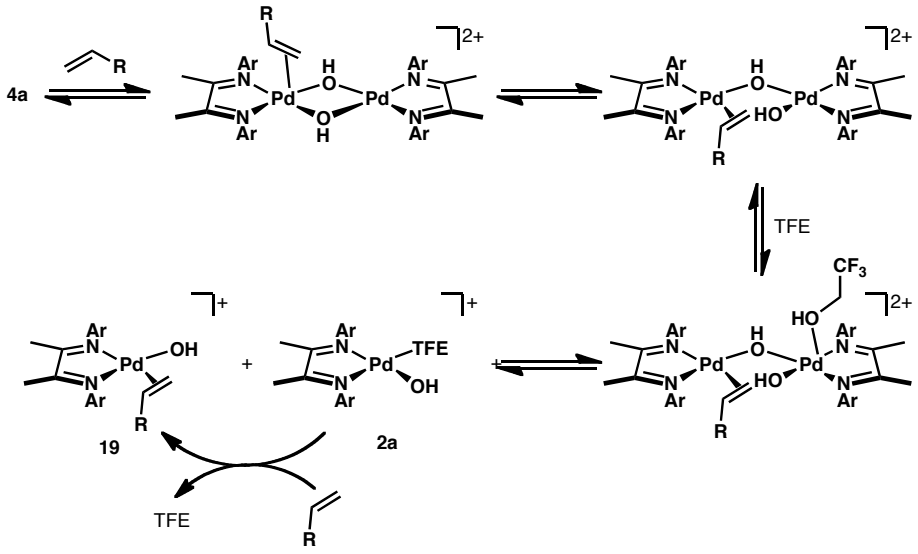

Scheme 4.17

In addition to assisting catalyst activation, TFE appears to stabilize one or more intermediates in the catalytic cycle. In the absence of TFE and olefin, palladium(II) methyl cation **2a** is relatively stable, but when olefin is added, significant decomposition to palladium metal is observed after an hour. The possibility that weakly acidic TFE simply protonates palladium(0) before aggregate formation is unlikely, since no deuterated products are formed by GC-MS or NMR when d^3-TFE is used as co-solvent (Scheme 4.18). Instead, TFE may simply stabilize one or more cationic palladium(II) intermediates by reversibly coordinating to the metal center. Further investigations are needed to determine the precise role TFE is playing.

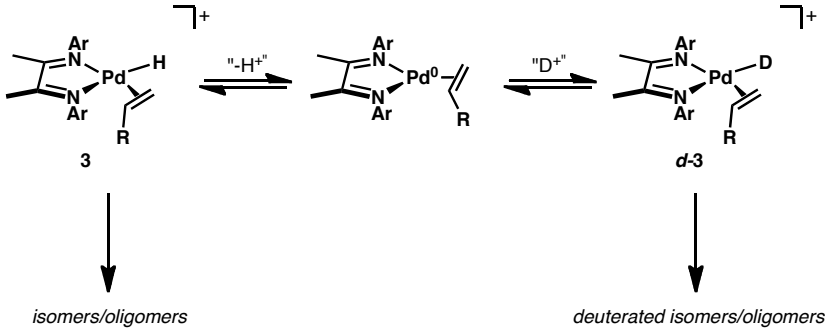

Scheme 4.18

Unlike TFE, more nucleophilic alcohols react directly with **4a** in the absence of olefin. With MeOH, an equilibrium heavily favoring dimer **4a** over what is likely bis(μ–methoxy) dimer **26a** is observed ($K_{eq} \sim 10^{-4}$, eq. 13). Each of these species can be observed in solution by titration of a CH_2Cl_2 solution of **4a** with MeOH, but the presumed asymmetrically bridged μ–hydroxy–μ–methoxy intermediate is never observed (Figure 4.23). Perhaps associative substitution by water or MeOH in this intermediate has a very low kinetic barrier, in which case the equilibrium constant does not accurately reflect the relative energies of **4a** and **26a**. More insight is clearly needed.

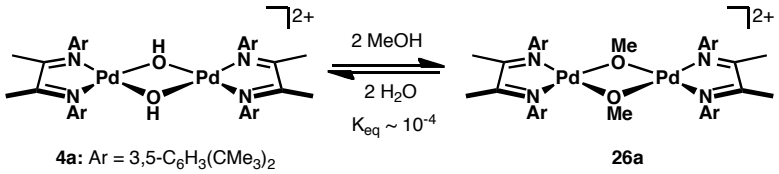

(13)

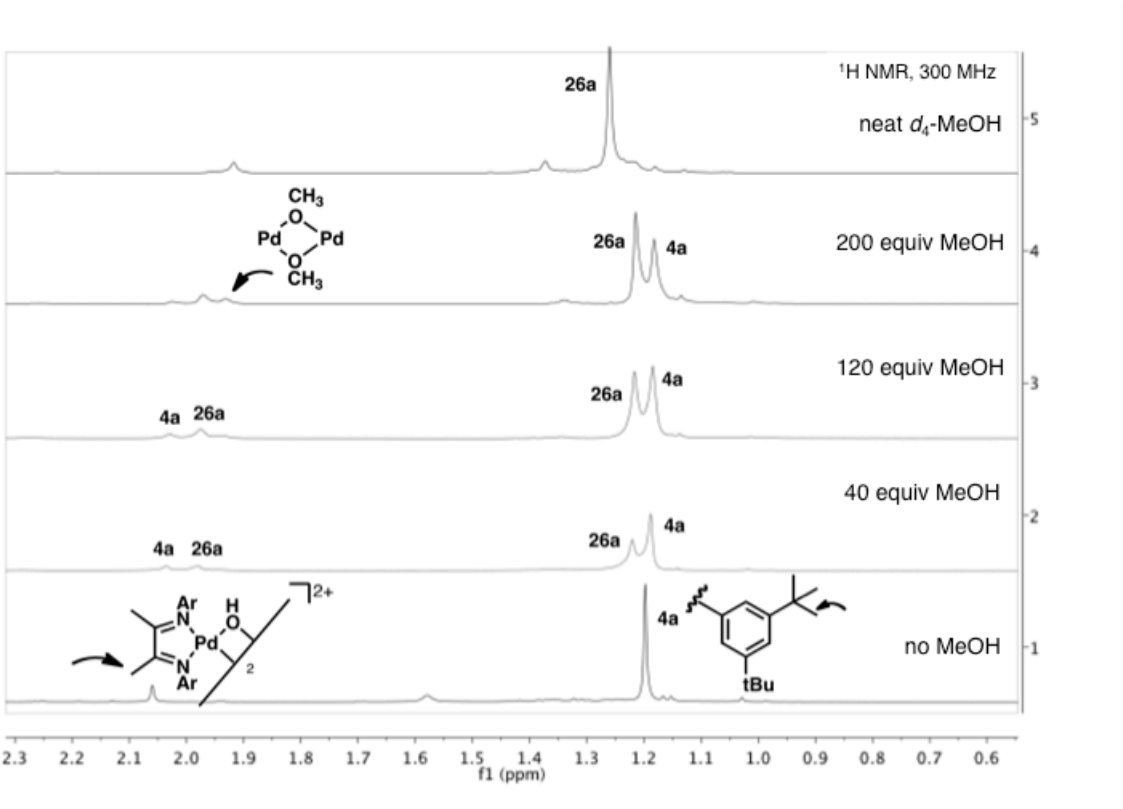

Figure 4.23. Selected region of ^{1}H NMR spectra over varying concentrations of MeOH

Addition of olefin substrates such as 1-hexene to a solution of bis(μ–methoxy) dimer **26** results in significant palladium metal deposition within minutes. Isomerized and oligomerized products *are* observed, however, indicating that **26a** is a precatalyst to an active palladium(II) hydride (**3**). In addition, under an ethylene atmosphere, small quantities of methylvinyl ether can be detected by NMR, although not quantified.

Methanol and ethanol-mediated decomposition of an intermediate in the catalytic cycle could involve a number of routes, only three of which are presented in Scheme 4.19: a coordination/β-hydride elimination sequence (pathway A) or Wacker-type C-O bond formation (pathways B and C). No ethers are detected by GC or NMR, suggesting

that the active catalyst does not decompose via pathways B or C, or via other similar C-O bond-forming processes. On the other hand, that the amount of formaldehyde or acetaldehyde generated in these reactions is comparable to the amount of added palladium supports an alcohol oxidation decomposition route similar to pathway A.

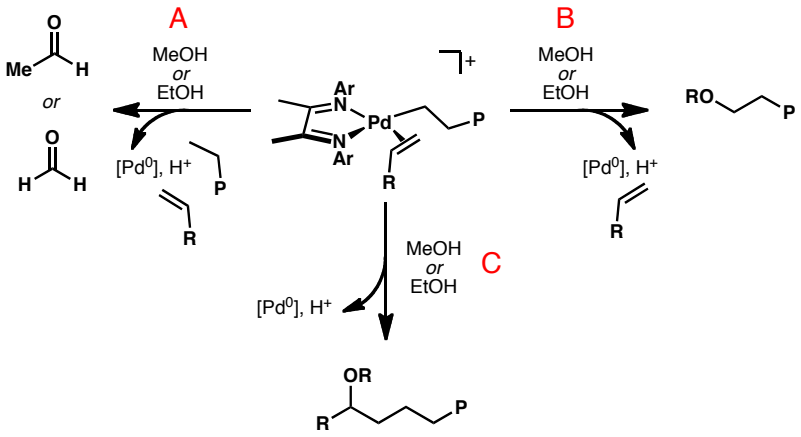

Scheme 4.19

Toward an Activator-Free Polymerization Catalyst

Ligand substitution in tetracoordinate (α-diimine)palladium(II) centers proceeds via an associative mechanism. As a consequence, complexes with bulky substituents at the *ortho*-positions of the α-diimine ligand aryl groups catalyze polymerization, rather than oligomerization; in these complexes, the axial face of the metal square plane is sterically blocked, inhibiting associative chain transfer relative to chain growth.

We prepared a bis(μ–hydroxy) dimer with such substituents, $[(^{iPr}DAB_{Me})Pd(OH)]_2(BF_4)_2$ (**4b**), in hopes of developing an activator-free polymerization catalyst capable of self-activating in the presence of olefin substrate. Synthesis of dimer **4b** is carried out via an analogous route to **4a** (Scheme 4.10). Likely due to the increased

steric bulk imparted by the *ortho iso*-propyl substituents on α-diimine ligand **16b**, a THF solvento-adduct could not be cleanly isolated upon treatment with silver(I). Instead, halide abstraction using a smaller co-solvent such as MeCN affords bis(acetonitrile) adduct $[(^{iPr}DAB_{Me})Pd(MeCN)_2][BF_4]_2$ (**18b**) in high yield, which is taken to **4b** under basic conditions in the presence of water.

To our surprise, dimer **4b** is unreactive toward ethylene, propylene, and 1-hexene, even at 80 °C (eq. 14). Furthermore, no reactivity was observed with 50 mol% **4b** (1:1 monomer:Pd). By NMR, the dimer remains intact and completely inert. Presumably, the steric effect of the 2,6-*iso*-propyl substituents blocks initial coordination of olefin and/or TFE needed to initiate catalyst activation (Figure 4.24). In fact, **4b** does not even undergo ligand exchange or dissociation in neat MeOH. Other small, nucleophilic co-solvents such as MeCN and H_2O also do not induce dissociation. Because an active catalyst is never accessed in the first place, **4b** (unlike **4a**) can be re-isolated after heating to 100 °C for 3 days in the presence of olefin and nucleophilic co-solvent.

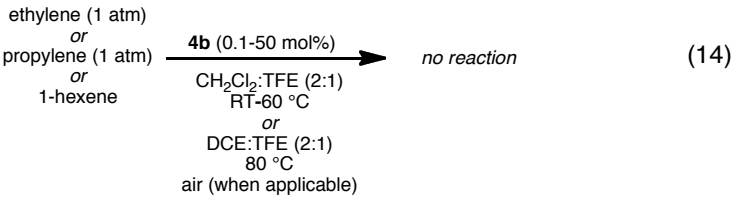

(14)

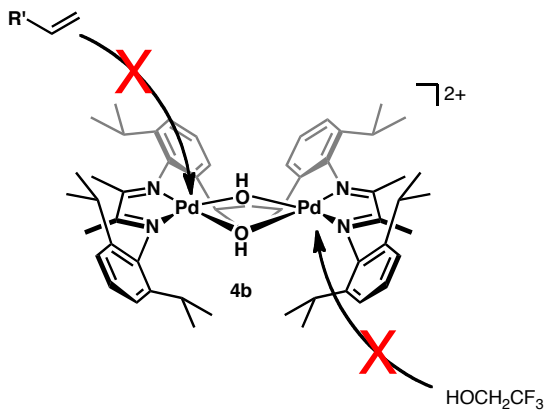

Figure 4.24. Bulky *ortho iso*-propyl substituents of **4b** block axial approach of olefin substrate and/or TFE to prevent dimer dissociation.

It should be mentioned that Feldman and coworkers have reported an activator-free polymerization of ethylene by the related $[(^{iPr}DAB_{Me})Pd(MeCN)_2](BF_4)_2$, but only at high pressures (20 atm), and with substantial inhibition by greater than trace amounts of water.[27] The mechanism of this system is not clear, although the authors suggest that the dicationic complex is sufficiently Lewis acidic to effect cationic polymerization.

Preliminary Studies and Reactivity of $[(^{Me}DAB_{Me})Pd(OH)]_2(BF_4)_2$

That catalyst activation depends on aryl ring substitution and steric bulk around the metal center prompted our investigation into other variously substituted bis((μ–hydroxy) palladium(II) dimers. We reasoned that α-diimine ligand **16c**, with 2,6-dimethyl substitution, may be sterically open enough to allow catalyst activation (if the precatalyst even activates via the same mechanism as **4a**), while maintaining polymerization behavior. Halide abstraction of dichloride **17c** by silver(I) in MeCN

affords acetonitrilo-adduct **18c**, which is immediately taken forward without purification to dimer **4c** under basic conditions in the presence of water (Scheme 4.20). This one-pot reaction proceeds in 40% yield over two steps.

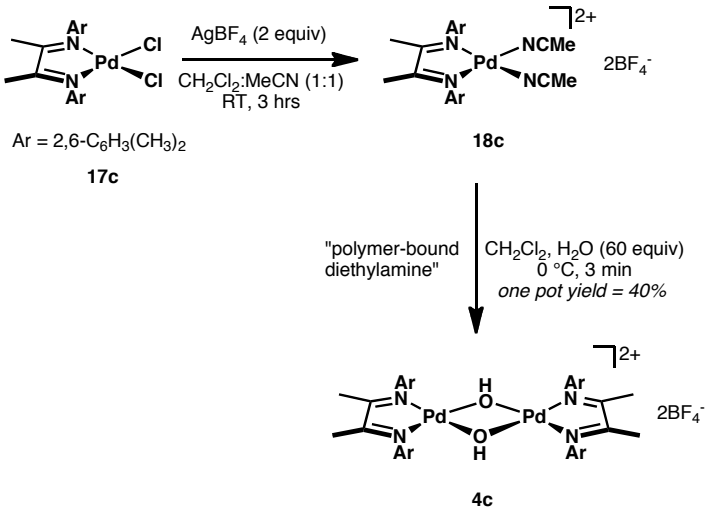

Scheme 4.20

Unlike **4a** and **4b**, dimer **4c** reacts with excess TFE at room temperature to establish an equilibrium with the asymmetrically bridged complex $[(^{Me}DAB_{Me})Pd(\mu\text{–}OH)(\mu\text{–}OCH_2CF_3)](BF_4)$ **(27)** ($K_{eq} \sim 10^{-2}$, eq. 15), which readily crystallizes. Unfortunately, the solid-state structure cannot be refined, but is sufficient to determine connectivity (Figure 4.25).

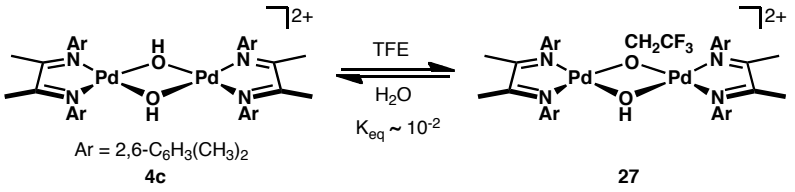

(15)

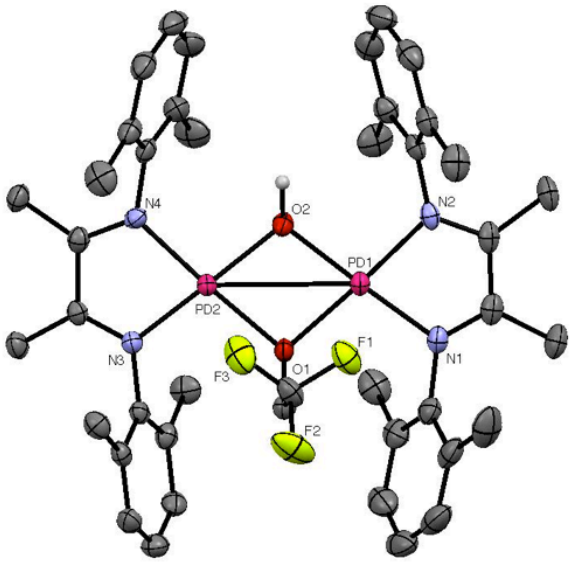

Figure 4.25. Thermal ellipsoid representation of [(^{Me}DAB$_{Me}$)Pd(μ–OH)(μ–OCH$_2$CF$_3$)](BF$_4$) (**27**) at the 50% probability level**.** Two BF_4^- anions and all protons except for OH are omitted for clarity. Atoms are color coded: carbon (gray), fluorine (yellow), nitrogen (blue), oxygen (red), palladium (pink)

Similar to **4a**, treating **4c** with excess MeOH results in an equilibrium between **4c** and symmetrically bridged bis(μ–methoxy) complex **26c** (K_{eq} ~ 10^{-1}, eq. 16). The non-refined solid-state structure of **26c** is illustrated in Figure 4.26.

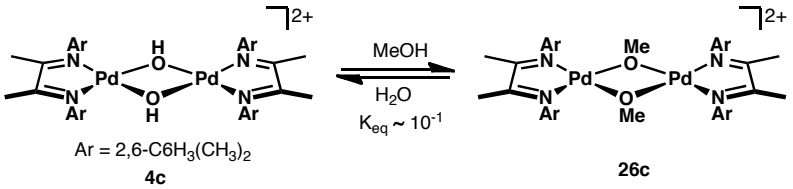

Ar = 2,6-C6H3(CH3)2

4c **26c** (16)

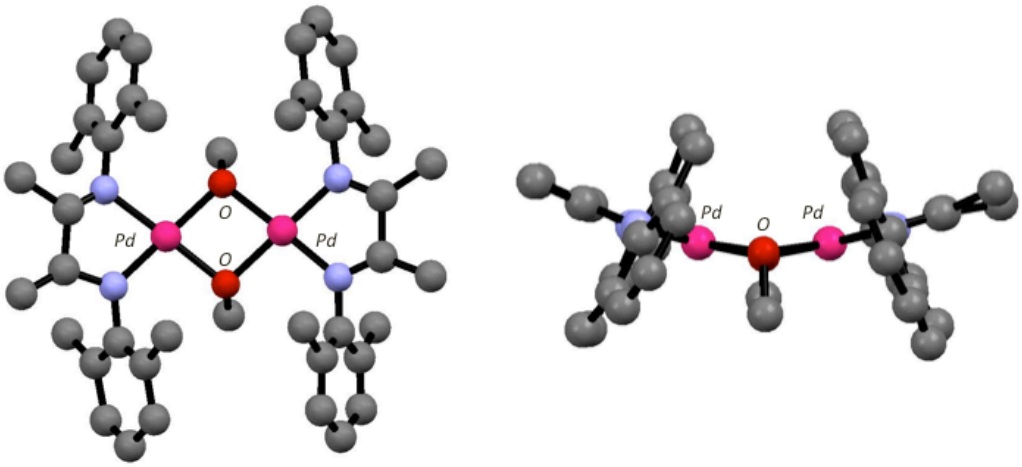

Figure 4.26. Isotropic, non-refined ball-and-stick top-down (left) and side-on (right) illustration of the solid-state structure of **26c.** Two BF_4^- anions and all protons are omitted for clarity. Atoms are color coded: carbon (gray), nitrogen (blue), oxygen (red), palladium (pink)

The reactivity of **4c** toward ligand substitution suggests that it may, at the very least, dissociate and potentially undergo activation under oligomerization/isomerization conditions. Complexes **4c, 26c,** and **27** catalyze the oligomerization of ethylene, but with TOFs of 10–20 h^{-1}. No polymer is observed, and substantial amounts of palladium metal are deposited after about 30 minutes in all cases. By GC and NMR, catalytic amounts of acetaldehyde or methylvinyl ether (depending on precatalyst) are detected. With all three precatalysts, the total amount of oxygenated products is of the same order of magnitude as the amount of added palladium. Further investigation is required to determine how the active catalyst decomposes. In addition, it must be determined whether **4c** dissociates faster than it reacts with TFE co-solvent to generate **27** under normal reaction conditions**.**

Olefin Oligomerization and Isomerization Reactivity of Analogous Platinum(II) Dimers

[^{tBu}DAB$_{Me}$Pt(OH)]$_2$(BF$_4$) (**11a**) was synthesized according to literature procedure,[15] but does not react with linear olefins. The dimer remains intact by NMR even at 60 °C. These studies are only preliminary, however. The effects of ligand and co-solvent on the behavior of these complexes is not fully understood.

CONCLUSIONS

Here we are able to access a reactive palladium(II) hydride from an air- and water- stable precursor, simply in the presence of substrate, without the need for any air- and water-sensitive activator or for careful exclusion of air and moisture. Mechanistic studies reveal that the active hydride catalyst is accessed via two oxidative transformations: C-H activation/β−hydride elimination and Wacker oxidation, the latter being approximately five times faster. Dimers with bulky *ortho iso*-propyl aryl substitution (**4b**) do not undergo dimer dissociation and activation, while those with less bulky *ortho* methyl aryl substitution (**4c**) can indeed activate, but the active species is not stable for prolonged periods of time. Future efforts will focus on screening small nucleophiles that can reversibly bind to palladium(II) to activate dimer **4b** to a potential olefin polymerization catalyst.

It is entirely possible that precatalysts **4a** or **4c** may polymerize ethylene under pressures greater than 1 atmosphere. Therefore, future investigations will focus on the behavior of the active hydride catalysts under such conditions. The reactivity of precatalysts supported by α−diimine ligands with electron-withdrawing substituents will

also be investigated. Further studies on the scope of these oligomerization and isomerization reactions, as well as extension to other catalyzed transformations, are continuing.

EXPERIMENTALS

General Considerations and Instrumentation. All air- and moisture-sensitive compounds were manipulated using standard high vacuum and Schlenk techniques or in a glovebox under a nitrogen atmosphere using degassed solvents. Where dry solvents were needed, TFE was stirred over $CaSO_4$ for 2 days and distilled; all other solvents were dried by the method of Grubbs.[28] All NMR solvents were purchased from Cambridge Isotopes; $(PhCN)_2PdCl_2$ and $AgBF_4$ were purchased from Strem Chemical; polymer-bound diethylamine was purchased from Sigma-Aldrich. All chemicals, unless otherwise noted, were used as received. 1,4-bis(3',5'-di-*tert*-butylphenyl)-2,3-dimethyl-1,4-diaza-1,3-butadiene ($^{tBu}DAB_{Me}$),[8b] 1,4-bis(2',6'-di-*iso*-propylphenyl)-2,3-dimethyl-1,4-diaza-1,3-butadiene ($^{iPr}DAB_{Me}$),[6] ($^{tBu}DAB_{Me}$)$PdCl_2$ (**17a**),[8h] (COD)$Pd(CH_3)_2$ (COD = 1,5-cyclooctadiene),[29] $H(Et_2O)_2BAr'_4$ (Ar' = 3,5-$(CF_3)_2$-C_6H_3),[30] and $(MeCN)_2PdCl_2$[31] were prepared according to literature procedures. ^1H, ^{13}C, and ^{19}F NMR spectra were recorded on Varian Mercury 300 or Varian INOVA-500 spectrometers at room temperature, unless otherwise indicated. The data are reported by chemical shift (ppm) from tetramethylsilane, multiplicity (s, singlet; d, doublet; t, triplet; m, multiplet; dd, double doublet; dt, double triplet), coupling constants (Hz), and integration. All ^{13}C NMR data were collected proton-decoupled ($^{13}C\{^1H\}$), except where specified. Mass spectra were

acquired on a Finnigan LCQ ion trap or Agilent 5973 Network mass selective detector and were obtained by peak matching.

[(^{tBu}DAB$_{Me}$)Pd(thf)$_2$](BF$_4$)$_2$ (18a). An oven-dried 1 L round-bottom flask equipped with a stir bar was charged with 1 (15.9 g, 25.0 mmol, 1.00 equiv). Dry CH_2Cl_2 (400 mL) and THF (200 mL) were added via syringe. $AgBF_4$ (9.74 g, 51.3 mmol, 2.05 equiv) dissolved in CH_2Cl_2 (100 mL) was added over two minutes to the stirring yellow suspension, during which AgCl precipitated and the suspension turned orange. The reaction was stirred for 3 hours at room temperature, then filtered through Celite and concentrated *in vacuo* to afford **18a** as a bright orange powder (18.8 g, 21.3 mmol). ^{1}H NMR (500 MHz, CD_2Cl_2, 298 K) δ: 1.36 (s, 44H), 2.19 (s, 6H), 3.66 (br s, 8H), 7.56 (t, J = 1.6 Hz, 4H), 7.60 (d, J = 1.6 Hz, 2H). ^{13}C NMR (125 MHz, CD_2Cl_2, 298 K) δ: 20.6, 24.7, 31.5, 35.8, 73.9, 117.3, 124.1, 144.0, 154.3, 186.0. Anal. Calcd for $C_{40}H_{64}B_2F_8N_2O_2Pd_2$: C, 54.29; H, 7.29; N, 3.17. Found: C, 54.35; H, 7.45; N, 3.30.

[(^{tBu}DAB$_{Me}$)Pd(OH)]$_2$(BF$_4$)$_2$ (4a). A 500 mL round-bottom flask was equipped with a stirbar and charged with 2 (12.6 g, 14.2 mmol, 1.00 equiv). CH_2Cl_2 (200 mL) was added via syringe. The suspension was cooled to 0 °C and stirred for 5 minutes. H_2O (15.3 g, 852 mmol, 60 equiv) was added with vigorous stirring at 0 °C. Polymer-bound diethylamine (25.0 g, 31.2 mmol, 2.20 equiv) was added portionwise at 0 °C. The suspension was stirred for 3 minutes and filtered through Celite, which was washed with 1:1 CH_2Cl_2:THF until no more colored material eluted. The yellow solution was concentrated *in vacuo* to afford **4a** (7.62 g, 5.68 mmol) as a yellow powder. Spectroscopic and analytic properties match those previously reported.[16] Anal. Calcd for $C_{64}H_{98}B_2F_8N_4O_2Pd_2$: C, 57.28; H, 7.36; N, 4.18. Found: C, 57.31; H, 7.50; N, 4.02.

[(^{tBu}DAB$_{Me}$)PdCl]$_2$(BF$_4$)$_2$ (21). An oven-dried 250 mL round-bottom flask equipped with a stirbar was charged with dichloride 1 (110 mg, 0.172 mmol, 1.00 equiv), which was dissolved in dry CH_2Cl_2 (35 mL) and cooled to 0 °C. A solution of $AgBF_4$ (33.5 mg, 0.172 mmol, 1.00 equiv) in 100:1 CH_2Cl_2:THF (5 mL) was added dropwise at 0 °C. The solution darkened slightly to orange. After addition, the reaction was warmed gradually to room temperature and stirred for 6 hours. The reaction was filtered through Celite and concentrated *in vacuo* to afford **21** (101 mg, 0.159 mmol) as a bright orange powder. ^{1}H NMR (500 MHz, TFE-d_3, 298 K) δ: 1.23 (s, 36H), 2.09 (s, 6H), 6.87 (d, J = 1.5 Hz, 4H), 7.51 (br s, 2H). ^{13}C NMR (125 MHz, CD_2Cl_2, 298 K) δ: 21.1, 32.0, 36.6, 118.0, 125.9, 145.0, 155.4, 186.0. Anal. Calcd for $C_{64}H_{96}B_2Cl_2F_8N_4Pd_2$: C, 55.75; H, 7.02; N, 4.06. Found: C, 56.01; H, 7.01; N, 4.03.

[(^{tBu}DAB$_{Me}$)Pd(η^3-C$_3$H$_5$)](BF$_4$) (22). A 20 mL vial equipped with a stirbar was charged with dimer 4 (50.0 mg, 0.0360 mmol, 1.00 equiv). CH_2Cl_2 (2 mL) was added via syringe. While stirring, allyltributyltin (26.2 mg, 0.0792 mmol, 2.20 equiv) was added. The bright orange suspension immediately became a yellow solution. Stirring was continued for 5 minutes. The reaction was concentrated *in vacuo* to afford a yellow powder. Tin-containing byproducts were removed by washing with Et_2O (5 mL) and hexanes (5 mL x 2) to afford **22** as a yellow powder (49.7 mg, 0.072 mmol). ^{1}H NMR (500 MHz, CD_2Cl_2, 298 K) δ: 1.35 (s, 36H), 2.37 (s, 6H), 3.20 (d, J = 12.7 Hz, 2H), 3.39 (d, J = 7.0 Hz, 22.9 Hz, 2H), 5.71 (tt, J = 7.1 Hz, 12.8 Hz, 1H), 6.96 (br s, 4H), 7.39 (t, J = 1.6 Hz, 2H). ^{13}C NMR (125 MHz, CD_2Cl_2, 298 K) δ: 20.3, 31.6, 35.6, 65.3, 115.4, 120.7, 122.1, 149.2, 153.2, 176.8. HRMS (FAB+) $C_{35}H_{53}N_2Pd$ (5-BF_4)$^+$: calcd mass 607.3244, measured mass 607.4031.

[(^{tBu}DAB$_{Me}$)Pd(η^3-cyclohexenyl)](BF$_4$) (23). For synthesis and spectroscopic details, see Appendix 3.

[(^{tBu}DAB$_{Me}$)Pd(η^3-(C$_3$H$_4$)CH$_2$OCH$_2$CF$_3$)](BF$_4$) (24). A 100 mL Schlenk flask equipped with a stirbar was charged with dimer **3** (110 mg, 0.0820 mmol). CH_2Cl_2 (17 mL) and TFE (3 mL) was added via syringe to afford a yellow solution, which was degassed by two freeze-pump-thaw cycles. The evacuated flask was back-filled with 1 atm of 1,3-butadiene, and the resulting yellow solution was stirred for 1 hour to ensure complete conversion. No color change was observed. The reaction was concentrated *in vacuo* to afford a yellow-orange powder. Washing with cold hexane afforded **24** (115 mg, 0.143 mmol) as a yellow powder. ^{1}H NMR (500 MHz, CD_2Cl_2, 298 K) δ: 1.35 (s, 18H), 1.36 (s, 18H), 2.33 (s, 3H), 2.35 (s, 3H), 2.55 (dd, J = 3.1 Hz, 12.2 Hz, 1H), 2.75 (dd, J = 6.7 Hz, 12.3 Hz), 3.31-3.50 (m, 4H), 3.58-3.66 (m, 1H), 5.56-5.66 (m, 1H), 6.75-6.89 (br s, 1H), 6.98 (br s, 2H), 7.04-7.18 (br s, 1H), 7.37 (t, J = 1.7 Hz, 2H), 7.41 (t, J = 1.7 Hz, 4H). ^{13}C NMR (125 MHz, CD_2Cl_2, 298 K) δ: 20.1, 20.3, 31.6, 35.6, 35.7, 67.2, 68.8 (q, J_{C-F} = 34.3 Hz), 70.2, 74.6, 114.6, 115.3, 118.2, 121.8, 122.0, 124.2 (q, J_{C-F} = 279.3 Hz), 125.3, 148.3, 149.3, 153.2, 176.7, 178.2. HRMS (FAB+) $C_{38}H_{56}F_3N_2OPd$ (**8**-BF$_4$)$^+$: calcd mass 719.3380, measured mass 719.3420.

[(^{tBu}DAB$_{Me}$)Pd(μ-C$_2$H$_3$O)]$_2$(BF$_4$) (25). An oven-dried 250 mL round-bottom flask equipped with a stirbar was charged with precatalyst **4b** (80 mg, 0.060 mmol, 1 equiv). Dry CH_2Cl_2 (80 mL) was added via syringe, followed by dry TFE (40 mL). At room temperature, dry ethylvinyl ether (432 mg, 6.00 mmol, 100 equiv) was added via syringe, and the reaction was stirred under argon for 1 hour. There is no color change. The volatiles are removed *in vacuo* and the yellow oil dissolved in CH_2Cl_2 (1 mL) and

triturated with petroleum ether (10 mL). The yellow solid is collected on a frit, washed with cold Et_2O (5 mL) and dried *in vacuo,* then dissolved in CH_2Cl_2 (1 mL) and crystallized by slow evaporation to afford **25** as small yellow crystals (64 mg, .046 mmol). ^{1}H NMR (300 MHz, CD_2Cl_2, 298 K) δ: 1.23 (s, 36 H), 1.32 (s, 36 H), 1.89 (m, 2H), 2.10 (s, 6 H), 2.19 (s, 6 H), 2.91 (dd, J = 2.2 Hz, 10.4 Hz, 2 H), 6.84 (t, J = 1.7 Hz, 2H), 7.06 (t, J = 1.7 Hz, 2H), 7.18 (t, J = 1.7 Hz, 4H), 7.30 (m, 2H), 7.33 (t, J = 1.7 Hz, 2H).

(^{tBu}DAB$_{Me}$)Pd(CH$_3$)$_2$ (1a). An oven-dried 100 mL round-bottom flask equipped with a stirbar was charged with (COD)Pd(CH_3)$_2$ (129 mg, 0.526 mmol, 1.00 equiv) and cooled to -30 °C. Et_2O (30 mL) was added via syringe to form a white suspension. ^{tBu}DAB$_{Me}$ (267 mg, 0.579 mmol, 1.10 equiv) was dissolved in Et_2O (12 mL) and added dropwise to the cool solution via syringe. The reaction darkened to orange and remained a suspension. Upon warming to 0 °C, the solution became a red slurry, which was stirred for 3.5 hours. The reaction was filtered through a frit to afford **1a** as a dark red solid (273 mg, 0.458 mmol). ^{1}H NMR (500 MHz, CD_2Cl_2, 298 K) δ: -0.27 (s, 6H), 1.35 (s, 36H), 2.06 (s, 6H), 6.73 (d, J = 1.7 Hz, 4H), 7.28 (t, J = 1.7 Hz, 2H). ^{1,3}C NMR (125 MHz, CD_2Cl_2, 298 K) δ: -5.4, 20.0, 31.6, 35.4, 115.8, 119.8, 147.5, 152.1, 170.0. HRMS (FAB+) $C_{34}H_{54}N_2Pd$ 6^+: calcd mass 597.3322, measured mass 597.3520.

[(^{tBu}DAB$_{Me}$)Pd(CH$_3$)(Et$_2$O)](BAr$_4$) (Ar = 3,5-(CH$_3$)$_2$-C$_6$H$_3$) (2a). To an oven-dried J. Young NMR tube was added **6** (40.0 mg, 0.0670 mmol, 1.00 equiv) and H(Et_2O)$_2$BAr$_4$ (Ar = 3,5-(CF_3)$_2$$C_6H_3$) (67.2 mg, 0.0663 mmol, 0.990 equiv). The tube was evacuated, and dry Et_2O (500 μL) was vacuum transferred onto the solids at -78 °C. The tube was slowly warmed to 0 °C in an ice bath, during which the red suspension became a canary

yellow solution. After 5 minutes, the solution was concentrated and dried *in vacuo* to afford a yellow oil (97.7 mg, 0.0643 mmol) that was used immediately to prevent decomposition, which was observed even at -40 °C. Due to the solubility of **2a** in hydrocarbons, x-ray quality crystals could not be obtained for analysis. ^{1}H NMR (500 MHz, CD_2Cl_2, 243 K) δ: 0.34 (br s, 3H), 1.29 (s, 24H), 1.30 (s, 18H), 2.13 (s, 3H), 2.17 (s, 3H), 3.21 (q, J = 6.6 Hz, 4H), 6.68 (d, J = 1.6 Hz, 2H), 6.73 (d, J = 1.6 Hz, 2H), 7.35 (t, J = 1.6 Hz, 1H), 7.37 (t, J = 1.6 Hz, 1H), 7.55* (br s, 4H), 7.72* (br s, 4 H). ^{13}C NMR (125 MHz, CD_2Cl_2, 243 K) δ: 8.2, 15.9, 19.8, 21.5, 31.0, 31.1, 35.1, 35.2, 71.7, 114.4, 115.1, 117.7,* 121.7, 121.8, 124.7* (q, J_{C-F} = 272.4 Hz), 128.9* (q, J_{C-F} = 31.4 Hz), 134.9*, 145.2, 146.0, 152.8, 153.0, 161.9* (q, J_{C-F} = 49.7 Hz), 171.5, 179.3. * denotes signals arising from BAr_4 anion.

(^{iPr}DAB$_{Me}$)PdCl$_2$ (**17b**). An oven-dried 250 mL round-bottom flask equipped with a stirbar was charged with $(MeCN)_2PdCl_2$ (1.66 g, 6.40 mmol, 1.00 equiv). Dry CH_2Cl_2 (100 mL) was added via syringe. To the stirring dark red suspension, 1,4-bis(2',6'-di-*iso*-propylphenyl)-2,3-dimethyl-1,4-diaza-1,3-butadiene (^{iPr}DAB$_{Me}$) (2.64 g, 6.53 mmol, 1.02 equiv) dissolved in CH_2Cl_2 (20 mL) was added dropwise over two minutes. The suspension became a red solution after about 1 hour stirring at room temperature. After 4 hours, the red solution was filtered through Celite and concentrated *in vacuo* to afford a chunky, bright orange solid, which was resuspended in Et_2O and sonicated for 10 minutes. After filtration, the solid was washed with Et_2O (3 x 30 mL) and petroleum ether (20 mL) to afford **17b** as an orange solid (3.71 g). ^{1}H NMR (500 MHz, CD_2Cl_2, 298 K) δ: 1.21 (d, J = 6.9 Hz, 12H), 1.46 (d, J = 6.8 Hz, 12H), 2.10 (s, 6H), 3.23 (hept, J = 6.8

Hz, 4H), 7.27 (d, J = 7.8 Hz, 4H), 7.39 (t, J = 7.7 Hz, 2H). ^{13}C NMR (125 MHz, CD_2Cl_2, 298 K) δ: 2.6, 21.8, 23.8, 24.1, 29.8, 123.7, 125.7, 132.0, 140.4, 140.8, 190.5.

[(^{iPr}DAB$_{Me}$)Pd(MeCN)$_2$](BF$_4$)$_2$ (18b). A 500 mL round-bottom flask equipped with a stirbar was charged with dichloride **1b** (1.00 g, 1.72 mmol, 1.00 equiv). After dissolving **1b** in dry CH_2Cl_2 (60 mL) and CH_3CN (30 mL), $AgBF_4$ (673 mg, 3.46 mmol, 2.01 equiv) in CH_2Cl_2 (15 mL) was added over two minutes to the stirring solution. AgCl immediately precipitated and the suspension turned yellow. After stirring for 5 hours, the yellow solution was decanted from the white AgCl. The solution was concentrated *in vacuo* to afford a yellow powder, which was dissolved in CH_2Cl_2 and filtered through Celite to remove residual AgCl. Concentration *in vacuo* afforded **18b** as a yellow powder (772 mg, 1.01 mmol). ^{1}H NMR (500 MHz, CD_2Cl_2, 298 K) δ: 1.33 (d, J = 6.7 Hz, 12H), 1.51 (d, J = 6.7 Hz, 12H), 1.97 (s, 6H), 2.53 (s, 6H), 3.23 (hept, J = 6.6 Hz, 4H), 7.37 (d, J = 7.8 Hz, 4H), 7.53 (t, J = 7.8 Hz, 2H). ^{13}C NMR (125 MHz, CD_2Cl_2, 298 K) δ: 2.6, 21.8, 23.8, 24.1, 29.8, 123.7, 125.7, 132.0, 140.4, 140.8, 190.5. Anal. Calcd for $C_{32}H_{46}B_2F_8N_4Pd$: C, 50.13; H, 6.05; N, 7.31. Found: C, 50.32; H, 6.31; N, 7.10.

[(^{iPr}DAB$_{Me}$)Pd(OH)]$_2$(BF$_4$)$_2$ (4b). A 100 mL round-bottom flask equipped with a stirbar was charged with **2b** (130 mg, 0.170 mmol, 1.00 equiv). CH_2Cl_2 (40 mL) was added and the suspension was cooled to 0 °C and stirred for 5 minutes. H_2O (184 mg, 10.2 mmol, 60.0 equiv) was added and the reaction stirred for 5 minutes at 0 °C. Polymer-bound diethylamine (150 mg, 0.187 mmol, 1.10 equiv) was added portionwise over 1 minute, and the reaction was stirred vigorously for 3 minutes at 0 °C. The suspension was quickly filtered through Celite, and washed with CH_2Cl_2. The yellow filtrates were concentrated *in vacuo* to afford **4b** as a yellow powder (84.0 mg, 0.068 mmol). ^{1}H NMR (500 MHz,

CD_2Cl_2, 298 K) δ: -4.45 (s, 2H), 1.18 (d, J = 6.8 Hz, 12H), 1.29 (d, J = 6.8 Hz, 12H), 2.24 (s, 6H), 2.89 (hept, J = 6.8 Hz, 4H), 7.12 (d, J = 7.8 Hz, 4H), 7.37 (t, J = 7.8 Hz, 2H). TFE-d_3 was added to help solubilize material: ^{13}C NMR (125 MHz, CD_2Cl_2 + 2 drops TFE-d_3, 298 K) δ: 23.5, 24.5, 29.9, 125.8 131.4, 137.7, 139.8, 182.8. (The a-diimine backbone CH_3 protons undergo exchange with deuterium from TFE-d_3.) HRMS (FAB+) $C_{56}H_{82}BF_4N_4O_2Pd_2$ (**3b**-BF_4)$^+$: calcd mass 1143.454, measured mass 1143.4570. Anal. Calcd for $C_{56}H_{82}B_2F_8N_4O_2Pd_2$: C, 54.70; H, 6.70; N, 4.56. Found: C, 54.72; H, 6.61; N, 4.51.

[(^{tBu}DAB$_{Me}$)Pd(OMe)]$_2$(BF$_4$)$_2$ (26a). An oven-dried J. Young NMR tube is charged with precatalyst **4a** (20 mg, 0.0149 mmol). Distilled d_3-MeOH/MeOH (9:1, 1.6 mL) is added via syringe. The solid immediately dissolves to form a yellow-orange solution. ^{1}H NMR (300 MHz, d_3-MeOH/MeOH (9:1), 298 K) δ: 1.26 (s, 72H), 1.87 (br s, no integration because OCH_3/OCD_3 bridge exchange), 1.92 (s, 6H), 7.01 (br s, 8H), 7.42 (br s, 4H).

[(^{Me}DAB$_{Me}$)Pd(OH)]$_2$(BF$_4$)$_2$ (4c). A 100 mL round-bottom flask equipped with a stirbar was charged with **2c** (56.4 mg, 0.120 mmol, 1.00 equiv). CH_2Cl_2 (40 mL) was added and the suspension was cooled to 0 °C and stirred for 5 minutes. H_2O (130 mg, 7.2 mmol, 60.0 equiv) was added and the reaction stirred for 5 minutes at 0 °C. Polymer-bound diethylamine (110 mg, 0.132 mmol, 1.10 equiv) was added portionwise over 1 minute, and the reaction was stirred vigorously for 3 minutes at 0 °C. The suspension was quickly filtered through Celite, and washed with CH_2Cl_2. The yellow filtrates were concentrated *in vacuo* to afford **4c** as a yellow powder (48.0 mg, 0.048 mmol). ^{1}H NMR (500 MHz, CD_2Cl_2, 298 K) δ: -3.82 (s, 2H), 2.18 (s, 12H), 2.37 (s, 24H) 7.04 (d, J = 6.9 Hz, 8H),

7.12 (t, J = 7.1 Hz, 4H). ^{13}C NMR unobtainable due to poor solubility (**26a** reacts rapidly with TFE.) Anal. Calcd for $C_{40}H_{50}B_2F_8N_4O_2Pd_2$: C, 47.79; H, 5.01; N, 5.57. Found: C, 48.11; H, 5.35; N, 5.47.

[(^{Me}DAB$_{Me}$)Pd(μ-OH)(μ-OCH$_2$CF$_3$)]$_2$(BF$_4$)$_2$ (27). An oven-dried J. Young NMR tube is charged with precatalyst **4c** (20 mg, 0.020 mmol). Distilled TFE (100 uL) is added via syringe. The solid immediately dissolves to form an orange solution. Orange crystals were grown from slow evaporation of a saturated CH_2Cl_2 solution. ^{1}H NMR (300 MHz, CD_2Cl_2, 298 K) δ: -4.30 (s, 1H), 0.59 (q, J = 8.3 Hz, 2H, TFE –CH_2- signal shifted upfield due to ring current), 2.13 (s, 12H), 2.19 (s, 12H), 2.29 (br s, 12H), 7.15 (m, 10H), 7.29 (m, 2H).

[(^{Me}DAB$_{Me}$)Pd(OMe)]$_2$(BF$_4$)$_2$ (26c). An oven-dried J. Young NMR tube is charged with precatalyst **4c** (30 mg, 0.030 mmol). Distilled d_3-MeOH/MeOH (9:1, 1.6 mL) is added via syringe. The solid immediately dissolves to form a yellow solution. ^{1}H NMR (300 MHz, d_3-MeOH/MeOH (9:1), 298 K) δ: 2.11 (s, 24H), 2.34 (s 12H), 2.04 (br s, no integration because OCH_3/OCD_3 bridge exchange), 6.98 (d, J = 7.1 Hz, 8H), 7.29 (t, J = 7.0 Hz, 4H

General Procedure for Catalytic Isomerization/Oligomerization. Under air, a round-bottom flask equipped with a stirbar was charged with precatalyst **4a** (8.8 mg, 6.56 μmol) and adamantane (internal standard, 30–70 mg). Benchtop CH_2Cl_2 or 1,2-dichloroethane (8 mL) and trifluoroethanol (4 mL) were added to afford a yellow solution. (CH_2Cl_2 was used for all olefins except pentene, for which 1,2-dichloroethane was used to avoid overlap in GC traces.)

For pentene and hexene, 6.56 mmol were added in one portion to the stirring reaction mixture. Aliquots (100 μL–200 μL) for analysis were removed at intervals and passed through a plug of silica to remove catalyst. The plug was then washed with ~1.5 mL CH_2Cl_2 or 1,2-dichloroethane to afford a clear, colorless solution, of which a small sample (4 μL) was injected into the gas chromatograph (GC).

For ethylene and propylene, a Schlenk flask and a calibrated gas bulb was used for quantitative gas transfer. The flask was evacuated and cooled to -78 °C, and the gas bulb, containing 6.56 mmol of gas, was opened to the flask. Using the gas bulb, enough air was added to the flask to ensure that the pressure in the vessel reached 1 atm upon warming to room temperature. Aliquots (100 μL–200 μL) were taken by syringe through the side-arm valve, which was capped with a septum to minimize loss of ethylene/propylene. To quantify butene formation during ethylene oligomerization, the flask was cooled to -20°C and aliquots (20 μL) were removed using a cooled, gas-tight syringe, which were directly injected (1–2 μL) into the GC.

Gas chromatography (GC) was performed using an Agilent 6890N instrument with a flame ionization detector (FID). Routine runs were performed using a DB-1 capillary column (10 m length, 0.10 mm diameter, 0.40 μm film) with the following program: hold at 35 °C for 2 min, ramp temperature at 2 °C/min to 50°C and hold for 2 min (total run time = 11.5 min), then ramp temperature at 100 °C/min to 290 °C and hold for 5 min (total run time = 18.9 min.) Response factors for olefins were calculated versus adamantane. A known mass of analyte and adamantane were added to a scintillation vial, then dissolved in ~1–2 mL CH_2Cl_2 or 1,2-dichloroethane. The solution (4 μL) was then

injected into the GC for analysis. Response factors for each analyte were calculated using the following formula:

Response factor = $[(mass_{analyte}) \times (area_{adamantane})] / [(area_{analyte}) \times (mass_{adamantane})]$

All linear butene, pentene and hexene isomers had response factors of 1.0; branched C_6 isomers had response factors of 1.0–1.1; 1-Octene, 1-decene, 1-dodecene, 1-tetraedecene, 1-hexadecene, 1-octadecene, and 1-eicosene had response factors of 1.0. A response factor of 1.0 was hence taken as a sufficiently accurate value for all reactants and products.

For the Schulz-Flory analysis, aliquots were taken at 20 hours. In the case of ethylene oligomerization the flask was cooled to -40 °C before removing an aliquot as described above; for all others the standard procedure described above was followed.

Catalytic Isomerization/Oligomerization Using [(^{tBu}DAB$_{Me}$)Pd(CH$_3$)(Et$_2$O)](BAr$_4$) (Ar = 3,5-(CH$_3$)$_2$-C$_6$H$_3$) (2a). 2a was prepared from **1a** according to the experimental procedure above. Following removal of Et_2O *in vacuo*, dry CH_2Cl_2 (8 mL) and TFE (4 mL) were vacuum transferred into a Schlenk flask containing **2a** as a yellow oil. Under an argon atmosphere, dry 1-hexene (800 μL) was syringed into the yellow solution. Aliquots (100 μL–200 μL) were removed through the side-arm under argon using a syringe, filtered through a silica plug (due to a different counterion, much of the metal salts do not adhere to the silica), and injected (4 μL) into the GC.

X-Ray Crystal Data: General Procedure. Crystals grown from CH_2Cl_2 (**22, 24, 26b, 27**) were removed quickly from a scintillation vial to a microscope slide coated with Paratone N oil. Samples were selected and mounted on a glass fiber with Paratone N oil.

Data collection was carried out on a Bruker KAPPA APEX II diffractometer with a 0.71073 Å MoKα source. The structures were solved by direct methods. All non-hydrogen atoms were refined anisotropically. Some details regarding refined data and cell parameters are available in Crystallographic Information. Selected bond distances and angles are supplied as well.

REFERENCES

1. (a) Keim, W.; Kowaldt, F. H.; Goddard, R.; Krüger, C. *Angew. Chem., Int. Ed.* **1978**, *17*, 466. (b) Keim, W. *Angew. Chem., Int. Ed.* **1990**, *29*, 235.
2. Small, B. L.; Brookhart, M. *J. Am. Chem. Soc.* **1998**, *120*, 7143.
3. Gibson, V. C.; Spitzmesser, S. K. *Chem. Rev.* **2003**, *103*, 283.
4. Speiser, F.; Braunstein, P.; Saussine, L. *Acc. Chem. Res.* **2005**, *38*, 784.
5. Skupinska, J. *Chem. Rev.* **1991**, *91*, 613.
6. (a) Johnson, L. K.; Killian, C. M.; Brookhart, M. *J. Am. Chem. Soc.* **1995**, *117*, 6414. (b) Tempel, D. J.; Johnson, L. K.; Huff, R. L.; White, P. S.; Brookhart, M. *J. Am. Chem. Soc.* **2000**, *122*, 6686. (c) Shultz, L. H.; Tempel, D. J.; Brookhart, M. *J. Am. Chem. Soc.* **2001**, *123*, 11539.
7. Svejday, S. A.; Brookhart, M. B. *Organometallics* **1999**, *18*, 65.
8. (a) Johansson, L.; Tilset, M.; Labinger, J. A.; Bercaw, J. E. *J. Am. Chem. Soc.* **2000**, *122*, 10846. (b) Zhong, H. A.; Labinger, J. A.; Bercaw, J. E. *J. Am. Chem. Soc.* **2001**, *124*, 1378. (c) Stahl, S.; Labinger, J. A.; Bercaw, J. E. *Angew. Chem. Int. Ed.* **1998**, *37*, 2181. (d) Labinger, J. A.; Herring, A. M.; Lyon, D. K.; Luinstra, G. A.; Bercaw, J. E.; Horvath, I. T.; Eller, K. *Organometallics* **1993**, *12*, 895. (e) Luinstra, G. A.; Wang, L.; Stahl, S. S.; Labinger, J. A.; Bercaw, J. E. *Organometallics* **1994**, *13*, 755. (f) Luinstra, G. A.; Labinger, J. A.; Bercaw, J. E. *J. Am. Chem. Soc.* **1993**, *115*, 3004. (g) Luinstra, G. A.; Wang, L.; Stahl, S. S.; Labinger, J. A.; Bercaw, J. E. *J. Organomet. Chem.* **1995**, *504*, 75. (h) Ackerman, L. J.; Sadighi, J. P.; Kurtz, D. M.; Labinger, J. A.; Bercaw, J. E. *Organometallics* **2003**, *22*, 3884.
9. (a) Gol'dshleger, N. F.; Es'kova, V. V.; Shilov, A. E.; Shteinman, A. A. *Zh. Fiz. Khim.* **1972**, *46*, 1353 (English translation **1972**, *46*, 785). (b) Shilov, A. E.; Shul'pin, G. B. *Activation and Catalytic Reactions of Saturated Hydrocarbons in the Presence of Metal Complexes*; Kluwer Academic Publishers: Dordrecht, 2000.
10. (a) Jintoku, T.; Taniguchi, H.; Fujiwara, Y. *Chem. Lett.* **1987**, 1865. (b) Jintoku, T.; Takaki, K.; Fujiwara, Y.; Fuchita, Y.; Hiraki, K. *Bull. Chem. Soc. Jpn.* **1990**, *63*, 438.

11. For examples, see: (a) Nishimura, T.; Onoue, T.; Ohe, K.; Uemura, S. *J. Org. Chem.* **1999**, *64*, 6750. (b) Peterson, K. P.; Larock, R. C. *J. Org. Chem.* **1998**, *63*, 3185. (c) Jensen, D. R.; Pugsley, J. S.; Sigman, M. S. *J. Am. Chem. Soc.* **2001**, *123*, 7475. (d) Ferreira, E. M.; Stoltz, B. M. *J. Am. Chem. Soc.* **2001**, *123*, 7725.
12. Khusnutdinova, J. R.; Zavalij, P. Y.; Vedernikov, A. N. *Organometallics* **2007**, *26*, 2402.
13. Fujii, A.; Hagiwara, E.; Sodeoka, M. *J. Am. Chem. Soc.* **1999**, *121*, 5450.
14. Sheldon, R. A.; Arends, I. W. C. E.; ten Brink, G. J.; Dijksman, A. *Acc. Chem. Res.* **2002**, *35*, 774.
15. Williams, T. J.; Caffyn, A. J. M.; Hazari, N.; Oblad, P. F.; Labinger, J. A.; Bercaw, J. E. *J. Am. Chem. Soc.* **2008**, *130*, 2418.
16. Bercaw, J. E.; Hazari, N.; Labinger, J. A.; Oblad, P. F. *Angew. Chem.* **2008**, *120*, 10089.
17. Oblad, P. F.; Bercaw, J. E.; Hazari, N.; Labinger, J. A. *Organometallics* **2010**, *29*, 789.
18. Stull, D. R.; Westrum, E. F., Jr.; Sinke, G. C., *The Chemical Thermodynamics of Organic Compounds*. John Wiley, New York, 1969.
19. Cox, J. D.; Pilcher, G. *Thermochemistry of Organic and Organometallic Compounds*. Academic Press, London, 1970.
20. Rossini, F. D. *Chemical Thermodynamics*. John Wiley, New York, 1950.
21. Kilpatrick, J. E.; Prosen, J. P.; Pitzer, K. S.; Rossini, F. D. *J. Res. Natl. Bur. Stand.* **1946**, *36*, 559.
22. Kirova, M. L.; Dahl, D. B.; Lloyd, W. G. *J. Mol. Cat. A.* **1994**, *88*, 301. (b) Dahl, D. B.; Davies, C.; Hyden, R.; Kirova, M. L.; Lloyd, W. G. *J. Mol. Cat. A.* **1997**, *123*, 91.
23. Foulds, G. A.; Bennett, A. M. A.; Thornton, D. A.; Brown, S. J.; Clutterbuck, L. M.; Hinton, C.; Humphreys, G. B.; Masters, A. F. *Polyhedron* **1992**, *11*, 1285.
24. Manuel, T. A. *J. Org. Chem.* **1962**, *27,* 3941.
25. Sealy, S. J.; Fraser, D. M.; Möller, K. P.; O'Connor, C. T. *Chem. Eng. Sci.* **1994**, *49*, 3307.

26. Keith, J. A.; Nielsen, R. J.; Oxgaard, J.; Goddard, W. A. *J. Am. Chem. Soc.* **2007**, *129*, 12342.
27. Feldman, J.; McLain, S. J.; Parthasarathy, A.; Marshall, W. J.; Calabrese, J. C.; Arthur, S. D. *Organometallics* **1997**, *16*, 1514.
28. Pangborn, A. B.; Giardello, M. A.; Grubbs, R. H.; Rosen, R. K.; Timmers, F. J. *Organometallics* 1996, 15, 1518.
29. Rudler-Chauvin, M.; Rudler, H. *J. Organomet. Chem.* **1977**, *134*, 115.
30. Brookhart, M.; Grant, B.; Volpe, A. F., Jr. *Organometallics* **1992**, *11*, 3920.
31. Anderson, G. K.; Lin, M. *Inorg. Synth.* **1990**, *28*, 60.

APPENDIX A

A Hexanuclear Gold(I) Cluster Stabilized by Dianionic Bidentate Bis(Phosphide) Ligands

ABSTRACT

Herein we report the first gold(I) phosphide cluster stabilized by bidentate bis(phosphide) ligands, using the pyridine-linked bis(phosphide) ligand discussed in Chapters 1 and 2 (PNP^{2-}, coordinating via only phosphorus.) Additionally stabilizing the hexanuclear cluster is the analogous neutral bidentate secondary phosphine ligand (PNP-H_2). In concert with bridging phosphides, aurophilic interactions between the gold atoms in the hexanuclear cluster confer a high degree of organization to this complex in the solid state.

INTRODUCTION

Since Puddephatt's synthesis of diphenylphosphide gold clusters [{Au(PPh_2)}$_n$] in 1976,[1] only a few gold(I) phosphides have been described,[2] most recently by Glueck and coworkers.[3] This is in contrast to not only main group[4] and transition metal phosphides,[5] but isoelectronic gold(I) thiolates [{Au(SR)}$_n$] as well,[6] which have important medical applications. In the solid state, phosphide ligands commonly participate in extensive bridging interactions with gold, resulting in the formation of clusters, oligomeric or polymeric chains, and polynuclear metallacycles. The overall geometry of these metal phosphides is often influenced by 'aurophilic bonding,'[7] an interaction between the formally closed-shell gold(I) centers that results in a weak covalent Au-Au bond. In fact, gold(I) complexes with small ligands will frequently form oligomers stabilized by these aurophilic interactions, which are typically weaker than covalent bonds. As such, the average length of an Au-Au bond is approximately 3 Å. Depending on ligand sterics, aurophilic bond lengths as low as 2.7 Å and as high as 3.3 Å have been observed, however. Aurophilic Au-Au bond lengths are appreciably less than the sum of the two van der Waals radii of each gold atom (3.7 Å).

We recently reported the synthesis of pyridine-linked bis(secondary phosphine) **1** and κ^3-PNP^{2-}-coordinated potassium and zirconium(IV) complexes (see Chapter 1).[8] The solid-state structure of the former complex — $K_4(PNP)_2(THF)_6$ — has a potassium-phosphide cluster core in which potassium and phosphorus atoms are arranged as alternating vertices of three conjoined quadrilateral, nearly square arrays. We reasoned that similarly elaborate gold(I) phosphide clusters could be stabilized by this novel ligand as well.

RESULTS AND DISCUSSION

Reaction of bis(phosphine) **1** with an equivalent of $(Me_2S)AuCl$ affords one diastereomer of $(PNP\text{-}H_2)AuCl$ (**2**) as the only product by diagnostic ^{31}P NMR spectroscopy and elemental analysis (eq. 1). The NMR signal at -17.7 ppm is split into a doublet by one-bond ^{1}H coupling ($^{1}J_{P\text{-}H}$ = 357.5 Hz). VT-NMR experiments suggest that the phosphine donors are equivalent, and that **2** is a single diastereomer in solution. The relative stereochemistry of the chiral phosphines cannot be definitively assigned, however. Unexpectedly, **2** decomposes to several unidentifiable species upon concentration or trituration by ^{31}P NMR.

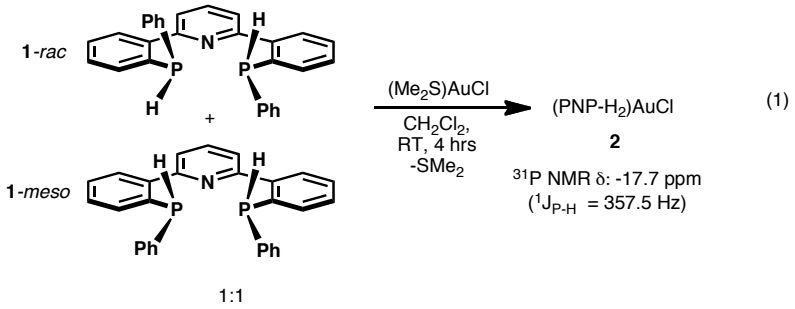

(1)

Slow evaporation of a saturated solution of **2** in CH_2Cl_2 affords large yellow crystals of x-ray diffraction quality in 57% yield, which reveal a much more elaborate solid-state structure than expected (**3**) (Figures A.1-A.3). Three molecules of ligand **1** arrange around a hexanuclear gold-phosphide core. Two of the three ligands coordinate in a bidentate fashion as the dianionic conjugate base PNP^{2-} (P1 and P2, P4 and P6); as expected, their phosphide donors are engaged in extensive bridging interactions between different gold(I) atoms. The neutral ligand is also bidentate, but its phosphines cannot form bridges (P3 and P5).

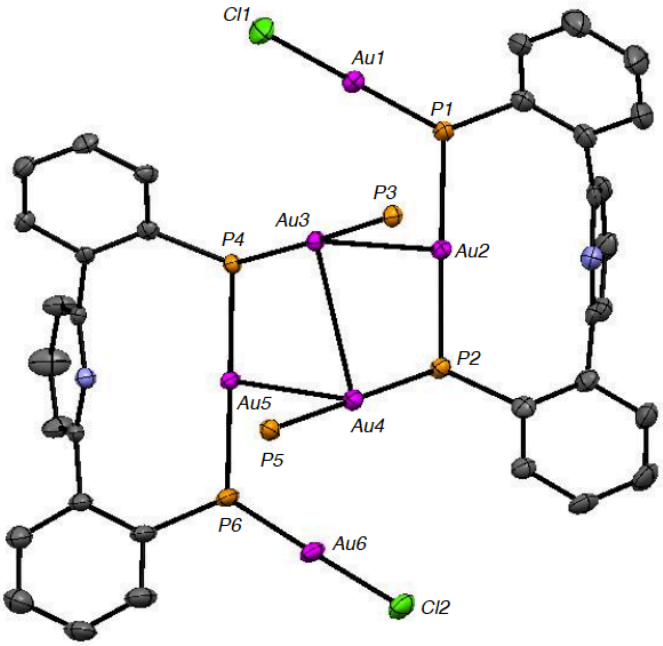

Figure A.1. Thermal ellipsoid representation of western and eastern PNP^{2-} ligands and gold-phosphide core of **3** at the 50% probability level. All protons, *P*-phenyl substituents, and the *P3*-to-*P5*-spanning PNP-H_2 ligand are omitted for clarity. Atoms are color coded: carbon (gray), chlorine (green), gold (purple), nitrogen (blue), phosphorus (orange)

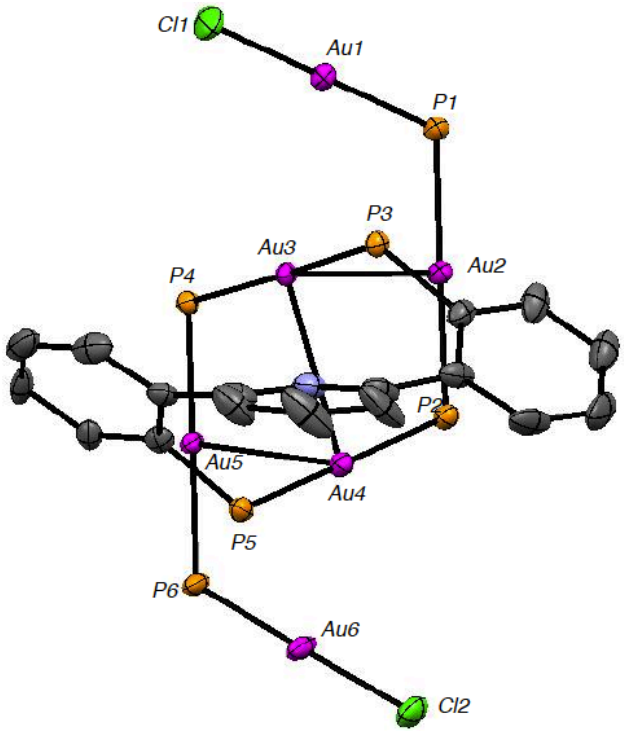

Figure A.2. Thermal ellipsoid representation of PNP-H_2 ligand and gold-phosphide core of **3** at the 50% probability level. All protons, *P*-phenyl substituents, and PNP^{2-} ligands are omitted for clarity. Atoms are color coded: carbon (gray), chlorine (green), gold (purple), nitrogen (blue), phosphorus (orange)

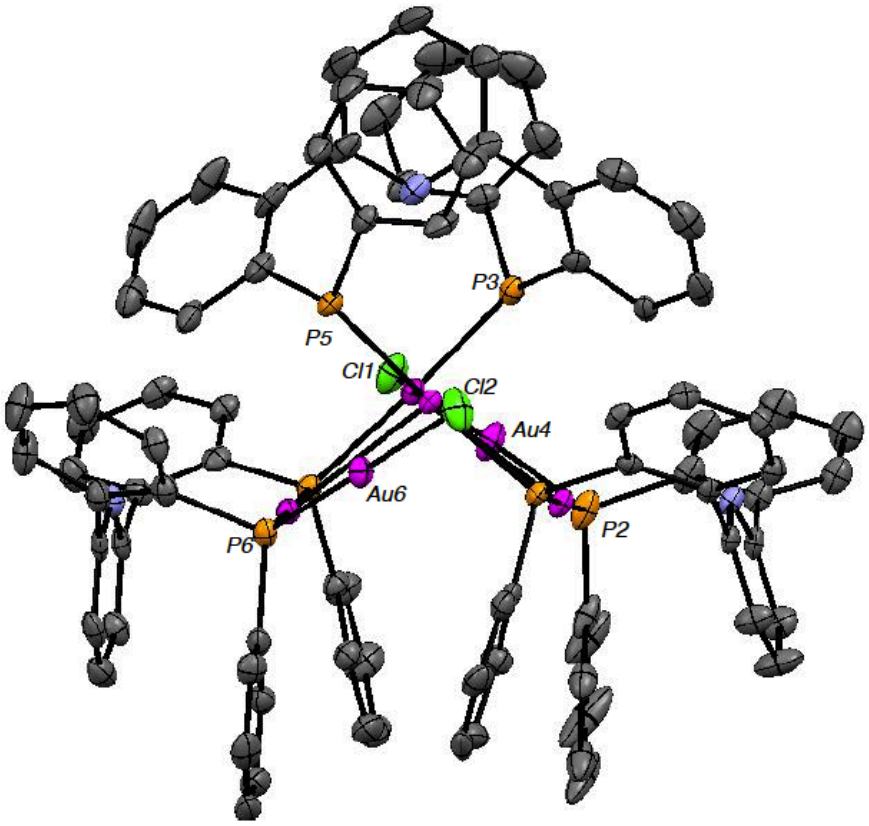

Figure A.3. Thermal ellipsoid representation of **3** at the 50% probability level. All protons and *P*-phenyl substituents are omitted for clarity. Atoms are color coded: carbon (gray), chlorine (green), gold (purple), nitrogen (blue), phosphorus (orange)

Despite its apparent complexity, **3** is roughly C_i-symmetric, with an inversion center at the middle of the Au3-Au4 bond. All gold atoms are in the +1 oxidation state, and the pyridine nitrogens of each ligand do not coordinate to any metal. All gold(I) atoms except terminal chloride-bound Au1 and Au6 are involved in possible aurophilic interactions that confer organization to the overall structure and gold-phosphide core of **3**. Furthermore, it appears that π–stacking between the *P*-phenyl substituents of the PNP^{2-} ligands (P1 and P2, P4 and P6) may also stabilize the structure in the solid state (Figure A.3); the centroid distances between the rings is 3.7–3.8 Å.

Table A.1. Gold(I)-phosphorus bond distances (Å) in the solid-state structure of **3**

	Au1	**Au2**	**Au3**	**Au4**	**Au5**	**Au6**
P1	2.2549(11)	2.3191(10)	-	-	-	-
P2	-	2.3187(10)	-	2.3273(11)	-	-
P3	-	-	2.3246(10)	-	-	-
P4	-	-	2.3286(9)	-	2.3052(10)	-
P5	-	-	-	2.3189(11)	-	-
P6	-	-	-	-	2.3086(11)	2.2500(11)

The gold(I)-phosphorus bond lengths within the core of **3** are described in Table A.1. It is interesting that the Au1-P1 and Au6-P6 bonds are so much smaller than the other gold(I)-phosphide bonds in the inner core of the complex, since Au1 and Au6 are coordinated to chloride anions and the phosphides are unambiguously L-type donors. These short gold(I)-phosphorus bonds are likely just a steric effect, resulting from the relatively small, linear [AuCl] fragments that make up the "termini" of the gold(I)-phosphorus core in **3**. Shortening of the inner gold(I)-phosphide bonds, however, would bring the bulky bidentate ligands unfavorably close to one another. The inner gold(I)-phosphide bonds ($Au\text{-}P_{average}$ = 2.3189(30) Å) agree very well with those in reported gold(I)-phosphide clusters (Au-P ~ 2.31–2.33).[3] The aurophilic bond lengths are unremarkable and as expected (Table A.2.)

Table A.2. Aurophilic bond distances (Å) in the solid-state structure of **3**

	Au2	**Au4**
Au3	2.9993(3)	3.1909(3)
Au5	-	3.0736(3)

Interestingly, the neutral PNP-H_2 component of **3** is the *meso*-PNP-H_2 diastereomer. This does not necessarily indicate that **2** is stabilized solely by the *meso*-

PNP-H_2 diastereomer as well, since *P*-stereocenter epimerization could occur just as rapidly upon formation of **3** as it does upon formation of **2**; furthermore, if **2** is monomeric, the environments around each *P*-stereocenter in the bidentate ligand are quite different.

Upon formation of **3**, 4 equivalents of HCl are generated *in situ*, which could presumably protonate the non-coordinated pyridine ring in unreacted **2.** The fate of the acid is not entirely clear, but by ^{1}H and ^{31}P NMR, as well as elemental analysis, the mother liquor following crystallization of **3** contains an intractable mixture of gold and phosphorus-containing material. Likewise, **3** fragments into several unidentifiable species (none of which are **2**) upon dissolving the crystals in CD_2Cl_2. This process appears to be reversible, however, since slow evaporation produces crystals of **3**, although in significantly lower yield.

CONCLUSIONS

Gold-phosphide cluster **3** is stabilized by numerous aurophilic and π-stacking interactions. This work highlights the propensity of secondary diarylphosphines to bridge soft gold atoms in relatively unexplored polynuclear gold-phosphide clusters to access structurally novel architectures, the reactivity of which could be explored further.

EXPERIMENTALS

General Considerations and Instrumentation. All air- and moisture-sensitive compounds were manipulated using standard high vacuum and Schlenk techniques or manipulated in a glovebox under a nitrogen atmosphere using degassed solvents. All

solvents were dried by the method of Grubbs.[9] PNP-H_2 (**1**) was prepared as described in Chapter 1. (Me_2S)AuCl was obtained from Strem Chemical. ^1H, ^{13}C, and ^{19}F NMR spectra were recorded on Varian Mercury 300 or Varian INOVA-500 spectrometers at room temperature, unless otherwise indicated. The data are reported by chemical shift (ppm) from tetramethylsilane, multiplicity (s, singlet; d, doublet; t, triplet; m, multiplet; dd, double doublet; dt, double triplet), coupling constants (Hz), and integration. All ^{13}C NMR data were collected proton-decoupled ($^{13}C\{^1H\}$), except where specified.

(PNP-H_2)AuCl (2). A vial equipped with a stir bar is charged with (Me_2S)AuCl (129 mg, 0.44 mmol, 1.00 equiv). CH_2Cl_2 (12 mL) is added to afford a white suspension. A solution of PNP-H_2 (**1,** 200 mg, 0.45 mmol, 1.02 equiv) in CH_2Cl_2 (3 mL) is added dropwise to the suspension, which turns into a yellow solution within seconds. The reaction is stirred for 4 hours. For NMR analysis, a small-scale reaction in CD_2Cl_2 was carried out. ^1H NMR (500 MHz, CD_2Cl_2, 298 K) δ: 6.62 (dd, J = 359 Hz, J = 28.4 Hz, 2H), 6.84 (m, 6H), 6.90 (t, J = 7.5 Hz, 4H), 7.15 (t, J = 7.2 Hz, 2H), 7.28 (t, J = 7.5 Hz, 2H), 7.60 (t, J = 7.6 Hz, 2H), 7.98 (d, J = 7.9 Hz, 2H), 8.11 (d, J = 7.7 Hz, 2H), 8.26 (t, J = 7.9 Hz, 1H). $^{31}P\{^1H\}$ NMR (202 MHz, CD_2Cl_2) δ: -17.7 (s). Anal. Calcd. for $C_{29}H_{23}AuClNP_2$: C, 51.23; H, 3.41; N, 2.06; P 9.11. Found: C, 51.02; H, 3.57; N, 2.03; P 8.95. To obtain crystals of **3**, the reaction solution was concentrated *in vacuo* to 2 mL. The solution was then slowly evaporated overnight to afford **3** as large yellow crystals in 57% yield (110 mg, 0.042 mmol).

Variable-Temperature NMR Procedure. All variable-temperature NMR experiments were performed on a Varian INOVA-500 spectrometer. In a glovebox, an oven-dried J. Young NMR tube was charged with 5–10 mg of analyte and 1.2 mL of CD_2Cl_2 was

added. The desired temperature of the NMR probe was set, and after reaching said temperature, the temperature of the tube was allowed to stabilize for 15 minutes before acquiring a spectrum.

X-Ray Crystal Data: General Procedure. Crystals of **3** grown from CH_2Cl_2 were removed quickly from a scintillation vial to a microscope slide coated with Paratone N oil. Samples were selected and mounted on a glass fiber with Paratone N oil. Data collection was carried out on a Bruker KAPPA APEX II diffractometer with a 0.71073 Å MoKα source. The structures were solved by direct methods. All non-hydrogen atoms were refined anisotropically. Some details regarding refined data and cell parameters are available in Crystallographic Information. Selected bond distances and angles are supplied as well.

REFERENCES

1. Puddephatt, R. J.; Thompson, P. J. *J. Organomet. Chem.* **1976**, *117*, 395.
2. (a) Pritchard, R. G.; Dyson, D. B.; Parish, R. V.; McAuliffe, C. A.; Beagley, B. *J. Chem. Soc., Chem. Commun.* **1987**, 371. (b) Dyson, D. B.; Parish, R. V.; McAuliffe, C. A.; Pritchard, R. G.; Fields, R.; Beagley, B. *J. Chem. Soc., Dalton Trans.* **1989**, 907. (c) Carriedo, G. A.; Riera, V.; Rodríguez, M. L.; Jones, P. G.; Lautner, J. *J. Chem. Soc., Dalton Trans.* **1989**, 639. (d) Livotto, F. S.; Vargas, M. D.; Braga, D.; Grepioni, F. *J. Chem. Soc., Dalton Trans.* **1992**, 577. (d) Vicente, J.; Chicote, M. T.; Jones, P. G. *Inorg. Chem.* **1993**, *32*, 4960. (e) Blanco, M. C.; Fernández, E. J.; Olmos, M. E.; Crespo, O.; Laguna, A.; Jones, P. G. *Organometallics* **2002**, *21*, 2426.
3. (a) Stefanescu, D. M.; Yuen, H. F.; Glueck, D. S.; Golen, J. A.; Rheingold, A. L. *Angew. Chem. Int. Ed.* **2003**, *42*, 1046. (b) Stefanescu, D. M.; Yuen, H. F.; Glueck, D. S.; Golen, J. A.; Zakharov, L. N.; Incarvito, C. D.; Rheingold, A. L. *Inorg. Chem.* **2003**, *42*, 8891. (c) Lane, E. M.; Chapp, T. W.; Hughes, R. P.; Glueck, D. S.; Feland, B. C.; Bernard, G. M.; Wasylishen, R. E.; Rheingold, A. L. *Inorg. Chem.* **2010**, *49*, 3950.
4. (a) Beachley, O. T., Jr.; Chao, S. L.; Churchill, M. R.; Lake, C. H. *Organometallics* **1996**, *15*, 3088. (b) Culp, R. D.; Cowley, A. H.; Decken, A.; Jones, R. A.; Bond, M. R.; Mokry, L. M.; Carrano, C. J. *Inorg. Chem*. **1997**, *36*, 5165. (c) Westerhausen, M.; Krofta, M.; Mayer, P.; Warchhold, M.; Nöth, H. *Inorg. Chem.* **2000**, *39*, 4721.
5. (a) Acum, G. A.; Mays, M. J.; Raithby, P. R.; Powel, H. R.; Solan, G. A. *J. Chem. Soc., Dalton Trans.* **1997**, 3427. (b) Wang, K.; Emge, T. J.; Goldman, A. S. *Inorg. Chim. Acta* **1997**, *255*, 395. (c) Johnson, B. F. G.; Lewis, J.; Nordlander, E.; Raithby, P. R.; Housecroft, C. E. *Inorg. Chim. Acta* **1997**, *259*, 345. (d) Doherty, S.; Waugh, M.; Scanlan, T. H.; Elsegood, M. R. J.; Clegg, W. *Organometallics* **1999**, *18*, 679. (e) Izod, K.; O'Shaughnessy, P.; Sheffield, J. M.; Clegg, W.; Liddle, S. T. *Inorg. Chem*. **2000**, *39*, 4741. (f) Wong, W.-Y.; Ting, F.-L.; Lam, W.-L. *J. Chem. Soc., Dalton Trans.* **2001**, 2981. (g) Eichele, K.; Wasylishen, R.

E.; Corrigan, J. F.; Taylor, N. J.; Carty, A. J.; Feindel, K. W.; Bernard, G. M. *J. Am. Chem. Soc.* **2002**, *124*, 1541.

6. For examples, see: (a) Shaw, C. F., III. *Chem. Rev.* **1999**, *99*, 2589. (b) Bardaji, M.; Calhorda, M. J.; Costa, P. J.; Jones, P. G.; Laguna, A.; Pérez, M. R.; Villacampa, M. D. *Inorg. Chem.* **2006**, *45*, 1059. (c) Barngrover, B. M.; Aikens, C. M. *J. Phys. Chem. Lett.* **2011**, *2*, 990.
7. For a review, see: Schmidbaur, H. *Gold Bulletin* **2000**, *33*, 3.
8. Winston, M. S; Bercaw, J. E. *Organometallics*, **2010**, *29*, 6408.
9. Pangborn, A. B.; Giardello, M. A.; Grubbs, R. H.; Rosen, R. K.; Timmers, F. J. *Organometallics* 1996, 15, 1518.

APPENDIX B

tert-Butylhydroperoxide-Mediated Wacker Oxidations Catalyzed by Air- and Water-Tolerant Palladium(II) Dimers

ABSTRACT

Herein we report a *tert*-butylhydroperoxide-mediated Wacker-type oxidation of olefins catalyzed by (α-diimine)Pd complexes. These reactions can be carried out under air at room temperature in benchtop solvent within 15 minutes using an aqueous solution of oxidant.. Excellent yields are observed using linear olefin substrates.

INTRODUCTION

In 1980, Mimoun and coworkers reported a modified palladium(II)-catalyzed Wacker-type oxidation of linear olefins using hydrogen peroxide.[1] When heated to 80 °C in the presence of superstoichiometric amounts of H_2O_2, α-olefins can be taken to 2-ketones by catalytic palladium(II) salts in >90% yield. This technology was ultimately adapted for use with alkylhydroperoxides, such as *tert*-butylhydroperoxide (TBHP).[2] Sigman has since shown conclusively that TBHP-mediated Wacker oxidations involve *syn*-peroxy-palladation from TBHP-coordinated palladium(II) olefin intermediates (**1,** Scheme B.1.)[2e]

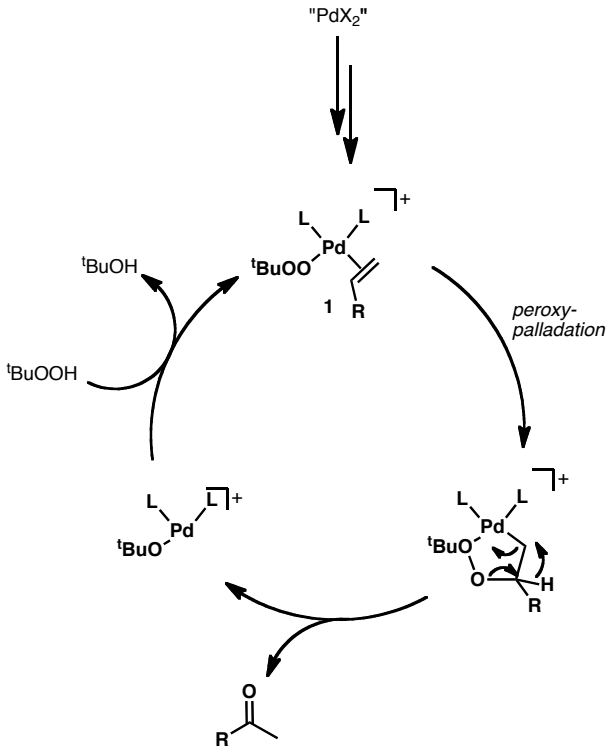

Scheme B.1. Mechanism of palladium-catalyzed, TBHP-mediated Wacker oxidation of olefins

Sigman and coworkers have reported that quinox-supported palladium(II) cations can catalyze the TBHP-mediated Wacker oxidation of olefins in very high yields under mild conditions.[2d,2e] While these transformations can be effected under air at room temperature for anywhere between 20 minutes and 20 hours, they generally require 12 equivalents of TBHP (aqueous solution), and silver salts to activate the Pd(Quinox)Cl_2 precatalyst.

RESULTS AND DISCUSSION

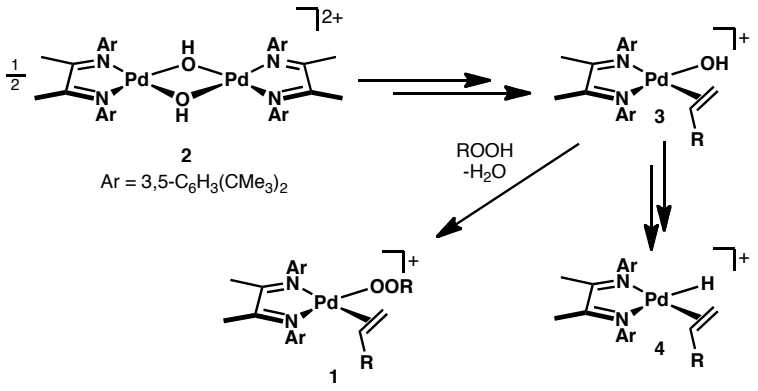

Scheme B.2. Plausible mechanisms of activation of bis(μ–hydroxy) dimer **2** to active Wacker-type catalyst **1**

We recently reported that α-diimine-supported palladium bis(μ–hydroxy) dimers (**2**) undergo rapid dissociation and hydroxy-palladation reactions in the presence of olefin and a nucleophilic co-solvent to generate a reactive palladium(II) hydride (Chapter 4). We envisioned that this Wacker-like reactivity could be exploited and commandeered in the presence of alkylhydroperoxide while avoiding the reactivity associated with the

reduced hydride species. Furthermore, given the stability of these systems in the presence of excess water, safe, commercially available aqueous solutions of alkylhydroperoxide could be used.

Bis(μ–hydroxy) dimers may be convenient entry points into catalytic cycles similar to Figure B.1, since they do not require silver(I) salts for activation. Olefin coordination has been shown to occur with dimer dissociation, and ligand exchange by proton transfer from alkylhydroperoxide to the Pd-OH bond may liberate water and afford the presumably active [$Pd(OOR)^+$] complex **1** (Scheme B.2). Clearly, oxidation of **3** by alkylhydroperoxide must be faster than intramolecular hydroxy-palladation and initiation of oligomerization/isomerization by hydride **4.**

Table B.1. Substrate scope

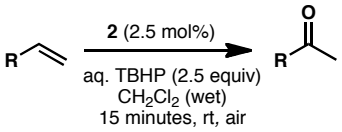

R	Yield (GC)
CH_3	94%
CH_2CH_3	94%
$(CH_2)_2CH_3$	92%
$(CH_2)_3CH_3$	92%
$C(CH_3)_3$	63%[a]
cyclohexyl	71%[a]
C_6H_5	6%
p-Me-C_6H_4	10%

[a]Reaction time 4 hours

Treating dimer **2** with 2.5 equivalents of 70 wt% aq. TBHP generates several asymmetrically substituted palladium(II) species by ^{1}H NMR within minutes at room

temperature. However, 15 minutes after adding linear α–olefin, almost no starting material can be detected (Table B.1). By GC, oxidized 2-ketones are formed in >90% yield. Importantly, in all cases, neither isomerized nor oligomerized starting material are detected by GC, suggesting that palladium(II) hydride **4** is either never accessed in the catalytic cycle or simply not long-lived enough to initiate. Finally, no oxidized products are observed in the absence of precatalyst **2**.

The reaction is fastest and highest yielding with linear α–olefin substrates. Olefins adjacent to secondary and tertiary carbons (i.e., neo-hexene, vinylcyclohexane) react relatively slower with the catalyst, requiring 4 hours to afford ketone product in moderate yields (60–75%). Precatalyst **2**, unfortunately, fails to oxidize styrenes with high turnover number. Within minutes, **2** is stoichiometrically and irreversibly consumed by the substrate to an unidentified species.

CONCLUSIONS

TBHP-mediated Wacker oxidations catalyzed by dimer **2** clearly require further investigation. However, these initial results are promising, and imply that reactivity beyond just oligomerization and isomerization of olefins can be realized. In this particular example, we exploit the ability of dimer **2** to dissociate in the presence of substrate to a reactive cation that may undergo fast ligand exchange with TBHP, accessing Wacker-type catalyst **1**. Mechanistic and kinetic studies must be done to determine whether a mechanism distinct from that shown by Sigman is at play.

This system shows great promise for optimization. α–Diimine ligands can be sterically and electronically tuned with ease to ultimately develop a general, efficient, and activator-free Wacker-like process. Perhaps bis(μ–hydroxy) palladium(II) dimers can even catalyze relatively similar oxidative transformations that typically require silver(I) salts for catalyst activation, such as oxidative cross-coupling or cyclization reactions.

EXPERIMENTALS

General Considerations and Instrumentation. $[(^{tBu}DAB_{Me})Pd(OH)]_2(BF_4)_2$ (**2**) was prepared as described in Chapter 4. 70 wt% tBuOOH (aq) was purchased from Sigma-Aldrich. All other chemicals and solvents were used as received.

Gas chromatography (GC) was performed using an Agilent 6890N instrument with a flame ionization detector (FID). Routine runs were performed using a DB-1 capillary column (10 m length, 0.10 mm diameter, 0.40 μm film) with the following program: hold at 35 °C for 2 min, ramp temperature at 2 °C/min to 50°C and hold for 2 min (total run time = 11.5 min), then ramp temperature at 100 °C/min to 290 °C and hold for 5 min (total run time = 18.9 min.) Response factors for olefins were calculated versus adamantane. A known mass of analyte and adamantane were added to a scintillation vial, then dissolved in ~1–2 mL CH_2Cl_2. The solution (4 μL) was then injected into the GC for analysis. Response factors for each analyte were calculated using the following formula: $[(mass_{analyte}) \times (area_{adamantane})] / [(area_{analyte}) \times (mass_{adamantane})]$

General Procedure for Wacker-type Oxidations of Olefins Catalyzed by 2. To a vial equipped with a stirbar, precatalyst **2** (12.0 mg, 0.009 mmol, .025 equiv) and adamantine

(internal GC standard, 30–70 mg) were added. Benchtop CH_2Cl_2 (12 mL) was added, followed by 70 wt% aq. tBuOOH (123 uL, 0.900 mmol, 2.5 equiv) at once. The yellow suspension instantaneously became an orange solution, which was stirred at room temperature for 5 minutes. Olefin substrate (0.36 mmol, 1.0 equiv) was added at once, and the orange reaction was stirred for 15 minutes. For GC analysis, an aliquot (~200 uL) was passed through a bed of silica, using CH_2Cl_2 as eluent, prior to injection. For workup, water (5 mL) was added, and the organic layer extracted. This was repeated three times, after which the organics were passed through a bed of silica, using CH_2Cl_2 as eluent, and dried over $MgSO_4$. The clear solution was filtered, and concentrated *in vacuo*, taking care not to evaporate volatile ketone products.

REFERENCES

1. Roussel, M.; Mimoun, H. *J. Org. Chem.* **1980**, *45* 5387.
2. (a) Mimoun, H.; Charpentier, R.; Mitschler, A.; Fischer, J.; Weiss, R. *J. Am. Chem. Soc.* **1980**, *102*, 1047. (b) Tsuji, J.; Nagashima, H.; Hori, K. *Chem. Lett.* **1980**, 257. (c) Nishimura, T.; Kakiuchi, N.; Onoue, T.; Ohe, K.; Uemura, S. *J. Chem. Soc., Perkin Trans. 1* **2000**, 1915. (d) Michel, B. W.; Camelio, A. M.; Cornell, C. N.; Sigman, M. S. *J. Am. Chem. Soc.* **2009**, *131*, 6076. (e) Michel, B. W.; Steffens, L. D.; Sigman, M. S. *J. Am. Chem. Soc.* **2009**, *133*, 8317.

APPENDIX C

Preliminary Mechanistic Studies on the Catalytic Aerobic Dehydrogenation of Cyclohexene by Palladium(II) Dimers: Evidence for an Olefin-Directed Homo-Allylic C-H Bond Activation

ABSTRACT

Palladium(II) bis(μ–hydroxy) dimers have been shown to C-H activate a variety of substrates stoichiometrically under relatively mild conditions. Catalytic C-H activation and oxidative functionalization has only been achieved with cyclohexene, however. Herein evidence is presented that suggests a mechanism other than allylic C-H activation and β-hydride elimination is at play.

INTRODUCTION

We recently reported that α-diimine-supported bis(μ–hydroxy) palladium(II) dimers (**1**) are precatalysts for the aerobic dehydrogenation of cyclohexene to benzene (eq. 1).[1]

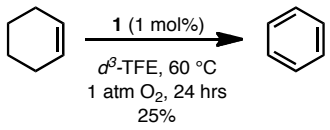

(1)

While the turnover frequency for this reaction is very low (~1/h), this was the first example of *catalytic* oxidation observed by dimer **1.** Based on previous observations, a mechanism involving a sequence of allylic C-H activation/β-hydride elimination/reoxidation was proposed (Scheme C.1).

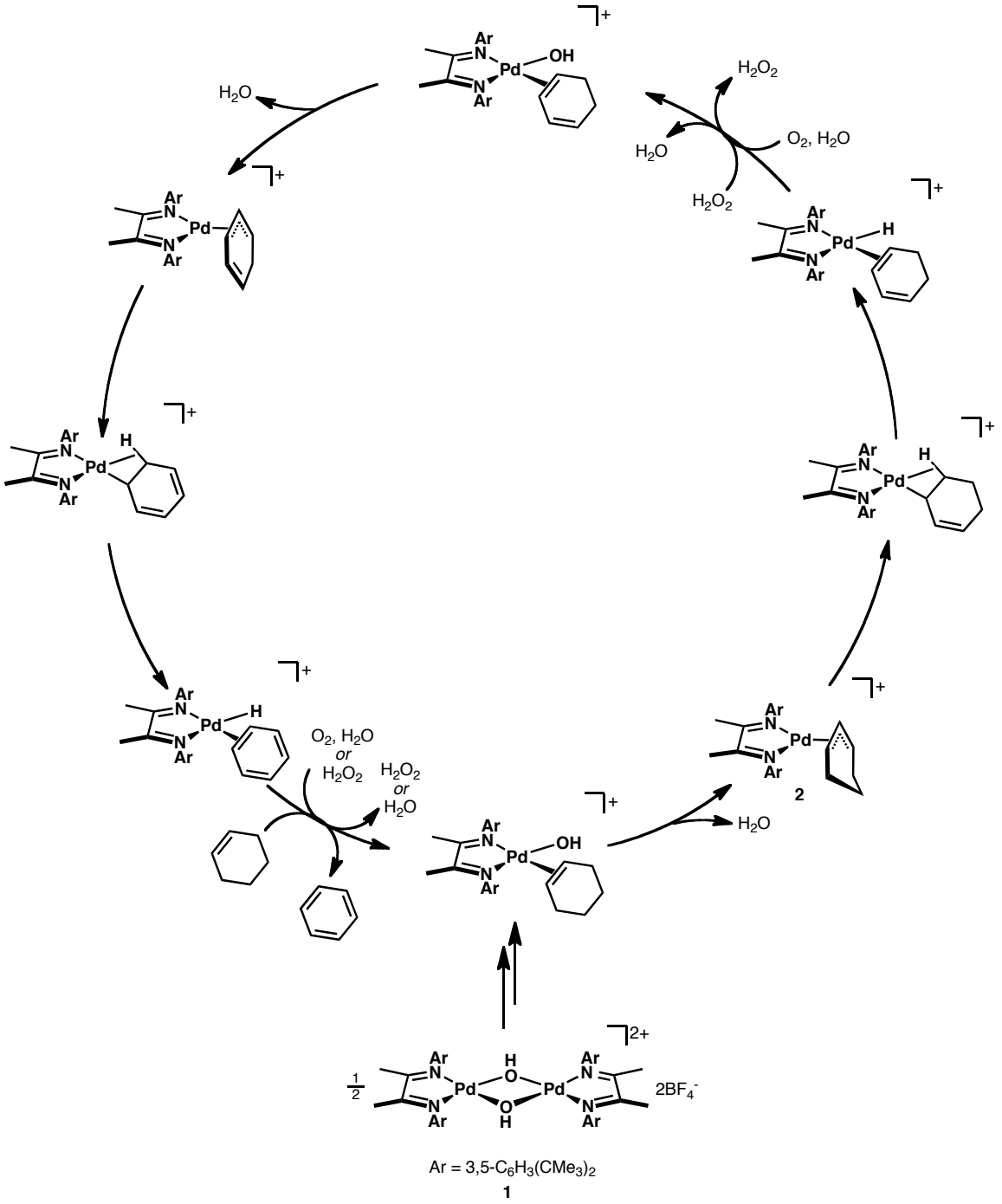

Scheme C.1. Plausible mechanism for the catalytic aerobic oxidation of cyclohexene by **1** involving allylic C-H bond activation

RESULTS AND DISCUSSION

To investigate whether aerobic dehydrogenation by **1** involves allylic C-H bond activation of cyclohexene, we independently synthesized the potential η^3-cyclohexenyl intermediate (**2**). Cyclohexene can be deprotonated under superbasic conditions and stannylated using $SnBu_3Cl$ to afford organostannane **3** in good yield (eq. 2). Bis(μ–chloro) dimer is treated with the stannane to immediately generate **2** in quantitative yield (eq. 3). X-ray diffraction analysis of crystals of **2** confirm η^3-coordination by palladium(II) (Figure C.1).

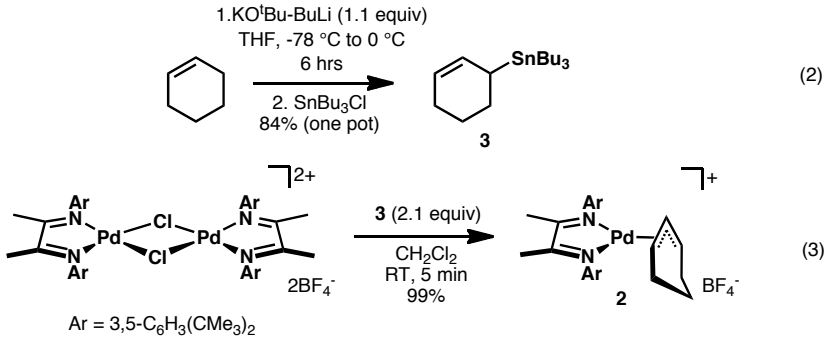

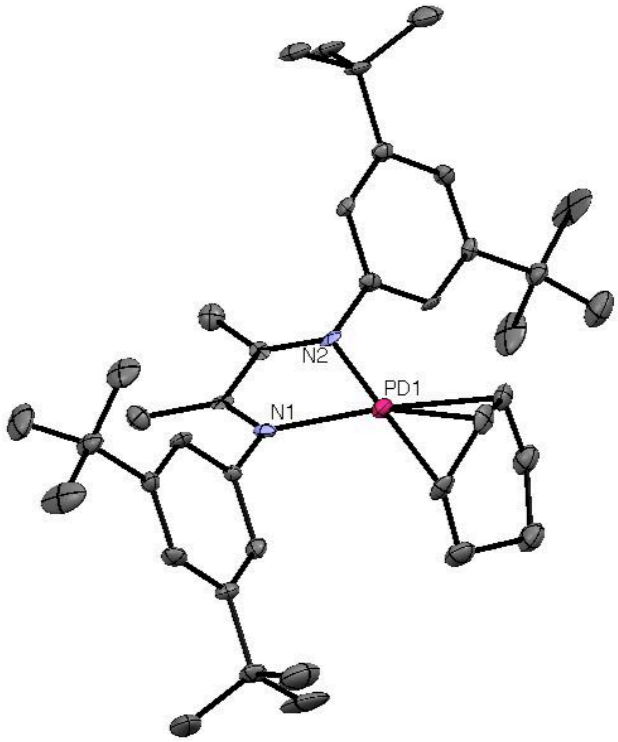

Figure C.1. Thermal ellipsoid representation of **2** at the 50% probability level. BF_4^- and all protons have been omitted for clarity. Atoms are color coded: carbon (gray), nitrogen (blue), palladium (pink)

Complex **2** is entirely unreactive in the presence of cyclohexene under aerobic dehydrogenation conditions (eq. 4). When **2** is heated to 100 °C for 3 days, the complex remains intact and neither cyclohexadiene nor benzene are observed. This is perhaps unsurprisingly giving the stability exhibited by analogous $[(^{tBu}DAB_{Me})Pd(\eta^3\text{-}C_3H_5)]^+$ toward olefin isomerization and oligomerization, a process that would we suspected might also require rearrangement to η^1-coordination (Chapter 4).

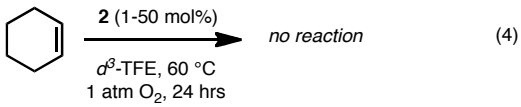

(4)

These results strongly suggest that aerobic dehydrogenation of cyclohexene does not involve an allylic C-H activated η^3–coordinated intermediate. Perhaps a C-H activated η^1 complex is formed directly; this would necessitate that β-hydride elimination be significantly faster than irreversible rearrangement to the η^3-cyclohexenyl complex **2**, since no signals corresponding to **2** are observed by ^{1}H NMR under catalytic conditions. Alternatively, an intriguing mechanism involving homo-allylic C-H activation of cyclohexene may be occurring (Scheme C.2). To our knowledge, olefin-directed homo-allylic C-H bond activations are unprecedented, although several formal homo-allylic functionalizations have been reported.[2] These involve β-hydride elimination from an allylic C-H activated species, and subsequent functionalization of the product diene. During our investigations into the stoichiometric C-H activation ability of bis((μ–hydroxy) platinum(II) dimers analogous to **1**, we isolated and characterized a platinum(II) cyclometalate that was generated upon C-H activation of the terminal methyl groups of neo-hexene (eq. 5).[3] Obviously the active platinum(II) complex cannot allylically C-H activate neo-hexene, but we were surprised to find that the homo-allylic, stronger terminal methyl C-H bonds could activate under mild conditions. This observation supports the possibility of homo-allylic C-H activation of cyclohexene by **1**, but why this pathway may be favored over allylic activation is not entirely clear.

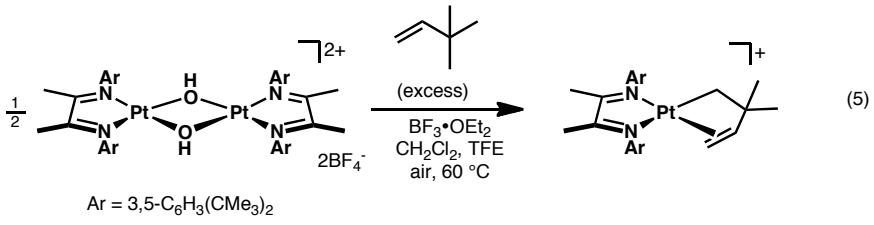

(5)

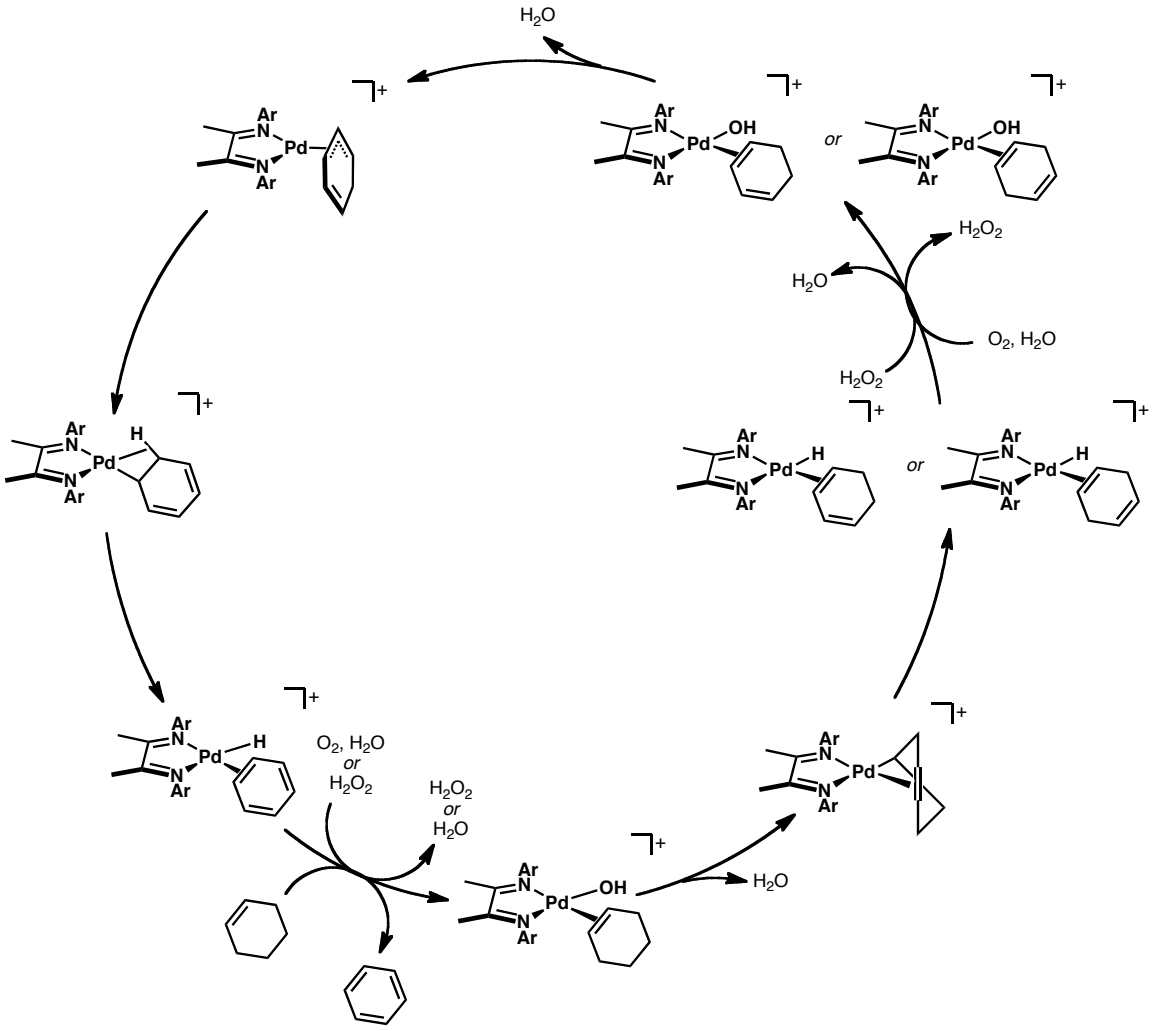

Scheme C.2. Plausible mechanism of catalytic aerobic oxidation of cyclohexene by **1** involving homo-allylic C-H activation

The question of C-H activation of cyclohexadiene, which is presumably an intermediate in the dehydrogenation of cyclohexene, still remains. Clearly, both isomers (1,3-cyclohexadiene and 1,4-cyclohexadiene) can only activate at allylic C-H bonds, suggesting that η^3-cyclohexa*dienyl* intermediates may not be a "thermodynamic well" and can exhibit further reactivity.

In these reactions, cyclohexanone is detected by GC, but the amount produced is less than the total amount of palladium added (0.65 mol cyclohexanone:Pd). Very small amounts of dimerized products are present (<5%), suggesting that once an active palladium(II) hydride is formed, it is rapidly re-oxidized by O_2 or H_2O_2 (or decomposes), in agreement with the mechanisms presented in Figures C.1 and C.3.

Interestingly, no cyclohexadiene is ever observed by GC in the reaction of **1** with cyclohexene under reaction conditions, suggesting that either cyclohexadiene never dissociates from the catalyst once formed in the cycle, or reacts much faster with the active catalyst than cyclohexene. While we cannot discount the first possibility, the latter almost certainly is true, since 15% of cyclohexadiene is converted to benzene by **1** within minutes under reaction conditions (TON = 90/h, eq. 6). At 10 minutes, no cyclohexadiene remains, having been converted to dimers and possibly trimers, which are observed by GC. Oxygenated products can be detected by GC-MS, but not quantified.

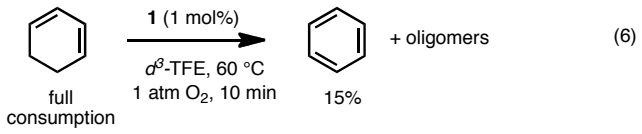

(6)

These results indicate that allylic C-H bond activation must necessarily occur for Pd-mediated cyclohexadiene dehydrogenation, and is substantially faster than C-H activation of cyclohexene. That the η^3-cyclohexadienyl intermediate can β-hydride eliminate suggests that the activation barrier to rearrangement to a η^1-coordination is significantly lower than that for η^3-cyclohexenyl complex **2.**

CONCLUSIONS

We have shown that the mechanism of aerobic dehydrogenation of cyclohexene by dimer **1** may involve both olefin-directed homo-allylic activation of a C-H bond, and allylic activation of the diene intermediate. The origins for the disparate reactivity of cyclohexene and cyclohexadiene are not fully understood, but investigating these issues will provide much needed insight into extending to other systems the dehydrogenation or C-H bond functionalization behavior of the dimers discussed above. Taken in concert with the observed dehydrogenation of linear α-olefins to access catalytically active palladium(II) hydrides (Chapter 4, a process that may also involve homo-allylic activation), these studies suggest that catalytic dehydrogenation of α-olefins is achievable.

EXPERIMENTALS

General Considerations and Instrumentation. $[(^{tBu}DAB_{Me})Pd(OH)]_2(BF_4)_2$ (**1**) and $[(^{tBu}DAB_{Me})Pd(Cl)]_2(BF_4)_2$ were prepared as described in Chapter 4. Organostannane **3** was prepared according to literature procedure.[5] ^1H and ^{13}C spectra were recorded on Varian Mercury 300 or Varian INOVA-500 spectrometers at room temperature, unless otherwise indicated. The data are reported by chemical shift (ppm) from tetramethylsilane, multiplicity (s, singlet; d, doublet; t, triplet; m, multiplet; dd, double doublet; dt, double triplet), coupling constants (Hz), and integration. All ^{13}C NMR data were collected proton-decoupled ($^{13}C\{^1H\}$), except where specified.

Gas chromatography (GC) was performed using an Agilent 6890N instrument with a flame ionization detector (FID). Routine runs were performed using a DB-1 capillary column (10 m length, 0.10 mm diameter, 0.40 μm film) with the following program: hold at 35 °C for 2 min, ramp temperature at 2 °C/min to 50°C and hold for 2 min (total run time = 11.5 min), then ramp temperature at 100 °C/min to 290 °C and hold for 5 min (total run time = 18.9 min.) Response factors for olefins were calculated versus adamantane. A known mass of analyte and adamantane were added to a scintillation vial, then dissolved in ~1–2 mL CH_2Cl_2. The solution (4 μL) was then injected into the GC for analysis. Response factors for each analyte were calculated using the following formula: $[(mass_{analyte}) \times (area_{adamantane})] / [(area_{analyte}) \times (mass_{adamantane})]$

[(^{tBu}DAB$_{Me}$)Pd(η^3-cyclohexenyl)](BF$_4$) (2). A vial equipped with a stirbar was charged with complex **3** (18.4 mg, 0.013 mmol, 1.0 equiv). CH_2Cl_2 (2 mL) was added. To the orange solution was added organostannane **2** (10.2 mg, .027 mmol, 2.1 equiv) at once. The reaction turned bright yellow instantaneously, and was stirred for 10 minutes. After concentration *in vacuo*, the yellow residue was washed thoroughly with petroleum ether to remove tin products, and dried *in vacuo* to afford **2** as a bright yellow powder (18.2 mg, .013 mmol). Crystals of **2** were obtained by slow evaporation of a saturated CH_2Cl_2 solution. ^{1}H NMR (300 MHz, CD_2Cl_2) δ: 1.27 (M, 4H), 1.36 (s, 36H), 1.82 (m, 2H), 2.34 (s, 6H), 4.36 (t, J = 6.2 Hz, 2H), 5.64 (t, J = 6.6 Hz, 1H), 6.93 (m, 4H), 7.38 (t, 1.7 Hz, 2H). Anal. Calcd. for $C_{38}H_{57}BF_4N_2Pd$: C, 62.09; H, 7.82; N, 3.81. Found: C, 61.99; H, 7.56; N, 3.54.

General Procedure for Aerobic Oxidation of Cyclohexene Catalyzed by 1. A 25 mL bomb equipped with a stirbar was charged with **1** (12 mg, 0.009 mmol, 0.01 equiv).

Benchtop TFE (1.8 mL) was added, followed by cyclohexene (64.8 mg, 0.79 mmol, 1.00 equiv) and adamantane (30–70 mg). The reaction was heated to 60 °C in an oil bath. The reaction was vigorously stirred. Aliquots for GC analysis (~200 uL) were removed under a constant stream of O_2, and diluted 10x with CH_2Cl_2 prior to injection.

X-Ray Crystal Data: General Procedure. Crystals of **2** grown from CH_2Cl_2 were removed quickly from a scintillation vial to a microscope slide coated with Paratone N oil. Samples were selected and mounted on a glass fiber with Paratone N oil. Data collection was carried out on a Bruker KAPPA APEX II diffractometer with a 0.71073 Å MoKα source. The structures were solved by direct methods. All non-hydrogen atoms were refined anisotropically. Some details regarding refined data and cell parameters are available in Crystallographic Information. Selected bond distances and angles are supplied as well.

REFERENCES

1. (a) Williams, T. J.; Caffyn, A. J. M.; Hazari, N.; Oblad, P. F.; Labinger, J. A.; Bercaw, J. E. *J. Am. Chem. Soc.* **2008**, *130*, 2418. (b) Bercaw, J. E.; Hazari, N.; Labinger, J. A.; Oblad, P. F. *Angew. Chem.* **2008**, *120*, 10089.
2. See, for example: Du, H.; Yuan, W.; Zhao, B.; Shi, Y. *J. Am. Chem. Soc.* **2007**, *129*, 7496.
3. Oblad, P. F. *Toward the upgrading of hydrocarbons: synthesis, characterization, and reactivity of platinum and palladium complexes (Thesis)*. California Institute of Technology, August 26 2011.
4. Pangborn, A. B.; Giardello, M. A.; Grubbs, R. H.; Rosen, R. K.; Timmers, F. J. *Organometallics* **1996**, *15*, 1518.
5. Kiyokawa, K.; Yasuda, M.; Baba, A. *Organometallics* **2011**, *30*, 2039.

APPENDIX D

X-Ray Crystallographic Tables

Chapter 1 X-Ray Crystallographic Tables

$[(PNP)K_2(THF)_3]_2$ (13, MSW11)

Table D.1.1. Crystal data and structure refinement for MSW11 (CCDC 787543)

Empirical formula	$C_{82}H_{90}K_4N_2O_6P_4$	
Formula weight	1479.84	
Crystallization Solvent	THF/pentane	
Crystal Habit	Column	
Crystal size	0.23 x 0.08 x 0.07 mm^3	
Crystal color	Red	
Data Collection		
Type of diffractometer	Bruker KAPPA APEX II	
Wavelength	0.71073 Å MoKα	
Data Collection Temperature	210(2) K	
θ range for 5485 reflections used in lattice determination	2.29 to 21.78°	
Unit cell dimensions	a = 10.1565(12) Å b = 11.1487(11) Å c = 17.888(2) Å	α= 85.015(5)° β= 87.679(5)° γ = 77.118(5)°
Volume	1966.6(4) $Å^3$	
Z	1	
Crystal system	Triclinic	
Space group	P-1	
Density (calculated)	1.250 Mg/m^3	
F(000)	780	
Data collection program	Bruker APEX2 v2009.7-0	
θ range for data collection	2.06 to 26.22°	
Completeness to θ = 26.22°	88.8 %	
Index ranges	$-12 \le h \le 12$, $-13 \le k \le 13$, $0 \le l \le 22$	
Data collection scan type	ω scans; 9 settings	
Data reduction program	Bruker SAINT-Plus v7.66A	
Reflections collected	7027	
Independent reflections	7027 [R_{int}= 0.0000]	
Absorption coefficient	0.360 mm^{-1}	
Absorption correction	TWINABS	

Max. and min. transmission	0.7453 and 0.5629

Structure Solution and Refinement

Structure solution program	SHELXS-97 (Sheldrick, 2008)
Primary solution method	Direct methods
Secondary solution method	Difference Fourier map
Hydrogen placement	Geometric positions
Structure refinement program	SHELXL-97 (Sheldrick, 2008)
Refinement method	Full matrix least-squares on F^2
Data / restraints / parameters	7027 / 0 / 442
Treatment of hydrogen atoms	Riding
Goodness-of-fit on F^2	1.627
Final R indices [$I>2\sigma(I)$, 4533 reflections]	R1 = 0.0560, *w*R2 = 0.0867
R indices (all data)	R1 = 0.1025, *w*R2 = 0.0907
Type of weighting scheme used	Sigma
Weighting scheme used	$w=1/\sigma^2(Fo^2)$
Max shift/error	0.000
Average shift/error	0.000
Largest diff. peak and hole	0.343 and -0.297 e

Table D.1.2. Atomic coordinates (x 10^4) and equivalent isotropic displacement parameters ($Å^2$x 10^3) for MSW11 (CCDC 787543). U(eq) is defined as the trace of the orthogonalized U^{ij} tensor.

	x	y	z	U_{eq}
K(1)	6922(1)	4014(1)	2797(1)	45(1)
K(2)	3724(1)	4722(1)	986(1)	49(1)
P(1)	3763(1)	3938(1)	2809(1)	41(1)
P(2)	6789(1)	5148(1)	886(1)	44(1)
O(1)	2393(3)	6950(2)	1327(1)	85(1)
O(2)	6706(2)	5876(2)	3664(1)	55(1)
O(3)	7793(2)	2256(2)	3916(1)	70(1)
N(1)	6123(2)	2157(2)	1898(1)	33(1)
C(1)	3619(3)	2363(2)	3025(1)	36(1)
C(2)	2978(3)	1912(3)	3670(2)	46(1)
C(3)	2923(3)	700(3)	3815(2)	56(1)
C(4)	3508(3)	-165(3)	3315(2)	62(1)
C(5)	4156(3)	220(2)	2680(2)	49(1)
C(6)	4230(3)	1445(2)	2530(2)	36(1)
C(7)	4962(3)	1760(2)	1827(2)	34(1)
C(8)	4505(3)	1613(2)	1126(2)	42(1)
C(9)	5237(3)	1863(2)	485(2)	44(1)
C(10)	6419(3)	2268(2)	555(2)	39(1)
C(11)	6827(3)	2396(2)	1271(2)	32(1)
C(12)	8130(3)	2766(2)	1402(1)	32(1)
C(13)	8239(3)	4012(2)	1232(1)	32(1)
C(14)	9466(3)	4279(2)	1441(1)	40(1)
C(15)	10475(3)	3410(3)	1792(2)	42(1)
C(16)	10349(3)	2211(3)	1951(2)	45(1)
C(17)	9163(3)	1904(2)	1758(1)	40(1)
C(18)	2474(3)	4859(2)	3393(1)	36(1)
C(19)	1173(3)	4670(3)	3563(2)	49(1)
C(20)	244(3)	5479(3)	3963(2)	61(1)
C(21)	558(4)	6515(3)	4206(2)	64(1)
C(22)	1817(3)	6750(3)	4034(2)	57(1)
C(23)	2756(3)	5926(2)	3638(2)	44(1)
C(24)	7425(3)	6577(2)	782(1)	38(1)
C(25)	8331(3)	6801(3)	212(2)	50(1)
C(26)	8689(3)	7925(3)	83(2)	62(1)
C(27)	8134(4)	8869(3)	522(2)	65(1)
C(28)	7254(3)	8683(3)	1094(2)	60(1)
C(29)	6906(3)	7543(2)	1230(2)	46(1)
C(30)	2875(4)	7902(3)	1601(2)	85(1)
C(31)	1650(5)	8845(4)	1750(3)	126(2)
C(32)	693(4)	8158(4)	2051(2)	105(1)
C(33)	1054(5)	7000(3)	1684(3)	97(2)
C(34)	6639(3)	7170(3)	3569(2)	61(1)
C(35)	6370(3)	7633(3)	4346(2)	63(1)
C(36)	5652(3)	6714(3)	4754(2)	57(1)
C(37)	6350(3)	5542(3)	4419(2)	61(1)
C(38)	7021(4)	1326(4)	3979(2)	80(1)
C(39)	7921(5)	263(4)	3641(2)	94(1)

C(40)	9321(4)	360(3)	3809(2)	85(1)
C(41)	9162(4)	1651(3)	4016(2)	74(1)

(PNP)Zr(NMe_2)$_2$ (15, MSW03)

Table D.1.3. Crystal data and structure refinement for MSW03 (CCDC 787542)

Empirical formula	$C_{33}H_{33}N_3P_2Zr \bullet ¼ (C_6H_6)$	
Formula weight	644.31	
Crystallization Solvent	Benzene/pentane	
Crystal Habit	Blade	
Crystal size	0.22 x 0.07 x 0.01 mm^3	
Crystal color	Orange/red	
Data Collection		
Type of diffractometer	Bruker KAPPA APEX II	
Wavelength	0.71073 Å MoKα	
Data Collection Temperature	100(2) K	
θ range for 9165 reflections used in lattice determination	2.45 to 24.48°	
Unit cell dimensions	a = 8.1980(9) Å b = 33.236(4) Å c = 23.311(2) Å	α= 90° β= 96.280(6)° γ = 90°
Volume	6313.4(12) Å^3	
Z	8	
Crystal system	Monoclinic	
Space group	P $2_1/c$	
Density (calculated)	1.356 Mg/m^3	
F(000)	2660	
θ range for data collection	1.23 to 25.35°	
Completeness to θ = 25.35°	89.0 %	
Index ranges	$-9 \le h \le 9$, $-39 \le k \le 38$, $-24 \le l \le 25$	
Data collection scan type	ω scans; 7 settings	
Reflections collected	51705	
Independent reflections	10283 [R_{int}= 0.0608]	
Absorption coefficient	0.477 mm^{-1}	
Absorption correction	Semi-empirical from equivalents	
Max. and min. transmission	0.7452 and 0.6212	

Structure Solution and Refinement

Structure solution program	SHELXS-97 (Sheldrick, 2008)
Primary solution method	Direct methods
Secondary solution method	Difference Fourier map
Hydrogen placement	Geometric positions
Structure refinement program	SHELXL-97 (Sheldrick, 2008)
Refinement method	Full matrix least-squares on F^2
Data / restraints / parameters	10283 / 0 / 723
Treatment of hydrogen atoms	Riding
Goodness-of-fit on F^2	2.255
Final R indices [I>2σ(I), 7388 reflections]	R1 = 0.0505, *w*R2 = 0.0734
R indices (all data)	R1 = 0.0852, *w*R2 = 0.0750
Type of weighting scheme used	Sigma
Weighting scheme used	$w=1/\sigma^2(Fo^2)$
Max shift/error	0.014
Average shift/error	0.000
Largest diff. peak and hole	1.692 and -0.913 e.Å^{-3}

Table D.1.4. Atomic coordinates (x 10^4) and equivalent isotropic displacement parameters ($Å^2$x 10^3) for MSW03 (CCDC 787542). U(eq) is defined as the trace of the orthogonalized U^{ij} tensor.

	x	y	z	U_{eq}	Occ
Zr(1)	5078(1)	257(1)	6790(1)	16(1)	1
P(1A)	6952(1)	-110(1)	7660(1)	18(1)	1
P(2A)	2802(1)	837(1)	6595(1)	17(1)	1
N(1A)	4978(4)	672(1)	7631(2)	16(1)	1
N(2A)	6733(4)	375(1)	6248(1)	19(1)	1
N(3A)	3706(4)	-192(1)	6419(1)	18(1)	1
C(1A)	4910(5)	-226(2)	7865(2)	17(1)	1
C(2A)	4184(5)	-619(2)	7823(2)	22(1)	1
C(3A)	2668(6)	-691(2)	8002(2)	25(1)	1
C(4A)	1819(6)	-393(2)	8246(2)	29(1)	1
C(5A)	2472(6)	-11(2)	8289(2)	24(1)	1
C(6A)	3979(5)	81(1)	8096(2)	16(1)	1
C(7A)	4531(5)	506(2)	8123(2)	19(1)	1
C(8A)	4513(5)	732(2)	8622(2)	22(1)	1
C(9A)	4941(6)	1129(2)	8620(2)	27(1)	1
C(10A)	5372(5)	1302(1)	8122(2)	21(1)	1
C(11A)	5356(5)	1069(1)	7625(2)	15(1)	1
C(12A)	5647(5)	1254(1)	7072(2)	15(1)	1
C(13A)	6916(5)	1530(1)	7048(2)	21(1)	1
C(14A)	7273(6)	1704(1)	6549(2)	26(1)	1
C(15A)	6306(6)	1605(1)	6044(2)	25(1)	1
C(16A)	5001(5)	1350(1)	6054(2)	21(1)	1
C(17A)	4595(5)	1164(1)	6560(2)	15(1)	1
C(18A)	7651(5)	-601(1)	7415(2)	17(1)	1
C(19A)	7997(5)	-921(2)	7806(2)	22(1)	1
C(20A)	8609(6)	-1281(2)	7641(2)	27(1)	1
C(21A)	8935(5)	-1337(2)	7079(2)	28(1)	1
C(22A)	8623(6)	-1030(2)	6688(2)	30(1)	1
C(23A)	7996(5)	-665(1)	6851(2)	22(1)	1
C(24A)	1791(5)	862(1)	5847(2)	16(1)	1
C(25A)	908(5)	1209(1)	5669(2)	22(1)	1
C(26A)	-4(5)	1225(2)	5135(2)	24(1)	1
C(27A)	-67(6)	899(2)	4773(2)	25(1)	1
C(28A)	780(5)	553(2)	4936(2)	26(1)	1
C(29A)	1725(5)	535(1)	5472(2)	22(1)	1
C(30A)	8282(5)	558(1)	6487(2)	32(1)	1
C(31A)	6557(6)	396(1)	5621(2)	31(1)	1
C(32A)	2112(5)	-306(1)	6594(2)	27(1)	1
C(33A)	4132(6)	-449(1)	5948(2)	30(1)	1
Zr(2)	654(1)	2119(1)	9326(1)	19(1)	1
P(1B)	-1736(2)	2210(1)	8456(1)	20(1)	1
P(2B)	2698(2)	1558(1)	9831(1)	22(1)	1
N(1B)	246(4)	1505(1)	8768(2)	18(1)	1
N(2B)	-547(5)	2338(1)	9961(2)	26(1)	1
N(3B)	2276(5)	2545(1)	9177(2)	23(1)	1

C(1B)	-173(5)	2203(1)	7952(2)	18(1)	1
C(2B)	134(5)	2531(1)	7594(2)	21(1)	1
C(3B)	1275(6)	2513(2)	7199(2)	27(1)	1
C(4B)	2152(6)	2165(2)	7136(2)	28(1)	1
C(5B)	1862(5)	1837(2)	7471(2)	22(1)	1
C(6B)	739(5)	1850(1)	7877(2)	15(1)	1
C(7B)	410(5)	1481(1)	8200(2)	18(1)	1
C(8B)	168(5)	1116(2)	7906(2)	23(1)	1
C(9B)	-330(6)	784(2)	8183(2)	29(1)	1
C(10B)	-541(5)	810(2)	8757(2)	28(1)	1
C(11B)	-216(5)	1173(2)	9049(2)	22(1)	1
C(12B)	-434(6)	1206(1)	9671(2)	23(1)	1
C(13B)	-1857(6)	1046(2)	9854(2)	37(2)	1
C(14B)	-2157(7)	1067(2)	10421(3)	49(2)	1
C(15B)	-1014(7)	1257(2)	10819(2)	45(2)	1
C(16B)	415(6)	1408(2)	10641(2)	32(1)	1
C(17B)	783(6)	1387(1)	10072(2)	23(1)	1
C(18B)	-2564(5)	2723(1)	8400(2)	20(1)	1
C(19B)	-3826(5)	2806(1)	7961(2)	24(1)	1
C(20B)	-4633(6)	3172(2)	7928(2)	28(1)	1
C(21B)	-4219(6)	3463(2)	8329(2)	30(1)	1
C(22B)	-3002(6)	3388(2)	8766(2)	46(2)	1
C(23B)	-2180(6)	3023(1)	8803(2)	35(2)	1
C(24B)	3766(5)	1777(2)	10491(2)	21(1)	1
C(25B)	4428(6)	1529(2)	10940(2)	36(2)	1
C(26B)	5358(7)	1687(2)	11410(2)	49(2)	1
C(27B)	5682(6)	2093(2)	11451(2)	42(2)	1
C(28B)	5015(6)	2342(2)	11020(2)	34(1)	1
C(29B)	4069(5)	2182(2)	10543(2)	28(1)	1
C(30B)	-2188(6)	2177(2)	10009(2)	45(2)	1
C(31B)	-57(6)	2603(2)	10442(2)	51(2)	1
C(32B)	3461(6)	2399(2)	8810(2)	40(2)	1
C(33B)	2564(6)	2965(1)	9335(2)	45(2)	1
C(1C)	989(7)	10115(3)	135(3)	74(4)	0.50
C(2C)	1768(11)	9884(3)	-251(4)	308(15)	0.50
C(3C)	3469(12)	9888(3)	-228(4)	299(15)	0.50
C(4C)	4392(7)	10122(3)	181(4)	76(4)	0.50
C(5C)	3613(7)	10353(2)	567(3)	36(3)	0.50
C(6C)	1912(7)	10350(2)	544(3)	23(2)	0.50

Chapter 2 X-Ray Crystallographic Tables

(*meso*-PNP-H_2)$PdCl_2$ (*meso*-6, MSW07)

Table D.2.1. Crystal data and structure refinement for MSW07 (CCDC 826390)

Empirical formula	$C_{29}H_{23}Cl_2NP_2Pd \bullet CH_2Cl_2$	
Formula weight	709.65	
Crystallization Solvent	Dichloromethane/toluene	
Crystal Habit	Block	
Crystal size	0.20 x 0.16 x 0.15 mm^3	
Crystal color	Yellow	
Data Collection		
Type of diffractometer	Bruker KAPPA APEX II	
Wavelength	0.71073 Å MoKα	
Data Collection Temperature	100(2) K	
θ range for 9635 reflections used in lattice determination	2.61 to 37.46°	
Unit cell dimensions	a = 8.5973(5) Å b = 20.1537(11) Å c = 17.2554(10) Å	α= 90° β= 101.395(3)° γ = 90°
Volume	2930.9(3) $Å^3$	
Z	4	
Crystal system	Monoclinic	
Space group	P $2_1/c$	
Density (calculated)	1.608 Mg/m^3	
F(000)	1424	
Data collection program	Bruker APEX2 v2009.7-0	
θ range for data collection	2.35 to 37.46°	
Completeness to θ = 37.46°	99.7 %	
Index ranges	$-14 \le h \le 14$, $-31 \le k \le 34$, $-29 \le l \le 29$	
Data collection scan type	ω scans; 10 settings	
Data reduction program	Bruker SAINT-Plus v7.66A	
Reflections collected	95436	
Independent reflections	15348 [R_{int}= 0.0327]	
Absorption coefficient	1.129 mm^{-1}	
Absorption correction	Semi-empirical from equivalents	
Max. and min. transmission	0.7473 and 0.6698	

Structure Solution and Refinement

Structure solution program	SHELXS-97 (Sheldrick, 2008)
Primary solution method	Direct methods
Secondary solution method	Difference Fourier map
Hydrogen placement	Difference Fourier map
Structure refinement program	SHELXL-97 (Sheldrick, 2008)
Refinement method	Full matrix least-squares on F^2
Data / restraints / parameters	15348 / 0 / 443
Treatment of hydrogen atoms	Unrestrained
Goodness-of-fit on F^2	2.464
Final R indices [I>2σ(I), 13315 reflections]	R1 = 0.0306, *w*R2 = 0.0572
R indices (all data)	R1 = 0.0383, *w*R2 = 0.0579
Type of weighting scheme used	Sigma
Weighting scheme used	$w=1/\sigma^2(Fo^2)$
Max shift/error	0.003
Average shift/error	0.000
Largest diff. peak and hole	2.224 and -1.953 e.Å^{-3}

Table D.2.2. Atomic coordinates (x 10^4) and equivalent isotropic displacement parameters ($Å^2$x 10^3) for MSW07 (CCDC 826390). U(eq) is defined as the trace of the orthogonalized U^{ij} tensor.

	x	y	z	U_{eq}
Pd(1)	2177(1)	9512(1)	3072(1)	10(1)
Cl(1)	2368(1)	10449(1)	2275(1)	15(1)
Cl(2)	1211(1)	10121(1)	4034(1)	15(1)
P(1)	3119(1)	8921(1)	2173(1)	11(1)
P(2)	1904(1)	8603(1)	3761(1)	11(1)
N(1)	112(1)	8110(1)	2165(1)	13(1)
C(1)	1938(1)	8900(1)	1181(1)	13(1)
C(2)	2146(2)	9399(1)	648(1)	16(1)
C(3)	1328(2)	9379(1)	-128(1)	21(1)
C(4)	304(2)	8859(1)	-389(1)	22(1)
C(5)	70(2)	8365(1)	137(1)	19(1)
C(6)	854(1)	8381(1)	928(1)	14(1)
C(7)	400(1)	7878(1)	1475(1)	14(1)
C(8)	142(2)	7216(1)	1245(1)	20(1)
C(9)	-484(2)	6788(1)	1726(1)	21(1)
C(10)	-877(2)	7031(1)	2410(1)	17(1)
C(11)	-565(1)	7693(1)	2612(1)	13(1)
C(12)	-1067(1)	7982(1)	3315(1)	13(1)
C(13)	-2580(2)	7827(1)	3446(1)	18(1)
C(14)	-3155(2)	8109(1)	4064(1)	20(1)
C(15)	-2241(2)	8560(1)	4563(1)	18(1)
C(16)	-718(1)	8713(1)	4456(1)	14(1)
C(17)	-122(1)	8423(1)	3842(1)	12(1)
C(18)	5100(1)	9178(1)	2090(1)	14(1)
C(19)	5744(2)	9020(1)	1429(1)	18(1)
C(20)	7279(2)	9214(1)	1403(1)	22(1)
C(21)	8179(2)	9563(1)	2025(1)	23(1)
C(22)	7559(2)	9716(1)	2684(1)	23(1)
C(23)	6017(1)	9525(1)	2717(1)	17(1)
C(24)	3094(1)	8537(1)	4749(1)	13(1)
C(25)	3279(2)	7911(1)	5099(1)	21(1)
C(26)	4229(2)	7832(1)	5842(1)	27(1)
C(27)	5002(2)	8374(1)	6238(1)	24(1)
C(28)	4839(2)	8993(1)	5889(1)	24(1)
C(29)	3884(2)	9080(1)	5148(1)	20(1)
C(41)	4376(2)	8976(1)	8539(1)	31(1)
Cl(3)	5782(1)	8696(1)	9352(1)	50(1)
Cl(4)	3234(1)	8315(1)	8083(1)	76(1)

(*meso*-PNP-H_2)$PdBr_2$ (*meso*-7, MSW15)

Table D.2.3. Crystal data and structure refinement for MSW15 (CCDC 826393)

Empirical formula	$C_{29}H_{23}NP_2Br_2Pd \bullet CH_2Cl_2$	
Formula weight	798.57	
Crystallization Solvent	Dichloromethane/pentane	
Crystal Habit	Block	
Crystal size	0.30 x 0.28 x 0.24 mm^3	
Crystal color	Yellow	
Data Collection		
Type of diffractometer	Bruker SMART 1000	
Wavelength	0.71073 Å MoKα	
Data Collection Temperature	100(2) K	
θ range for 9148 reflections used in lattice determination	2.31 to 27.49°	
Unit cell dimensions	a = 8.6480(2) Å b = 20.6074(5) Å c = 17.4380(4) Å	α= 90° β= 101.4870(10)° γ = 90°
Volume	3045.43(12) $Å^3$	
Z	4	
Crystal system	Monoclinic	
Space group	P $2_1/c$	
Density (calculated)	1.742 Mg/m^3	
F(000)	1568	
θ range for data collection	1.55 to 27.52°	
Completeness to θ = 27.52°	99.9 %	
Index ranges	$-11 \le h \le 11$, $-26 \le k \le 26$, $-22 \le l \le 22$	
Data collection scan type	ω scans at 14 settings	
Reflections collected	101185	
Independent reflections	7008 [R_{int}= 0.0274]	
Absorption coefficient	3.535 mm^{-1}	
Absorption correction	Semi-empirical from equivalents	
Max. and min. transmission	0.7456 and 0.6399	

Structure Solution and Refinement

Structure solution program	SHELXS-97 (Sheldrick, 2008)
Primary solution method	Direct methods
Secondary solution method	Difference Fourier map
Hydrogen placement	Difference Fourier map
Structure refinement program	SHELXL-97 (Sheldrick, 2008)
Refinement method	Full matrix least-squares on F^2
Data / restraints / parameters	7008 / 0 / 463
Treatment of hydrogen atoms	Unrestrained
Goodness-of-fit on F^2	3.002
Final R indices [I>2σ(I), 6720 reflections]	R1 = 0.0167, *w*R2 = 0.0354
R indices (all data)	R1 = 0.0180, *w*R2 = 0.0354
Type of weighting scheme used	Sigma
Weighting scheme used	$w=1/\sigma^2(Fo^2)$
Max shift/error	0.004
Average shift/error	0.000
Largest diff. peak and hole	0.452 and -0.231 e.Å^{-3}

Table D.2.4. Atomic coordinates (x 10^4) and equivalent isotropic displacement parameters ($Å^2$x 10^3) for MSW15 (CCDC 826393). U(eq) is defined asthe trace of the orthogonalized U^{ij} tensor.

	x	y	z	U_{eq}	Occ
Pd(1)	7815(1)	514(1)	6925(1)	11(1)	1
Br(1)	8779(1)	-107(1)	5902(1)	17(1)	1
Br(2)	7635(1)	-464(1)	7734(1)	17(1)	1
P(1)	8071(1)	1418(1)	6256(1)	12(1)	1
P(2)	6899(1)	1081(1)	7839(1)	13(1)	1
N(1)	9875(1)	1889(1)	7851(1)	15(1)	1
C(1)	10080(2)	1613(1)	6174(1)	14(1)	1
C(2)	10671(2)	1346(1)	5552(1)	17(1)	1
C(3)	12177(2)	1504(1)	5448(1)	21(1)	1
C(4)	13093(2)	1936(1)	5953(1)	24(1)	1
C(5)	12517(2)	2199(1)	6575(1)	21(1)	1
C(6)	11023(2)	2035(1)	6704(1)	16(1)	1
C(7)	10521(2)	2305(1)	7409(1)	16(1)	1
C(8)	10811(2)	2954(1)	7613(1)	22(1)	1
C(9)	10418(2)	3183(1)	8296(1)	26(1)	1
C(10)	9818(2)	2755(1)	8770(1)	25(1)	1
C(11)	9585(2)	2106(1)	8536(1)	17(1)	1
C(12)	9150(2)	1610(1)	9075(1)	17(1)	1
C(13)	9933(2)	1625(1)	9860(1)	23(1)	1
C(14)	9710(2)	1141(1)	10379(1)	26(1)	1
C(15)	8695(2)	630(1)	10123(1)	24(1)	1
C(16)	7872(2)	611(1)	9354(1)	19(1)	1
C(17)	8078(2)	1101(1)	8826(1)	15(1)	1
C(18)	6872(2)	1504(1)	5278(1)	16(1)	1
C(19)	6027(2)	990(1)	4881(1)	23(1)	1
C(20)	5098(2)	1089(1)	4141(1)	28(1)	1
C(21)	5002(2)	1698(1)	3804(1)	30(1)	1
C(22)	5821(2)	2212(1)	4201(1)	33(1)	1
C(23)	6756(2)	2120(1)	4939(1)	25(1)	1
C(24)	4922(2)	833(1)	7923(1)	17(1)	1
C(25)	4293(2)	987(1)	8579(1)	23(1)	1
C(26)	2755(2)	803(1)	8604(1)	28(1)	1
C(27)	1850(2)	472(1)	7986(1)	30(1)	1
C(28)	2461(2)	321(1)	7334(1)	29(1)	1
C(29)	3999(2)	501(1)	7301(1)	22(1)	1
Cl(3A)	4272(3)	3671(1)	5670(2)	48(1)	0.577(12)
Cl(4A)	6933(8)	3393(3)	6906(2)	85(2)	0.577(12)
C(40A)	5730(9)	3979(3)	6467(4)	26(1)	0.577(12)
Cl(3B)	4494(9)	3875(6)	5638(2)	100(2)	0.423(12)
Cl(4B)	6424(4)	3185(1)	6946(2)	47(1)	0.423(12)
C(40B)	5850(20)	3942(8)	6456(11)	82(6)	0.423(12)

(*rac*-PNP-H$_2$)PdBr$_2$ (*rac*-7, MSW14)

Table D.2.5. Crystal data and structure refinement for MSW14 (CCDC 826392)

Empirical formula	$C_{29}H_{23}NP_2Br_2Pd$
Formula weight	713.64
Crystallization Solvent	Dichloromethane/pentane
Crystal Habit	Blade
Crystal size	0.38 x 0.23 x 0.21 mm^3
Crystal color	Pale yellow

Data Collection

Type of diffractometer	Bruker SMART 1000	
Wavelength	0.71073 Å MoKα	
Data Collection Temperature	100(2) K	
θ range for 9942 reflections used in lattice determination	2.28 to 33.78°	
Unit cell dimensions	a = 16.0163(4) Å b = 17.8940(5) Å c = 18.3935(5) Å	α= 90° β= 100.4990(10)° γ = 90°
Volume	5183.2(2) Å^3	
Z	8	
Crystal system	Monoclinic	
Space group	P $2_1/c$	
Density (calculated)	1.829 Mg/m^3	
F(000)	2800	
Data collection program	Bruker SMART v5.630	
θ range for data collection	1.29 to 33.92°	
Completeness to θ = 33.92°	99.4 %	
Index ranges	$-25 \le h \le 25$, $-28 \le k \le 28$, $-28 \le l \le 28$	
Data collection scan type	ω scans; 12 settings	
Data reduction program	Bruker SAINT-Plus v7.66A	
Reflections collected	222414	
Independent reflections	20877 [R_{int}= 0.0492]	
Absorption coefficient	3.943 mm^{-1}	
Absorption correction	Semi-empirical from equivalents	
Max. and min. transmission	0.7467 and 0.6080	

Structure Solution and Refinement

Structure solution program	SHELXS-97 (Sheldrick, 2008)
Primary solution method	Direct methods
Secondary solution method	Difference Fourier map
Hydrogen placement	Difference Fourier map
Structure refinement program	SHELXL-97 (Sheldrick, 2008)
Refinement method	Full matrix least-squares on F^2
Data / restraints / parameters	20877 / 0 / 815
Treatment of hydrogen atoms	Unrestrained
Goodness-of-fit on F^2	1.948
Final R indices [I>2σ(I), 16348 reflections]	R1 = 0.0299, *w*R2 = 0.0456
R indices (all data)	R1 = 0.0460, *w*R2 = 0.0470
Type of weighting scheme used	Sigma
Weighting scheme used	$w=1/\sigma^2(Fo^2)$
Max shift/error	0.004
Average shift/error	0.000
Largest diff. peak and hole	1.449 and -0.508 e.Å^{-3}

Table D.2.6. Atomic coordinates (x 10^4) and equivalent isotropic displacement parameters ($Å^2$x 10^3) for MSW14 (CCDC 826392). U(eq) is defined as the trace of the orthogonalized U^{ij} tensor.

	x	y	z	U_{eq}
Pd(1)	4030(1)	4840(1)	5607(1)	12(1)
Br(1)	4259(1)	6015(1)	6355(1)	17(1)
Br(2)	5528(1)	4446(1)	6044(1)	16(1)
P(1A)	2645(1)	5193(1)	5301(1)	13(1)
P(2A)	3971(1)	3783(1)	4947(1)	14(1)
N(1)	2197(1)	3788(1)	5457(1)	13(1)
C(1A)	2116(1)	5189(1)	6096(1)	14(1)
C(2A)	2015(1)	5889(1)	6410(1)	16(1)
C(3A)	1685(1)	5948(1)	7054(1)	17(1)
C(4A)	1451(1)	5313(1)	7393(1)	18(1)
C(5A)	1526(1)	4619(1)	7084(1)	16(1)
C(6A)	1867(1)	4534(1)	6437(1)	14(1)
C(7A)	1922(1)	3788(1)	6104(1)	14(1)
C(8A)	1642(1)	3129(1)	6392(1)	20(1)
C(9A)	1582(1)	2483(1)	5971(1)	22(1)
C(10A)	1800(1)	2504(1)	5275(1)	20(1)
C(11A)	2124(1)	3166(1)	5040(1)	14(1)
C(12A)	2346(1)	3243(1)	4291(1)	15(1)
C(13A)	1747(1)	3034(1)	3677(1)	19(1)
C(14A)	1902(1)	3141(1)	2964(1)	22(1)
C(15A)	2667(1)	3440(1)	2854(1)	21(1)
C(16A)	3283(1)	3640(1)	3464(1)	19(1)
C(17A)	3123(1)	3546(1)	4182(1)	16(1)
C(18A)	1881(1)	5011(1)	4459(1)	16(1)
C(19A)	1053(1)	4768(1)	4478(1)	17(1)
C(20A)	479(1)	4678(1)	3830(1)	17(1)
C(21A)	718(1)	4824(1)	3147(1)	22(1)
C(22A)	1539(1)	5078(1)	3127(1)	22(1)
C(23A)	2115(1)	5171(1)	3781(1)	19(1)
C(24A)	4124(1)	2923(1)	5480(1)	17(1)
C(25A)	4103(1)	2904(1)	6229(1)	22(1)
C(26A)	4218(2)	2229(1)	6614(1)	29(1)
C(27A)	4354(1)	1579(1)	6247(1)	30(1)
C(28A)	4383(1)	1594(1)	5500(1)	29(1)
C(29A)	4267(1)	2262(1)	5114(1)	24(1)
Pd(2)	964(1)	9895(1)	4380(1)	11(1)
Br(3)	788(1)	11134(1)	3743(1)	15(1)
Br(4)	-565(1)	9607(1)	3936(1)	16(1)
P(1B)	2366(1)	10191(1)	4725(1)	12(1)
P(2B)	981(1)	8748(1)	4871(1)	14(1)
N(2)	2791(1)	8815(1)	4396(1)	13(1)
C(1B)	2908(1)	10293(1)	3942(1)	14(1)
C(2B)	2988(1)	11030(1)	3699(1)	17(1)
C(3B)	3324(1)	11175(1)	3065(1)	19(1)
C(4B)	3582(1)	10591(1)	2673(1)	21(1)
C(5B)	3524(1)	9864(1)	2913(1)	18(1)
C(6B)	3180(1)	9695(1)	3545(1)	15(1)

C(7B)	3130(1)	8911(1)	3787(1)	14(1)
C(8B)	3473(1)	8308(1)	3453(1)	20(1)
C(9B)	3497(1)	7611(1)	3783(1)	23(1)
C(10B)	3198(1)	7524(1)	4440(1)	20(1)
C(11B)	2846(1)	8144(1)	4731(1)	15(1)
C(12B)	2585(1)	8116(1)	5468(1)	16(1)
C(13B)	3161(1)	7820(1)	6058(1)	21(1)
C(14B)	2976(1)	7815(1)	6767(1)	24(1)
C(15B)	2210(1)	8096(1)	6898(1)	23(1)
C(16B)	1628(1)	8383(1)	6316(1)	20(1)
C(17B)	1806(1)	8399(1)	5600(1)	16(1)
C(18B)	3110(1)	9899(1)	5548(1)	15(1)
C(19B)	3936(1)	9671(1)	5514(1)	17(1)
C(20B)	4498(1)	9504(1)	6148(1)	18(1)
C(21B)	4246(1)	9560(1)	6843(1)	21(1)
C(22B)	3423(1)	9796(1)	6877(1)	21(1)
C(23B)	2862(1)	9961(1)	6235(1)	18(1)
C(24B)	800(1)	7992(1)	4195(1)	18(1)
C(25B)	642(1)	8139(1)	3440(1)	23(1)
C(26B)	462(1)	7557(1)	2924(1)	27(1)
C(27B)	446(1)	6830(1)	3172(1)	31(1)
C(28B)	607(2)	6679(1)	3916(1)	35(1)
C(29B)	783(1)	7256(1)	4434(1)	29(1)

(*meso*-PNP-H_2)PdI_2 (*meso*-8, msw18)

Table D.2.7. Crystal data and structure analysis details for msw18

Empirical formula	C30 H23 Cl2 I2 N P2 Pd
Formula weight	890.53
Crystallization solvent	CH_2Cl_2
Crystal shape	blade
Crystal color	dichroic light/dark orange
Crystal size	0.03 x 0.21 x 0.36 mm

Data Collection

Preliminary photograph(s)	rotation	
Type of diffractometer	Bruker SMART 1000 CCD	
Wavelength	0.71073 Å MoK	
Data collection temperature	100 K	
Theta range for 4845 reflections used in lattice determination	2.35 to 29.56°	
Unit cell dimensions	a = 12.8113(14) Å b = 15.4034(16) Å c = 15.7905(17) Å	α= 88.163(2)° β= 78.075(2)° γ = 86.922(2)°
Volume	3043.7(6) $Å^3$	
Z	4	
Crystal system	triclinic	
Space group	P -1 (# 2)	
Density (calculated)	1.943 g/cm^3	
F(000)	1704	
Theta range for data collection	1.9 to 30.1°	
Completeness to theta = 25.00°	98.0%	
Index ranges	$-17 \le h \le 17$, $-21 \le k \le 21$, $0 \le l \le 21$	
Data collection scan type	and scans	
Reflections collected	15543	
Independent reflections	15543 [R_{int}= 0.0000]	
Reflections > 2σ(I)	13607	
Average σ(I)/(net I)	0.0493	
Absorption coefficient	2.94 mm^{-1}	
Absorption correction	Semi-empirical from equivalents	

Max. and min. transmission	1.000000 and 0.751706

Structure Solution and Refinement

Primary solution method	direct
Secondary solution method	difmap
Hydrogen placement	geom
Refinement method	Full-matrix least-squares on F^2
Data / restraints / parameters	15543 / 0 / 686
Treatment of hydrogen atoms	constr
Goodness-of-fit on F^2	1.72
Final R indices [I>2 ∫(I), 13607 reflections]	R1 = 0.0392, wR2 = 0.0674
R indices (all data)	R1 = 0.0511, wR2 = 0.0686
Type of weighting scheme used	calc
Weighting scheme used	calc w=1/[^2^(Fo^2^)]
Max shift/error	0.001
Average shift/error	0.000
Largest diff. peak and hole	2.21 and -1.13 e·$Å^{-3}$

Table D.2.8. Atomic coordinates (x 10^4) and equivalent isotropic displacement parameters ($Å^2$x 10^3) for msw18. U(eq) is defined as one third of the trace of the orthogonalized U^{ij} tensor.

	x	y	z	U(eq)
Pd(1A)	7501(1)	2676(1)	1714(1)	9(1)
I(1A)	7059(1)	1629(1)	549(1)	16(1)
I(2A)	7995(1)	1341(1)	2681(1)	14(1)
P(1A)	7152(1)	3863(1)	930(1)	11(1)
P(2A)	7680(1)	3601(1)	2747(1)	10(1)
N(1A)	5380(3)	3999(3)	2486(3)	13(1)
C(1A)	5932(4)	3843(4)	519(4)	14(1)
C(2A)	6019(4)	3578(4)	-316(4)	15(1)
C(3A)	5109(5)	3495(4)	-654(4)	19(1)
C(4A)	4123(5)	3709(4)	-143(4)	19(1)
C(5A)	4032(5)	3977(4)	695(4)	19(1)
C(6A)	4924(4)	4067(4)	1048(4)	14(1)
C(7A)	4777(4)	4363(4)	1959(4)	15(1)
C(8A)	3978(4)	5004(4)	2240(4)	16(1)
C(9A)	3792(5)	5255(4)	3081(4)	20(1)
C(10A)	4378(4)	4869(4)	3632(4)	17(1)
C(11A)	5162(4)	4207(4)	3318(4)	12(1)
C(12A)	5714(4)	3739(4)	3945(3)	13(1)
C(13A)	5110(5)	3593(4)	4789(4)	19(1)
C(14A)	5552(5)	3163(4)	5423(4)	17(1)
C(15A)	6591(5)	2848(4)	5250(3)	17(1)
C(16A)	7211(5)	2987(4)	4431(4)	17(1)
C(17A)	6781(4)	3427(4)	3783(3)	8(1)
C(18A)	8226(4)	4161(4)	43(3)	14(1)
C(19A)	8889(5)	3523(4)	-433(4)	21(1)
C(20A)	9726(5)	3765(4)	-1087(4)	23(1)
C(21A)	9901(5)	4647(4)	-1268(4)	23(1)
C(22A)	9258(4)	5271(4)	-786(4)	23(1)
C(23A)	8426(4)	5036(4)	-131(4)	17(1)
C(24A)	8991(4)	3708(4)	2973(3)	12(1)
C(25A)	9126(5)	4354(4)	3531(4)	21(1)
C(26A)	10134(5)	4474(5)	3694(4)	27(2)
C(27A)	11014(5)	3919(4)	3289(4)	24(2)
C(28A)	10871(5)	3312(5)	2742(4)	23(2)
C(29A)	9853(4)	3183(4)	2589(4)	13(1)
Pd(1B)	7510(1)	7653(1)	3295(1)	8(1)
I(1B)	7917(1)	6617(1)	4562(1)	13(1)
I(2B)	7097(1)	6333(1)	2395(1)	15(1)
P(1B)	7806(1)	8797(1)	4052(1)	10(1)
P(2B)	7276(1)	8607(1)	2229(1)	10(1)
N(1B)	9551(3)	8935(3)	2470(3)	10(1)
C(1B)	9042(4)	8768(4)	4428(4)	11(1)
C(2B)	9029(4)	8502(4)	5293(4)	13(1)
C(3B)	9962(5)	8496(4)	5605(4)	16(1)
C(4B)	10899(4)	8743(4)	5086(3)	16(1)
C(5B)	10926(4)	8987(4)	4242(4)	13(1)

C(6B)	9999(4)	9032(4)	3887(3)	11(1)
C(7B)	10107(4)	9334(4)	2972(3)	10(1)
C(8B)	10812(4)	9981(4)	2656(4)	16(1)
C(9B)	10984(4)	10219(4)	1801(4)	16(1)
C(10B)	10446(4)	9793(4)	1272(4)	17(1)
C(11B)	9740(4)	9159(4)	1615(4)	12(1)
C(12B)	9234(4)	8677(3)	1024(3)	12(1)
C(13B)	9861(4)	8470(4)	215(3)	15(1)
C(14B)	9475(4)	8006(4)	-382(4)	16(1)
C(15B)	8440(5)	7758(4)	-197(4)	18(1)
C(16B)	7787(4)	7935(4)	587(3)	13(1)
C(17B)	8172(4)	8407(4)	1214(3)	12(1)
C(18B)	6722(4)	9042(3)	4952(3)	11(1)
C(19B)	5778(4)	8633(4)	5029(4)	18(1)
C(20B)	4899(5)	8853(4)	5681(4)	23(1)
C(21B)	4970(5)	9515(4)	6241(4)	18(1)
C(22B)	5904(5)	9933(4)	6160(4)	24(1)
C(23B)	6791(5)	9709(4)	5525(3)	20(1)
C(24B)	5956(4)	8744(4)	2000(3)	11(1)
C(25B)	5732(5)	9402(5)	1443(4)	27(2)
C(26B)	4728(6)	9517(6)	1235(5)	41(2)
C(27B)	3934(5)	8983(5)	1629(4)	31(2)
C(28B)	4123(5)	8341(4)	2209(4)	26(2)
C(29B)	5140(4)	8221(4)	2387(4)	18(1)
Cl(1A)	1692(1)	7302(1)	2346(1)	55(1)
Cl(2A)	1103(1)	6581(1)	4100(1)	41(1)
C(30A)	673(5)	6836(5)	3116(4)	37(2)
Cl(1B)	6538(2)	8260(1)	8541(1)	46(1)
Cl(2B)	6501(1)	7511(1)	6875(1)	30(1)
C(30B)	5737(5)	8012(5)	7820(4)	30(2)

(*rac*-PNP-H$_2$)PdI$_2$ (*rac*-8, MSW12)

Table D.2.9. Crystal data and structure refinement for MSW12 (CCDC 826391)

Empirical formula	$C_{29}H_{23}NP_2I_2Pd \bullet C_4H_8O$	
Formula weight	879.73	
Crystallization Solvent	THF/dichlormethane/pentane	
Crystal Habit	Block	
Crystal size	0.27 x 0.22 x 0.15 mm^3	
Crystal color	Red/brown	
Data Collection		
Type of diffractometer	Bruker KAPPA APEX II	
Wavelength	0.71073 Å MoKα	
Data Collection Temperature	100(2) K	
θ range for 9864 reflections used in lattice determination	2.61 to 35.39°	
Unit cell dimensions	a = 11.6216(5) Å b = 10.6917(4) Å c = 25.0348(10) Å	α= 90° β= 99.455(2)° γ = 90°
Volume	3068.4(2) Å^3	
Z	4	
Crystal system	Monoclinic	
Space group	P $2_1/n$	
Density (calculated)	1.904 Mg/m^3	
F(000)	1704	
Data collection program	Bruker APEX2 v2009.7-0	
θ range for data collection	2.08 to 35.84°	
Completeness to θ = 35.84°	91.0 %	
Index ranges	$-17 \le h \le 17$, $-16 \le k \le 17$, $-39 \le l \le 41$	
Data collection scan type	ω scans; 6 settings	
Data reduction program	Bruker SAINT-Plus v7.66A	
Reflections collected	40735	
Independent reflections	13072 [R_{int}= 0.0316]	
Absorption coefficient	2.749 mm^{-1}	
Absorption correction	Semi-empirical from equivalents	
Max. and min. transmission	0.7471 and 0.6284	

Structure Solution and Refinement

Structure solution program	SHELXS-97 (Sheldrick, 2008)
Primary solution method	Direct methods
Secondary solution method	Difference Fourier map
Hydrogen placement	Difference Fourier map
Structure refinement program	SHELXL-97 (Sheldrick, 2008)
Refinement method	Full matrix least-squares on F^2
Data / restraints / parameters	13072 / 0 / 485
Treatment of hydrogen atoms	Unrestrained
Goodness-of-fit on F^2	1.885
Final R indices [I>2σ(I), 10348 reflections]	R1 = 0.0422, *w*R2 = 0.0613
R indices (all data)	R1 = 0.0588, *w*R2 = 0.0629
Type of weighting scheme used	Sigma
Weighting scheme used	$w=1/\sigma^2(Fo^2)$
Max shift/error	0.005
Average shift/error	0.000
Largest diff. peak and hole	3.861 and -2.039 e.Å^{-3}

Table D.2.10. Atomic coordinates (x 10^4) and equivalent isotropic displacement parameters (Å^{2}x 10^3) for MSW12 (CCDC 826391). U(eq) is defined as the trace of the orthogonalized U^{ij} tensor.

	x	y	z	U_{eq}
Pd(1)	311(1)	113(1)	944(1)	15(1)
I(1)	-1758(1)	-929(1)	970(1)	23(1)
I(2)	975(1)	-1680(1)	336(1)	22(1)
P(1)	5(1)	1576(1)	1558(1)	17(1)
P(2)	2057(1)	983(1)	888(1)	17(1)
N(1)	1508(2)	-324(2)	2076(1)	17(1)
C(1)	-649(2)	1051(2)	2136(1)	19(1)
C(2)	-1492(3)	1786(3)	2317(1)	23(1)
C(3)	-2009(3)	1415(3)	2756(1)	29(1)
C(4)	-1700(3)	283(3)	3005(1)	32(1)
C(5)	-867(3)	-452(3)	2830(1)	26(1)
C(6)	-323(2)	-96(2)	2401(1)	20(1)
C(7)	602(2)	-904(2)	2241(1)	19(1)
C(8)	545(3)	-2219(3)	2275(1)	24(1)
C(9)	1457(3)	-2922(2)	2151(1)	25(1)
C(10)	2396(3)	-2324(2)	1993(1)	22(1)
C(11)	2390(2)	-1022(2)	1948(1)	18(1)
C(12)	3410(2)	-388(2)	1778(1)	18(1)
C(13)	4510(3)	-703(3)	2064(1)	24(1)
C(14)	5521(3)	-201(3)	1939(1)	28(1)
C(15)	5474(3)	613(3)	1510(2)	29(1)
C(16)	4415(3)	924(2)	1212(1)	24(1)
C(17)	3363(2)	448(2)	1339(1)	19(1)
C(18)	-794(2)	2964(2)	1291(1)	20(1)
C(19)	-283(3)	4133(2)	1408(1)	23(1)
C(20)	-818(3)	5205(3)	1172(1)	28(1)
C(21)	-1862(3)	5115(3)	828(1)	29(1)
C(22)	-2393(3)	3965(3)	713(1)	30(1)
C(23)	-1850(3)	2874(3)	941(1)	25(1)
C(24)	2167(2)	2682(2)	944(1)	16(1)
C(25)	2763(3)	3282(2)	1398(1)	21(1)
C(26)	2807(3)	4576(2)	1421(1)	24(1)
C(27)	2254(3)	5276(2)	991(1)	25(1)
C(28)	1661(3)	4698(2)	538(1)	23(1)
C(29)	1620(3)	3396(3)	509(1)	21(1)
C(40)	10575(4)	8176(4)	5072(2)	41(1)
C(43)	9556(4)	6482(4)	5269(2)	54(1)
C(41)	10178(6)	8458(5)	5603(2)	68(2)
C(42)	9597(6)	7337(4)	5743(2)	61(1)
O(1)	9779(2)	7262(2)	4828(1)	50(1)

Chapter 4 X-Ray Crystallographic Tables

[(^{tBu}DAB$_{Me}$)Pd(η^3-(C$_3$H$_4$)CH$_2$OCH$_2$CF$_3$)](BF$_4$) (24, msw27)

Table 4.D.1. Crystal data and structure analysis details for msw27

Empirical formula	C39 H58 B Cl2 F7 N2 O Pd
Formula weight	891.98
Crystallization solvent	CH_2Cl_2
Crystal shape	blade
Crystal color	orange

Data Collection

Preliminary photograph(s)	rotation	
Type of diffractometer	Bruker SMART 1000 CCD	
Wavelength	0.71073 Å MoK	
Data collection temperature	100 K	
Theta range for 4845 reflections used in lattice determination	2.35 to 29.56°	
Unit cell dimensions	a = 16.0798(7) Å b = 24.0835(11) Å c = 11.2791(5) Å	α= 90° β= 97.999(2)° γ = 90°
Volume	4325.4(3) Å^3	
Z	4	
Crystal system	monoclinic	
Space group	P2(1)/c	
Density (calculated)	1.370 g/cm^3	
F(000)	1848	
Theta range for data collection	1.69 to 26.43°	
Completeness to theta = 26.43°	99.8%	
Index ranges	-20 ≤ h ≤ 20, -20 ≤ k ≤ 20, -13 ≤ l ≤ 14	
Reflections collected	105716	
Independent reflections	8880 [R_{int}= 0.0381]	
Absorption correction	None	
Max. and min. transmission	0.9190 and 0.7654	

Structure Solution and Refinement

Refinement method	Full-matrix least-squares on F^2
Data / restraints / parameters	8880 / 0 / 492
Goodness-of-fit on F^2	1.008
Final R indices [I>2 ∫(I), 13607 reflections]	R1 = 0.0305, wR2 = 0.0727
R indices (all data)	R1 = 0.0337, wR2 = 0.0754
Largest diff. peak and hole	1.091and -1.13 e·Å^{-3}

Table D.4.2. Atomic coordinates (x 10^4) and equivalent isotropic displacement parameters (Å^{2}x 10^3) for 14. U(eq) is defined as one third of the trace of the orthogonalized U^{ij} tensor.

	x	y	z	U(eq)
Pd(1)	4140(1)	1438(1)	4588(1)	13(1)
C(46)	4662(2)	145(1)	1648(2)	32(1)
B(1)	3945(2)	1371(1)	9547(2)	24(1)
Cl(2)	3781(1)	45(1)	2401(1)	46(1)
Cl(1)	5483(1)	473(1)	2582(1)	49(1)
F(3)	4169(1)	867(1)	9108(1)	44(1)
F(4)	3113(1)	1374(1)	9631(3)	108(1)
N(1)	4986(1)	1944(1)	3807(1)	13(1)
C(2)	6101(1)	2581(1)	4600(2)	15(1)
N(2)	3368(1)	1844(1)	3228(2)	15(1)
C(4)	1988(1)	2218(1)	3402(2)	16(1)
C(5)	4669(1)	2202(1)	2854(2)	14(1)
C(6)	6912(1)	2682(1)	5162(2)	17(1)
C(7)	774(1)	1650(1)	2890(2)	17(1)
C(8)	2469(1)	1789(1)	3056(2)	15(1)
C(9)	3738(1)	2143(1)	2518(2)	14(1)
C(10)	2121(1)	1291(1)	2613(2)	17(1)
O	2086(1)	621(1)	6228(1)	26(1)
C(12)	5839(1)	2041(1)	4329(2)	14(1)
C(13)	1117(1)	2156(1)	3305(2)	16(1)
C(14)	7186(1)	1682(1)	5168(2)	16(1)
C(15)	1258(1)	1214(1)	2533(2)	17(1)
C(16)	6370(1)	1593(1)	4615(2)	15(1)
C(17)	7441(1)	2228(1)	5437(2)	18(1)
F(5)	1605(1)	-312(1)	7325(2)	44(1)
C(19)	839(1)	661(1)	2135(2)	21(1)
C(20)	3351(1)	879(1)	5394(2)	21(1)
C(21)	7425(1)	643(1)	5073(2)	25(1)
C(22)	7204(1)	3275(1)	5502(2)	22(1)
C(23)	7799(1)	1202(1)	5505(2)	20(1)
C(24)	4088(1)	984(1)	6197(2)	24(1)
C(25)	577(1)	2628(1)	3697(2)	20(1)
F(7)	1177(1)	420(1)	8133(1)	37(1)
C(27)	2511(1)	1057(1)	5706(2)	24(1)
C(28)	3298(1)	2443(1)	1457(2)	20(1)
C(29)	5137(1)	2551(1)	2076(2)	21(1)
C(30)	6630(2)	3713(1)	4830(3)	45(1)
C(31)	1863(2)	134(1)	7963(2)	30(1)
C(32)	4866(1)	902(1)	5817(2)	25(1)
C(33)	526(2)	392(1)	3225(2)	31(1)
F(6)	2219(1)	-43(1)	9030(2)	49(1)
C(35)	890(2)	3192(1)	3319(3)	37(1)
C(36)	1451(2)	260(1)	1652(3)	33(1)
C(37)	621(2)	2607(1)	5061(2)	35(1)
C(38)	8015(2)	1182(1)	6873(2)	34(1)
C(39)	2470(1)	481(1)	7388(2)	26(1)
C(44)	-343(1)	2572(1)	3147(2)	28(1)

C(41)	8085(2)	3373(1)	5204(3)	39(1)
C(43)	97(2)	758(1)	1149(2)	32(1)
C(42)	8607(1)	1294(1)	4949(3)	32(1)
C(40)	7188(3)	3355(1)	6834(3)	71(1)
F(2)	4389(1)	1476(1)	10640(2)	65(1)
F(1)	4074(2)	1780(1)	8789(2)	98(1)

[(^{Me}DAB$_{Me}$)Pd(μ−OH)(μ−OCH$_2$CF$_3$)](BF$_4$)$_2$ (27, msw25)

Table D.4.3. Crystal data and structure analysis details for msw25

Empirical formula	C48.50 H61 B2 Cl F20 N4 O5 Pd2
Formula weight	1429.88
Crystallization solvent	CH_2Cl_2/TFE
Crystal shape	block
Crystal color	yellow
Crystal size	0.26 x 0.30 x 0.36 mm

Data Collection

Preliminary photograph(s)	rotation	
Type of diffractometer	Bruker APEX-II CCD	
Wavelength	0.71073 Å MoK	
Data collection temperature	130 K	
Theta range for 9735 reflections used in lattice determination	2.42 to 34.15°	
Unit cell dimensions	a = 13.5306(6) Å b = 25.9279(13) Å c = 17.8268(9) Å	⟨= 90° ®= 109.119(2)° © = 90°
Volume	5909.0(5) Å^3	
Z	4	
Crystal system	monoclinic	
Space group	P 1 21/c 1 (# 14)	
Density (calculated)	1.607 g/cm^3	
F(000)	2876	
Theta range for data collection	1.6 to 38.2°	
Completeness to theta = 25.00°	99.5%	
Index ranges	-22 ″ h ″ 23, -44 ″ k ″ 43, -30 ″ l ″ 29	
Data collection scan type	and scans	
Reflections collected	277146	
Independent reflections	30556 [R_{int}= 0.0612]	
Reflections > 2σ(I)	22553	
Average σ(I)/(net I)	0.0412	
Absorption coefficient	0.76 mm^{-1}	
Absorption correction	Semi-empirical from equivalents	

Max. and min. transmission	1.0000 and 0.9049

Structure Solution and Refinement

Primary solution method	iterative
Secondary solution method	difmap
Hydrogen placement	geom
Refinement method	Full-matrix least-squares on F^2
Data / restraints / parameters	30556 / 0 / 753
Treatment of hydrogen atoms	constr
Goodness-of-fit on F^2	4.82
Final R indices [I>2 ∫(I), 22553 reflections]	R1 = 0.0821, wR2 = 0.1549
R indices (all data)	R1 = 0.1134, wR2 = 0.1561
Type of weighting scheme used	calc
Weighting scheme used	calc w=1/[^2^(Fo^2^)]
Max shift/error	0.001
Average shift/error	0.000
Largest diff. peak and hole	3.38 and -3.54 $e \cdot Å^{-3}$

Table D.4.4. Atomic coordinates (x 10^4) and equivalent isotropic displacement parameters (Å^{2}x 10^3) for msw25. U(eq) is defined as one third of the trace of the orthogonalized U^{ij} tensor.

	x	y	z	U_{eq}
Pd(1)	6553(1)	3518(1)	6545(1)	20(1)
Pd(2)	4329(1)	3242(1)	5455(1)	19(1)
F(1)	6909(2)	2369(1)	6711(1)	42(1)
F(2)	6682(3)	1795(1)	5797(2)	56(1)
F(3)	5354(2)	2119(1)	6049(2)	49(1)
O(1)	5850(2)	3110(1)	5534(1)	22(1)
O(2)	5101(2)	3429(1)	6611(1)	23(1)
N(1)	8001(2)	3613(1)	6516(2)	25(1)
N(2)	7168(2)	3941(1)	7502(2)	22(1)
N(3)	3555(2)	3083(1)	4316(2)	21(1)
N(4)	2886(2)	3406(1)	5413(2)	22(1)
C(41)	6227(3)	2634(1)	5368(2)	27(1)
C(1)	8604(3)	3889(1)	7063(2)	27(1)
C(42)	6283(3)	2228(2)	5976(2)	34(1)
C(2)	8141(3)	4077(1)	7652(2)	26(1)
C(3)	9714(3)	4021(2)	7143(3)	37(1)
C(4)	8734(3)	4404(2)	8339(2)	34(1)
C(5)	8302(3)	3377(2)	5883(2)	31(1)
C(6)	8903(3)	2929(2)	6034(3)	38(1)
C(7)	9083(3)	2692(2)	5396(3)	50(1)
C(8)	8682(4)	2890(2)	4641(3)	53(1)
C(9)	8111(4)	3337(2)	4511(3)	46(1)
C(10)	7903(3)	3598(2)	5129(2)	34(1)
C(11)	9327(4)	2697(2)	6857(3)	53(1)
C(12)	7261(4)	4080(2)	4991(3)	43(1)
C(13)	6560(3)	4087(1)	7995(2)	24(1)
C(14)	5865(3)	4508(2)	7747(2)	30(1)
C(15)	5251(3)	4624(2)	8199(3)	40(1)
C(16)	5313(4)	4351(2)	8879(3)	41(1)
C(17)	5998(3)	3944(2)	9100(2)	40(1)
C(18)	6627(3)	3795(2)	8660(2)	30(1)
C(19)	5829(4)	4809(2)	7024(3)	42(1)
C(20)	7336(3)	3343(2)	8884(3)	41(1)
C(21)	2570(3)	3175(1)	4078(2)	22(1)
C(22)	2163(3)	3355(1)	4722(2)	24(1)
C(23)	1864(3)	3110(2)	3255(2)	30(1)
C(24)	1028(3)	3454(2)	4563(2)	31(1)
C(25)	4076(3)	2893(1)	3791(2)	21(1)
C(26)	4557(3)	3243(2)	3431(2)	26(1)
C(27)	5065(3)	3043(2)	2943(2)	29(1)
C(28)	5080(3)	2524(2)	2810(2)	33(1)
C(29)	4608(3)	2187(2)	3180(2)	30(1)
C(30)	4099(3)	2360(1)	3685(2)	24(1)
C(31)	4512(3)	3811(2)	3564(2)	34(1)
C(32)	3632(3)	1997(2)	4138(2)	31(1)
C(33)	2650(3)	3564(2)	6100(2)	25(1)

C(34)	2356(3)	3184(2)	6537(2)	29(1)
C(35)	2178(3)	3348(2)	7223(2)	38(1)
C(36)	2324(3)	3846(2)	7476(2)	41(1)
C(37)	2628(3)	4212(2)	7029(3)	42(1)
C(38)	2807(3)	4075(2)	6336(2)	34(1)
C(39)	2256(4)	2630(2)	6293(3)	41(1)
C(40)	3116(4)	4469(2)	5833(3)	46(1)
F(4)	2296(2)	4262(1)	3883(2)	48(1)
F(5)	654(2)	4423(1)	3086(2)	74(1)
F(6)	1878(3)	5063(1)	3417(2)	62(1)
F(7)	1983(3)	4422(1)	2583(2)	64(1)
B(1)	1706(4)	4548(2)	3251(3)	44(1)
F(8)	1159(2)	1398(1)	3956(2)	66(1)
F(9)	1132(3)	2243(1)	4209(3)	93(1)
F(10)	503(4)	1697(2)	4872(2)	98(1)
F(11)	-377(2)	1795(1)	3598(2)	80(1)
B(2)	595(4)	1783(2)	4156(3)	40(1)
F(12)	5636(3)	5877(2)	9370(3)	117(2)
F(13)	6843(3)	6395(1)	9330(2)	90(1)
F(14)	6186(4)	5848(2)	8396(2)	119(2)
O(3)	7531(4)	5574(2)	10426(3)	85(1)
C(43)	6496(5)	5906(2)	9169(3)	64(2)
C(44)	7275(5)	5527(2)	9596(4)	69(2)
F(15)	6709(4)	4395(2)	2715(2)	100(1)
F(16)	8242(4)	4425(3)	2737(3)	168(3)
F(17)	7413(5)	3722(2)	2426(3)	132(2)
O(4)	6859(5)	4915(2)	1415(3)	110(2)
C(45)	7297(5)	4221(2)	2315(4)	67(2)
C(46)	7016(6)	4374(2)	1519(4)	81(2)
F(18)	9446(3)	4734(1)	1174(2)	95(1)
F(19)	10069(3)	4468(2)	280(2)	108(2)
F(20)	8568(3)	4210(2)	283(2)	103(1)
O(5)	9602(4)	3774(2)	1827(3)	94(1)
C(47)	9549(5)	4318(3)	748(3)	75(2)
C(48)	10072(5)	3899(3)	1272(3)	73(2)
C(49)	809(15)	5367(7)	5716(10)	118(6)
Cl(1)	-21(13)	5271(6)	4594(9)	614(10)

Appendix A X-Ray Crystallographic Tables

$(PNP)_2(PNP\text{-}H_2)Au_6Cl_2$ (3, msw09)

Table D.A.1. Crystal data and structure analysis details for msw09

Empirical formula	C93.84 H77.91 Au6 Cl9.54 N3 P6
Formula weight	2953.59
Crystallization solvent	CH_cCl_2/pentane
Crystal shape	rough
Crystal color	colorless
Crystal size	0.18 x 0.2 x 0.22 mm

Data Collection

Preliminary photograph(s)	rotation	
Type of diffractometer	Bruker APEX-II CCD	
Wavelength	0.71073 Å MoK	
Data collection temperature	100 K	
Theta range for 9829 reflections used in lattice determination	2.26 to 29.41°	
Unit cell dimensions	a = 13.6566(11) Å b = 43.863(3) Å c = 15.8517(13) Å	α= 90° β= 90.927(4)° γ = 90°
Volume	9494.3(13) $Å^3$	
Z	4	
Crystal system	monoclinic	
Space group	P 1 21/c 1 (# 14)	
Density (calculated)	2.065 g/cm^3	
F(000)	5549	
Theta range for data collection	1.8 to 30.1°	
Completeness to theta = 25.00°	100.0%	
Index ranges	$-19 \le h \le 14$, $-60 \le k \le 60$, $-21 \le l \le 22$	
Data collection scan type	and scans	
Reflections collected	149294	
Independent reflections	26931 [R_{int}= 0.0443]	
Reflections > 2σ(I)	22586	
Average σ(I)/(net I)	0.0343	
Absorption coefficient	9.65 mm^{-1}	

Absorption correction	Semi-empirical from equivalents
Max. and min. transmission	0.7460 and 0.5995

Structure Solution and Refinement

Primary solution method	dual
Secondary solution method	difmap
Hydrogen placement	geom
Refinement method	Full-matrix least-squares on F^2
Data / restraints / parameters	26931 / 6 / 1085
Treatment of hydrogen atoms	constr
Goodness-of-fit on F^2	1.73
Final R indices [I>2σ(I), 22586 reflections]	R1 = 0.0346, wR2 = 0.0489
R indices (all data)	R1 = 0.0473, wR2 = 0.0499
Type of weighting scheme used	calc
Weighting scheme used	calc w=1/[^2^(Fo^2^)]
Max shift/error	0.033
Average shift/error	0.001
Largest diff. peak and hole	2.46 and -1.66 $e \cdot Å^{-3}$

Table D.A.2. Atomic coordinates (x 10^4) and equivalent isotropic displacement parameters ($Å^2$x 10^3) for msw09. U(eq) is defined as one third of the trace of the orthogonalized U^{ij} tensor.

	x	y	z	U_{eq}
Au(1)	2152(1)	412(1)	3215(1)	21(1)
Au(2)	1870(1)	1208(1)	2286(1)	17(1)
Au(3)	3810(1)	934(1)	2772(1)	15(1)
Au(4)	4311(1)	1604(1)	2123(1)	18(1)
Au(5)	4875(1)	1165(1)	700(1)	17(1)
Au(6)	5266(1)	2020(1)	636(1)	28(1)
Cl(1)	3233(1)	41(1)	3660(1)	38(1)
Cl(2)	4989(1)	2475(1)	1314(1)	34(1)
P(1)	1090(1)	776(1)	2783(1)	19(1)
P(2)	2644(1)	1646(1)	1820(1)	19(1)
P(3)	3430(1)	1092(1)	4128(1)	18(1)
P(4)	5955(1)	1567(1)	2498(1)	20(1)
P(5)	4288(1)	757(1)	1457(1)	15(1)
P(6)	5487(1)	1575(1)	-38(1)	26(1)
N(1)	361(2)	1614(1)	2987(2)	24(1)
N(2)	5335(3)	1410(1)	4261(2)	25(1)
N(3)	6429(2)	803(1)	110(2)	19(1)
C(1)	231(3)	621(1)	1991(3)	21(1)
C(2)	-257(3)	348(1)	2137(3)	26(1)
C(3)	-903(3)	235(1)	1539(3)	31(1)
C(4)	-1075(3)	390(1)	787(3)	32(1)
C(5)	-589(3)	658(1)	643(3)	30(1)
C(6)	68(3)	774(1)	1237(3)	25(1)
C(7)	328(3)	885(1)	3681(3)	24(1)
C(8)	323(3)	704(1)	4396(3)	27(1)
C(9)	-146(3)	791(1)	5129(3)	38(1)
C(10)	-619(4)	1068(1)	5146(3)	43(1)
C(11)	-652(3)	1253(1)	4445(3)	36(1)
C(12)	-185(3)	1162(1)	3698(3)	26(1)
C(13)	-251(3)	1371(1)	2955(3)	23(1)
C(14)	-865(3)	1312(1)	2277(3)	27(1)
C(15)	-854(3)	1504(1)	1584(3)	29(1)
C(16)	-210(3)	1746(1)	1588(3)	27(1)
C(17)	389(3)	1792(1)	2297(3)	21(1)
C(18)	1115(3)	2048(1)	2349(3)	22(1)
C(19)	769(3)	2332(1)	2568(3)	30(1)
C(20)	1395(4)	2579(1)	2655(3)	36(1)
C(21)	2386(3)	2541(1)	2527(3)	28(1)
C(22)	2745(3)	2256(1)	2319(2)	22(1)
C(23)	2125(3)	2007(1)	2217(2)	21(1)
C(24)	2416(3)	1691(1)	679(2)	21(1)
C(25)	1927(3)	1466(1)	226(3)	24(1)
C(26)	1749(3)	1499(1)	-632(3)	31(1)
C(27)	2058(4)	1758(1)	-1041(3)	34(1)
C(28)	2543(4)	1985(1)	-593(3)	38(1)
C(29)	2722(3)	1952(1)	260(3)	30(1)

C(30)	4131(3)	900(1)	4949(2)	20(1)
C(31)	4706(3)	656(1)	4733(3)	30(1)
C(32)	5253(4)	501(1)	5335(3)	34(1)
C(33)	5245(4)	594(1)	6156(3)	37(1)
C(34)	4679(4)	841(1)	6386(3)	48(2)
C(35)	4113(4)	992(1)	5789(3)	37(1)
C(36)	3237(3)	1492(1)	4401(2)	23(1)
C(37)	2281(4)	1597(1)	4252(3)	32(1)
C(38)	2027(4)	1894(1)	4421(3)	40(1)
C(39)	2725(5)	2092(1)	4755(4)	52(2)
C(40)	3654(4)	1992(1)	4903(3)	44(2)
C(41)	3950(4)	1691(1)	4717(3)	30(1)
C(42)	4967(3)	1595(1)	4856(3)	28(1)
C(43)	5501(4)	1686(1)	5551(3)	50(2)
C(44)	6425(4)	1565(1)	5680(3)	58(2)
C(45)	6794(4)	1364(1)	5091(3)	42(1)
C(46)	6239(3)	1300(1)	4372(3)	29(1)
C(47)	6613(3)	1112(1)	3675(3)	23(1)
C(48)	7105(3)	840(1)	3851(3)	35(1)
C(49)	7435(3)	657(1)	3210(3)	36(1)
C(50)	7266(3)	738(1)	2380(3)	31(1)
C(51)	6807(3)	1014(1)	2187(3)	22(1)
C(52)	6487(3)	1203(1)	2832(3)	21(1)
C(53)	6457(3)	1866(1)	3165(3)	25(1)
C(54)	7453(4)	1882(1)	3323(3)	41(1)
C(55)	7840(4)	2110(1)	3832(4)	57(2)
C(56)	7229(5)	2321(1)	4188(3)	50(2)
C(57)	6232(4)	2313(1)	4024(3)	42(1)
C(58)	5853(4)	2085(1)	3505(3)	28(1)
C(59)	3257(3)	576(1)	897(2)	18(1)
C(60)	2841(3)	306(1)	1192(3)	23(1)
C(61)	2016(3)	186(1)	798(3)	28(1)
C(62)	1596(3)	329(1)	106(3)	31(1)
C(63)	2012(3)	590(1)	-205(3)	33(1)
C(64)	2837(3)	716(1)	195(3)	28(1)
C(65)	5188(3)	446(1)	1547(2)	17(1)
C(66)	5190(3)	269(1)	2283(2)	20(1)
C(67)	5803(3)	23(1)	2384(3)	22(1)
C(68)	6426(3)	-61(1)	1743(3)	23(1)
C(69)	6426(3)	108(1)	1005(3)	20(1)
C(70)	5838(3)	367(1)	897(2)	15(1)
C(71)	5949(3)	535(1)	85(2)	16(1)
C(72)	5626(3)	407(1)	-662(3)	29(1)
C(73)	5785(4)	560(1)	-1410(3)	42(1)
C(74)	6271(3)	836(1)	-1390(3)	30(1)
C(75)	6579(3)	948(1)	-620(2)	19(1)
C(76)	7164(3)	1239(1)	-578(3)	22(1)
C(77)	8131(3)	1228(1)	-860(3)	29(1)
C(78)	8730(4)	1481(1)	-833(3)	37(1)
C(79)	8362(4)	1752(1)	-530(3)	36(1)
C(80)	7411(4)	1769(1)	-267(3)	35(1)
C(81)	6787(3)	1520(1)	-292(3)	27(1)
C(82)	4905(4)	1595(1)	-1086(3)	31(1)
C(83)	4276(3)	1372(1)	-1376(3)	32(1)

C(84)	3804(4)	1397(1)	-2156(3)	43(1)
C(85)	3965(5)	1649(1)	-2646(3)	58(2)
C(86)	4562(6)	1869(1)	-2373(3)	73(2)
C(87)	5031(5)	1848(1)	-1606(3)	54(2)
Cl(3)	8044(1)	2667(1)	6476(1)	75(1)
Cl(4)	7904(2)	2107(1)	7482(1)	104(1)
C(88)	7340(5)	2383(2)	6880(5)	82(2)
Cl(5)	2024(2)	464(1)	6525(1)	100(1)
Cl(6)	1282(1)	-27(1)	5477(1)	79(1)
C(89)	2269(5)	213(2)	5709(4)	79(2)
Cl(7)	8034(2)	751(1)	6880(1)	106(1)
Cl(8)	9443(2)	503(1)	8108(2)	112(1)
C(90)	8627(9)	437(2)	7306(5)	151(5)
Cl(9)	206(3)	2531(1)	4910(3)	60(1)
Cl(10)	-518(4)	1948(1)	5490(3)	71(1)
C(91)	194(11)	2318(3)	5558(10)	51(4)
Cl(11)	1893(3)	1652(1)	6524(3)	66(1)
Cl(12)	781(6)	1170(2)	7144(3)	114(2)
C(92)	969(19)	1420(6)	6292(14)	149(11)
C(93)	-64(14)	2132(4)	5880(13)	160(8)
C(94)	168(12)	1802(3)	6342(10)	130(6)
C(95)	89(8)	1613(2)	6993(7)	68(3)
C(96)	730(20)	1317(5)	7133(17)	240(20)
C(97)	1491(11)	1282(4)	6432(10)	114(5)

Appendix C X-ray Crystallographic Tables

[(^{tBu}DAB$_{Me}$)Pd(η^3-cyclohexenyl)](BF$_4$) (2, msw21)

Table D.C.1. Crystal data and structure analysis details for msw21

Empirical formula	C39 H59 B Cl2 F4 N2 Pd
Formula weight	819.99
Crystallization solvent	CH_2Cl_2
Crystal shape	needle
Crystal color	yellow
Crystal size	0.02 x 0.04 x 0.31 mm

Data Collection

Preliminary photograph(s)	rotation	
Type of diffractometer	Bruker APEX-II CCD	
Wavelength	0.71073 Å MoK	
Data collection temperature	100 K	
Theta range for 4825 reflections used in lattice determination	2.49 to 19.03°	
Unit cell dimensions	a = 32.5254(17) Å b = 11.0958(5) Å c = 24.1395(13) Å	a= 90° b= 112.589(3)° g = 90°
Volume	8043.5(7) Å^3	
Z	8	
Crystal system	monoclinic	
Space group	C 1 2/c 1 (# 15)	
Density (calculated)	1.354 g/cm^3	
F(000)	3424	
Theta range for data collection	1.8 to 27.3°	
Completeness to theta = 25.00°	99.9%	
Index ranges	-41 ≤ h ≤ 41, -14 ≤ k ≤ 13, -28 ≤ l ≤ 30	
Data collection scan type	and scans	
Reflections collected	73442	
Independent reflections	8353 [R_{int}= 0.1435]	
Reflections > 2s(I)	5091	

Average s(I)/(net I)	0.1262
Absorption coefficient	0.64 mm^{-1}
Absorption correction	Semi-empirical from equivalents
Max. and min. transmission	1.0000 and 0.9230

Structure Solution and Refinement

Primary solution method	direct
Secondary solution method	difmap
Hydrogen placement	geom
Refinement method	Full-matrix least-squares on F^2
Data / restraints / parameters	8353 / 0 / 456
Treatment of hydrogen atoms	constr
Goodness-of-fit on F^2	1.37
Final R indices [I>2s(I), 5091 reflections]	R1 = 0.0561, wR2 = 0.0584
R indices (all data)	R1 = 0.1288, wR2 = 0.0645
Type of weighting scheme used	calc
Weighting scheme used	calc w=1/[^2^(Fo^2^)]
Max shift/error	0.002
Average shift/error	0.000
Largest diff. peak and hole	0.61 and -0.72 $e \cdot Å^{-3}$

Table D.C.2. Atomic coordinates (x 10^4) and equivalent isotropic displacement parameters ($Å^2$x 10^3) for msw21. U(eq) is defined as one third of the trace of the orthogonalized U^{ij} tensor.

	x	y	z	U_{eq}
Pd(1)	7119(1)	9148(1)	6767(1)	14(1)
N(1)	6648(1)	10188(2)	6087(1)	12(1)
N(2)	7468(1)	9654(2)	6223(1)	12(1)
C(1)	6765(1)	10468(3)	5651(2)	13(1)
C(2)	7227(1)	10155(3)	5731(2)	11(1)
C(3)	6470(1)	11064(3)	5081(2)	19(1)
C(4)	7375(1)	10453(3)	5228(2)	20(1)
C(5)	6228(1)	10580(3)	6089(2)	11(1)
C(6)	5927(1)	9721(3)	6115(2)	15(1)
C(7)	5520(1)	10059(3)	6122(2)	15(1)
C(8)	5428(1)	11289(3)	6111(2)	17(1)
C(9)	5723(1)	12170(3)	6090(2)	14(1)
C(10)	6130(1)	11801(3)	6085(2)	16(1)
C(11)	5182(1)	9136(3)	6160(2)	18(1)
C(12)	5328(1)	7841(3)	6110(2)	50(2)
C(13)	5150(1)	9231(4)	6773(2)	44(1)
C(14)	4733(1)	9342(4)	5677(2)	56(2)
C(15)	5617(1)	13538(3)	6058(2)	22(1)
C(16)	5159(1)	13783(3)	6080(2)	49(2)
C(17)	5620(1)	14042(3)	5471(2)	37(1)
C(18)	5967(1)	14181(3)	6583(2)	30(1)
C(19)	7937(1)	9451(3)	6371(2)	13(1)
C(20)	8212(1)	10433(3)	6410(2)	12(1)
C(21)	8662(1)	10263(3)	6547(2)	13(1)
C(22)	8826(1)	9078(3)	6650(2)	14(1)
C(23)	8561(1)	8090(3)	6621(2)	12(1)
C(24)	8108(1)	8297(3)	6479(2)	13(1)
C(25)	8981(1)	11295(3)	6575(2)	17(1)
C(26)	8756(1)	12526(3)	6508(2)	23(1)
C(27)	9140(1)	11143(3)	6062(2)	28(1)
C(28)	9380(1)	11279(3)	7176(2)	34(1)
C(29)	8746(1)	6805(3)	6738(2)	19(1)
C(30)	9241(1)	6755(3)	6892(2)	56(2)
C(31)	8656(1)	6260(3)	7262(2)	37(1)
C(32)	8508(1)	6044(3)	6190(2)	45(1)
C(33)	7231(1)	8547(3)	7638(2)	20(1)
C(34)	7544(1)	7971(3)	7448(2)	20(1)
C(35)	7437(1)	6708(3)	7188(2)	26(1)
C(36)	7011(1)	6213(3)	7227(2)	27(1)
C(37)	6629(1)	7125(3)	6989(2)	27(1)
C(38)	6779(1)	8354(3)	7274(2)	17(1)
B(1)	7143(2)	13777(4)	5843(2)	21(1)
F(1)	7306(1)	12656(2)	6040(1)	58(1)
F(2)	7485(1)	14600(2)	6006(1)	50(1)
F(3)	6905(1)	13773(2)	5232(1)	32(1)
F(4)	6862(1)	14114(2)	6126(1)	54(1)

Cl(1)	3913(1)	2642(1)	4940(1)	61(1)
Cl(2)	2972(1)	2762(1)	4720(1)	50(1)
C(39)	3471(1)	3563(3)	4922(2)	44(1)